UNIVERSITY OF OTTAWA

Faculty of Pure and Applied Science

Department of Electrical Engineering

Ottawa, Canada

A THESIS:

AN IMMERSION PROBE FOR MEASUREMENT OF THE PLASMA ELECTRICAL CONDUCTIVITY AND HALL EFFECT

by

E. J. Stubbe

Submitted in partial fulfilment of
the requirements for the degree of
Doctor of Philosophy in Electrical
Engineering

ABSTRACT

The feasibility of measuring the spatial distribution of the electrical conductivity of plasmas by means of an immersed cylindrical plasma probe has been studied.

From a solution of the Maxwell-Helmholtz equation for this configuration, the response of the coil impedance to the presence of an isotropic or anisotropic plasma is predicted. Experiments in electrolytes, shock tube plasmas and mercury showed that the theoretical predictions are borne out in practice, thereby achieving an absolute measuring technique. The components of the electrical conductivity tensor are calculated for an argon plasma using the Shkarofsky method based on the Frost-Phelps momentum transfer cross-sections. The generally good agreement between predicted and measured probe response in anisotropic plasmas demonstrates the usefulness of this probe to detect Hall effects. The analysis is extended to deal with non-uniform plasmas with a conductivity profile of the form: $\sigma = \sigma_o + \frac{P_2}{r^2} + \frac{P_3}{r^3}$ resulting from boundary layer cooling effects.

An optimised parallel-T bridge, followed by two phase sensitive detectors, channeling the information from both the resistance and reactance change of the coil impedance, proved instrumental in achieving good sensitivity over a very wide range of conductivities.

ACKNOWLEDGEMENT

The author wishes to express his sincere thanks to Professor G.S. Glinski and Dr. P. Savic whose thoughtful supervision and encouragement provided continuing guidance for this work.

Gratitude is also due to Mr. A.J. Bachmeier, Head of the Gas Dynamics Laboratory, and Dr. D.C. MacPhail, Director of the Division of Mechanical Engineering, National Research Council of Canada, for permission to present this work as a thesis.

I would like to thank the many scientists whose discussions contributed a number of valuable ideas for this project. In particular, I would like to thank Dr. B.A. Wightman of the N.R.C. Computation Centre for adapting the Hankel function subroutines needed for the numerical work.

The technical assistance of E. Mills in the experimental work is also appreciated.

TABLE OF CONTENTS

PAGE

LIST OF SYMBOLS

a	coil radius
a_1	radius of inner layer of coil
a_2	radius of the outer layer of coil
a_s	speed of sound
$\overline{A}$	magnetic vector potential
b	outer radius of probe
$\overline{B}$	magnetic flux density
B_o	absolute value of magnetic flux density
c	stretched spatial coordinate (eq. 4.5)
C_p	specific heat at constant pressure
C	constant (Chapter II, eq. 2.20)
C	capacitance
C_s	stray capacitance
d	$= (k^2 + j\mu\omega)^{1/2}$
$\overline{D}$	electric displacement vector
e	electron charge
$\overline{\mathcal{E}}$	electric field
E	function of x (eq. 3.19)
E_o	function of x (eq. 1.28)
f	Shkarofsky correction coefficient (eq. 2.14)
f_o	frequency
F	$= s_o/s_1$
g	Shkarofsky correction coefficient (eq. 2.40)
G	$= s_3/s_1$
h	enthalpy (Chapter II)

h	$= a/b$ filling factor of coil
h_1	$= a_1/b$
h_2	$= a_2/b$
H	$= s_2/s_1$ Hall parameter
I	current
$I_m(k)$	modified Bessel function of first kind, order m
j	imaginary unit
$\bar{J}$	current density
$J_m(k)$	Bessel function of first kind, order m
k	integration variable
k	Boltzmann constant (Chapter II)
$K_m(k)$	modified Bessel function of second kind, order m
K_n	Nagaoka constant (eq. 1.30)
ℓ	coil length
l	distance (Chapter IV)
$\mathcal{L}$	inductance
m	$= jp_3\mu\omega d$
m_e	electron mass
M	mutual inductance
M_s	incident shock Mach number
n	$= (1 + jp_2\mu\omega)^{1/2}$ (Chapter IV)
n	number of turns per unit length
n_e	electron density
N	total number of turns
p	pressure

p	$= nb$ (Chapter I)
p	stretched time coordinate (Chapter IV)
p_2	profile coefficient (Chapter IV)
p_3	profile coefficient (Chapter IV)
P_i^j	associated Legendre functions
q	time interval (Chapter IV)
q	free charge density
Q	quality factor
Q	$= (4\mathcal{L}/C - R^2)^{1/2}$ (Appendix B)
Q_{en}	electron-neutral momentum transfer cross section
r	radius or radial coordinate
r	electron velocity exponent (Chapter II)
R	gas constant (Chapter II)
R	resistance
R_P	function for radial component of plasma magnetic field
R_R	function for radial component of reflected magnetic field
s	$= \sigma\mu\omega b^2$ (called s parameter)
s_1	$= s_T\sigma_P$ (Chapter III)
s_2	$= s_H\sigma_P$ (Chapter III)
s_3	$= s_P\sigma_P$ (Chapter III)
s_d	$= \epsilon\mu\omega^2 b^2$ (Chapter I)
s_H	$= \sigma_H/(\sigma_T{}^2 + \sigma_H{}^2)$
s_P	$= 1/\sigma_P$
s_T	$= \sigma_T/(\sigma_T{}^2 + \sigma_H{}^2)$
t	time

T	absolute temperature
T_P	function for azimuthal component of plasma magnetic field
T_R	function for azimuthal component of reflected magnetic field
u	integration variable (Chapter IV)
u	electron energy (Chapter II)
U	$= y^2 + jF$ (Chapter III)
v	velocity
V	electric potential
w	$= \ell/b$ length ratio parameter of coil
x	$= db$
y	$= kb$
$Y_m(k)$	Bessel function of second kind, order m
z	axial component
Z	impedance
Z_P	function for axial component of plasma magnetic field
Z_R	function for axial component of reflected magnetic field
α	degree of ionisation (Chapter II)
α	resistive calibration constant
β	reactive calibration constant
γ	ratio of specific heat
δ	$= (2/\sigma\mu\omega)^{1/2}$ skin depth
Δ	increment
$\overline{\Delta R}$	non-dimensional resistance change $(=\Delta R/\mu\omega a)$
$\overline{\Delta L}$	non-dimensional reactance change $(=\Delta L/\mu a)$

ϵ	dielectric constant
$\varkappa$	thermal diffusivity
λ	coil pitch
λ	thermal conductivity (Chapter IV)
ν	collision frequency
μ	magnetic permeability
ρ	density
σ	plasma conductivity
σ_{ij}	i,j component of the electrical conductivity tensor
σ_H	Hall component of electrical conductivity tensor
σ_P	parallel component of electrical conductivity tensor
σ_T	transverse component of electrical conductivity tensor
τ	inverse of the averaged total collision frequency
φ	azimuthal component
ω	circular frequency
ω_c	cyclotron frequency
$\bar{\bar{\nabla}}$	(Nabla) symbolic vectorial derivative

<u>Subscripts</u>

A	argon atoms
D	driving field component
ei	electron-ion
en	electron-neutral
g	gas
p	parallel
P	plasma field component

r	radial
R	reflected field component
s	series
z	axial
ϕ	azimuthal
< >	average quantity

INTRODUCTION

The growing interest in the field of plasma physics is mainly due to the fact that a gaseous plasma behaves as a conductor, with much higher electrical conductivity than any ordinary gas which makes it very attractive for numerous applications. Furthermore, in the presence of a magnetic field, a plasma exhibits some anisotropic behaviour. Theoretical treatment of this behaviour predicts the occurrence within a plasma of many intriguing phenomena unknown in other states of the matter, which have attracted the attention of astrophysicists and geologists, are being studied in the fields of communication and propulsion, and offer some attractive possibilities for MHD power generation and controlled thermonuclear fusion.

In view of this, the measurement of the electrical conductivity and the degree of anisotropy of a gaseous plasma is a very important task of the diagnostic study of plasmas and a survey of the literature will indicate that numerous schemes have been devised to deal with the problem.

The probe techniques developed for measuring the electrical conductivity in dense plasmas, can mainly be classified under two different categories, the direct contact methods, and the electrodeless or inductive methods.

Instruments of the first class are used extensively in chemistry, to investigate liquids, and in solid state physics to measure sheet conductivities of doped semiconductor crystals (e.g. the four-point probe). This method was used extensively in earlier days for diagnosing plasmas (Ref. 1, 2, 3). Even now, these methods are still being used with some success (Ref. 4, 5) to obtain reasonably accurate data in spite of the inevitable cooling of plasmas by the solid electrodes and the sheath formation, which leads to abnormal potential gradients.

The principle underlying the second class, the electrodeless or eddy current method, has long been exploited in the field of non-destructive testing of materials (Ref. 6, 7, 8). These methods were also used to determine the electrical conductivity in solids (Ref. 9, 10, 11, 12, 13) and was recently used by J. Neighbor (Ref. 14) to measure the anisotropic resistivity in crystals.

V. H. Blackman (Ref. 15) was probably the first to apply this idea to measure the conductivity of plasmas. Since then, numerous techniques have been developed, based on the impedance variation of a coil in the presence of a plasma. Detailed studies of the electromagnetic induction field, directed toward the full understanding of the phenomena (Ref. 16, 17, 18) indicate that basically two different methods could be used to measure the electrical conductivity. Either the reactive component of the coil impedance (Ref. 19, 20, 21, 22, 23), or the resistive component (Ref. 24, 25, 26) were used as the detecting quantity. A few methods utilise a combination of these two techniques by monitoring the variation in the quality factor of the probing coil (Ref. 27, 28). In some applications, the mutual coupling through the plasma between two or more coils was exploited (Ref. 29, 30).

Other schemes are based on the shielding by the plasma of an externally applied a.c. field, and use a pick-up coil to monitor the field disturbance which can be correlated to an effective plasma conductivity (Ref. 31).

Devices have been developed whereby the test conductor acts as a single turn coil which threads through the primary and secondary windings of a transformer (Ref. 32, 33, 34). Some very popular schemes involve the measurement of the conductivity and/or velocity of plasmas concurrently (Ref. 35, 36, 37).

When dealing with non-uniform plasmas, a number of methods have been worked out to explore the spatial gradient of the electrical conductivity (Ref. 38, 39, 40, 41, 42).

Exact analytical solutions predicting the response of a short coil completely immersed in an anisotropic conductor have been reported by Selamoglu and Maeder (Ref. 43) although this solution has limited utility as no insulating boundary is provided. Using a filamentary coil outside a conducting core, P. Savic et al. (Ref. 44) calculated and measured the Hall effect for an anisotropic semi-conductor.

Due to the large body of literature on this topic, this survey should be complemented by a study by K. Cruse (Ref. 45), who analyses various inductive and capacitive systems. A summary of the various probe conductor configurations, together with an extensive review of the literature is presented by P. Savic and E. Stubbe (Ref. 46), and A. Fuhs (Ref. 47) coordinates and summarises all important diagnostic methods in plasma research as they apply to conductivity and velocity measurements. With this wealth of studied and proven techniques, it may seem unnecessary to devote more effort on this subject. It is the purpose of this study to demonstrate that the immersed plasma conductivity probe, which was conceived by Olson and Lary (Ref. 48) to measure conductivities of flames, proves to be a powerful device for measuring plasma conductivities over a wide range of conductivities, regardless of whether or not the plasma is uniform or isotropic.

Indeed, the range of conductivities that can be measured with this device is extended to six orders of magnitude, from the electrolytic conductivity (1 mho/m) beyond the conductivity of mercury (10^6 mho/m). This was achieved by taking advantage of the information from both the resistive and reactive change of the coil impedance.

As far as diagnosing anisotropic plasmas is concerned, this is, to the author's knowledge, the first successful attempt of using an electrodeless device to detect Hall effects in gaseous plasmas. Furthermore, the small size of the probe is responsible for achieving a very good spatial resolution which makes it an attractive device for measuring conductivity profiles in plasmas.

The full potential of this type of probe has never been explored simply because of the disturbance it produces in plasmas. It will be shown that this major drawback can be partly overcome by proper probe design, fast response electronics, and a proper analysis of the cooling phenomena so that adequate corrections can be applied.

A last point to be emphasised is the development of an absolute measuring procedure, which is very important in the study of plasmas with conductivities in the range of 1000 mho/m, for which no suitable alternative calibration standards are available. To achieve this, one needs a rigorous mathematical analysis of the relevant field equations applied to the particular probe geometry. This is the reason why a large proportion of this study is devoted to theory.

The theoretical part comprises four chapters. The first chapter deals with the analysis of the probe response in uniform isotropic plasmas.

In order to compare the experimental data with the calculated electrical conductivities, a second chapter is devoted to the calculation of the components of the electrical conductivity tensor, using the Shkarofsky approach to plasma kinetic theory.

An exact analytical solution of the probe response in anisotropic plasmas is the object of a third chapter.

The theoretical part concludes with the study of thermal effects on the probe response and the resulting development of non-uniform conductivity profiles.

The experimental part of this work starts in Chapter V with a design study of the conductivity probe followed by a full description of the associated equipment and instrumentation.

In Chapter VI, the experimental data are analysed and compared with theory for isotropic uniform conductive media. This is followed by a discussion of the data in anisotropic plasmas. This chapter concludes with a comparison between measured and calculated thermal effects on the probe response in shock tubes.

Parts of this study dealing with the immersed probe performance in isotropic uniform conducting media were published under the title:

"An absolute immersion-type electrical plasma conductivity probe"

Proc. IEEE, vol. 56, No 9, September 1968.

A reprint is included at the end of this work.

PART I

THEORY AND NUMERICAL WORK

Chapter I

ANALYSIS OF THE INTERNAL COIL IMPEDANCE IN THE PRESENCE OF A UNIFORM, ISOTROPIC, ELECTRICALLY CONDUCTING MEDIUM

This chapter deals mainly with the rigorous analysis to calculate the coil impedance change. Starting with the presentation of an equivalent circuit to obtain the gross qualitative behaviour, the exact expressions are derived next, followed by the numerical solutions for different probe geometries. In some cases, one can avoid the labour of solving the exact equations; under such conditions approximate expressions are given for the low s regime. Since a practical coil differs from the ideal theoretical model, a section is devoted to the effect of a small number of turns on the coil response. Displacement currents are usually neglected in such treatment, but it is important to appreciate that, while this is so in most cases, measurements in low conducting electrolytes could exhibit discrepancies. This chapter closes with the modification needed in the theory when dealing with double layer coils which are used in most of the present experiments for the purpose of enhancing the sensitivity of the device.

1.1 Equivalent Circuit Presentation

The behaviour of an inductive plasma conductivity probe has often been explained in terms of a transformer analog network (Ref. 27, 46, 49).

When a coil is fed by an R.F. current, the resulting magnetic field produces eddy currents in any conductor in the vicinity of the coil. The driving current in the coil and the induced eddy currents, coupled by the magnetic field, form essentially the primary and secondary current, respectively, of a transformer, Fig. (1.a). If V is an R.F. voltage source, frequency ω, $\mathcal{L}_1$ and $\mathcal{L}_2$ are the inductances of the primary and secondary, R_1 and R_2 are their resistances, M the mutual inductance, the response of the circuit can be analysed with the equivalent circuit of Fig. (1.b). The loading of the secondary, which carries the eddy currents in the plasma, can be expressed as an effective change in the impedance of the primary:

$$\Delta Z = -\frac{Z_c^2}{Z_2} = \frac{\omega^2 M^2}{R_2^2 + \omega^2 \mathcal{L}_2^2} R_2 - j \frac{\omega^2 M^2}{R_2^2 + \omega^2 \mathcal{L}_2^2} \omega \mathcal{L}_2 \qquad (1.1)$$

After separating real and imaginary parts of the impedance change and introducing the plasma conductivity σ , which is proportional to $1/R_2$, we obtain:

$$\Delta R = \beta \frac{\sigma \omega^2}{1 + (\sigma \omega \mathcal{L}_2)^2} \qquad (1.2a)$$

$$\Delta \mathcal{L} = -\beta \frac{\sigma^2 \omega^2 \mathcal{L}_2}{1 + (\sigma \omega \mathcal{L}_2)^2} \qquad (1.2b)$$

wherein β is a constant.

The general trend of these expressions is shown in Fig. (1.c) and represents the qualitative behaviour of the device:

1. The conductivity appears in a product $\sigma\omega$.
2. The resistance changes linearly for small conductivities, rises to a maximum and decays to zero for infinite conductivity.
3. The reactance changes as $(\sigma\omega)^2$ for small conductivities and approaches asymptotically a fixed value for $\sigma\omega \rightarrow \infty$.

The main shortcoming of such a model is the absence of skin effect which becomes progressively more important for increasing values of $\sigma\omega$. Therefore, this analogy is only correct for small values of $\sigma\omega$ and breaks down at higher values of $\sigma\omega$.

1.2 Analysis

The following assumptions are made to obtain a simple but realistic model for the problem:

1. The coil consists of a finite number of loops (radius a) of wire of vanishingly thin radial dimension. The coil has a turn density $n(=N/\ell)$ and length ℓ. The coil is inserted into an insulating tube coaxial with the coil, outer radius b and theoretically infinite length (Fig. 2).

2. The coil is driven by a current source of frequency f_o, the coil current being small enough not to cause joule heating in the surrounding conductor.

3. The surrounding medium extends to infinity in all directions, is uniform, at rest and isotropic.

4. The dielectric constant and magnetic permeability of the medium are scalar and are assigned the values for

vacuum.

5. The electrical conductivity of the medium is finite and is of a scalar nature.

These approximations need some justification:

1. The first assumption eliminates the effects due to the coil thickness which modifies the electric field because the geometrical boundaries are different from those of the ideal model. It is possible that this assumption is violated in cases where proximity effect could occur (e.g. measurements in mercury as will be shown).

2. Since the probe is part of a parallel-T bridge, the current levels are quite small as the bridge is very sensitive around the balanced condition, so that the second assumption is satisfied in practice.

3. Since the probe dimensions are very small compared to the size of the conducting medium, it is safe to assume an infinite probing volume. Indeed, the dipole field of the probe decays as $1/r^3$, hence a volume with a typical dimension of ten times the probe size can be considered as infinite.

The plasma created around the probe is not uniform, except at time zero, due to cooling of the gas. This is a serious limitation which will be discussed in Chapter IV.

The plasma created behind the reflected shock is, strictly speaking, not at rest due to departures from ideal shock tube behaviour. A critical measure of the effect of the plasma motion on the probe response can be extracted from Maxwell's equations for a moving medium. The criterion becomes: $V/\omega L \ll 1$ or the Strouhal number should be much smaller than unity. For typical plasma parameters, this condition is always satisfied.

4. This assumption is strictly valid unless the magnetic field or frequencies are unusually large, in which case dispersive properties of the medium must be taken into account.

Because of the axial symmetry, we choose a circular-cylindrical coordinate system with origin at centre of coil with z-axis coinciding with the coil axis.

Due to the isotropy of the conducting medium, the induced eddy currents in the plasma only have an azimuthal component. Then, from Maxwell's law, the vector potential $\bar{A}$ can only have an azimuthal component which simplifies the analysis considerably. The components of the magnetic field can easily be calculated using the relationship $\bar{B} = \bar{\nabla} \times \bar{A}$.

The differential equations for the vector potential are derived from Maxwell's equations with the assumption of cylindrical symmetry. This differential equation will be solved to obtain a closed form solution in terms of integrals to Bessel functions.

The driving current is a sinusoidal function of time. $I = I_o\, e^{j\omega t}$. Therefore the vector potential is likewise a sinusoidal function of time $\bar{A} = \bar{A}_o\, e^{j\omega t}$. In the subsequent analysis, this time factor will cancel and hence will not appear explicitly.

According to Maxwell's third law, the induced voltage in a length of wire located in the field of a vector Potential $\bar{A}$, is:

$$V_i = j\omega \oint \bar{A} \cdot d\bar{\ell} \qquad (1.3)$$

For an axially symmetric coil with single loop of wire with radius a, the induced voltage becomes:

$$V_i = j\omega a \int_0^{2\pi} A_\varphi(a,z)\, d\varphi = 2\pi a\, j\omega\, A_\varphi(a,z) \qquad (1.4)$$

The total voltage induced in a coil of N identical turns each with radius a located at z:

$$V_t = 2\pi a\, j\omega \sum_{i=0}^{N} A_\varphi(a, z_i) \qquad (1.5)$$

It will be shown later that for the coil configuration used in the experiments, this summation can be replaced by an integration. The turn density of the coil is $n(= N/\ell)$ and the coil is located between $z = -\ell/2$ and $z = +\ell/2$ whence:

$$V_t = 2\pi a\, j\omega n \int_{-\ell/2}^{+\ell/2} A_\varphi(a,z)\, dz \qquad (1.6)$$

in which $A_\varphi(a,z)$ is the azimuthal component of the vector potential evaluated at position (a,z) and produced by any coaxial coil. If, however, the coil that creates the vector potential, called coil "1", is the same as the coil that senses the induced voltage coil "2", the self-induced voltage becomes:

$$V_t = 2\pi a\, j\omega\, n^2 \int_{-\ell/2}^{+\ell/2}\int_{-\ell/2}^{+\ell/2} A_\varphi(a,z)\Big|_{z_1-z_2} dz_1\, dz_2 \tag{1.7}$$

The coil impedance follows from (1.7) with Ohm's law:

$$Z = \frac{V}{I}$$

where I is the magnitude of the sinusoidal coil current $I = I_o\, e^{j\omega t}$.

The problem of calculating the coil impedance variation as a function of the electrical conductivity of the surrounding medium is reduced to the evaluation of the vector potential $A_\varphi(a,z)$ as a function of the electrical conductivity.

First, suppose that the medium is non-conducting; the coil currents create a driving vector potential, $\overline{A}_D(r,z)$ which is periodic in time and has only an azimuthal component. However, no currents are induced and no energy dissipation occurs. The electromagnetic field is basically an induction field close to the coil, and at large distance from the coil resembles a radiation field originating from an oscillating magnetic dipole located at the centre of the coil. If the medium is conducting in the space r > b, eddy currents are induced under the influence of the driving vector potential, which by virtue of the energy dissipation decays much more strongly. We call $\bar{A}_p(r,z)$ the plasma vector potential existing in the conducting space for $r > b$.

At the same time, a magnetic field is induced by the same eddy currents, which superimposes on the driving magnetic field in the cylindrical space $r < b$. A so-called reflected vector potential $\bar{A}_R(r,z)$ is created by the induced eddy currents and can be added to the original driving vector potential $\bar{A}_D(r,z)$ since we are dealing with a linear problem.

In fact, as we are only interested in the changes of the coil impedance caused by the presence of a conducting medium rather than a vacuum, we can focus our attention on the calculation of the reflected vector potential $\bar{A}_R(r,z)$ only, which carries the needed information about the plasma back to the probe coil, and is not present when we have no conducting medium.

Hence, the total impedance change experienced by the coil can then be expressed as

$$\Delta Z = \frac{2\pi a j \omega n^2}{I} \int_{-\ell/2}^{+\ell/2} \int_{-\ell/2}^{+\ell/2} A_{\varphi R}(a,z)\Big|_{z_1-z_2} dz_1\, dz_2 \qquad (1.8)$$

simply by substituting $A_{\varphi R}(a,z)$ for $A_{\varphi}(a,z)$ in expression (1.7).

The differential equations for the vector potential will be derived from the four Maxwell equations together with the two constitutive equations which are respectively:

$$\bar{\nabla} \cdot \bar{D} = q \qquad\qquad \bar{D} = \varepsilon \bar{\mathcal{E}}$$

$$\bar{\nabla} \cdot \bar{B} = 0 \qquad\qquad \bar{B} = \mu \bar{H}$$

$$\bar{\nabla} \times \bar{\mathcal{E}} = - \frac{\partial \bar{B}}{\partial t}$$

$$\bar{\nabla} \times \bar{H} = \bar{J} + \frac{\partial \bar{D}}{\partial t}$$

The differential equation for the driving vector potential $\bar{A}_D(r,z)$ can be constructed from the second and fourth law of Maxwell, combined with the vector relationship $\bar{B} = \bar{\nabla} \times \bar{A}$, and reduces to the vector Laplacian $\nabla^2 \bar{A}_D = 0$.

The solution for a single coil filament is given by Smythe (Ref. 50) and the derivation is shown in detail in Appendix A, since this forms the basis of forthcoming expressions. Omitting the time dependence, which occurs in the form $e^{j\omega t}$, the solution is:

$$A_{\varphi D} = \int_0^\infty I_1(ak)\, K_1(kr) \cos(kz)\, dk \tag{1.9}$$

The differential equation for the plasma vector potential can be set up in the same way. Using Ohm's law for an isotropic plasma in the form $\bar{J} = \sigma \bar{\mathcal{E}}$ to account for the eddy currents in the conducting space, the following vector Helmholtz equation emerges:

$$\nabla^2 \bar{A}_P = (j\sigma\mu\omega - \varepsilon\mu\omega^2)\bar{A}_P \tag{1.10}$$

wherein: σ = electrical conductivity of the plasma

ε = dielectric constant.

The first term on the R.H.S. is due to the conduction current (eddy currents) while the second term expresses the effect of displacement currents in the plasma.

The criterion for neglecting the displacement current in comparison with the conduction current takes the form $\sigma >> \epsilon\omega$. Since this inequality is true for conductivities larger than 10^{-3} mho/m at the carrier frequency $f_o = 10.7$ MHz, displacement currents can be neglected for shock tube plasmas ($\sigma > 100$ mho/m). This is no longer true for experiments with electrolytes as will be explained in section (1.6).

Neglecting displacement currents, the vector Helmholtz equation (1.10) can be expressed in cylindrical coordinates as follows:

$$\frac{\partial^2 A_{\varphi P}}{\partial r^2} + \frac{1}{r}\frac{\partial A_{\varphi P}}{\partial r} - \frac{A_{\varphi P}}{r^2} + \frac{\partial^2 A_{\varphi P}}{\partial z^2} - j\sigma\mu\omega A_{\varphi P} = 0 \quad (1.11)$$

The solution proceeds in similar fashion as that of the vector Laplacian. Separation of variables leads to a solution of the z dependent variables in the form:

$$\frac{1}{Z(z)}\frac{\partial^2 Z(z)}{\partial z^2} = -k^2 \quad (1.12)$$

with solution:

$$Z(z) = C\cos(kz) + D\sin(kz) \quad (1.13)$$

By introducing the following parameter: $d^2 = k^2 + j\sigma\mu\omega$, (1.14)
the R dependent part of $A_{\varphi P}$ becomes:

$$(dr)^2\frac{\partial^2 R(r)}{\partial (dr)^2} + dr\frac{\partial R(r)}{\partial (dr)} - R(r).\left[1 + (dr)^2\right] = 0 \quad (1.15)$$

This is a first order modified Bessel equation with solution:

$$R(r) = A\, I_1(\alpha r) + B\, K_1(\alpha r) \qquad (1.16)$$

Combining the solutions (1.13) and 1.16) leads to:

$$A_{\varphi p}(r,z) = \left[A\, I_1(\alpha r) + B\, K_1(\alpha r)\right] \cdot \left[C \cos(kz) + D \sin(kz)\right]$$

The four constants A, B, C, D, are functions of the separation constant k and are usually different for each value of k. The complete solution would be a sum of all the individual solutions, but since the region extends to infinity in z and is symmetric about z = 0, the complete solution is an integral over the entire positive range of k. Thus, the general solution is:

$$A_{\varphi p}(r,z) = \int_0^\infty \left[A(k)\, I_1(\alpha r) + B(k)\, K_1(\alpha r)\right] \cdot \left[C(k) \cos(kz) + D(k) \sin(kz)\right] dk \qquad (1.17)$$

Due to the coil geometry, the function of z must be symmetric and even; hence D(k) = 0. Since the plasma region extends for $b < r < \infty$, the vector potential must decay to zero for $r \rightarrow \infty$, hence A(k) = 0. The solution of the plasma vector potential can thus be written as:

$$A_{\varphi p} = \int_0^\infty f_p(k)\, K_1(\alpha r) \cos(kz)\, dk \qquad (1.18)$$

wherein $f_p(k)$ is an unknown function of the separation constant k.

Finally, the third step involves the calculation of the reflected vector potential in the cylindrical volume $r < b$.

Since no currents can flow in this non-conducting region, the solution of the reflected magnetic vector potential again reduces to the solution of the vector Laplacian $\nabla^2 \overline{A}_R = 0$.

The solution follows similar steps as the solution for (1.10) except for the absence of the R.H.S.

After transformation in cylindrical coordinates, separating the variables, using a separation constant $k^2 = -\frac{1}{Z}\frac{\partial^2 Z}{\partial z^2}$; we obtain the general solution (cf. 1.17):

$$A_{\varphi R}(r,z) = \int_0^\infty \left[A(k)\, I_1(kr) + B(k)\, K_1(kr)\right]\cdot\left[C(k)\cos(kz) + D(k)\sin(kz)\right] dk$$

Due to axial symmetry around z = 0, we must have D(k) = 0. Since we are dealing with the cylindrical space for $r < b$, we must avoid the singularity at the origin for r = o, for which we know that the magnetic vector potential $A_{\varphi R} = 0$, or B(k) = 0 and the solution of the reflected vector potential becomes:

$$A_{\varphi R}(r,z) = \int_0^\infty f_R(k)\, I_1(kr)\cos(kz)\, dk \tag{1.19}$$

wherein $f_R(k)$ is a function of (k).

The two unknown functions of the variable k can be calculated from the boundary conditions at r = b where the regions must have matching properties.

In terms of the magnetic vector potential the two boundary conditions are:

(a) The tangential components of the magnetic vector potential $\bar{A}$ are continuous, or

$$\left[\bar{A}_D + \bar{A}_R\right]_{r=b} = \left[A_p\right]_{r=b} \tag{1.20}$$

(b) Since the magnetic permeability is constant throughout, the tangential components of the magnetic field $\bar{B}$ are continuous or:

since $B_z = (\bar{\nabla} \times \bar{A})_z = \frac{1}{r}\frac{\partial}{\partial r}(rA_{\varphi})$ we have the condition:

$$\left[\frac{\partial}{\partial r}\left(r\bar{A}_D + r\bar{A}_R\right)\right]_{r=b} = \left[\frac{\partial}{\partial r}\left(r\bar{A}_p\right)\right]_{r=b} \tag{1.21}$$

S. I. Pai (Ref. 51) expresses the jumps in the tangential component of the magnetic field across a surface current sheath as: $\Delta B_t = \mu J$. This means that these boundary conditions apply only in the absence of a current sheet. Therefore, any highly conducting coating of the probe, which is often used to prevent capacitive coupling with the plasma, should be designed to prevent closed circuit eddy currents in the coating. A longitudinal slit will usually serve this purpose.

By substituting Eqs. (1.9, 1.18 and 1.19) into the first boundary condition, we obtain:

$$\frac{\mu a I}{\pi} I_1(ak)K_1(kb) + f_R(k)I_1(kb) = f_p(k)K_1(db) \tag{1.22}$$

Similarly, for the second boundary condition, using the recurrence formulas for Bessel functions (Ref. 52), we obtain:

$$\frac{\mu a I}{\pi} I_1(ak).kb.K_0(kb) - f_R(k).kb.I_0(kb) = f_p(k).db.K_0(db) \tag{1.23}$$

As explained earlier, we only have to know the reflected magnetic vector potential to calculate the coil impedance change under the influence of a conducting medium (Eq. 1.8).

Hence, we solve the two boundary conditions for the unknown function of k, i.e. $f_R(k)$, and the solution for the reflected magnetic vector potential becomes:

$$A_{\varphi R}(r,z) = \frac{\mu a I}{\pi} \int_0^{\infty} I_1(ak)\, I_1(kr) \cdot \frac{k\, K_0(kb)\, K_1(db) - d\, K_1(kb)\, K_0(db)}{d\, I_1(kb)\, K_0(db) + k\, I_0(kb)\, K_1(db)} \cos(kz)\, dk \tag{1.24}$$

Substituting this expression into Eq. (1.8) and working out the double integral over the coil length with the result

$$\int_{-\ell/2}^{+\ell/2} \int_{-\ell/2}^{+\ell/2} \cos\left[k(z_1 - z_2)\right] dz_1\, dz_2 = \frac{2}{k^2}\left[1 - \cos(k\ell)\right]$$

one obtains the final solution:

$$\Delta Z = 4 a j \omega n^2 \mu a \int_0^{\infty} \frac{I_1^2(ak)}{k^2} \cdot \frac{k\, K_0(kb)\, K_1(db) - d\, K_1(kb)\, K_0(db)}{d\, I_1(kb)\, K_0(db) + k\, I_0(kb)\, K_1(db)} \cdot \left[1 - \cos(k\ell)\right] dk \tag{1.25}$$

The following non-dimensional quantities can be introduced:

$$y = kb$$

$$x = db \qquad s = \sigma\mu\omega b^2 \text{ (called the s parameter)}$$

$$h = a/b \text{ (called the filling factor)} \qquad (1.26)$$

$$w = \ell/b$$

From expression (1.14) it follows that:

$$x^2 = y^2 + js \qquad (1.27)$$

and the expression for the exact impedance change for an immersed coil is as follows:

$$\frac{\Delta Z}{\omega\mu a} = 4jhb^2n^2 \int_0^\infty \frac{I_1^2(hy)}{y^2} \cdot \frac{y K_0(y) - E_0 K_1(y)}{y I_0(y) + E_0 I_1(y)} \cdot \left[1 - \cos(wy)\right] dy \qquad (1.28)$$

wherein $E_o = x \dfrac{K_o(x)}{K_1(x)}$ is complex.

From this expression, the non-dimensional resistance change ($= \Delta R/\omega\mu a$) and the non-dimensional reactance change ($= \Delta\mathcal{L}/\mu a$) can be obtained by separating the real and imaginary part.

1.3 Exact Numerical Solutions

Equation 1.28 was solved exactly using the available subroutine package for the modified Bessel functions with complex arguments, i.e. $K_o(x)$, $K_1(x)$. A complete listing for this program which was written in Fortran IV is included in this study. Since the final expression for the coil impedance change, including Hall effect, is quite similar to Eq. (1.28), this program can be used for cases with or without Hall effect.

The programming procedure involves the following special features:

- A coordinate transformation in the integration variable of the form $Y = \ln y$ proved useful to avoid singularities in the integrand at the origin.
- The upper limit for y is mainly dictated by the function

$$\frac{y K_0(y) - E_0 K_1(y)}{y I_0(y) + E_0 I_1(y)}$$

which reduces to negligible values for $y \approx 12$.
- Simpson's rule for integration was done over 350 steps of the value of y. The integration should be closely monitored in the range of y for which the oscillatory nature of the function $(1 - \cos wy)$ may become troublesome.
- Since the Hankel function subroutine was only valid for arguments less than 30, the range was extended to deal with very high conductivities, by switching over to the asymptotic expansion of modified Bessel functions for very large values of the complex argument.

A full parametric study of an immersed coil involves the combination of the parameters h, w, s.

The results shown on Figures 3 and 4 involve the solution of the probe response function for a probe with constant length ratio (w = 6.3), and variable filling factors h = 1/3, 1/2, 2/3 and 1, respectively. The non-dimensional resistance change ($= \Delta R/\omega\mu a$) is plotted versus the s parameter in Figure 3. Figure 4 shows the variation of the non-dimensional inductance change ($\Delta\mathcal{L}/\mu a$) versus s.

These curves are similar in character to the curves shown in Figure 1c based on a crude transformer analogy in the small s regime.

Indeed, the series resistance increases linearly with s for small conductivities, reaches a maximum for the s parameter of the order of unity and decays to zero for increasing conductivities, proportional to $1/\sqrt{s}$ in the limit.

For sufficiently small values of the electrical conductivity, the R.F. field produced by the probe penetrates through the conducting medium without appreciable attenuation, and the dipolar magnetic field of the solenoid decreases in magnitude proportional to r^{-3} for large distances. The amount of power dissipation, which reflects back as a change in the coil resistance, being proportional to $\sigma\mathcal{E}_\varphi^2$ per unit volume is therefore simply proportional to σ which explains the linear behaviour of $\Delta R/\omega\mu a$ versus s in this small s regime.

At very large values of the conductivity, the R.F. field penetration depth in the plasma is limited by the skin effect. Although the conductivity is large, the volume wherein dissipation occurs shrinks rapidly so that in the limit of infinite conductivity, no dissipation can occur which means that the resistance of the coil drops back to its intrinsic value as in the non-conducting medium case. The resistance change in this regime is proportional to the skin depth $\delta (= \sqrt{\frac{2}{\sigma\mu\omega}})$, i.e. proportional to $(s)^{-\frac{1}{2}}$. The s parameter, $(s = \sigma\mu\omega b^2)$ can also be expressed in terms of the skin depth or $s = \left(\frac{b}{\delta}\right)^2$. The maximum dissipation occurs for s of the order of unity, for which the penetration depth is of the order of the probe dimensions. This fact illustrates the good space resolution of the immersed probe, which makes it a powerful tool to measure conductivity profiles, e.g. in plasma jets or MHD power generators.

Since the inductance of a coil is proportional to the energy stored in the magnetic field produced by the coil current, the inductance change in the small s regime is extremely low, since the R.F. field penetration is hardly affected by the small conductivity.

However, for increasing values of the conductivity, the skin depth is gradually limiting the volume wherein magnetic energy is stored. Due to the eddy currents in the conductor, the magnetic field is excluded from a region in space thereby reducing the inductance of the coil which is reflected in the inductance variation shown in Figure 4. By extrapolating this behaviour to the theoretical limit of infinite conductivity, a coil with unit filling factor cannot store magnetic energy, since the flux lines cannot close and no magnetic field can exist because $\bar{\nabla} \cdot \bar{B} = 0$. One concludes that, in this case, the change in inductance equals the value of the nominal coil inductance for free space to reduce the effective inductance to zero. The nominal inductance for a single layer coil can be evaluated by using the Nagaoka constant Kn as follows:

$$\mathcal{L} = \frac{\mu N^2 A}{l} K_n \qquad (1.29)$$

wherein A is the coil cross-sectional area

$$K_n = \frac{1}{1 + 0.9\, a/l - 0.02\,(a/l)^2} \qquad (1.30)$$

For an s parameter larger than 5×10^3, the difference between the absolute inductance change and the nominal inductance calculated from (1.29) was less than 1 percent, which provides a check on the accuracy of the analysis and numerical calculation.

The monotonically decreasing value of the series inductance of the coil for increasing values of the conductivity produces a phase shift between the primary current and the induced eddy currents. This allows us to monitor the change in series resistance and series inductance separately using phase detectors.

The effect of the filling factor on the probe sensitivity can be obtained from Figures 3 and 4. Over the complete s range, the variation in $\overline{\Delta R}$ and $\overline{\Delta \mathcal{L}}$ is approximately proportional to h^3 and is thus a most effective parameter for optimising the probe sensitivity.

Finally, the effect of the coil length on the probe response was studied at a constant filling factor h = 1/2 and the result is represented in the form of an impedance diagram, Fig. 5, for four different length ratios:

w = 2, 4, 6 and 8 respectively. Each curve in this diagram traces out all values of the s parameter in a coordinate frame with the non-dimensional inductance change as ordinate and the non-dimensional resistance change as abscissa. This is the customary way of plotting probe responses dealing with eddy current testing of materials (Ref. 6, 8). The dashed curves in this figure trace out all values of w at fixed conductivity.

The resistive change at fixed conductivity is proportional to w^{α} wherein α is an exponent between 1 and 2. The dependence of inductance on w cannot be generalised over the entire s regimes except by saying that the inductance change is always proportional to w to a power somewhat greater than unity.

This presentation of the probe response indicates clearly the usefulness of the two methods for measuring conductivities. In the small s regime, the inductance change is too small to be of use so that only the resistance change is useful to monitor conductivities. In the s regime between $1 < s < 20$, the resistance change is ambiguous while the inductance changes are very sensitive to conductivities. Finally, for extremely large values of s, the inductance is very insensitive so that again the resistance should be monitored in this range.

1.4 Approximate Numerical, Analytical and Empirical Solution for the Small s Regime ($s \leq 0.1$)

For this regime, we found that the coil series resistance variation was proportional to s, while the inductance change is negligible. Therefore, an approximate solution must exist which does not involve complex quantities and should be easier to evaluate.

If the conductivity is small, the expression (1.27) can be approximated as

$$x \approx y + j\frac{s}{2y} \tag{1.31}$$

All Bessel functions with argument x can be expanded in a Taylor series around y. If only the first order terms are retained we can write:

$$\begin{aligned} K_0(x) &\approx K_0(y) - j\frac{s}{2y} K_1(y) \\ K_1(x) &\approx K_1(y) - j\frac{s}{2y}\left[K_0(y) + \frac{1}{y} K_1(y)\right] \end{aligned} \tag{1.32}$$

By substituting these expressions for $K_0(x)$ and $K_1(x)$ in the general expression (1.28) and taking advantage of the Wronskian: $\frac{1}{y} = K_1(y)\ I_0(y) + K_0(y)\ I_1(y)$, we obtain a first order approximation:

$$\frac{\Delta Z}{\omega\mu a} = 2hsb^2n^2 \int_0^\infty \frac{I_1^2(hy)}{y^2} \cdot \left[K_0(y)K_2(y) - K_1^2(y)\right] \cdot \left[1-\cos(wy)\right] dy \tag{1.33}$$

which is real. Hence a purely resistive change of the coil impedance will result from this expression. The integrand is strictly a function of the geometric parameters h and w only, and the numerical solution of the integral in (1.33) as a function of these two parameters is presented in Fig. 6 from which the relative importance of the filling factor h and the length ratio w on the probe sensitivity can be estimated.

An approximate analytical solution for this small s approximation can be obtained by using series expansions for the modified Bessel function $I_1(hy)$ and $\cos(wy)$. Using two Mellin transforms, expression (1.33) can be expressed as an infinite series which can be written as follows by including the first three terms in the expansion:

$$\frac{\Delta R}{\omega \mu a} = s\, h^3 w^2 n^2 b^2 \frac{\pi^2}{4}\left[\frac{3}{16} + \frac{15}{356}\left(\frac{h^2}{4} - \frac{w^2}{12}\right) + \frac{315}{2048}\left(\frac{w^4}{360} + \frac{5h^4}{192} - \frac{h^2 w^2}{48}\right) + \cdots\right] \quad (1.34)$$

For better comparison between the approximate numerical solution and the approximate analytical solution of (1.34), the following expressions are plotted in Fig. 7 for a filling factor h = 0.554.

$$F_o = \frac{I(h,w)}{w^2} \qquad \text{for the numerical solution,}$$

$$F_{1a} = \frac{\pi^2 h^2}{8}\left[\frac{3}{16} + \frac{15}{356}\left(\frac{h^2}{4} - \frac{w^2}{12}\right) + \frac{315}{2048}\left(\frac{w^4}{360} + \frac{5h^4}{192} - \frac{h^2 w^2}{48}\right)\right]$$

$$F_{1b} = \frac{\pi^2 h^2}{8}\left[\frac{3}{16} + \frac{15}{356}\left(\frac{h^2}{4} - \frac{w^2}{12}\right)\right] \quad (1.35)$$

Owing to the discrepancy between F_1 and F_o, this series expansion solution can only be used for very short coils $(w < 1)$. For longer coils, further terms of the cosine expansion are needed. A more accurate analytical solution for longer coils can be obtained by using hypergeometric functions.

Expression (1.33) can also be written:

$$\frac{\Delta Z}{\omega\mu a} = 2 s h n^2 b^2 \int_0^\infty \frac{I_1^2(hy)}{y^2} \cdot \left[K_0^2(y) + \frac{2K_0(y)K_1(y)}{y} - K_1^2(y)\right] \cdot \left[1 - \cos(wy)\right] dy$$

Applying a series expansion for $I_1(hy)$ together with a cosine integral transform, this can be transformed to:

$$\frac{\Delta Z}{\omega\mu a} = \frac{s h^3 n^2 b^2}{2} \cdot \left[Y_{30} + 2Y_{10} - Y_{20}\right] \tag{1.36}$$

where:

$$Y_{10} \equiv \int_0^\infty \frac{K_0(y)K_1(y)}{y} \cdot \left[1 - \cos(wy)\right] dy = -\frac{\pi^2 w^2}{2}\left[1 + \frac{w^2}{4}\right]^{1/2} \left[P^{1}_{-1/2}\left(1 + \frac{w^2}{2}\right)\right]$$

$$Y_{20} \equiv \int_0^\infty K_1^2(y)\left[1 - \cos(wy)\right] dy = \frac{\pi^2}{4}\left[P^{0}_{1/2}\left(1 + \frac{w^2}{2}\right) - 1\right] \tag{1.37}$$

$$Y_{30} \equiv \int_0^\infty K_0^2(y)\left[1 - \cos(wy)\right] dy = \frac{\pi^2}{4}\left[1 - P^{0}_{-1/2}\left(1 + \frac{w^2}{2}\right)\right]$$

wherein P_i^j are associated Legendre functions and are tabulated in Ref. 53. These functions can be converted to the more popular elliptic integrals. Again for comparison with the approximate numerical solution, the following expression is plotted in Fig. 7:

$$F_2 \equiv \frac{h^2}{4w^2}\left[Y_{30} + 2Y_{10} - Y_{20}\right] \quad \text{for } h = 0.554 \tag{1.38}$$

The agreement between Eq. (1.38) and the numerical solution for $\frac{I(h,w)}{w^2}$ is very good for coil parameters up to w = 5.

Finally, if the data obtained by solving expression (1.33) are plotted on a log-log scale, it turns out that the curves are linear over a wide range, resulting in a convenient empirical expression for the small s regime ($s < 0.1$). The following expression correlates the coil resistance change as a function of the conductivity of the medium:

$$\frac{\Delta R}{\omega \mu a} = 0.47\, s\, h^3 w^{1.82} n^2 b^2 = 0.47\, s\, h^3 N^2 w^{-0.18} \qquad (1.39)$$

This expression gives an error bracket of less than 5 percent if it is applied to coils with parameters:

$$0.2 < h < 0.9$$

$$1 < w < 5$$

This empirical expression can be used in approximate design estimates for a conductivity probe for the small s regime. Since $s = \sigma\mu\omega b^2$, this low regime can be obtained by suitable choice of variables. It also indicates to what degree the different coil parameters influence the sensitivity of the immersed conductivity probe and confirm the conclusions made for the exact solutions.

1.5 Effect of Small Number of Turns on the Exact Solution

For coils with small number of turns, integration over the total number of turns (1.6) may over-estimate the value of the impedance change. In this case, a summation of the value for the reflected magnetic vector potential $A_{\omega R}$ over the total number of turns should replace the integral. The summation for a cosine can be expressed as: (Ref. 54)

$$\sum_{t=0}^{m} \cos(kt) = \frac{\cos\left(\frac{km}{2}\right)\sin\left(k\frac{m+1}{2}\right)}{\sin\left(\frac{k}{2}\right)}$$

Substituting above expression for the double integral performed over the cos kz term in the expression for $A_{\varphi R}$ (1.24), the following expression could be used for coils with a discrete number of turns:

$$\frac{\Delta Z}{\omega\mu a} = 2jh\int_0^{\infty} I_1^2(hy)\cdot\frac{y\,K_0(y) - E_0\,K_1(y)}{y\,I_0(y) + E_0\,I_1(y)}\cdot\left[2\,\frac{\cos\left(\frac{pw-1}{4p}y\right)\cdot\sin\left(\frac{pw+1}{4p}y\right)}{\sin\left(\frac{y}{2p}\right)} - 1\right]^2 dy \qquad (1.40)$$

wherein: $p = nb = N/w$

n = number of turns per unit length.

Numerical solutions of expression (1.40) were compared with those obtained from expression (1.28) for different coil geometries and for varying number of turns. The results show that the error is negligible (< 1 percent) even down to coils with only a small number of turns.

1.6 Effect of Displacement Currents

So far we have neglected the displacement current in the Maxwell's equation on the grounds that $\sigma \gg \epsilon\omega$. Since the experimental data obtained with electrolytic solutions of HNO_3 will be compared with theoretical values, we have to verify the above inequality.

Expression (1.10) is the exact differential equation including displacement currents. This vector Helmholtz eq. can also be written:

$$\sum_{t=0}^{m} \cos(kt) = \frac{\cos\left(\frac{km}{2}\right)\sin\left(k\frac{m+1}{2}\right)}{\sin\left(\frac{k}{2}\right)}$$

Substituting above expression for the double integral performed over the cos kz term in the expression for $A_{\varphi R}$ (1.24), the following expression could be used for coils with a discrete number of turns:

$$\frac{\Delta Z}{\omega\mu a} = 2jh\int_0^{\infty} I_1^2(hy)\cdot\frac{yK_0(y) - E_0K_1(y)}{yI_0(y) + E_0I_1(y)}\cdot\left[2\,\frac{\cos\left(\frac{pw-1}{4p}y\right)\cdot\sin\left(\frac{pw+1}{4p}y\right)}{\sin\left(\frac{y}{2p}\right)} - 1\right]^2 dy \qquad (1.40)$$

wherein: $p = nb = N/w$

n = number of turns per unit length.

Numerical solutions of expression (1.40) were compared with those obtained from expression (1.28) for different coil geometries and for varying number of turns. The results show that the error is negligible (< 1 percent) even down to coils with only a small number of turns.

1.6 Effect of Displacement Currents

So far we have neglected the displacement current in the Maxwell's equation on the grounds that $\sigma \gg \varepsilon\omega$. Since the experimental data obtained with electrolytic solutions of HNO_3 will be compared with theoretical values, we have to verify the above inequality.

Expression (1.10) is the exact differential equation including displacement currents. This vector Helmholtz eq. can also be written:

$$\nabla^2 \overline{A}_p = js\left(1 + j\frac{\varepsilon\omega}{\sigma}\right)\overline{A}_p \tag{1.41}$$

Obviously, this correction is only needed for very low conductivities, since the relative dielectric constant for water is of the order of 80, and $\frac{\varepsilon\omega}{\sigma}$ approaches unity for electrical conductivities lower than 0.1 mho/m, for which the small s approximation can be applied.

According to (1.41), the expression (1.27) can be modified as follows to include displacement currents:

$$x^2 = y^2 + js\left(1 + j\frac{\varepsilon\omega}{\sigma}\right) = y^2 + js - s_d$$

wherein: $s_d = \varepsilon\mu\omega^2 b^2$

Since s and s_d are very small compared to unity, we can approximate

$$x = y\sqrt{1 + \frac{js - s_d}{y^2}}$$

$$x \approx y\left[1 + \frac{js - s_d}{2y^2} - \frac{1}{8y^4}\left(-s^2 - 2jss_d + s_d^2\right)\cdots\right] \tag{1.42}$$

The expression for the impedance change (1.33) for the small s regime indicates that only the resistive component of the impedance changes proportional to s or:

$\Delta Z_o = \alpha s$ wherein α is a constant.

Expression (1.42) indicates that, in the absence of displacement currents ($s_d = 0$), a second order term in the expansion for x would have resulted in a reactive change of the coil impedance, so that in the small s regime without displacement currents the impedance change can conveniently be expressed as:

$$\Delta Z_o = \alpha s - j\beta s^2 \tag{1.43}$$

wherein β again is a proportionality factor.
The subscript o in ΔZ_o indicates an impedance change without correction for displacement currents.

Including displacement currents, the impedance change can be expressed, according to Eq. (1.42) in the small s regime as follows:

$$\Delta Z = \alpha (s + j s_d) - j\beta (s^2 + 2j s s_d) \tag{1.44}$$

Separating real and imaginary parts and using the real and imaginary part from (1.43) in the form:

$$\Delta R_o = \alpha s \quad \text{and} \quad \Delta X_o = -\beta s^2$$

we obtain from (1.44)

$$\begin{aligned} \Delta R &= \alpha s + 2\beta s s_d = \Delta R_o - 2\Delta X_o s_d/s \\ \Delta X &= -\beta s^2 + \alpha s_d = \Delta X_o + \Delta R_o s_d/s \end{aligned} \tag{1.45}$$

The effect of the displacement current is to increase the coil series resistance by $2\omega\Delta L_o s_d/s$, which is very small considering that the inductance change ΔL_o is a second order effect at small conductivities. However, the coil inductance drop ΔX_o, is reduced by an amount proportional to $\Delta R_o s_d/s$ which is a first order correction.

To substantiate these findings, an exact numerical solution was obtained by solving expression (1.28) which was modified by using the vector Helmholtz Eq. (1.41) with correction for displacement currents. A relative dielectric constant of 60 was used, instead of 80 for water, to account for substitution of some H_2O molecules by electrolyte in strong electrolytic solutions.

The table shows the exact impedance changes with and without displacement correction for a particular probe.

s	σ (mho/m)	ΔR_o (ohm)	ΔL_o (nH)	ΔR (ohm)	ΔL (nH)
0.005	8.6	0.013305	-0.011851	0.013310	-0.011057
0.011	21	0.031529	-0.043534	0.031536	-0.042786
0.027	52	0.073014	-0.15544	0.073024	-0.015476
0.050	95	0.12529	-0.35462	0.012530	-0.035400

We conclude that the resistance correction is negligible in this range of electrolytic conductivities. However, the drop in inductance is decreased by 7 percent at the low conductivity of 8.6 mho/m due to displacement currents, while this effect is only of the order of 1 percent at 50 mho/m.

In polar liquids, the dielectric constant ϵ_r includes a large contribution due to the orientation of the permanent molecular dipoles in an R.F. field. Since the orientation process requires a finite time, the dielectric constant decreases as the frequency of the applied field increases. The available data (Ref. 55) would indicate that the dielectric relaxation time for H_2O is of the order of picoseconds in comparison with which a carrier frequency of 10 mHz is almost a D.C. However, orientation of the molecules against viscous forces leads to an energy dissipation in R.F. fields, indicating that the dielectric constant becomes complex and of the form: $\epsilon = (\epsilon_r + j\,\epsilon_d)\epsilon_o$ wherein ϵ_o is the dielectric constant for vacuum, ϵ_d, which is a function of frequency, contains the dissipative part of the dielectric constant. Inserting this expression of ϵ in the fourth Maxwell equation:

$$\bar{\nabla} * \bar{B} = \mu \bar{\mathcal{E}} \left[\sigma + j\omega\, \epsilon_o (\epsilon_r + j\,\epsilon_d)\right]$$

shows that the dissipative part of the dielectric constant has the same effect as modifying the electrical conductivity. The lack of data concerning dispersion effects does not allow us to verify this, but it seems possible that our probe could be used to investigate this effect in liquids with very small conductivities.

1.7 Double Layer Coils

In order to bring the response of the probe within detectable levels for experiments with electrolytes, it was decided to use double layer coils. The empirical expression (1.39) suggests that the sensitivity of the probe being proportional to n^2, will quadruple, by using two identical layers of wire. Improving the filling factor was impossible from a material point of view while increasing the coil length would indeed increase the sensitivity. However, a short coil is important to reduce the response time of the probe in shock tubes. Moreover, the sensitivity of the probe to detect Hall effect varies inversely with the coil length as will be shown in Chapter III. Although this design violates even more the first assumption made for the theoretical treatment, it also has the beneficial effect that the alternating current in the coil is now distributed more uniformly along the coil length which is implicitly assumed in the analysis. Due to the finite size of the wire diameter, an adjustment to the treatment of the first part is needed, to account for the two different radii of the layers which we will denote with subscripts 1 and 2 respectively.

If a_1 is the coil radius of the inner layer,

a_2 the coil radius of the outer layer,

the total reflected vector potential can be expressed in terms of the potentials at the two radii, and Eq. (1.24) becomes:

$$A_{\varphi R}(r,z) = \int_0^\infty \left[\frac{\mu a_1 I}{\pi} I_1(a_1 k) + \frac{\mu a_2 I}{\pi} I_1(a_2 k) \right] . F(k) \cos(kz)\, dk \qquad (1.46)$$

wherein $F(k) = \dfrac{kb\, K_0(kb) - E_0 K_1(kb)}{kb\, I_0(kb) + E_0 I_1(kb)}$.

E_0 has the same meaning as in Eq. (1.28).

The total voltage induced in a double layer coil with identical turn density n is:

$$V = V_1 + V_2 = 2\pi a_1 n^2 j\omega A_{\varphi R}\Big|_{r=a_1} + 2\pi a_2 n^2 j\omega A_{\varphi R}\Big|_{r=a_2} \qquad (1.47)$$

By substituting expression (1.46) into (1.47) and non-dimensionalising one obtains:

$$\frac{\Delta Z}{\omega\mu b} = \frac{\Delta Z_{11}}{\omega\mu b} + 2\frac{\Delta Z_{12}}{\omega\mu b} + \frac{\Delta Z_{22}}{\omega\mu b} \qquad (1.48)$$

wherein:

$$\frac{\Delta Z_{ij}}{\omega\mu b} = 4j\, h_i h_j b^2 n^2 \cdot \int_0^\infty \frac{I_1(h_i y)\, I_1(h_j y)}{y^2} \cdot \frac{y K_0(y) - E_0 K_1(y)}{y I_0(y) + E_0 I_1(y)} \cdot \left[1 - \cos(wy)\right] dy.$$

This expression was used exclusively to predict the probe response for the experiments. Since the sensitivity of the probe is a very strong function of the filling factor (Fig. 3, 4), the contribution from the outer layer is much larger than the contribution from the inner layer and for the type of coil used in the experiments, the response is equivalent to that of a single layer coil with double the turn density and filling factor $h \approx 0.7\ (h_2 - h_1) + h_1$.

Chapter II

CALCULATION OF TRANSPORT PROPERTIES OF SHOCK-HEATED ARGON

Argon is frequently used as a working fluid in shock tube experiments; being a monatomic gas, it can only absorb energy in its translational mode. At higher energy levels, excitation and ionisation are the only departures from the ideal gas conditions. The choice of argon is based on the fact that a great deal of physical data are available for this gas and also because of its relatively low ionisation potential which makes it an attractive working fluid for plasma physicists. This chapter is divided into two parts, the first dealing with the shock tube relations for calculating the thermodynamic parameters of the shocked gas, the second part deals with the calculation of the electrical conductivity using shkarofsky's method.

2.1 Calculation of the Thermodynamic Argon Plasma Parameters Behind an Incident Shock

The conservation equations can be found in any textbook dealing with shock waves, e.g. Ref. 56, and will be presented here with the familiar shock tube symbolism in stationary coordinates:

continuity equation: $$\rho_1 v_1 = \rho_2 v_2 \qquad (2.1)$$

momentum equation: $$p_1 + \rho_1 v_1^2 = p_2 + \rho_2 v_2^2 \qquad (2.2)$$

energy equation: $$v_1^2/2 + h_1 = v_2^2/2 + h_2 \qquad (2.3)$$

equation of state: $$\gamma_1 p/\rho = a_{s1}^2 = \gamma_1 RT \qquad (2.4)$$

Combining equations 2.1, 2.2 and 2.4, we obtain:

$$\frac{P_2}{P_1} = 1 + \gamma M_s^2 \left(1 - \rho_1/\rho_2\right) \tag{2.5}$$

When ionisation occurs, the enthalpy can be expressed as:

$$h_2 = c_p (1+\alpha) T + \alpha \ell_i \tag{2.6}$$

α: degree of ionisation $= \dfrac{n_e}{n_e + n_A}$

ℓ_i: ionisation energy per molecule ($= q_i\ RT$)

q_i: ionisation potential for argon (in volt).

Excitation energy of the shock-heated gas can conveniently be neglected because the energy levels for excitation are very close to the ionisation potential and at the experimental conditions, the degree of ionisation is quite high so that the excitation energy is very small compared to the total enthalpy of the shock-heated gas. $\gamma_1 = 5/3$ for argon.

Combining expressions (2.3, 2.4, 2.6) we obtain:

$$\frac{T_2}{T_1} = \frac{1}{1+\alpha} \left[1 + \frac{\gamma - 1}{2} M_s^2 \left(1 - \frac{\rho_1^2}{\rho_2^2}\right) - \frac{\gamma - 1}{\gamma} \frac{\alpha q_i}{RT_1} \right] \tag{2.7}$$

The equation of state can be written as:

$$\frac{P_2}{P_1} = \frac{\rho_2}{\rho_1} \frac{T_2}{T_1} (1 + \alpha) \tag{2.8}$$

The only remaining equation to solve for the four unknown (P_2, ρ_2, T_2 and α) is the Saha equation which for singly ionised argon plasma reduces to: See reference 56.

$$\alpha = \left[3.04\ 10^6 \frac{P_2}{T_2^{5/2}} \exp(q_i/kT_2) \frac{Z_A}{Z_i Z_e} + 1 \right]^{-1/2} \tag{2.9}$$

for P_2 in atmospheres and T_2 in degrees Kelvin.

In order to obtain the highest accuracy in the theoretical calculation of the plasma composition, a few corrections have to be considered. These are: lowering of the ionisation potential due to the presence of ions, cut-off of the partition function and Debye polarisation contribution to the total pressure.

H.N. Olsen in Ref. (57) claims that the lowering of the ionisation potential, when applied to a plasma of 1 atm. and 10,000°K amounts to a change of 0.2 percent. Since this effect becomes smaller at lower temperatures we can neglect this effect entirely and assume an ionisation potential q_i = 15.755 volts.

The values of the partition functions Z_A, Z_i and Z_o are obtained from Ref. (58) which includes the corrections mentioned above. A plot of the ratio of the partition functions $\frac{Z_A}{Z_i Z_e}$ versus temperature at 1 atmosphere indicates that an average value of 11.2 gives an error in $\frac{Z_A}{Z_i Z_e}$ of less than 1 percent over the temperature range of interest. Hence, the Saha equation used in this calculation becomes:

$$\alpha = \left[357.14 \frac{P_2}{T_2^{5/2}} \exp\left(1.829\, 10^5 / T_2\right) + 1 \right]^{-1/2} \qquad (2.10)$$

wherein P_2 is expressed in Torr.

2.2 Calculation of Thermodynamic Argon Plasma Parameters Behind a Reflected Shock

The gas conditions behind the reflected shock are indicated by a subscript 5 and the following conservation equations can be written in stationary coordinates (Ref.

(56):

continuity equation: $\rho_5 v_5 = \rho_2 (v_2 - v_1 + v_5)$ (2.11)

momentum equation: $p_5 + \rho_5 v_5^2 = p_2 + \rho_2 (v_2 - v_1 + v_5)^2$ (2.12)

energy equation: $v_5^2/2 + h_5 = (v_2 - v_1 + v_5)^2/2 + h_2$ (2.13)

By combining these expressions with the incident shock relations (2.5, 2.7 and 2.8) we obtain the following ratios across the reflected shock as a function of the known ratios across the incident shock.

$$\frac{p_5}{p_1} = \frac{p_2}{p_1} + \gamma M_s^2 \frac{\rho_5}{\rho_1} \left[\frac{\rho_2/\rho_1 - 1}{\rho_5/\rho_1 - \rho_2/\rho_1} \right]^2 \cdot \left[\frac{\rho_5/\rho_1}{\rho_2/\rho_1} - 1 \right] \tag{2.14}$$

$$\frac{T_5}{T_1} = \frac{1}{1+\alpha} \left[1 + \frac{\gamma_1 - 1}{2} M_s^2 \left[1 - \left(\frac{\rho_1}{\rho_2} \right)^2 \right] \right.$$

$$\left. + \frac{\gamma_1 - 1}{2} M_s^2 \left[\frac{\rho_2/\rho_1 - 1}{\rho_5/\rho_1 - \rho_2/\rho_1} \right]^2 \cdot \left[\left(\frac{\rho_5/\rho_1}{\rho_2/\rho_1} \right)^2 - 1 \right] - \frac{2\alpha}{5} \frac{\ell_i}{RT_1} \right] \tag{2.15}$$

the Saha equation is unaffected:

$$\alpha = \left[357.14 \frac{p_5}{T_5^{5/2}} \exp\left(1.829\, 10^5 / T_5 \right) + 1 \right]^{-1/2} \tag{2.16}$$

Equation of state:

$$\frac{p_5}{p_1} = \frac{\rho_5}{\rho_1} \frac{T_5}{T_1} (1 + \alpha) \tag{2.17}$$

The two sets of four implicit equations (2.5, 2.7, 2.8, 2.10) and (2.14, 2.15, 2.16, 2.17) are solved numerically using a non-linear regression subroutine and the resulting values of temperature, pressure, density and degree of ionisation, which are obtained as a function of the initial pressure and shock Mach number, are used to calculate the electrical conductivity as shown in the next section.

Solutions are presented in Table I for an initial argon pressure of 10 Torr at various incident shock Mach numbers between 5.5 and 9.

2.3 Electronic Conductivity of Shock Ionised Argon

Among the transport properties of ionised gases, the electrical conductivity has probably received the greatest attention. Therefore, different theories have been proposed in the past and are generally in agreement with the experimental data if one applies the expression in the proper regime.

In weakly ionised gases, i.e. $n_e < 10^{12}\ cm^{-3}$ and $\alpha < 10^{-5}$ electron-atom encounters form the main contribution to the electrical conductivity. Chapman and Cowling (Ref.29) developed a theory on the assumption that the gas can be treated as a neutral and the electrical conductivity for small degree of ionisation becomes:

$$\sigma = 3.34\ 10^{-12}\ \alpha / (Q_{en} T^{1/2}) \qquad \text{mho/cm.} \qquad (2.18)$$

wherein Q_{en} is the electron-neutral momentum transfer cross-section for argon. Allis (Ref. 60) develops the expression for the tensor conductivity in this regime.

For strongly ionised gases, i.e. $n_e > 10^{16}$/cc and $\alpha > 10^{-3}$, the effective electron-ion collision frequency $< \nu_{ei} >$ exceeds the electron-atom collision frequency by at least a factor of 10. In this case, the majority of the collisions are distant encounters due to Coulomb interactions between charged particles and this completely changes the transport mechanism. The scalar electron-ion conductivity has been calculated by Spitzer and Härm (Ref. 61) and the tensor conductivity by Landshoff (Ref. 62) and Shkarofsky (Ref. 63).

A convenient form of the Spitzer-Härm equation for argon can be written as:

$$\sigma = \frac{1.56\ 10^{-4}\ T^{3/2}}{\ln\left(1.23\ 10^{4}\ T^{3/2}/n_e^{1/2}\right)} \quad \text{in mho/cm.} \qquad (2.19)$$

For the present experiments, the electrical conductivities fall in the intermediate range wherein long distance Coulomb encounters and short range electron-atom encounters equally affect the conductivity. A common approach proposed by Lin et al. (Ref. 35) consists in calculating the effective plasma resistivity by adding the reciprocals of the electron-atom and electron-ion conductivities. However, Frost (Ref. 64) points out that, instead of adding the reciprocals of the conductivities, one should add the two collision frequencies to arrive at a better estimate of the conductivity in the intermediate region. He gives an empirical rule for combining the effects of electron scattering by neutrals and by ions.

To date, the most general method for calculating the electrical conductivity of gases in any state of ionisation has been developed by Shkarofsky (Ref.65). The effective electrical conductivity for any degree of ionisation was calculated by taking the Laguerre polynomial series expansion and substituting it into the Boltzmann equation terms describing the electron-neutral collisions and the Fokker-Planck equation terms dealing with the long range Coulomb encounters. This method is useful only when the collision frequency can be expressed by a simple exponent of the electron velocity.

In a recent paper (Ref. 67), W.L. Nighan calculates the electrical conductivity of several noble gases for arbitrary degree of ionisation for electron temperatures in the $300^{o}K$ to $30{,}000^{o}K$ range. He employs a variational method to calculate the conductivity, rather than determining the electron velocity distribution function by direct integration of the Boltzmann-Fokker-Planck equation.

The latest available data concerning the electron-neutral momentum transfer cross-section for argon are probably the data calculated by Frost and Phelps (Ref. 66), which are reproduced in Figure 8.

The argon plasma created behind the reflected shock can be assumed to be in a state of local thermodynamic equilibrium. Using a Maxwellian distribution function, the electron energies of the plasma can be expected to range between 0.35 ev and 1 ev, for plasma temperatures varying between 6000 and $12{,}000^{o}K$, except for the electron energies in the tail of the distribution function. In this range, the momentum transfer cross-section for the electron-neutral interactions can conveniently be expressed by a simple power of the electron energy of the form: $\nu_{en} = C\ V^{r}$, which is the form required for applying the Shkarofsky method. For this interval, the best fitting curve is shown on Fig. 8 with the resulting expression for the cross-sections:

$$Q_{en} = 1.1 \times 10^{-20} \left(\frac{U}{U_o}\right)^{1.64} \text{ in } m^2, \text{ wherein } U = \frac{mv^2}{2e} \text{ in ev.}$$

From $\nu_{en} = n_A Q_{en} V$, follows the expression of the electron-neutral collision cross-section: $\nu_{en} = C\, V^r$ wherein

$$C = 1.1 \times 10^{-20}\, n_A \left(\frac{m_e}{2e}\right)^{1.64} \qquad (2.20)$$

$$r = 4.28 \qquad (2.21)$$

for electron energies varying between 0.35 and 1 ev.

Shkarofsky (Ref. 65) shows that the D.C. electronic conductivity matrix for a plasma in any state of ionisation, with a magnetic field aligned along the z-axis of an orthogonal coordinate system, without applied electric field can be presented in the form:

$$\bar{\bar{\sigma}} = \begin{pmatrix} \sigma_{11} & \sigma_{12} & 0 \\ \sigma_{21} & \sigma_{22} & 0 \\ 0 & 0 & \sigma_{33} \end{pmatrix} \qquad (2.22)$$

wherein:

$$\sigma_{11} = \sigma_{22} = \frac{n_e e^2}{2m_e}\left(\frac{1}{g\langle\nu_g\rangle + j\omega_b f} + \frac{1}{g\langle\nu_g\rangle - j\omega_b f}\right) \qquad (2.23)$$

$$\sigma_{21} = -\sigma_{12} = j\,\frac{n_e e^2}{2m_e}\left(\frac{1}{g\langle\nu_g\rangle + j\omega_b f} - \frac{1}{g\langle\nu_g\rangle - j\omega_b f}\right) \qquad (2.24)$$

$$\sigma_{33} = \frac{n_e e^2}{m_e g_o \langle\nu_g\rangle} \qquad (2.25)$$

n_e = electron number density

m_e = electron mass

$< \nu_g > = < \nu_{en} > + < \nu_{ei} >$: Total collision frequencies averaged over a Maxwellian distribution function.

g, f : Shkarofsky correction coefficients.

g_o : Shkarofsky correction coefficient for an isotropic plasma.

ω_b = cyclotron frequency = $\frac{eB}{m_e}$

e = electron charge.

These formulae can also be expressed as:

$$\sigma_{33} = \frac{n_e e^2}{m_e g_o \langle \nu_g \rangle} \tag{2.26}$$

$$\sigma_{11} = \sigma_{22} = \sigma_{33} \frac{g_o}{g} \left[1 + \left(\frac{\omega_b f}{g \langle \nu_g \rangle} \right)^2 \right]^{-1} \tag{2.27}$$

$$\sigma_{12} = -\sigma_{21} = -\sigma_{33} \frac{\omega_b f g_o}{g^2 \langle \nu_g \rangle} \cdot \left[1 + \left(\frac{\omega_b f}{g \langle \nu_g \rangle} \right)^2 \right]^{-1} \tag{2.28}$$

These expressions should be compared with the simple equations for the tensor conductivities as given, for example in Ref. 68.

$$\sigma_p = \sigma_o = \frac{n_e e^2}{m_e \nu_g^*} \tag{2.29}$$

$$\sigma_t = \sigma_o \left[1 + \left(\frac{\omega_b}{\nu_g^*} \right)^2 \right]^{-1} \tag{2.30}$$

$$\sigma_H = -\sigma_0 \left(\frac{\omega_b}{\nu_g^*}\right)\cdot\left[1+\left(\frac{\omega_b}{\nu_g^*}\right)^2\right]^{-1} \tag{2.31}$$

wherein:

$$\nu_g^* = \nu_{en}^* + \nu_{ei}^* = \left(\frac{8kT_e}{\pi m_e}\right)^{1/2}\cdot\left(n_n \overline{Q_{en}} + n_e \overline{Q_{ei}}\right) \tag{2.32}$$

These expressions are based on Spitzer's free path theory which ignores the inter-particle forces and assumes a constant collision frequency. For a Maxwellian distribution, Eq. (2.32) follows immediately.

Comparing expressions 2.27, 2.28, 2.30 and 2.31, we note that the g and f coefficients introduced by Shkarofsky are in fact correction factors, which for a single ionised argon plasma are functions of the effective collision frequency ratio $\frac{< \nu_{en} >}{< \nu_{ei} >}$ and the Hall coefficient $\omega_b / < \nu_g >$. They can be interpreted as correction factors to the averaged collision frequency to obtain the effective collision frequency for conductivity as: $\nu_{eff} = g < \nu_g >$ and an effective cyclotron frequency $\omega_{b\ eff} = f \cdot \omega_b$.

We also note that the usual relationship between the tensor components for the electrical conductivity for a Lorentzian gas is no longer valid.

For Lorentzian plasma we have: $\dfrac{\sigma_t \cdot \sigma_p}{\sigma_t^2 + \sigma_H^2} = 1$

For Shkarofsky plasma we obtain: $\dfrac{\sigma_{11} \cdot \sigma_{33}}{\sigma_{11}^2 + \sigma_{12}^2} = \dfrac{g}{g_0}$ (2.33)

2.4 Numerical Calculation of Electrical Conductivity Tensor

(a) Calculation of the averaged electron-neutral and electron-ion collision frequency:

Z. Al-Attar et al. (Ref. 69) discuss the criteria for averaging the collision frequencies either over a Druyvenstein distribution function or a Maxwellian distribution function for the electrons. The ratio $\mathcal{E}/p$ should be less than 1 V/cm, Torr in order to allow a Maxwellian distribution function for the electrons to be assumed. However, it turns out that for argon, a Maxwellian-averaged curve for the collision frequencies follows very closely a Druyvenstein-averaged curve, so that no significant error is introduced by using a Maxwellian-averaging technique, even for moderate values of E/p. By definition of the average we have for a Maxwellian distribution function:

$$\langle \nu_{en} \rangle = \left[\frac{1}{v^2} \frac{d}{dv} \left(\frac{v^3 \nu_{en}}{3} \right) \right]_{average.}$$

$$= \frac{1}{n} \int_0^\infty \frac{4\pi}{v^2} \frac{d}{dv} \left(\frac{v^3 \nu_{en}}{3} \right) f_0 \, v^2 \, dv$$

wherein f_o = Maxwellian distribution function for electrons =

$$= n_e \left(\frac{m_e}{2\pi k T_e} \right)^{3/2} \exp\left(- \frac{m_e v^2}{2 k T_e} \right)$$

$\nu_{en} = C\, V^r$ as determined in (2.20) and (2.21).

After substitution and evaluation of the integral, one obtains:

$$\langle \nu_{en} \rangle = \frac{4C}{3\sqrt{\pi}} \cdot \left[\frac{2kT_e}{m_e} \right]^{r/2} \cdot \Gamma\left(\frac{r+5}{2}\right) \qquad (2.34)$$

wherein Γ denotes a gamma function.

For the electron-ion collision frequency, the same could be repeated knowing that the electron-ion collision frequency varies inversely with the cube of the electron velocity.

The following expressions are taken from Ref. (65):

$$\nu_{ei} = \frac{4\pi n_e}{v^3} \left(\frac{e^2}{4\pi \varepsilon_0 m_e} \right)^2 \cdot \ln \Lambda \qquad (2.35)$$

wherein $$\Lambda = \frac{3}{2e^3} \frac{(4\pi \varepsilon_0 kT)^{3/2}}{(\pi n_e)^{1/2}} \qquad (2.36)$$

When averaged over a Maxwellian distribution function, one obtains:

$$\langle \nu_{ei} \rangle = \frac{4}{3}\sqrt{2\pi}\, n_e e^4 (4\pi \varepsilon_0 kT)^{-2} \cdot \left(\frac{kT_e}{m_e}\right)^{1/2} \ln \Lambda \qquad (2.37)$$

Finally, we define the total averaged collision frequency:

$$\langle \nu_g \rangle = \langle \nu_{en} \rangle + \langle \nu_{ei} \rangle \qquad (2.38)$$

Expressions (2.34) and (2.37) can be evaluated with the aid of the argon plasma parameters behind the reflected shock.

The electron density and the neutral particle density for a single ionised plasma follow directly from the definition of the degree of ionisation or:

$$n_e = n_{A^+} = \frac{\rho \alpha}{m_A} \qquad (2.39)$$

wherein m_A is the mass of an argon atom or 6.63×10^{-26} kgr.

$$n_A = (1-\alpha)\frac{\rho}{m_A} \qquad (2.40)$$

Relevant data are listed in Table I for an argon plasma behind the reflected shock created at initial conditions of a 10 Torr initial pressure and incident shock Mach numbers ranging from 5.5 up to 9. The data listed are respectively:

Electron density (EN) in $\#/m^3$.

Neutral particle density (NN) in $\#/m^3$.

Averaged electron-ion collision frequency (< NUEI >)

Averaged electron-neutral collision frequency (< NUEN >)

Total averaged collision frequency (< NUG >)

The ratio $<\nu_{en}>/<\nu_{ei}>$ (< NUEN >/< NUEI >)

The plasma frequency $\left(\omega_p^2 = \frac{e^2 n_e}{m_e \varepsilon_0}\right)$

The Debye length in m. $\left(= \sqrt{\frac{\varepsilon_0 kT}{e^2 n_e}}\right)$

(b) Calculation of the Shkarofsky Correction Coefficients g and f:

As in the calculation by Al Attar et al. (Ref. 69), we solve for the quantities g and f for the power law r = 4.28 using a 4 x 4 matrix scheme; the correction factors can be expressed as:

$$g = \mathcal{R}\left\{ \frac{|\Delta|}{|\Delta_{00}|} \cdot \left\{ \frac{\langle \nu_g \rangle}{\langle \nu_{ei} \rangle} \right\}^{-1} \right\} \qquad (2.41)$$

$$f = J \left\{ \frac{|\Delta|}{|\Delta_{oo}|} \cdot \left\{ \frac{\omega_b}{\langle \nu_{ei} \rangle} \right\}^{-1} \right\} \tag{2.42}$$

wherein $|\Delta|$ is the determinant of a composite matrix Δ given in Ref. (65), Eq. (55c). Each element of this matrix is the sum of three contributions: from the electron-neutral interactions (wherein the power law r enters), from the electron-ion interaction and the electron-electron interaction. These three matrices are given respectively in Ref. (65), Eqa. (48, 49 and 53).

$|\Delta oo|$ is the 00 minor of $|\Delta|$.

Knowing the velocity exponent for the collision frequencies, the determinants can be calculated. For every plasma condition the ratios $< \nu_{en}>/< \nu_{ei} >$ and $\omega_b/< \nu_g >$ are obtained and the correction factors g and f are calculated.

A note of caution should be voiced about this procedure. As pointed out by Al Attar et al. (Ref. 69), the convergence of the Laguerre expansion has to be checked, especially when using a velocity power law larger than 3.

In our case, a power law $r = 4.28$ could result in an overestimation of g and an underestimation of f particularly for large $< \nu_{en} >/< \nu_{ei} >$ ratios. Al Attar, using the same power law, states that these numerical results should not be extrapolated below $M_s = 8$ for which a ratio $<\nu_{en}>/<\nu_{ei}> = 5$ exists at initial pressure of 5 Torr. The same ratio for the reflected shock experiments is obtained for an incident shock Mach number of 5.5 at 5 Torr initial pressure, indicating that the procedure can be used in our range of interest for $M_{si} > 5.5$.

(c) Calculation of the Tensor Components of the Plasma Conductivity:

Knowing the Shkarofsky correction factors, which agree with the g and f factors given in Ref. (69), it is straightforward to calculate the tensor components from Eqs. (2.26, 2.27 and 2.28).

Figure 9 shows the calculated values of the scalar electrical conductivity for an argon plasma at 1 atmosphere versus temperature for a power law $r = 4.28$.

E.H. Dudgeon (Ref. 70) and J. Lau (Ref. 71) evaluated the electrical conductivity for an argon plasma using Shkarofsky's method for a velocity power law $r = 3.7$. This power law results from a best fit of the electron-neutral momentum transfer cross-sections for argon from Frost (Ref. 66) over an interval of electron energy between 0.3 and 10 ev. To show the effect of a different power law on the resulting conductivity, the data for $r = 3.7$ are plotted in Fig. 9. Also shown are the data for conductivities using Lin's method (Ref. 35) with Frost's cross-sections. R. J. Arave et al. (Ref. 72) compiled extensive data about argon, including the electrical conductivities which are also shown in Fig. 9.

It is interesting to observe that, as Frost pointed out (Ref. 64), the conductivities calculated with Lin's method show a discrepancy in the intermediate range (7000°K) for which

Frost applied a correction factor. Agreement between the curves improves on approaching either the low conductivity or the high conductivity regime as expected. Comparing the two curves for the different exponents indicates that the conductivity is not a sensitive function of the exponent r.

Figure 10 shows the three components of the conductivity tensor versus incident shock Mach number for an argon plasma behind the reflected shock. They are presented for a shock tube initial pressure of 10 Torr and three values of the external applied magnetic field of 2, 4, 6 Tesla respectively.

Chapter III

THEORY OF HALL CONDUCTIVITY PROBE

In the field of plasma physics, one often encounters situations whereby large magnetic fields are used, either to confine a plasma or to extract energy from a plasma such as in MHD generators. In many cases, the plasma loses its isotropic nature and the electrical conductivity becomes tensorial. The design of MHD generators is often based on the magnitude of the Hall effect; in the extreme case one talks about Hall generators.

The Hall effect can also be a powerful plasma diagnostic tool in measuring tensor conductivities, electron densities and collision frequency as was observed by Zauderer (Ref. 73) and M. Nagata (Ref. 74). Here also, inductive probes have a clear advantage over electrodes since no sheath effects have to be taken into account.

Reference (46) lists a few attempts that have been made to include Hall effects in determining the response of an inductive probe. Selamoglu and Maeder (Ref. 43) consider the response of a short coil immersed in a conducting medium and give an exact treatment of the problem for unit filling factor only, which limits the usefulness of the device. Savic and Stock (Ref. 44) give an exact treatment for a filamentary coil outside a conducting core. The nature of the Hall effect implies a second order effect on the coil and often, very large magnetic fields are required to detect any anisotropy. The present probe configuration relies on the stray field of the coil and it will be shown that this provides larger sensitivity to detect Hall effects.

The objective of this study is to establish a relationship between the tensor conductivity and the resistive and reactive changes of the coil impedance. This, combined with a proper calibration of the probe and the detection circuit makes it feasible to measure the Hall effect in plasmas. After presenting a mathematical model of the probe, the analysis is worked out for the immersed coil. The presentation of the numerical results follows in the form of a parametric study and this chapter concludes with some observations and comparisons with other probe configurations.

3.1 Presentation of the Problem

A coil of finite length is immersed in an electrically conducting medium. A D.C. external magnetic field, aligned with the axis of the probe coil, makes the medium anisotropic and modifies the electric and magnetic fields generated by the coil in the plasma. Since the resulting vector potential in the plasma ($\overline{A}_p$), contains an axial component, the analysis will be done in terms of the magnetic field components themselves.

The following assumptions are made to render the mathematical model manageable.

(a) The coil consists of an infinitely thin circular cylindrical sheath with radius a, length ℓ, and consists of N ribbons of wire with resulting turn density $n = N/\ell$. The outside radius of the probe is b. Each turn is circular (zero pitch).

(b) The alternating current in the coil, at 10.7 MHz, is distributed uniformly along the coil. The current is small enough to allow Joule heating of the plasma to be neglected.

(c) The medium in which the probe is immersed extends to infinity in all directions, is homogeneous and at rest.

(d) Dielectric constant and magnetic permeability of the medium are scalar constants and were assigned the value for vacuum.

(e) The electrical conductivity of the medium is finite and is different for different directions (i.e. a tensor).

(f) The external magnetic field is constant, parallel to the probe axis and uniform over the probing volume.

(g) Displacement currents are ignored.

A qualitative picture of the phenomena follows closely the description given for the probe in an isotropic plasma. However, due to the presence of a strong axial magnetic field, the azimuthal induced field $\mathcal{E}_\varpi$, will produce a current in the plasma which is no longer purely azimuthal but has three space components. The component of the current in the radial direction is the Hall current. Since the probe wall is non-conducting, the Hall voltage driven currents must form closed loops. Since the coil has a finite length, the radial Hall voltage will be strongest in the centre of the coil and is zero past the coil ends. Under this axial gradient, the Hall currents will close with a return path past the coil end. If we freeze, for a moment, the azimuthal component of these eddy currents, we notice two current loops, in meridian planes going through the coil axis, which modify the impedance of the probe coil. From this description, it follows that the Hall effect will show up as a second order effect.

3.2 Analysis of Hall Probe

Shkarofsky shows that the electrical conductivity matrix for a plasma which is under the influence of a magnetic field along the z-axis of a cylindrical coordinate framework for a zero applied electric field is:

$$\bar{\bar{\sigma}} = \begin{pmatrix} \sigma_T & \sigma_H & 0 \\ -\sigma_H & \sigma_T & 0 \\ 0 & 0 & \sigma_P \end{pmatrix}$$

The components $\sigma_T (= \sigma_{11})$, $\sigma_H (= \sigma_{12})$, and $\sigma_P (= \sigma_{33})$ are calculated in Chapter II. The subscripts T, H and P stand for transverse, Hall and parallel respectively. (3.1)

According to Ohm's law $\bar{J} = \bar{\bar{\sigma}} \bar{\mathcal{E}}$, the components of the current density in the r, φ, z direction are:

$$\begin{aligned} j_r &= \sigma_T \mathcal{E}_r + \sigma_H \mathcal{E}_\varphi \\ j_\varphi &= -\sigma_H \mathcal{E}_r + \sigma_T \mathcal{E}_\varphi \\ j_z &= \sigma_P \mathcal{E}_z \end{aligned} \qquad (3.2)$$

which can be solved explicitly for the electric field:

$$\begin{aligned} \mathcal{E}_r &= S_T\, j_r - S_H\, j_\varphi \\ \mathcal{E}_\varphi &= S_H\, j_r + S_T\, j_\varphi \\ \mathcal{E}_z &= j_z \cdot S_P \end{aligned} \tag{3.3}$$

wherein: $S_T = \dfrac{\sigma_T}{\sigma_T^2 + \sigma_H^2}$, $S_H = \dfrac{\sigma_H}{\sigma_T^2 + \sigma_H^2}$, $S_P = \dfrac{1}{\sigma_P}$

This analysis follows closely the analysis done by P. Savic et al. (Ref. 44) for the external filamentary coil. While, in that paper, the assumption was introduced that $S_T/S_P = 1$, which is true for the classical Lorentz plasma, as pointed out by P. Savic, we did not use this assumption since we mentioned in Chapter II, Eq. (2.33), that this simplification is not strictly valid for a Shkarofsky plasma, e.g. at an incident shock Mach number of 6, and a magnetic field of 5 Tesla, this ratio is approximately 1.1.

In order to determine the magnetic field from the plasma current, we use the fourth Maxwell equation without displacement current:

$$\bar{\nabla} \times \bar{B} = \mu\, \bar{j}$$

which can be expressed in cylindrical coordinates using azimuthal symmetry:

$$\begin{aligned} j_r &= -\frac{1}{\mu}\frac{\partial B_\varphi}{\partial z} \\ j_\varphi &= \frac{1}{\mu}\left(\frac{\partial B_r}{\partial z} - \frac{\partial B_z}{\partial r}\right) \\ j_z &= \frac{1}{\mu r}\frac{\partial}{\partial r}\left(r\, B_\varphi\right) \end{aligned} \tag{3.4}$$

In order to eliminate the electric field from Eqs. (3.3) and (3.4), the third Maxwell equation can be used:

From $\bar{\nabla} \times \bar{\mathcal{E}} = -\frac{\partial \bar{B}}{\partial t}$ we obtain in cylindrical coordinates:

$$\frac{\partial B_r}{\partial t} = \frac{\partial \mathcal{E}_\varphi}{\partial z}$$

$$\frac{\partial B_\varphi}{\partial t} = \frac{\partial \mathcal{E}_z}{\partial r} - \frac{\partial \mathcal{E}_r}{\partial z} \tag{3.5}$$

$$\frac{\partial B_z}{\partial t} = -\frac{1}{r}\frac{\partial}{\partial r}\left(r\,\mathcal{E}_\varphi\right)$$

Solving for the components of the magnetic field generated by the coil currents ($\bar{B}_D$), the plasma currents ($\bar{B}_P$), and the reflected magnetic field ($\bar{B}_R$), it is convenient to postulate the functional form of these fields. The expressions developed in Chapter I can serve as a useful guide in finding the proper functional form.

The expressions for the vector potential derived in Chapter I can be transformed into equations for the magnetic field by using the vector relationship: $\bar{B} = \bar{\nabla} \times \bar{A}$ and performing the curl operations in cylindrical coordinates.

Again, we distinguish three regions and use the same subscripts as in Chapter I.

Subscript D: Driving magnetic field ($a \le r \le b$)

P: Magnetic field in the plasma ($r > b$)

R: Reflected magnetic field ($r \le b$)

By including the time dependence of the magnetic field, one can write Eq (1.9) as follows:

$$A_{\varphi D} = \frac{\mu a I}{\pi}\int_0^\infty I_1(ak)\,K_1(kr)\exp(j\omega t + jkz)\,dk$$

from which we obtain the magnetic field components:

$$B_{rD} = -\frac{\partial A_\varphi}{\partial z} = -\frac{\mu a I}{\pi}\int_0^\infty jk\, I_1(ak)\, K_1(kr)\exp(j\omega t + jkz)\,dk \tag{3.6}$$

$$B_{\varphi D} = 0$$

$$B_{zD} = \frac{1}{r}\frac{\partial}{\partial r}(r A_\varphi) = -\frac{\mu a I}{\pi}\int_0^\infty k\, I_1(ak)\, K_0(kr)\exp(j\omega t + jkz)\,dk.$$

For the case with Hall effect, the reflected magnetic field has three components due to the presence of Hall currents in the plasma. Again, the functional form of the z component of the reflected magnetic field can be derived from the vector potential in the case without Hall effect (Eq. 1.19):

$$A_{\varphi R} = \int_0^\infty f_R(k)\, I_1(kr)\exp(j\omega t + jkz)\,dk$$

The radial component of the magnetic field must vanish at r = 0, because $\bar{\nabla} \cdot \bar{B} = 0$; the same is true for the azimuthal component, so it is reasonable to postulate a $I_1(kr)$ relationship. Hence:

$$B_{rR} = \int_0^\infty R_R(k)\, I_1(kr)\exp(j\omega t + jkz)\,dk$$

$$B_{\varphi R} = \int_0^\infty T_R(k)\, I_1(kr)\exp(j\omega t + jkz)\,dk \tag{3.7}$$

$$B_{zR} = \frac{1}{r}\frac{\partial}{\partial r}(r A_{\varphi R}) = \int_0^\infty Z_R(k)\, I_0(kr)\exp(j\omega t + jkz)\,dk$$

wherein R_R, T_R and Z_R are unknown functions of the parameter k.

To postulate the expressions for the magnetic field in the plasma, it is convenient to derive the z component from the expression (1.18) of the magnetic vector potential for a plasma without Hall current:

$$A_{\varphi p} = \int_0^\infty f_p(k)\, K_1(dr) \exp(j\omega t + jkz)\, dk$$

The radial and azimuthal components of the magnetic field in the plasma should vanish at infinity, which indicates the need for a $K_1(dr)$ relationship. Hence:

$$\begin{aligned} B_{rp} &= \int_0^\infty R_p(d)\, K_1(dr) \exp(j\omega t + jkz)\, dk \\ B_{\varphi p} &= \int_0^\infty T_p(d)\, K_1(dr) \exp(j\omega t + jkz)\, dk \\ B_{zp} = \frac{1}{r}\frac{\partial}{\partial r}\left(r A_{\varphi p}\right) &= \int_0^\infty Z_p(d)\, K_0(dr) \exp(j\omega t + jkz)\, dk \end{aligned} \qquad (3.8)$$

In order to obtain a relationship for the unknowns R_p, T_p, Z_p, we first calculate the current density in the plasma by substituting expressions (3.8) in (3.4):

$$\begin{aligned} J_r &= -\frac{1}{\mu} \int_0^\infty jk\, T_p(d)\, K_1(dr) \exp(j\omega t + jkz)\, dk \\ J_\varphi &= \frac{1}{\mu} \int_0^\infty \left(jk\, R_p(d) + d\, Z_p(d)\right) K_1(dr) \exp(j\omega t + jkz)\, dk \\ J_z &= -\frac{1}{\mu} \int_0^\infty d\, T_p(d)\, K_0(dr) \exp(j\omega t + jkz)\, dk \end{aligned} \qquad (3.9)$$

Next, the electric field can be calculated from expressions (3.3):

$$\mathcal{E}_r = -\frac{1}{\mu}\int_0^\infty \Big[S_T jk T_p(d) + S_H\big(jk R_p(d) + d Z_p(d)\big)\Big]$$

$$\cdot\, K_1(dr)\exp(j\omega t + jkz)\,dk$$

$$\mathcal{E}_\varphi = -\frac{1}{\mu}\int_0^\infty \Big[S_H jk T_p(d) - S_T\big(jk R_p(d) + d Z_p(d)\big)\Big]$$

$$\cdot\, K_1(dr)\exp(j\omega t + jkz)\,dk$$

$$\mathcal{E}_z = -\frac{1}{\mu}\int_0^\infty S_p d T_p(d)\exp(j\omega t + jkz)\,dk$$

(3.10)

from which the following relationships result by substituting (3.10) and (3.8) in (3.5) and cancelling the common integrals on both sides

$$j\mu\omega R_p(d) = -S_T k^2 R_p(d) + S_H k^2 T_p(d) + S_T jkd Z_p(d)$$

$$j\mu\omega T_p(d) = -S_H k^2 R_p(d) + S_p d^2 T_p(d) - S_T k^2 T_p(d) + jS_H dk Z_p(d)$$

$$j\mu\omega Z_p(d) = jS_T kd R_p(d) - jS_H kd T_p(d) + S_T d^2 Z_p(d).$$

(3.11)

This is a system of three homogeneous linear algebraic equations for the functions $R_p(d)$, $T_p(d)$ and $Z_p(d)$ which have solutions only if they are compatible, i.e. the determinant of the coefficients mush vanish. The three equations do not contain any eigen functions which follows from the judicial choice of the functional relationships in expressions (3.8).

This system of three homogeneous equations can be simplified by using the second Maxwell law: $\bar{\nabla}\cdot\bar{B} = 0$ which, applied to equations (3.8), reduces to:

$$d\, R_p(d) - jk\, Z_p(d) = 0 \tag{3.12}$$

By eliminating $Z_p(d)$ from (3.11a) and 3.11c) using (3.12), it turns out that two equations are identical. Hence the set of equations (3.11) is identical to a set of equations (3.12, 3.11a and 3.11b) from which $Z_p(d)$ can be eliminated. This reduces the set to two homogeneous linear algebraic equations for which the determinant has to vanish, or:

$$\begin{vmatrix} j\mu\omega + S_T(k^2-d^2) & -S_H k^2 \\ S_H(k^2-d^2) & j\mu\omega + S_T k^2 - S_p d^2 \end{vmatrix} = 0 \tag{3.13}$$

At this point it is useful to introduce the following non-dimensional quantities:

$$S_0 = \sigma_p \mu \omega b^2 \quad , \quad S_1 = S_T \sigma_p \ , \quad S_2 = S_H \sigma_p \quad , \quad S_3 = S_p \sigma_p$$

$$y = kb \ , \qquad x = db = \left(k^2 + j\sigma_p \mu\omega\right)^{1/2} b$$

$$H = \frac{S_2}{S_1} = \text{Hall parameter} = \omega\tau$$

$$G = \frac{S_3}{S_1}$$

$$F = \frac{S_0}{S_1}$$

$$U = y^2 + jF$$

The compatibility equation reduces to:

$$x_{1,2} = \left\{ \frac{(1+G)U + H^2 y^2}{2\,G} \pm \left[\left(\frac{(1+G)U + H^2 y^2}{2\,G} \right)^2 - \left(\frac{U^2 + H^2 y^4}{G} \right) \right]^{1/2} \right\}^{1/2} \qquad (3.14)$$

This gives two values for x from which follows that each of the constants $R_p(x)$, $T_p(x)$ and $Z_p(x)$ have two values for which the set of equations (3.11) has a solution.

This means then that we have nine unknown constants:

$$R_p(x_1)\;,\; R_p(x_2)\;,\; R_R(y)$$

$$T_p(x_1)\;,\; T_p(x_2)\;,\; T_R(y)$$

$$Z_p(x_1)\;,\; Z_p(x_2)\;,\; Z_R(y)$$

for which nine equations are required. These remaining equations are given by the following boundary conditions:

(a) At infinity: The choice of K as the modified Bessel function satisfies the condition that the magnetic field vanishes at infinity.

(b) At the surface of the conductor: (r = b), both the tangential and normal magnetic field components must be continuous since the magnetic permeabilities on both sides of the probe boundary are equal.

From: $$\left[\bar{B}_D + \bar{B}_R\right]_{r=b} = \left[\bar{B}_P\right]_{r=b}$$

we obtain the following three boundary conditions:

$$-\frac{\mu h I}{\pi} j y \, I_1(hy) K_1(y) + R_R(y) I_1(y) = R_P(x_1) K_1(x_1) + R_P(x_1) K_1(x_2)$$

$$T_R(y) I_1(y) = T_P(x_1) K_1(x_1) + T_P(x_2) K_1(x_2) \tag{3.15}$$

$$-\frac{\mu h I}{\pi} y \, I_1(hy) K_0(y) + Z_R(y) I_0(y) = Z_P(x_1) K_0(x_1) + Z_P(x_2) K_0(x_2)$$

(c) At the probe wall no radial current can exist or $J_r = 0$ at $r = b$. Applying equation (3.4a) for $B_{\varphi R}$, $B_{\varphi P}$, two more boundary conditions result:

$$j y\, T_R(y)\, I_1(y) = 0 \qquad \text{or} \qquad T_R(y) = 0$$

and

$$j y\, T_P(x_1)\, K_1(x_1) + j y\, T_P(x_2)\, K_1(x_2) = 0 \qquad (3.16)$$

$$\text{or} \quad T_P(x_1)\, K_1(x_1) + T_P(x_2)\, K_1(x_2) = 0$$

(d) Since the magnetic field is source free we can write for the three magnetic fields:

$$\bar{\nabla} \cdot \bar{B}_P = 0$$

$$\bar{\nabla} \cdot \bar{B}_D = 0$$

$$\bar{\nabla} \cdot \bar{B}_R = 0$$

The first is already made use of (Eq. 3.12), the second equation is automatically satisfied by the postulated expression for the driving field and there remains one extra condition concerning the reflected magnetic field which results in:

$$R_R(y) + j\, Z_R(y) = 0 \qquad (3.17)$$

This gives the nine required equations to solve for the nine unknowns. The compatibility requirement for the set of equations (3.11) reduces it to two pairs of independent equations, one pair of which can be replaced by the pair of equations (3.12) for convenience. The nine independent equations are:

from (3.11a): $\left(j S_0 + S_1 y^2 - S_1 x_1^2 \right) R_P(x_1) - S_2 y^2\, T_P(x_1) = 0$

$$\left(j S_0 + S_1 y^2 - S_1 x_2^2 \right) R_P(x_2) - S_2 y^2\, T_P(x_2) = 0$$

from (3.12): $x_1\, R_P(x_1) - j y\, Z_P(x_1) = 0$

$$x_2\, R_P(x_2) - j y\, Z_P(x_2) = 0$$

3.15a: $R_p(x_1)\,K_1(x_1) + R_p(x_2)\,K_1(x_2) - R_R(y)\,I_1(y)$

$$= -\frac{\mu h I}{\pi}\, j y\, I_1(hy)\, K_1(y)$$

3.15c: $Z_p(x_1)\,K_0(x_1) + Z_p(x_2)\,K_0(x_2) - Z_R(y)\,I_0(y)$

$$= -\frac{\mu h I}{\pi}\, y\, I_1(hy)\, K_0(y)$$

3.16a: $T_R(y) = 0$ (3.18)

3.16b: $T_p(x_1)\,K_1(x_1) + T_p(x_2)\,K_1(x_2) = 0$

3.17: $R_R(y) + j\,Z_R(y) = 0$

Any change of the voltage measured across the coil is attributed to the temporal change of the reflected magnetic field across each wire loop of the coil. Since each loop of the coil lies in a plane whose normal is parallel to the z-axis of the coil, only the z component of the reflected magnetic field can modify the voltage across the coil. Hence we have to solve the set of equations (3.18) for Z_R. After repeated substitutions and eliminations the following expression emerges:

$$Z_R(y) = y\,\frac{\mu h I}{\pi}\, I_1(hy)\,\frac{y\,K_0(y) - E\,K_1(y)}{y\,I_0(y) + E\,I_1(y)} \qquad (3.19)$$

wherein:

$$E = x_1\,\frac{C_2}{C_2 - C_1}\cdot\frac{K_0(x_1)}{K_1(x_1)} - x_2\,\frac{C_1}{C_2 - C_1}\cdot\frac{K_0(x_2)}{K_1(x_2)}.$$

$$C_1 = j\,s_0 + s_1\,(y^2 - x_1^2)$$

$$C_2 = j\,s_0 + s_1\,(y^2 - x_2^2).$$

The voltage induced in a single turn coil with radius a, due to the presence of a conducting medium can be calculated from Maxwell's third law.

$$\Delta V = \oint \bar{\mathcal{E}}_R \cdot \bar{dl} = -\frac{d}{dt}\iint B_{zR}\, dS = -2\pi j\omega \int_0^a r B_{zR}\, dr \qquad (3.20)$$

By substituting the expression for B_{zR} from (3.7c) and (3.19) into (3.20), and carrying out the integration over the radius, the following expression results for the induced impedance in a single turn coil situated at z = 0:

$$\Delta Z = 2a\, j\omega\mu h \exp(j\omega t) \cdot \int_0^\infty I_1^2(hy)\, \frac{yK_0(y) - EK_1(y)}{yI_0(y) + EI_1(y)} \cos\left(\frac{z}{b}y\right) dy \qquad (3.21)$$

From this expression, the change of impedance for a multi-turn single-layer coil, situated between $-\ell/2$ and $+\ell/2$, with a turn density $n(=N/\ell)$ can be calculated by integrating the single z dependent term in (3.21) twice between the coil boundaries $-\ell/2$ and $+\ell/2$.

Since $$\int_{-\ell/2}^{+\ell/2}\int_{-\ell/2}^{+\ell/2} \cos\left(\frac{z}{b}y\right) dz_1\, dz_2 = \frac{2b^2}{y^2}\left(1-\cos wy\right)$$

wherein $w = \ell/b$,

The final expression for the impedance change for the immersed coil after the time dependent term exp(jωt) is omitted can be written as:

$$\frac{\Delta Z}{\omega\mu a} = 4jhb^2n^2 \int_0^\infty \frac{I_1^2(hy)}{y^2}\, \frac{yK_0(y) - EK_1(y)}{yI_0(y) + EI_1(y)} \left(1-\cos(wy)\right) dy \qquad (3.22)$$

This expression is identical in form with the expression derived in the first chapter except for the E factor which expresses the anisotropy of the plasma. Since E is complex, the impedance change again will contain both a resistive and a reactive component.

3.3 Numerical Solution

Numerical solution of equation (3.22) follows the same pattern as in the case without Hall effect except for the added compatibility requirement.

In order to present a parametric study of a single layer coil, a classical Lorentz plasma was considered in order to avoid the problem of calculating the ratio g_o/g of the Shkarofsky correction coefficients. The error, however, is very small as noted in Chapter II.

The controlling parameters for a Hall plasma probe are:

(a) s number ($=\mu\sigma\omega b^2$) or the square of the ratio of probe radius to the electromagnetic skin depth.

(b) h (= a/b) the filling factor of the probe.

(c) w ($=\ell/b$) length ratio of the coil.

(d) H: The Hall parameter defined earlier as s_2/s_1 which reduces to $H = \omega/<\nu_g>$ by using the expression for the tensor components of the conductivity defined in Chapter II. Defining $\tau = 1/<\nu_g>$, the Hall parameter is often written as $H = \omega\tau$.

In order to illustrate the sensitivity of the probe response to Hall effect, the following study concerning a single layer coil with a fixed length ratio ($w = 6.3$), variable s number, variable filling factor h and variable Hall parameter for a Lorentzian plasma was carried out.

Figure 11 illustrates the variation of the normalised probe response for both channels ($\Delta R/\omega\mu a$, $\Delta L/\mu a$), as a function of the s parameter for filling factor $h = 1/3$ and fixed length ratio ($w = 6.3$) which is close to the geometry of a practical coil. Each family consists of five curves for corresponding values of the Hall parameter.

These curves should be compared with Figure 5 of Ref. (44) which corresponds with a filling factor $h = 3$ for the external coil.

In Figure 12 the normalised inductance change ($\Delta L/\mu a$) has been plotted against the normalised resistance change ($\Delta R/\omega\mu a$) for three different filling factors, $h = 1/3$, $1/2$, $2/3$, which constitute the three distinct families of curves.

In each family, each of the curves corresponds to a different value of the Hall parameter, $H = 0$, 5, 10, 15 and 20, respectively. Each curve in this family traces out all possible values of s. The transverse lines crossing the upward going curves describe a path at constant conductivity for various Hall coefficients. The radial dashed lines centred at origin join the points at the three families of curves with identical s number and Hall parameter; in this case, the radial lines are shown for $s = 11$.

3.4 Discussion of the Numerical Results

First, we consider the operating region which, for shock tube plasmas, is centered around s = 0.3 (Fig. 11). In this region, the dependence of the inductance on the Hall parameter H is much stronger than that of the resistance, which is confirmed by experiments. While the sensitivity of the impedance change in the measurement of scalar electrical conductivity increases strongly for increasing filling factor (Fig. 3, 4), the relative sensitivity to Hall effect is practically independent of the filling factor in the operating region around s = 0.3.

By comparing Fig. 11 with the equivalent graph in Ref. (44), Fig. 5, for the external coil in the same operating region s = 0.3, one concludes that the relative sensitivity to Hall effect for the immersed probe is more than double the sensitivity for the external coil. As pointed out in Ref. (44), Hall currents can only flow in the fringe field of the external coil while the immersed coil senses the plasma only by way of the return flux which has a larger radial field component. However, one cannot extrapolate this conclusion to different s regimes. Figure 11 indicates clearly that the resistive channel will give ambiguous results for $1 < s < 10$. Beyond that region, the change in resistance due to Hall effect is reversed and sensitivity is not very good. As indicated already, for $s < 1$ the inductance change is very sensitive to Hall effect while the sensitivity is reduced for increasing s. For s > 10, the reactive channel becomes unsuitable to detect Hall effect. The impedance diagram of Fig. 12 illustrates the same conclusion and shows that this is true for any filling factor. This figure also illustrates that the points in each family corresponding to the same s number are colinear not only for the scalar conductivity but also for the case with Hall effect.

The last parameter to be discussed is the length ratio parameter w. We recall from Chapter I that the sensitivity for measuring scalar conductivities increases as $w^{1.82}$ (Eq. 1.39) in the small s regime when all other parameters are constant. However, the sensitivity for detecting Hall effect decreases for increasing length ratios. This is shown in the table below for a case where the filling factor h = 0.5, at s = 0.3 which corresponds to shock tube plasma conductivities, for four different length ratios. The relative sensitivity is calculated for a Hall coefficient of 5 and expressed as $\frac{\overline{\Delta R_o} - \overline{\Delta R_5}}{\overline{\Delta R_o}}$ and $\frac{\overline{\Delta L_o} - \overline{\Delta L_5}}{\overline{\Delta L_o}}$ in percentage. The bars over the symbols indicate non-dimensionalised units.

w	$\overline{\Delta R_o}$	$\overline{\Delta R_5}$	o/o	$\overline{\Delta L_o}$	$\overline{\Delta L_5}$	o/o
2	3.89	2.62	33	1.61	0.63	61
4	12.19	9.07	26	5.77	2.49	57
6	21.81	17.70	19	11.44	5.53	52
8	31.78	27.59	13	17.87	9.65	46

This reduction in sensitivity in detecting Hall effect by increasing length ratios indicates again that Hall currents flow only in the fringe field of the coil. In theory, an infinitely long coil would be very sensitive to measuring conductivities but would not detect Hall effect in plasmas.

Chapter IV

IMMERSION PROBE RESPONSE IN NON-UNIFORM PLASMAS

The small size and simplicity in handling is the main advantage of the immersed conductivity probe. The small probe acts as a local detector and measures the conductivity in a very small volume thus resulting in a high spatial resolution. But, as Poberezhskii points out in Ref. (41), this method does not completely eliminate the problem of nonuniformity of the conductivity profile, since a boundary layer is formed around the surface of the probe, and its relative influence is greater, the smaller the dimension of the detector. This then is the main drawback of such a system, and it suggests that there is a limit to the spatial resolution which is dictated by the dimension of the boundary layer.

Some attempts are cited in the literature to determine the probe response in a nonuniform medium with arbitrary conductivity profiles. In a recent paper by M. Ciampi and N. Talini (Ref. 42) an attempt is made to determine numerically the probe impedance for nonuniform plasmas with conductivity profiles of the type $\sigma(\tau) = \sigma_{max}(1-mr^{n})$ and concludes that a weighted conductivity average can be defined, but that a useful average conductivity can only be obtained at low frequencies.

For an immersed conductivity probe, the effect of a thermal boundary layer can easily be calculated, assuming the conductivity profile approximates to a step profile, simply by changing the effective probe radius. This is not an unreasonable assumption, as Emmons and Land (Ref. 75) have shown that plasma conductivity is such a strong function of temperature (cf fig. 9), that cooling by the probe has roughly the effect of moving the (almost discontinuous) plasma boundary further away from the probe. However, this assumption presupposes that the inverse logarithmic space derivative of conductivity is small compared with the characteristic probe dimension.

Figure 13 shows the sensitivity curves for both the resistance and reactance change of the probe coil for various effective probe radii. As was mentioned in Ref. (46), a measurement of both impedance components can give some information about the conductivity profile and boundary layer thickness, because of the different sensitivities for the impedance components. This technique could be useful in the range around unity s parameter, where resistance and reactance variations are sensitive to changes in the conductivity profile and boundary layer thickness.

In this chapter, a study is made of the thermal boundary layer in a stagnant hot gas behind the reflected shock in a shock tube. This temperature profile can be transformed into an electrical conductivity profile using the Shkarofsky approach, and one calculates the probe response for such conductivity profile.

This chapter consists of two parts. The temperature profile is evaluated on the basis of conductive and convective heat transfer, this then is converted to a conductivity profile which is cast into an analytical form using a least square fitting technique. In the second part, the probe response is analysed on the basis of a conductivity profile of the form $\sigma = \sigma_0 + p_2/r^2 + p_3/r^3$.

4.1 Study of the Temperature Profile in Thermal Boundary Layers

Throughout this analysis, we assume ideal shock tube condition behind the reflected shock, i.e. the gas is stagnant and no interaction occurs between the reflected shock and the viscous boundary layer formed around the probe by the passage of the incident shock.

Carslaw and Jaeger (Ref. 77) treat the problem of the transient heat conduction in cylindrical solids after a sudden change of the inner surface temperature, assuming that the characteristic parameters of the medium are independent of temperature. The solution for a sudden cooling of a hot gas surrounding a cold probe can be written:

$$\frac{T - T_w}{T_o - T_w} = \frac{2}{\pi} \int_0^\infty \exp(-\varkappa v^2 t) \cdot \frac{J_0(vr)Y_0(vb) - Y_0(vr)\,J_0(vb)}{J_0^2(vb) + Y_0^2(vb)} \frac{du}{v} \tag{4.1}$$

wherein: J_o : zero order Bessel function of first kind

Y_o : zero order Bessel function of second kind

$T(r.t)$ = temperature profile

T_w : wall temperature of probe

T_o : ambient gas temperature

t = time

u = integration variable (dimension 1/L)

$\varkappa$: diffusivity of gas ($=\lambda/\rho C_p$)

A calculation of the initial jump in the probe wall temperature for a quartz probe shows that the wall temperature remains approximately unchanged due to the very poor heat conductivity of quartz. This is verified by experimental data obtained from a thermocouple inserted in the probe. The temperature rise during testing time was less than 5^oC which is negligible compared to the plasma temperature.

The temperature profiles resulting from (4.1) must be modified due to the highly non-linear nature of the plasma parameters, which is caused mainly by the occurrence of ionisation. In order to obtain more realistic temperature profiles, the thermodynamic parameters for argon are needed, such as the temperature dependence of heat conductivity, heat capacity, and density.

The differential equation for unsteady heat conduction can be derived from the principle of conservation of energy, which, after insertion of Fourier's law of heat conduction, becomes:

$$\bar{\nabla} \cdot \left(\lambda \bar{\nabla} T \right) - \rho C_p \frac{\partial T}{\partial t} = 0 \tag{4.2}$$

wherein: $\lambda(T)$: thermal conductivity in Kcal/sec,m,^{o}K

$\rho(T)$: density in Kgr/m^3

$C_p(T)$: specific heat at constant pressure (Kcal/gr,^{o}K)

All these parameters are a function of temperature. In cylindrical coordinates, expression (4.2) takes the form:

$$\frac{1}{r} \frac{\partial}{\partial r} \left(\lambda r \frac{\partial T}{\partial r} \right) - \rho C_p \frac{\partial T}{\partial t} = 0 \tag{4.3}$$

Non-dimensionalising this expression, we introduce the following quantities:

r_o : radius of the probe

T_o : temperature of plasma behind reflected shock

$\rho_o, \lambda_o, C_{po}$: respectively density, thermal conductivity and specific heat at temperature T_o.

We define:

$$\lambda^* = \lambda/\lambda_o$$

$$r^* = r/r_o$$

$$T^* = T/T_o$$

$$\rho^* = \rho/\rho_o$$

$$C_p^{*} = C_p/C_{po}$$

$$t^{*} = t\ \frac{\lambda_o}{\rho_o C_{po}}\ \ r_o^{2}$$

Inserting these nondimensional quantities in (4.3) we obtain

$$\frac{1}{r^*}\ \frac{\partial}{\partial r^*}\left(\lambda^* r^* \frac{\partial T^*}{\partial r^*}\right) - \rho^* C_p^* \ \frac{\partial T^*}{\partial t^*} = 0 \qquad (4.4)$$

In the following, the asterisks will be omitted for convenience. A possible way to solve this nonlinear second order partial differential equation, is to convert it to a difference equation and solve numerically.

Judging from the results obtained from the analytical solution of eq. (4.1), the temperature profile will change rapidly at the time of the passage of the reflected shock over the probe-coil, also very steep spatial gradients occur close to the probe wall so that some stretching of the spatial and time coordinates is needed.

Stretching of the spatial coordinate is effected by $r = e^c$ while stretching of the time close to the origin is done by $t = \ln \frac{1}{p}$. This transforms expression (4.4) into:

$$\frac{\lambda}{e^{2c}}\ \frac{\partial^2 T}{\partial c^2} + \frac{1}{e^{2c}}\ \frac{\partial \lambda}{\partial T}\left(\frac{\partial T}{\partial c}\right)^2 + \rho c_p\, p\, \frac{\partial T}{\partial p} = 0 \qquad (4.5)$$

In order to calculate the temperature profile, we construct a two dimensional grid whereby the spatial coordinate c $[=(n-1)*\ell]$ is divided into n equal segments of length ℓ and the time coordinate is divided in k equal sections of duration q such that the stretched time coordinate p = 1-(k-1)q (Fig. 14). In order to address a cell in this grid we use a subscript n to locate the distance and a superscript k to indicate the time. When a centered difference scheme is used for the spatial coordinate and a forward difference scheme for the time coordinate, we can express eq. (4.5) as follows:

$$\frac{\lambda_n^k}{e^{2c}} \cdot \frac{T_{n+1}^k + T_{n-1}^k - 2T_n^k}{\ell^2} + \frac{1}{e^{2c}} \cdot \frac{\partial \lambda}{\partial T} \cdot \left[\frac{T_{n+1}^k - T_{n-1}^k}{2\ell}\right]^2 = \frac{\rho_n^k C_{pn}^k}{q} p \left[T_n^{k+1} - T_n^k\right] \qquad (4.6)$$

which is an explicit expression to calculate the temperature T_n^{k+1} when the temperature is known at time interval k at the three positions n-1, n, and n+1.

$$T_n^{k+1} = T_n^k + \frac{q}{\rho_n^k C_{pn}^k p} \cdot \left[\frac{\lambda_n^k}{\tau^2} \frac{T_{n+1}^k + T_{n-1}^k - 2T_n^k}{\ell^2} + \frac{1}{\tau^2} \frac{\partial \lambda}{\partial T} \left(\frac{T_{n+1}^k - T_{n-1}^k}{2\ell}\right)^2\right] \qquad (4.7)$$

Boundary conditions:

a - At time t=0 (or k=1), the temperature is the reservoir temperature everywhere except at the probe wall or:

$$T_n^1 = 1 \text{ for } n > 1$$

b - At all times, the temperature of the probe wall remains quasi steady at room temperature which is justified during the short duration of the experiment, or:

$$T_1^k = \frac{300}{T_o} \quad \text{for all values of } k$$

c - The temperature far away from the probe has not been perturbed by the presence of a cold probe during the short time interval of the experiment, or:

$$T_{N+1}^k = 1 \quad \text{wherein } N \text{ is a suitable large value of } n$$

Once the temperature is calculated in a cell, we have to evaluate the value of the parameters λ, ρ, C_p and also $\frac{\partial\lambda}{\partial T}$ before proceeding to the next cell.

a - Calculation of $\lambda(T)$:

Extensive data about thermal conductivity of argon plasma are contained in Boeing report (Ref. 72). Since the thermal conductivity for argon plasma is virtually independent of pressure, a curve fitting (using a least square method) procedure of the thermal conductivity versus temperature in the range of interest (i.e. up to 12000°K) was carried out. The following third degree polynomial in T gave errors not exceeding 5 percent:

$$\lambda(T) = aT^3 + bT^2 + cT + d \qquad cal/cm, sec, {}^\circ K \quad (4.8)$$

wherein:

$$a = 0.231935\ 10^{-14}$$
$$b = -0.221204\ 10^{-10}$$
$$c = 0.122202\ 10^{-6}$$
$$d = -0.298764\ 10^{-5}$$

b - Calculation of ρ, C_p:

The assumption of constant pressure during the cooling in the thermal boundary layer is generally accepted in boundary layer work. In this case, the Saha equation can be used to calculate the degree of ionisation for temperatures below 12000°K. Using the temperature T and pressure P_o behind the reflected shock, as calculated from the shock equation, the Saha equation

$$\alpha = \left[2.72\ 10^5 \frac{p_o}{T^{5/2}} \exp(\vartheta i/T) + 1 \right]^{-1/2}$$

gives the degree of ionisation for a gas in thermal equilibrium.

From Ref. (56) the specific heat at constant pressure can be expressed as:

$$C_p = \frac{5}{2} R(1+\alpha) + \frac{R\alpha}{2}(1-\alpha^2)\left(\frac{5}{2} + \frac{\theta_i}{T}\right)^2 \qquad (4.9)$$

For argon: $\theta_i = 182900^\circ K$

$R = 4.974\ 10^{-2}$ cal/gr,$^\circ K$

The density can then be calculated from the equation of state

$$\rho = \frac{p_o}{(1+\alpha)RT}$$

<u>Results</u>:

The accuracy of such difference schemes to solve the partial differential equation was checked by using constant parameters and comparing this temperature profile with the analytical solutions according to eq. (4.1). The agreement was good, which is an indication that the step size was properly chosen and the truncation error was negligible.

The real gas effect on the thermal boundary layer cooling resulting from conduction only is to steepen the temperature gradient close to the wall. This is due to the latent heat of ionisation which tends to keep the temperature up in the range where the degree of ionisation decreases (above $6000^\circ K$).

A further refinement of the temperature profile study is achieved by introducing convective heat transfer mechanisms.

It is customary to assume constant gas pressure. T.A. Thomson (Ref. 78) uses an order of magnitude reasoning to show that the pressure change is negligible and concludes that only the continuity equation and the energy equation are required to solve the problem. Bunting et al (Ref. 79) solve the problem in plane geometry assuming negligible viscous dissipation and constant gas pressure, by applying a similarity transformation.

Such a transformation cannot be readily applied in cylindrical geometry, which is the reason why we solve the problem by transforming the differential equations into a set of finite difference equations for the conservation of mass and the conservation of energy. The density can be calculated from the equation of state, based on a constant pressure assumption.

By neglecting the momentum equation, one assumes that the gas has no inertia and hence can attain very high velocities.

The following set of equations was solved in cylindrical coordinates.

Conservation of mass: $$\frac{\partial \rho}{\partial t} + \frac{1}{r}\frac{\partial}{\partial r}(\rho r v) = 0$$

Conservation of energy:

$$r \rho C_p \frac{\partial T}{\partial t} + (r \rho v) C_p \frac{\partial T}{\partial r} - \frac{\partial}{\partial r}\left(r \lambda \frac{\partial T}{\partial r}\right) = 0$$

Together with the equation of state we can determine the quantities T, ρ, V.

Using the same coordinate stretching technique to expand the regions close to the origin we arrive at the following set of explicit finite difference equations.

$$\frac{\rho_n^{k+1} r_n V_n^{k+1} - \rho_{n-1}^{k+1} r_{n-1} V_{n-1}^{k+1}}{\ell} = - \frac{r_n^2}{q} p^{k+1} \left(\rho_n^{k+1} - \rho_n^k \right)$$

$$\frac{T_n^{k+1} - T_n^k}{q} = - \frac{V_n^k}{r_n p^{k+1}} \left[\frac{T_{n+1}^k - T_{n-1}^k}{2\ell} \right]$$

$$+ \frac{1}{r_n^2 \rho_n^k C_{pn}^k p^{k+1}} \left[\lambda_n^k \frac{T_{n+1}^k + T_{n-1}^k - 2T_n^k}{\ell^2} + \frac{\partial \lambda}{\partial T} \left(\frac{T_{n+1}^k - T_{n-1}^k}{2\ell} \right)^2 \right]$$

(4.10)

The additional boundary conditions for the velocity can simply be written as:

$V_n^1 = o$: velocity is zero everywhere at t = o

$V_1^k = o$: velocity is zero at all times at the probe wall

The calculation proceeds as follows:

Starting from known conditions at time k, at all positions n, we first calculate the temperature T_n^{k+1} using the explicit difference expression for the conservation of energy. Since we assume constant pressure, the density ρ_n^{k+1} can be calculated from the equation of state using the Saha equation. Knowing ρ_n^k and ρ_n^{k+1} we calculate V_n^{k+1} from the difference expression for the conservation of mass using a forward marching scheme. Since such an extrapolation scheme is very sensitive to accumulating errors, an iteration procedure was adopted together with an averaging technique for the gas parameters λ, C_p, V. The iteration is repeated until the difference in the temperatures calculated becomes negligibly small.

This procedure was tested against the analytical method used by Bunting (Ref. 79) for a planar case and the agreement was very good. Including the effect of convection, this results in an increase in the temperature gradient at the probe wall and at some distance the profiles including convection differ by as much as 15 percent from the profiles resulting from conduction only.

Using the expressions developed in Chapter 2 correlating the electrical conductivity and the temperature and pressure, the electrical conductivity profiles can easily be calculated numerically.

Figure 15 shows the results for a conductivity profile obtained behind a reflected shock with entry conditions $M_s = 7.75$, $p_1 = 5$ Torr. The data are shown for time intervals at 25, 50, 100, 150, 200 and 300 μsec.

On this figure is also shown the percentage drop in the probe response, resistive and reactive, assuming a step-profile for an electrical conducting medium of 2500 mho/m. The data have been normalised versus the stagnant reservoir conditions. In abscissa are given the radial distances as $\ln(r/b)$.

In order to evaluate the probe response for such conductivity profiles, it is necessary to express the profile data in analytical form. Using a least square method, a curve fitting procedure was applied for each calculated profile to obtain a matching profile of the form:

$$\frac{\sigma}{\sigma_0} = A(t) + \frac{B(t)}{r^2} + \frac{C(t)}{r^3} \qquad (4.11)$$

whereby the coefficients A(t), B(t) and C(t), which are a function of time, can be evaluated numerically.

Such a profile was chosen because it gives fairly good matching for the numerically calculated conductivity profiles (Fig. 15), while at the same time, an approximate solution, using a Matthieu-Bessel expansion, for the vector Helmholtz equation is not too complex.

The slope of the conductivity profile at the probe radius is zero, hence the profiles show an inflection point for $\sigma/\sigma_o < 10$ percent. An analytical expression for σ/σ_o of the form given in eq. 4.11 cannot accommodate the real profiles at low conductivity and the curve fitting was carried out only for values of $\sigma/\sigma_o > 5$ percent. The matching conductivities resulting from eq. 4.11 become negative close to the material probe radius. This problem was avoided by calculating a new fictitious probe radius, determined by the solution of the cubic $A(t)r^3 + B(t)r^2 + C(t) = 0$. Since the penetration of the R.F. field in the plasma is of the order of the skindepth δ (cf. Chapter 1), the fitting procedure can be cut off at a distance δ beyond the radius where a conductivity ratio of 99 percent exists.

The analytical conductivity profiles resulting from such a fitting technique are shown in fig. 15 as solid lines for time intervals of 25, 50, 100, 150, 200 and 300 μsec respectively, corresponding with the actual profile data obtained at each mesh point for the same time intervals.

On the same graph are shown the percentage responses for ΔR and ΔL to a conductivity of 2500 mho/m with a step profile at the radius indicated in abscissa.

The profile coefficients A(t), B(t), and C(t) can be non-dimensionalised with respect to the physical probe radius and are listed in table II for the corresponding time intervals shown in fig. 15. Also listed is the fictitious probe radius b'.

4.2 Calculation of the Probe Response for a Conductivity Profile of the Form:

$$\sigma = \sigma_0 + \frac{p_2}{r^2} + \frac{p_3}{r^3} \tag{4.12}$$

The procedure is quite analogous to the study done in the first chapter dealing with a step profile of the electrical conductivity. Again, we solve for the vector Laplacian to obtain the vector potentials for the driving current, the plasma vector potential and the reflected vector potential. This treatment deviates from Chapter I in the calculation of the plasma vector potential by solving for the vector Helmholtz equation.

Starting from expression (1.12) and substituting the expression (4.12) for the actual conductivity profile, we obtain the following equations after separation of the variables:

$$\frac{1}{Z(z)} \frac{\partial^2 Z(z)}{\partial z^2} = -k^2$$

$$r^2 \frac{\partial^2 R(r)}{\partial r^2} + r \frac{\partial R(r)}{\partial r} - R(r)\left[1 + k^2 r^2 + j\left(\sigma_0 + \frac{p_2}{r^2} + \frac{p_3}{r^3}\right)\mu\omega r^2\right] = 0 \tag{4.13}$$

whereby $A_{\varphi p} = R(r)Z(z)$.

By introducing the following non-dimensional quantities

$$\begin{aligned} V^2 &= (\alpha r)^2 = (k^2 + j\sigma_0 \mu\omega) r^2 \\ n^2 &= 1 + j p_2 \mu\omega \\ m &= j p_3 \mu\omega\alpha \end{aligned} \tag{4.14}$$

and dividing expression (4.13) by V^2 we obtain:

$$\frac{\partial^2 R(v)}{\partial V^2} + \frac{1}{V}\frac{\partial R(v)}{\partial v} - R(v)\left[1 + \frac{n^2}{V^2} + \frac{m}{V^3}\right] = 0 \qquad (4.15)$$

This expression does not lead to a Bessel function for R. Since we try to obtain a Bessel function as a solution in order to facilitate the matching of the boundary conditions at the probe wall, we attempt to solve expression (4.15) by successive approximation.

1) First term approximation (m = o)

Solution of

$$\frac{\partial^2 R(v)}{\partial v^2} + \frac{1}{V}\frac{\partial R(v)}{\partial v} - R(v)\left[1 + \frac{n^2}{V^2}\right] = 0 \qquad (4.16)$$

is the sum of two modified Bessel functions of order n.

$$R(V) = AI_n(V) + BK_n(V)$$

However, since the potential cannot be infinite for $r \to \infty$, A must be zero, and the solution is:

$$R(V) = BK_n(V) \qquad (4.17)$$

which is a modified Bessel function of second kind with complex argument $V \left(= r\sqrt{k^2 + j\sigma_0\mu\omega}\right)$

and complex order $n \left(= \sqrt{1 + j\rho_2\mu\omega}\right)$

2) Second term correction (n = 1, m ≠ o)

The following equations will be solved:

$$\frac{\partial^2 R(v)}{\partial v^2} + \frac{1}{v}\frac{\partial R(v)}{\partial v} - R(v)\left[1 + \frac{1}{v^2} + \frac{m}{v^3}\right] = 0 \qquad (4.18)$$

$$\frac{1}{Z(z)}\frac{\partial^2 Z(z)}{\partial z^2} = -k^2$$

wherein the non-dimensional quantities are given by (4.14). This can be solved approximately by a Matthieu-Bessel expansion (Ref. 80).

Assume $$R(v) = \sum_{N=-\infty}^{N=+\infty} A_N K_{1+N}(v) \qquad (4.19)$$

to be a solution.

Substitution into (4.18) gives

$$\sum_{N=-\infty}^{N=+\infty} A_N \left[K''_{1+N}(v) + \frac{1}{V}K'_{1+N}(v) - K_{1+N}\left(1 + \frac{1}{v^2} + \frac{m}{v^3}\right)\right] = 0 \qquad (4.20)$$

or

$$\sum_{N=-\infty}^{N=+\infty} A_N \left[K''_{1+N}(v) + \frac{1}{V}K'_{1+N}(v) - K_{1+N}\left(1 + \frac{(1+N)^2}{V^2} - \frac{2N+N^2}{V^2} + \frac{m}{V^3}\right)\right] = 0 \quad (4.21)$$

whereby the argument of K_{N+1} is in such form that the first term solution is a K_{N+1} Bessel function. The notation $K''_{1+N}(V)$ stands for $\dfrac{\partial^2 K_{1+N}(v)}{\partial v^2}$

Consider three terms in the infinite series (4.21) for N-1, N, N+1, and use the following relationship between the order of the K Bessel functions in order to reduce all terms to a common denominator:

$$K_{\nu-1}(z) - K_{\nu+1}(z) = -\frac{2\nu}{z} K_\nu(z)$$

The following three expressions can be picked up from this series:

$$A_{N-1}\left[K_N \frac{2(N-1)+(N-1)^2}{V^2} - \frac{m}{V^2}\left(\frac{1}{2N}\left(K_{N+1} - K_{N-1}\right)\right)\right]$$

$$+ A_N\left[K_{N+1}\frac{2N+N^2}{V^2} - \frac{m}{V^2}\left(\frac{1}{2(N+1)}\left(K_{N+2} - K_N\right)\right)\right] \qquad (4.22)$$

$$+ A_{N+1}\left[K_{N+2}\frac{2(N+1)+(N+1)^2}{V^2} - \frac{m}{V^2}\left(\frac{1}{2(N+2)}\left(K_{N+3} - K_{N+1}\right)\right)\right] + \cdots$$

For these terms to vanish, we obtain the following recurrence formula for the coefficients:

$$2N + N^2 - \frac{m}{2N}\left(\frac{A_{N-1}}{A_N}\right) + \frac{m}{2(N+2)}\frac{A_{N+1}}{A_N} = 0 \qquad (4.23)$$

which can be solved either for $\frac{A_N}{A_{N+1}}$ or $\frac{A_N}{A_{N-1}}$ and we get:

$$\frac{A_N}{A_{N+1}} = \frac{-m/(2N+4)}{2N+N^2 - \frac{m}{2N}\left(\frac{A_{N-1}}{A_N}\right)} \qquad (4.24)$$

$$\frac{A_N}{A_{N-1}} = \frac{m/2N}{2N + N^2 + \frac{m}{2(N+2)}\left(\frac{A_{N+1}}{A_N}\right)} \qquad (4.25)$$

If the profile constant m is much smaller than unity, the above expressions are decoupled. Recalling that we are looking for some perturbations around the Bessel function K of first order, we put N=0 and obtain the following recurrence formula for the coefficients:

$$\frac{A_{-1}}{A_0} = \frac{m}{2} \tag{4.26}$$

$$\frac{A_1}{A_0} = \frac{m}{6} \tag{4.27}$$

and the solution (4.19) becomes

$$R(v) = A_0 \frac{m}{2} K_0(v) + A_0 K_1(v) + \frac{m}{6} A_0 K_2(v) \tag{4.28}$$

The final solution, resulting from the contributions of the first term approximation (eq. 4.17) and second term approximation (4.28) added together can be written as:

$$R(v) = A\left[K_m(v) + \frac{m}{2} K_0(v) + \frac{m}{6} K_2(v) \right] \tag{4.29}$$

together with $\quad \dfrac{1}{Z(z)} \dfrac{\partial^2 Z(z)}{\partial z^2} = -k^2$

The complete solution for the plasma vector potential becomes:

$$A_{\varphi p} = \int_0^{\infty} f_p(k) \left[K_m(v) + \frac{m}{2} K_0(v) + \frac{m}{6} K_2(v) \right] \cos(kz)\, dk \tag{4.30}$$

From here on we again follow the procedure as in Chapter I and solve for the unknown coefficients $f_P(K)$ and $f_R(K)$ by introducing the two boundary conditions (1.20) and (1.21). The solution for $f_R(K)$ can be written:

$$f_R(k) = \frac{\mu a I}{\pi} I_1(hy) \frac{y K_0(y) - U K_1(y)}{y I_0(y) + U I_1(y)} \tag{4.31}$$

wherein

$$U = - \frac{x K_n'(x) + K_n(x) + \frac{m}{2} g_1(x)}{K_n(x) + \frac{m}{2} g_0(x)} \tag{4.32}$$

$$g_0(x) = K_0(x) + \frac{1}{3} K_2(x) \tag{4.33}$$

$$g_1(x) = K_0(x) - \frac{4}{3} x K_1(x) - \frac{1}{3} K_2(x) \tag{4.34}$$

and the final expression for the impedance change for a coil immersed in an electrical conducting medium with profile

$$\sigma = \sigma_0 + \frac{P_2}{r^2} + \frac{P_3}{r^3}$$

becomes

$$\frac{\Delta Z}{\omega \mu a} = 4 j h b^2 n^2 \int_0^\infty \frac{I_1^2(hy)}{y^2} \cdot \frac{y K_0(y) - U K_1(y)}{y I_0(y) + U I_1(y)} \left(1 - \cos(wy)\right) dy. \tag{4.35}$$

3) Approximate solution for first term correction if n^2 is close to unity

The exact solution gave rise to a Bessel function with complex argument and complex order. However, if the term $jp_2\mu\omega$ in (4.14) is smaller than unity, the following expansion for the square root is possible:

$$n = \sqrt{1+2\varepsilon} = 1 + \varepsilon - \frac{\varepsilon^2}{2} + \frac{\varepsilon^3}{3} - \cdots \qquad (4.36)$$

wherein $$\varepsilon = \frac{jp_2\mu\omega}{2} \qquad (4.37)$$

Since Bessel functions are continuous functions of their order, we can expand the first order Bessel function in a Taylor series with respect to the order or:

$$K_{1+\varepsilon}(v) = K_1(v) + \varepsilon \frac{\partial K_n(v)}{\partial n} \qquad (4.38)$$

Since $$\left[\frac{\partial K_n(v)}{\partial n}\right]_{n=1} = \frac{1}{v} K_0(v)$$

we obtain

$$K_n(v) \approx K_{1+\varepsilon}(v) \approx K_1(v) + \frac{\varepsilon}{v} K_0(v) \qquad (4.39)$$

for $-1 < 2\varepsilon \leq +1$

This condition is satisfied during most of the testing time except during the first 75 μsec.

The complete solution for the plasma vector potential, including second term correction becomes now (eq. 4.30):

$$A_{\varphi p} = \int_0^\infty f_p(k)$$

$$\cdot \left[K_1(v) + \frac{\varepsilon}{v} K_0(v) + \frac{m}{2} K_0(v) + \frac{m}{6} K_2(v) \right] \cos kz \, dk \qquad (4.40)$$

and the final expression for the impedance change now is:

$$\frac{\Delta Z}{\omega \mu a} = 4 j h b^2 n^2 \int_0^\infty \frac{I_1^2(hy)}{y^2} \cdot \frac{y K_0(y) - U' K_1(y)}{y I_0(y) + U' I_1(y)} \left(1 - \cos(wy)\right) dy . \qquad (4.41)$$

wherein

$$U' = \frac{x K_0(x) + \varepsilon K_1(x) + \frac{m}{2} g_1(x)}{K_1(x) + \frac{\varepsilon}{x} K_0(x) + \frac{m}{2} g_0(x)} \qquad (4.42)$$

wherein $g_0(x)$ and $g_1(x)$ are defined in eqs. 4.33 and 4.34 respectively.

Since the expression 4.41 is identical in form with the expressions 1.28 and 3.22, dealing respectively with the probe response in an isotropic and an anisotropic plasma for a conductivity profile with a step function at the probe wall, it was possible to incorporate the thermal effects on the probe response into a general computer program, provided the coefficients of the conductivity profile $\sigma/\sigma_0 = A + \frac{B}{r^2} + \frac{C}{r^3}$ are known. A complete listing is included at the end of this work.

The expression (4.41) was solved for the conductivity profiles shown in fig. 15. The resulting data for ΔR and ΔL are plotted on fig. 16 in percent of the data obtained at time zero. On the same figure is plotted the percentage probe response to a conductivity of 2500 mho/cm with a step profile at the fictitious probe radius corresponding to the time interval indicated in the abscissa.

4.3 Discussion of the Numerical Results

The analytical conductivity profiles (fig. 15) show a noticeable overshoot for time intervals smaller than 100 μsec at a radius roughly twice the probe radius, while the conductivity levels off to a value of 80 percent at large distance. Furthermore, the approximate solution (eq. 4.41) is not strictly valid for time intervals shorter than 100 μsec after the passage of the reflected shock since the condition for a series expansion of the square root, i.e. $|j\rho_2\mu\omega| < 1$ is not met. Hence the results for this time interval are questionable and often lead to excessive data for the probe impedance. Judging from the data listed in table II which apply to fig. 16, the accuracy of the numerical solutions should improve for larger time intervals.

This study was repeated for a few different combinations of initial pressures and shock Mach numbers resulting from a constant shock tube driver pressure of 300 psi of H_2. The resulting cooling decay curves for the probe impedance differ slightly at earlier times but practically coincide at later times. This enables us to use these two curves to apply the corrections to the shock tube results obtained at the various initial pressures and shock Mach numbers as will be shown in section 6.3.

To refine this study, several improvements could be implemented:

- At temperatures in excess of $10000^{o}K$, the radiation heat transfer cannot be neglected. If the gas in the cold boundary layer can be assumed to be optically thick, the energy input in this region due to continuum radiation from the surrounding hot gases, should increase the temperature gradients thereby reducing the cooling effect on the probe response.
- A better matching between the numerical and analytical conductivity profiles can be obtained by including higher order terms in the matching polynomial. However, the vector Helmholtz equation can no longer be solved in terms of a series of Bessel functions which complicates the analysis considerably.
- With the present profile $\sigma/\sigma_o = A + \frac{B}{r^2} + \frac{C}{r^3}$, a solution of the exact equation 4.17, which involves modified Bessel functions with complex order and complex argument, should improve the results during the first 100 μsec of the testing time. Furthermore, the recurrence formulas (4.26) and (4.27) are strictly valid only if the profile

coefficient $m(=jp_3\mu\omega d)$ is much smaller than unity. Since this coefficient depends on the integration variable, this condition is satisfied except close to the upper limit of the integration interval.

Notwithstanding these approximations to the real problem, the following main conclusions can be drawn from this study: any non-uniformity in the plasma around the probe effects the resistive probe response more than the reactive probe response. This feature can successfully be exploited to measure simultaneously the electrical conductivity of the plasma and the effective probe radius, which is a measure of the thermal boundary layer thickness.

While P. Savic (Ref. 46) uses two external coils with different coil diameters to obtain the information for the electrical conductivity and the effective external plasma diameter, the output from the two channels in this experiment enables us to obtain the same information as follows: One prepares a graph with the theoretical values of the resistance and inductance change plotted versus the effective probe radius r $(r > b)$ for several values of the electrical conductivity for a uniform plasma. In order to estimate the electrical conductivity and the effective boundary layer thickness, one enters the readings for ΔR and ΔL measured at a certain time interval. One draws two horizontal lines through these data points and observes at what unique radius these horizontal lines intersect a corresponding curve from each family corresponding to the same electrical conductivity. The radius obtained in this way is the inner radius of a uniform cylindrical plasma at the specified time interval which gives an identical probe response as the real non-uniform plasma. The resulting value of the electrical conductivity then corresponds to the ideal conductivity for a uniform plasma.

PART II

EXPERIMENTS

Chapter V

EXPERIMENTAL APPARATUS AND INSTRUMENTATION

The first part of this chapter deals with the construction and calibration of the probe and associated equipment needed to monitor the conductivity. Next follows a short description of the shock tube, the magnetic field coil and the capacitor bank. This chapter concludes by a description of the synchromisation and the display techniques.

5.1 Electrical Conductivity Probe

5.1.1 Design parameters and construction of the probe

The immersed coil geometry is mainly dictated by the proposed application and is optimised to obtain maximum sensitivity. In order to take full advantage of the very good spatial resolution of such a probe, it is imperative to choose a minimum probe radius b. Since the experiments are done with a 1 1/2" shock tube in the presence of a strong magnetic field, it is advisable to minimise shock distortion by the probe. Furthermore, as de Leeuw indicated in Ref. (81), magnetic interaction could occur if a strong cross flow is introduced in the plasma. A probe diameter of 1/8" was selected with a very sharp-nosed conical point facing the oncoming flow. The probe material was quartz to prevent ablation cooling at the tip. Since the sensitivity of the device to monitor the electrical conductivity depends strongly on the filling factor (figs. 3 and 4), the coil diameter was maximized within the available space.

The length of the coil is determined by considerations of the sensitivity of the probe to monitor the electrical conductivity ($\approx W^{1.8}$), the sensitivity of the probe to detect Hall effect, which decreases for increasing coil length, and the need for a fast probe response which is required because of the cooling problem. A typical coil length is 6 mm. A small wire diameter enhances the sensitivity since the impedance change is proportional to the square of the turn density. This however is partly offset by the decrease of the quality factor of the coil if the resistance of the coil becomes too large.

The probe sensitivity is an increasing function of the carrier frequency, however, plasma properties limit the carrier frequency. In order to measure D.C. conductivity, the frequency should be orders of magnitude smaller than the collision frequency of the plasma. Since the plasma is created in the presence of a strong magnetic field, the carrier frequency should be smaller than the electron cyclotron frequency; moreover one must avoid any frequency characteristic of the plasma under test (e.g. plasma frequency). Another serious limitation on the upper frequency level is governed by the resonance characteristic of the probe coil. In order to avoid critical phase and amplitude variations, one must work well below the resonance frequency. Another consideration is the skin effect which should be minimized, and this ties in with the choice of the wire material. Manganine wire was chosen because it has a negligible temperature coefficient in the temperature range between 15 and 35°C, which is an important factor when measuring electrolytic conductivities. Because of its high resistivity, skin effect is drastically reduced. A carrier frequency of 10.7 MHz did satisfy the conditions mentioned above and a manganine wire diameter of 0.005" has a skin effect ratio less than 1 percent at this frequency. Furthermore, electronic components such as crystals and tuners are readily available for this frequency.

A double layer coil is wound on a ceramic tube (1 mm OD). This coil former fits over the central conductor of a miniature coaxial cable (Microdot 250-3919). Some anomalous behaviour of the probe could result from the presence of a highly conducting wire through the center of the coil and for this reason, a short piece of central conductor was inserted in the ceramic former only to align the coil with the cable, but the coil ends are soldered respectively to the central conductor and the braid at the same side of the coil.

This assembly is inserted into a quartz tube of 2 mm ID and 3 mm OD. The microdot cable, 1 ft. long, connects the coil to the parallel-T bridge. In the following, this assembly is referred to as the probe. Figure 17 gives an enlarged view of the coil, the connector and the quartz tube.

Typical probe parameters for probe H are:

Manganine wire gauge 36, formel insulation

$a_1 = 0.6$ mm	$h_1 = 0.382$
$a_2 = 0.77$ mm	$h_2 = 0.49$
$\ell = 6.40$ mm	$w = 4.08$
$N = 80$ turns	$n_1 = n_2 = 6.25$ turns/mm
$b = 1.57$ mm	

For symbols, see fig. 2.

At 10.7 MHz: the following data are obtained with a Boonton R-X bridge Model 250.

$$R_p = 738 \text{ Ohm}$$

$$C_p = -60.88 \text{ pf.}$$

$$C_{stray} = 60 \text{ pf.}$$

$$Q = 6$$

$$L_S = 1.78\ \mu H$$

$$R_S = 19.9 \text{ Ohm}$$

5.1.2 Description of the two phase impedance measuring system

The results of the theoretical analysis indicate both a resistive and reactive change for the probe coil impedance when immersed in an electrically conducting medium. Since information from both channels is very useful in diagnosing the state of the plasma, a two-phase system was developed to extract the resistance and the reactance changes separately.

A block diagram of the system is shown in fig. 18.

A 10.7 MHz crystal controlled oscillator generates a stable frequency for the system by feeding two buffer stages (fig. 19) which separate the load from the oscillator. These buffer amplifiers are of the FET cascode design which has a very high input impedance, a very low reverse transfer conductance due to the heavy mismatch between the common source FET and the common gate FET, a variable gain to adjust the output level and a very low output impedance achieved by the use of a complementary emitter-follower circuit which gives symmetric waveforms to feed a 50 Ω system.

The heart of the system is a parallel-T bridge which is shown in fig. 20 and has attracted much attention in the technical literature because of its ability to produce an infinite attenuation at a specified frequency. When balanced, the network is capable of detecting very small changes in the inductance or the resistance of a coil which forms part of the parallel-T bridge. The bridge is balanced for null transmission by means of two coarse dials and two fine dials which independently control the resistive and reactive balance. From this pre-set null condition, any minute variation in the coil impedance produces an out of balance

R.F. signal which is amplitude modulated in proportion with the degree of unbalance, and with a phase shift controlled by relative magnitudes of unbalance due to resistive and reactive change of the coilimpedance. Since higher harmonics of the carrier, generated by the oscillator, pass through the parallel-T bridge almost unattenuated, the useful R.F. signal is often buried under these higher harmonics and a double tuned amplifier (fig. 21) is used to filter out the wanted signal. Demodulation of the carrier can now be accomplished since the proper reference signal is provided by the second buffer stage which feeds a phase shifter (Model PS-3-10.7 Merrimac Research and Development, Inc.). This is needed to phase align the reference signal with the R.F. signal and compensates for any steady phase shift occurring in the parallel-T bridge. In order to extract the in-phase component (resistive change) and the quadrature phase component (reactive change) from the R.F. signal, two reference signals are required which are precisely 90° out of phase. This is achieved by using a quadrature hybrid (model QH-3-10.7 Merrimac Research and Development, Inc.) following the phase shifter, which provides two signals at the standard frequency, equal in amplitude and exactly 90° out of phase which feed the two phase detectors. Following the double tuned amplifier is a power splitter (model PD-20-17 Merrimac Research and Development, Inc.) to produce two R.F. signals, equal in phase and in amplitude, which are highly isolated and then fed into the two mixers (type 10514 Hewlett-Packard Co.). The output signal obtained from the mixer with reference signal in phase with an R.F. signal originating from a purely resistive change of the coil impedance, is a D.C. signal proportional to the magnitude of the resistive unbalance. Similarly, the D.C. signal obtained from a second mixer will be proportional only to the reactive change of the coil impedance. (It is assumed that the changes are small compared with the initial impedance values.)

Since these D.C. voltage levels are very small and often contain higher harmonics, D.C. amplification is required, in both channels, especially for measuring electrical conductivity of electrolytes. Proper amplification is achieved by using an integrated circuit with feedback controlled gain (fig. 22). Unwanted harmonics are excluded by using a rejection filter following the operational amplifier.

Typical voltage levels are of the order of 10 mV/mho/cm and the rise time is of the order of 1 μsec.

5.1.3 Study of the transfer function of a parallel-T bridge

Application of the "Twin-T" networks for measuring impedance is well known (Ref. 82). It eliminates most shielding and grounding problems due to a common ground connection for input, output, the probe and the two balancing capacitors. Such a network has a very sharp rejection notch at the balance point and hence, is well suited for measuring minute changes of the probe impedance.

However, in order to detect changes in the coil resistance and coil reactance separately, it is important to obtain two independent signals. Under such condition only will a pure change in the coil resistance give rise to a signal detected at the R-mixer only, while no signal appears at the X-mixer and vice versa.

In order to minimise the cross talk between the two channels, a full analysis of the transfer functions was carried out.

By using a "star" to "delta" transformation, the two branches of the parallel-T bridge (fig. 20) can be converted to two π sections which can be combined to a single π section from which the transfer function can be derived. Using the notation from fig. 20, the following exact expression results:

$$F(s) = \frac{A + Bs + Cs^2 + Ds^3}{FA + FBs + FCs^2 + FDs^3} \qquad (5.1)$$

wherein: $s = j\omega$, ω being the carrier frequency in radians/sec.

$A = 1$

$B = L_p/R_p$

$C = L_p(C_p + 2C_o + C_o^2/C_1)$

$D = L_p(1 + C_2/C_1)\ RC_o^2$

$$FA = 1 + C_2/C_1 + C_o/C_1$$

$$FB = (L_p/R_p)FA + RC_o(1 + C_2/C_1)$$

$$FC = L_p\left[FA(C_p + C_o) + C_o(C_2/C_1 + 1)(1 + R/R_p)\right]$$

$$FD = RC_oL_p(C_2/C_1 + 1)(C_p + C_o)$$

A crude representation of the probe impedance consists of a coil resistance R_s in series with the coil inductance L_s. This impedance is paralleled by the probe capacitance C_s. In order to calculate the impedance, a series to parallel transformation is needed whereby the new probe impedance now consists of a probe resistance R_p, in parallel with a probe inductance L_p. The symbol L_p in this transfer function combines the actual parallel probe inductance L_p in parallel with the inductance of the booster coil, denoted as L_p in fig. 20.

For a particular probe impedance, the values of the dial capacitances C_p and C_2 were calculated from the above expression for $F(s) = 0$. Next, the transfer function was repeatedly solved either for variations in the series resistance or variations in the series inductance of the probe coil about its original values R_{so} and L_{so}, and the resulting complex values are plotted in a complex plane (fig. 23). This results in two families of curves which are orthogonal and correspond respectively to the solution of the transfer function obtained for varying series resistance at constant inductance, or varying inductance at constant resistance. By rotating the coordinates of the complex plane (which is actually accomplished by shifting the phase of the reference signal), such that the curve for constant R_o, going through the origin, is tangential to the imaginary axis at the origin, then the curve for L_o = cte going through the origin, will be tangential to the real axis due to the orthogonality of the two families. However, due to the curvature of the characteristics, it is impossible to avoid cross-talk between the two channels for larger variations of the coil impedance. This means that a change in the coil resistance alone will not only vary the real part of the transfer function, but to a small degree will also change the imaginary component of the transfer function. A possible way to eliminate such interference is to optimise the components of the circuit such that the characteristics become straight. A numerical study indicates that linearisation is possible to a certain degree and the most effective way is by trimming the Co capacitors. Figure 24 shows the net of characteristics for optimum value of the Co capacitors, which are linear within 1 degree around the balance condition in an area in the complex plane which covers the experimental range for shock tube results, as shown in this figure.

Using a Hewlett-Packard vector voltmeter, the adjustment of the Co capacitors was easily achieved and good decoupling was obtained with such an optimised network.

5.1.4 Calibration of probe and circuitry

Since the range of electrical conductivities most often encountered in dense laboratory plasmas (between 100 and 10000 mho/ m falls outside the readily available range of calibrating materials, particular emphasis is placed on the development of an alternative method to make this, as far as possible, an absolute sensing instrument independent of available calibration standard materials.

It should be mentioned that some materials exist with suitable conductivities, but most present some difficulties. Examples include the following:

1) Fused salts fall in the proper range only at elevated temperatures.
2) Semiconductors are anisotropic or contain grain boundaries, and hence are frequency dependent.
3) Metal-ammonia solutions at subzero temperatures have electrical conductivities varying from 10^{-1} to 10^{5} mho/ m. However special cryogenic techniques must be used to produce and conserve these solutions.

Since the presence of an electrically conducting medium manifests itself by changing the series resistance and series inductance of the probe coil, a calibration can be achieved by artifically changing the coil impedance. Since it is very difficult to change the coil series resistance and coil inductance due to the inevitable introduction of additional stray capacitance, a parallel calibration technique was used instead. A simple crude model of the probe impedance is sketched in fig. 25 whereby C_s lumps together the stray capacitance of the coil, the cable capacitance and the capacitance of the connectors. Since the coaxial cable from coil to the parallel-T bridge is approximately 40 cm long, this can be considered a short transmission line at 10.7 MHz with negligible loss resistance. This representation of the actual coil impedance can be transformed into an equivalent parallel circuit for which the following relations hold:

$$R_s = \frac{R_p}{1 + Q^2} \tag{5.2}$$

$$L_s = \frac{R_p^{\,2}(C_s - C_p)}{1 + Q^2} \tag{5.3}$$

wherein Q is the quality factor of the probe coil without stray capacitance and can be expressed as $Q = \frac{\omega L_s}{R_s}$ for the series representation or $Q = R_p(C_p - C_s)\omega$ for the equivalent parallel representation. From these expressions, it is obvious that shunting the probe with a parallel calibrating resistor will change both the equivalent series resistance and inductance of the coil; the same is true for a pure parallel calibrating capacitor. Also, varying the resistive dial of the parallel-T bridge, being an effective parallel capacitor, is equivalent to a change in both the series resistance and series inductance of the probe so that alternate means must be used to find the proper phase setting for which a pure change in coil series resistance results in a voltage change in the resistive channel only and similarly for the coil inductance. An analog lumped model of the probe coil was built with controls for varying the components C_s, L_s and R_s (fig. 26). Part of the series resistance was substituted by a thermistor with a negative temperature coefficient and it was verified with an R-X meter that cooling of the thermistor increased the series resistance of the analog while the series inductance or stray capacitance was not affected.

The procedure for finding the proper phase setting was as follows:

The parallel-T bridge was balanced with the probe to be calibrated in circuit. The probe was next replaced by the analog which was adjusted to obtain again a balance. Using liquid nitrogen, the thermistor was cooled and the phase shifter was adjusted so that only the resistive channel responded to the effective change in the series resistance of the analog. Invoking the principle of orthogonality in the transfer function for the parallel-T bridge, this phase setting automatically satisfies the condition that a change in pure series inductance of the coil would effect only the reactance channel output.

The calibration of the probe can now be carried out as follows:

a - The value of the total parallel capacitance C_s is determined by measuring the capacitance on the R-X meter at various frequencies. These data plotted versus $1/\omega^2$ are colinear and the extrapolated value for $1/\omega^2 = 0$ gives the stray capacitance C_s.

b - The frequency of the R-X meter is set at the carrier frequency (10.7 MHz) and the values of R_p and C_p are recorded for a set of high-quality resistors shunting the probe. The equivalent series resistance change can be calculated from eq. (5.2).

c - The probe now is connected to the parallel-T bridge and the output voltage on the resistive channel is now recorded for the same set of calibrating resistors, and plotted versus ΔR_s, the equivalent series resistance change calculated above.

These points are shown in fig. 27. These points lie on a straight line with a slope equal to the sensitivity of the resistive channel. This calibration curve is linear in the region of interest but does not pass through the origin, because of the presence of some additional stray capacitance in the shunting resistor which affects the equivalent series resistance. To avoid this, two calibrating resistors were made whose stray capacitance was tuned out with a coil resonating at the carrier frequency. The data of these two calibrations are also shown in fig. 27.

The same procedure is repeated for calibrating the reactive channel by using parallel capacitors, shunting the probe coil. Such a calibration curve is shown on fig. 28.

From the theory we establish a relationship between the electrical conductivity and the change in the coil resistance and coil inductance. This calibration gives a relationship between the output voltage on both channels in terms of the change in coil series resistance and inductance respectively. Cross correlation allows us to measure the conductivity using both output channels.

5.2 Shock Tube

The shock tube was built by J. Lau who used it to verify Shkarofsky's method for calculating the electrical conductivity in plasmas (Ref. 71), using an external coil. The shock tube used for this experiment consists of a driver section, about 6 feet long, and a cylindrical driven section about 25 ft. long and inside diameter of 2.5" and is made of stainless steel. The test section is a 1 ft. long perspex tube with a precisely machined inside surface of 1.5" diameter. Upstream of this test section was a stainless steel tube about 4 ft. long which inserts into the driven section and proved to be very effective in trapping any debris coming from the diaphragm, thereby avoiding damage to the conductivity probe which was inserted into the shock tube test section at the center of the shock tube end wall. Another function of this insert is to trap the turbulent boundary layer gases induced behind the shock.

The lower limit for the shock tube length was dictated by the discharge period of the capacitor bank into the coil which was about 10 msec. Hence, the time of arrival of the shock at the test section should not be less than a quarter period when the bank is triggered without delay at the rupture of the diaphragm.

In ideal shock tube performance, there is no upper limit to the shock tube length. Roshko (Ref. 84), states, however, that due to the shock attenuation caused by boundary layer drag, there is an optimum length beyond which no gain in shock tube testing time can be achieved.

Mylar sheets were used as diaphragms and very consistent runs were obtained by increasing the hydrogen pressure until spontaneous rupture of the diaphragm occurred. In this mode, with argon as the test gas, incident shock Mach numbers between 5.5 and 8 were achieved for initial channel pressures between 12 and 3 Torr of argon. Before each run the shock tube was pumped down to a pressure of 10^{-2} Torr at which a small leakage rate was observed. Next, the shock tube was flushed with argon to reduce the impurity level and pumped down again before setting the initial argon pressure.

The shock tube was equipped with a breaking wire trigger close to the diaphragm, to trigger the capacitor bank and the oscilloscopes. Two piezoelectric pressure transducers were installed at each end of the test section in order to monitor the speed of the incident shock.

Figure 29 shows a complete block diagram of the instrumentation. Figure 30 gives a view of the equipment used at the test section.

5.3 The Magnetic Field Coil and Capacitor Bank

In order to measure Hall effect in shock tube plasmas, it is essential to create a magnetic field which is steady during the available testing time and of a magnitude such that the Hall parameter is as large as possible.

The capacitor bank available for this experiment consists of 132 high-voltage energy storage capacitors in parallel, with a nominal rating of 3.75 μf and 10 KV each. Hence the total capacitance was 495 μf with total stored energy of 25 KJ. However, due to the age of these units, the voltage was never allowed to exceed 6 KV so that the available energy was of the order of 9 KJ.

The coil design was based on the following considerations:

a) A quasi-steady axial magnetic field of 6 Tesla should exist with less than 2 percent variation during a testing time of 400 μsec.

b) Since the electrical conductivity probe was about 7.5 cm from the end wall, the total length of the coil should be at least 15 cm with an inside diameter equal to the test section outside diameter of 5 cm.

c) The coil thickness should be such that the axial component of the magnetic field variation should be less than 1 percent over the control volume, and the radial magnetic field at the coil ends should be small enough to avoid magnetic interaction with the test plasma at the coil entrance (see Ref. 81). This last is not a very stringent requirement. The magnetic interaction parameter, being proportional to incident gas velocity and electrical conductivities, is very small for the incident shock because the conductivity behind it is very low, while behind the reflected shock, the gas is almost stagnant.

The actual calculation of the coil configuration based on the data of Ref. 85 is given in detail in Appendix B.

The coil material is single coated FORMSET magnetic wire, gauge 13, with square cross section to optimise the filling factor. The coil consists of 6 layers of 75 turns each with insulating paper between the layers. Physical coil dimensions are:

inside radius : 2.5 cm

outside radius: 3.75 cm

length: 15 cm

The axial and radial field distribution along the coil is shown in fig. 31, and satisfies the above mentioned requirements, assuming a probe control volume to be a cylinder with 1 cm diameter and 3 cm length. Also shown in this figure is the axial and radial field component at the shock tube wall ($r/a_1 \approx 0.75$) for estimating the magnetic interaction between plasma and magnetic field.

A special current measuring resistor was installed in series with the coil to monitor the current (proportional to the magnetic field) during each discharge. This resistor was made from a short length of Inconel tubing with the voltage pick-off connected on the inside to eliminate the effect of self inductance. The resistance between the two points measured 1.536 ± 0.01 mΩ.

Inconel was chosen for its high specific resistance (98.1 $\mu\Omega$-cm) and very low temperature coefficient (7×10^{-5} $\mu\Omega$-cm/$^{\circ}$K). The total LCR circuit had the following parameters:

$$R = 0.617 \ \Omega$$

$$L = 4.613 \text{ mH}$$

$$C = 0.496 \text{ mF}$$

This results in a discharge period of approximately 10 msec. The calibration of the discharge system was achieved using the immersed conductivity probe as a magnetic pick-up coil and integrating the output signal. Figure 32 shows the relationship between the bank voltage, the peak magnetic field and the peak current.

Figure 33 shows a lay-out of the power supply for the capacitor bank, which was designed around an oil filled power pack (HV300-502) with an automatic reset controlled by a flash detector and a manual reset in case of emergency. With the three way switch in OFF or FILAMENTS, bleed resistors are connected across the capacitor bank for safety.

Figure 34 shows the circuit diagram of the LRC circuit including the monitoring devices for current and voltage, the bleed resistors and the three-electrode spark gap switch.

To avoid premature breakdown of the spark gap switch either due to uncontrollable atmospheric conditions or varying voltages across the electrodes, argon was supplied to the enclosed switch and the pressure was increased in proportion with the bank voltage.

A premature discharge, while the bank is still charging, could produce surge currents through the high voltage rectifier (HVC-10) far in excess of its rated surge current. A flash detector was therefore installed using a light activated SCR mounted in front of a window of the spark-gap switch which activates the automatic reset during each discharge, thereby cutting off the power to the power supply and connecting the bleed resistors across the capacitor bank.

5.4 Synchronisation and Display

The instrumentation falls mainly into two categories: piezoelectric pressure transducers to determine the shock Mach number and the circuitry to synchronise and trigger the capacitor bank spark gap switch.

5.4.1 Shock speed measuring technique

Piezoelectric pressure gauges (Kistler model 603) were installed at both ends of the test section. The charge output, converted to volts in a pressure transducer, was fed into an oscilloscope (Tektronic model 551) for recording the pressure history. It also feeds a pulse shaping network. The circuit diagram of such a network is shown in fig. 35 and served mainly the purpose to obtain a noise-free, fast-rise trigger pulse of fixed amplitude with adjustable trigger level. It also has a manual pushbutton to test the proper triggering of the instrumentation. Such pulse shaping network consists of a non-inverting feedback amplifier followed by a comparator with fast rise time and an emitter follower as output stage.

The triggering level was adjustable between 20 mv and 2 volt. The rise time is of the order of 200 nsec, independent of the shape of the input signal. The output amplitude is typically -6 volt for positive input signal. Two such networks feed respectively the start and stop inputs of a submicrosecond counter (General Radio type 1191) from which the shock Mach number could be determined.

5.4.2 Synchronisation network

Because of the rather long quarter period of the current discharge (2.5 msec), triggering of the capacitor bank must be accomplished close to the diaphragm. A fine wire was connected across the shock tube 2" downstream of the diaphragm. Rupture of the wire produced a voltage pulse which was fed into the pulse transmitter for impedance conversion mainly to be able to feed the output signal through a long coaxial cable with negligible reduction in rise time. A pulse shaping network of identical design as that shown in fig. 35 detects the rupture of the diaphragm and triggers the upper beam of an oscilloscope (Tektronix model 555). The output is also fed into a pulse delay circuit with adjustable delay time to synchronise the peak current through the coil with the arrival of the incident shock at the test section. This delayed pulse was amplified in a trigger amplifier, to about 10 KV, and applied to the trigger electrode of the three-electrode spark gap switch to break down the gap between the two main electrodes.

5.4.3 Description of the displayed features on the oscilloscope records

Since it was physically impossible to remove the instrumentation far enough away from the test section, the presence of a very strong AC magnetic field did require special attention to reject any pick-up voltage.

To reduce the pick-up noise from stray flux, a magnetic shield was built around the coil to confine the magnetic return flux. The shield was made of 1010 cold rolled steel and consists of 3 concentric cylindrical boxes with wall thickness of 1/8". A longitudinal cut in the shield prevented azimuthal eddy currents.

Although the immersed conductivity probe also acts as a magnetic pick-up, the induced voltage does not propagate through the system because of the selectivity of the amplifiers, which have a rather narrow pass band centered at the carrier frequency. However, multiple grounds between the system and scopes are susceptible to magnetic pick-up since the induced currents in the ground loops produce noticeable modulation of the carrier. This pick-up was avoided by cutting the braid off one end of all coaxial cables feeding the scopes, except one, and removing the groundlines from the power supply of the scopes. This removed the magnetic pick-up but the resulting penalty is an increase in the noise level.

The scope records shown later were recorded in the following sequence: The upper channel of a Tektronix oscilloscope was triggered by the rupture of the diaphragm wire and displays the modulated carrier from the conductivity probe response, superimposed on the voltage drop obtained across the small inconel resistor in series with the field-coil. In order to display both signals with equal sensitivity, attenuation of this current signal is required. This superposition allows a direct check on the synchronisation between the peak magnetic field and the arrival of the reflected shock at the immersed conductivity probe coil. The second channel of the oscilloscope was triggered internally after a preset delay time and displays the modulation voltages from the resistance and reactance channels of the probe system, with faster sweep rate.

The second oscilloscope was triggered externally from the gating signal on the second channel of the first oscilloscope, and displays the pressure history at the two stations across the test section. The pressure records are needed to detect any anomalous runs (e.g. due to faulty diaphragm rupture) and to calculate the shock Mach number in the Hall effect experiments, since, in this case, the counter did not trigger properly due to excessive magnetic pick-up.

Chapter VI

EXPERIMENTAL RESULTS

All experimental results presented here were obtained with the same probe, labeled H, whose dimensions and electrical parameters were listed in Chapter V. The probe response on both channels was first compared with the theory for an isotropic, uniform, conducting medium. The Hall effect runs are discussed next and finally, the effect of probe cooling as observed in shock tube plasmas is compared with the calculated drop in probe response for a plasma conductivity profile as discussed in Chapter IV.

6.1 Comparison between Numerical and Experimental Data for the Probe Response in an Isotropic, Uniform, Conducting Medium

Figure 36 presents the probe response as calculated numerically for the resistance and inductance change versus electrical conductivity for probe H. The calibration constants for the two channels are

$$\alpha = 77 \text{ mV/Ohm (Fig. 27)} \quad \text{and} \quad \beta = 5.4 \text{ mV/nH (Fig. 28)}$$

On the same graph are shown the experimental points for three conductivity ranges: electrolytes, shock tube plasmas and mercury.

6.1.1 Experiments with electrolytic solutions

Electrolytic solutions of HNO_3 provide a range of electrical conductivities depending on concentration. A maximum conductivity of 85 mho/m is obtained for a concentration of 5.5 mole/lit at 22°C.

The data measured on the resistive channel are shown in fig. 37 and compare favorably with the theoretical values. These data were obtained from a balanced reference level in distilled water. A constant off-set voltage of about 4 mV exists between the reference in distilled water and the reference in air. This is mainly due to the high dielectric constant of water. While conductivity is practically negligible, the displacement currents cannot be neglected and cause a drop in the Q factor of the coil.

The reactance channel can hardly be used mainly because of the very small inductance change resulting from a low conductivity (see fig. 36) and also because of the effective parallel capacitance due to capacitive coupling between coil and the conducting medium.

Most experimental data are obtained without an electrostatic shield between the probe coil and the electrically conducting medium. Moulin and Massé (Ref. 86) analyse an equivalent circuit including the effect of coupling capacitance. A bypass for the R.F. current in the coil exists through the cylindrical coupling capacitance between the coil and the plasma, in series with a leakage resistance in the conducting medium. The phase of this bypass current referred to the driving current can be obtained from:

$$tg\theta = \frac{2}{R_{\ell} C_c \omega} \qquad (6.1)$$

wherein R_{ℓ} is the resistance of a plasma cylinder with outer radius = 2b and length equal to the coil length.

C_c = cylindrical coupling capacitance.

For a plasma with electrical conductivity of 2500 mho/m, the following estimates of R_{ℓ} and C_c were arrived at:

$$R_{\ell} = 7.5\ 10^{-2}\ \text{Ohm}$$

$$C_c = 1\ \text{pf.}$$

For these values, the expression 6.1 shows that the bypass current is almost 90° out of phase with the driving current and hence this coupling effect appears only on the reactive channel and should not influence the readings on the resistive channel.

These effects could be removed by coating the probe, such as with a platinum conducting film. Since the probe was used also for detecting Hall effects in plasma, such a coating could short-circuit the axial Hall voltage component and could result in an apparent excessive Hall effect.

6.1.2 Shock tube experiments

Figure 38 shows the records obtained for a typical run with initial argon pressure of 5 Torr and driver pressure of 300 psi of hydrogen. The first record shows the modulated carrier with a sweep of 1 msec/cm at 10 mV/cm sensitivity. The output from the resistive and reactive channels respectively are recorded at a sweep of 200 μsec/cm and sensitivity of 100 mV/cm and correspond to the time interval of the upper beam which shows up with higher intensity.

The second record shows the pressures at two locations and the reactive output of the system at a sweep of 100 μsec/cm. The upper trace displays the pressure at the end plate of the shock tube. The middle trace shows the pressure at a location 286 mm upstream of the end plate. The lower trace shows the detailed features of the reactive response with the same sensitivity of 100 mV/cm.

Since the probe is uncoated, the effect of capacitive coupling shows up mainly in the reactive response in the time interval between passage of incident shock and reflected shock. The resistive signal shows also a small jump which is due to the fact that a parallel capacitance shows up in both channels when the phase is adjusted with the probe analog circuit. This capacitive jump in the resistance is absent if the phase was aligned with the parallel-T bridge but this setting does not decouple the two channels when the series coil elements are changed. At the time the reflected shock sweeps over the probe, the electrical conductivity increases at a rate limited by the phenomenon of ionisation relaxation. Due to the rapid growth of a thermal boundary layer around the probe, the conductivity decreases until the shock is reflected off the advancing contact surface. In this process the plasma is heated again resulting in an increase in conductivity. This process of multiple reflection continues until the contact surface reaches the probe coil and reduces the plasma conductivity to negligible values. The sudden increase in conductivity behind the reflected shock produces a positive going signal in the resistance channel, and a negative going signal in the reactance channel due to the sudden decrease in the coil series inductance as predicted by theory.

The electrical conductivity behind the incident shock, for the record shown at initial pressure of 5 Torr and shock Mach number of 7.7, is about 80 mho/m. This corresponds to a resistance change of 0.17 Ohm which would show up as a positive jump of 13 mV. However, since equilibrium ionisation is not attained within the time interval between incident and reflected shock for such low temperatures (5000^{o}K), no conductivity can be detected on the record.

The lower limit for the experiments is determined by the ionisation relaxation time which should be small compared to the time at which appreciable cooling shows up.

With mylar diaphragm the driver pressure is limited to 300 psi. This limits the maximum attainable incident shock Mach number to about 8.

Figure 39 shows the experimental data for both channels and is compared with the ideal conductivities for argon. The electrical conductivities for argon behind a single reflected shock are not very sensitive to variations in the initial argon pressure. Since these data are obtained with constant driver pressure and with initial pressures ranging from 2 Torr at high shock Mach numbers to 13 Torr at low shock Mach numbers, the theoretical conductivity curve is adjusted over the full range to coincide with the ideal values at every shock Mach number.

The data shown on fig. 39 are obtained from measuring the peaks in the recorded changes for the resistance and reactance respectively. The presence of a growing thermal boundary layer and a finite ionisation relaxation time vitiates monitoring the actual conductivity for a uniform plasma behind the reflected shock.

However, even without any corrections for cooling, the average error is of the order of 15 percent for both channels which can be considered acceptable in view of the experimental errors and the absence of a complete theory for estimating the electrical conductivity.

The persistent discrepancy between the outputs from the two channels can either arise from a calibration error, or from the different sensitivites to thermal effects for the two channels. As will be shown in section 6.3, attempts are made to include correction factors for this thermal effect of the probe on the plasma, and the corrected readings will result in an apparent electrical conductivity which is larger than the ideal calculated value.

6.1.3 Experiments with mercury

To verify the agreement between theory and experiments at very high conductivities, some data are presented whereby the probe with variable outside radius is immersed in mercury.

Figure 40 shows the measured and calculated values of the probe response versus a variable probe radius. In this regime of high s numbers, the phase of the eddy currents is close to 90° and a slight misalignment in the phase setting does not influence the amplitude from the reactance channel whose response is completely predicted by theory, but effects strongly the amplitude from the resistance channel, which shows a growing discrepancy for increasing radius. This can be verified by changing the phase setting by approximately 1° such that the resistive channel data, also plotted in fig. 40 now agree very well with the calculated response over the complete range, except for very small values of the probe radius. The reactive channel response is not changed by this process. Two possible explanations can be given for the persistent discrepancy at very small radius:

1. Since the inductance change for these high conductivities is of the order of 0.1 μH, we are exceeding the linear range of the parallel-T bridge characteristics (fig. 24), thereby losing the complete decoupling effect of the two channels. This shows up preferably in the channel with the smallest response, i.e. the resistive channel.
2. The skin depth for mercury at the carrier frequency is about 0.15 mm. The probe response becomes very sensitive to minute errors in the exact probe dimensions for determining the filling factor h. A change in the effective coil radius could be due to proximity effect. This effect manifests itself by attracting opposing currents (Ref. 86) resulting in an effective increase in the probe filling factor resulting in a larger probe response. Dwight (Ref. 87) calculates the proximity effect in a return circuit of two adjacent strap conductors. Based on such a model, the effective increase in the resistance ratio $\frac{R_{AC}}{R_{DC}}$ due to the driver currents in the coil winding and the eddy currents in mercury in the proximity of the driver current, amounts to 16 percent which could partly explain the discrepancy.

We conclude the experiments on isotropic uniform conducting media by observing that the theory developed in Chapter I can effectively be used to predict the immersed probe response (fig. 36). The choice of the channel depends on the range of s number involved. For $s \leq 10$ the resistive channel, showing the largest response should be used. For higher values of the s parameter, both channels can effectively be used as is demonstrated for shock tube plasmas. Finally, in the range of very high s parameters ($s > 10^3$), the sensitivity of the reactive channel decreases rapidly so that only the resistive channel can be used.

6.2 Hall Effect Measurements in a Uniform Plasma

Figures 41 and 42 show the resistive and reactive probe response respectively for probe H. The probe response is plotted versus incident shock Mach number for an initial argon pressure of 3 Torr and various magnetic field strengths up to 6 Tesla. The drastic decrease in Hall effect for increasing shock Mach numbers, due to the increase in the effective collision frequency, places a ceiling on the Mach number range of interest. This combined with a lower limit due to the effect of nonequilibrium ionisation gives a rather narrow working range.

Comparison between the probe sensitivity to Hall effect of the two channels shows clearly the advantage of the reactive channel for detecting any anisotropy in the plasma.

Figure 43 shows the variation of the Hall parameter as a function of the shock Mach number for various initial argon pressures for a fixed magnetic field of 5 Tesla. On this graph is also shown the operating area for the shock tube, operating with a fixed driver pressure of 300 psi of hydrogen and a double mylar diaphragm of 0.2 mm thickness. One can observe that the Hall parameter is only moderately affected and is of the order of 2. The beneficial effect of the low initial pressure on the magnitude of the Hall parameter is offset by the resulting higher shock Mach numbers and vice versa for high initial pressures. Any attempt to decrease the shock Mach number results in an increase of the ionisation relaxation time.

The discrepancies in the experimental data for an isotropic plasma could obscure the effect under study. Since we are interested only in the relative drop in response on both channels due to Hall effect, it is possible to adjust the data obtained for an isotropic plasma to agree with the ideal values. This eliminates possible errors due to calibration of the equipment. The measured experimental results for an isotropic plasma agree with the theoretical calculated data if the baseline on the records is taken as a reference and the effect of capacitive coupling is ignored.

A typical shock tube record for an anisotropic plasma is shown on fig. 44 for the following conditions:

$P_1 = 3$ Torr, $M_s = 8.05$, $B_o = 5$ Tesla and the resulting data are included in figs. 41 and 42. The display conditions in the records are identical with records of fig. 38. The first trace has the modulated carrier added to the discharge current signal. This verifies the synchronisation between the arrival of the reflected shock with the peak intensity of the magnetic field.

It is of interest to observe that the conductivity of the plasma increases towards the end of the testing time which is most probably due to the multiple reflections. In most records without magnetic field, the amplitude of the probe response at the end of the testing time is very close to the response obtained at the beginning of the testing time. With a magnetic field, this amplitude remains practically unchanged. This could be explained by the increase in the collision frequency due to multiple reflections whereby the Hall parameter becomes sufficiently small and the plasma becomes isotropic. This feature could be exploited in certain conditions to estimate the Hall effect in a single run by taking the ratios of the signal amplitudes at the beginning and at the end of the testing time respectively, thereby avoiding possible calibration errors of the channels.

The experimental data for an initial pressure of 3 Torr are plotted in figs. 42 and 43. While the data for the resistive change are ambiguous, due to the relative insensitivity to Hall effect, the data obtained from the inductance change agree well with the predicted data. Indeed, for a Hall parameter of 2.5, the effect shows up as a drop of 30 percent for the reactive channel output and far exceeds the scatter in the experimental data. This confirms the usefulness of such a probe to detect Hall effects.

Further experiments were analysed for two initial pressures of 3 and 5 Torr respectively and the measured results are compared with the ideal values ΔR_i and ΔL_i in table III.

To give an indication of the relative magnitude of the Hall effect, the theoretical probe response ΔR_o and ΔL_o for an isotropic plasma is also listed in table III. The overall agreement between predicted and observed values of the probe impedance change is satisfactory.

It is important to realise that the Hall effect shows up only as a secondary order effect, a fact which compounds the experimental errors of both the first order effect (scalar conductivity) and the second order effect.

It is feasible to design a probe which would detect tne degree of anisotropy of a plasma as a first order effect. Such a probe would consist of two coils on the same axis but driven with opposing currents. A small toroidal coil at the center would only detect the Hall currents in the plasma.

6.3 Analysis of the Thermal Effects Observed in Shock Tube Experiments for an Isotropic Plasma

By combining the results of the analysis for thermal boundary layer effects (Chapter IV) and the measured shock tube data plotted in fig. 39, it is possible to apply a correction to these data. By observing the time at which the maximum impedance change was recorded, one can obtain the correction factor from fig. 16 for both channels. Since the attenuation due to cooling is practically identical for all shock tube experiments carried out with the same driving conditions, the same correction applies to all shock tube runs regardless of the initial pressure on the shock Mach number. The results of such correction are summarised in table IV.

One concludes immediately that the corrected readings from the two channels lead to almost identical values of the electrical conductivity. The discrepancy observed in fig. 39 disappears because of the difference in sensitivity to thermal effects for the two channels. However, the electrical conductivity as obtained from these corrected measurements is well in excess of the calculated value.

Lacking a rigorous mathematical treatment of the cooling effect, it is difficult to draw conclusions about the exact electrical conductivity or the calibration technique for the conductivity monitoring system.

In order to check the rate of decay of the probe response due to cooling, and to compare with the estimated attenuation, some shock tube records were analysed at various time intervals after the passage of the reflected shock. To represent the data on a single graph, the measurements for ΔR and ΔL were normalised and fixed to the estimated probe response at 100 μsec being 72 percent and 90 percent for the resistance change and the reactance change respectively (fig. 16). The normalised data are presented on fig. 16 for 50, 150, 200 and 300 μsec. Concerning the resistive output data, the measurements at 50 μsec fall below the estimated values mainly due to the absence of full ionisation at this time interval. While the data obtained at 150 μsec and 200 μsec agree well with the theory, the measurements at 300 μsec fall well above the expected values. This is mainly due to the onset of multiple reflections whereby the conductivity is increased.

The measured decay of the inductive response does not agree so well with the expected drop in the probe response, and would suggest that the attenuation is stronger than expected on the basis of our analysis.

To complete this study, some shock tube records were obtained at higher initial pressures and moderate shock Mach numbers. These are obtained in a shock tube equipped with a copper diaphragm and a driver pressure of 400 psi of hydrogen. Figure 45 shows a record obtained at an initial argon pressure of 15 Torr and shock Mach number of 7. A different probe was used for this experiment. The sensitivity of the two channels for probe D are: 117 mv/Ohm for the resistive channel and 7.8 mv/nH for the reactive channel. This probe was covered with a platinum coating.

On the same figure are reproduced the records for ΔR and ΔL respectively on an expanded scale and the calculated probe response as a function of time for the two channels calculated for this condition.

One can observe that the cooling rate on both channels under such conditions is much smaller than for the records analysed above. Also clearly visible is the difference in the attenuation rate for the two channels confirming the conclusion reached in Chapter IV.

While the slope of the decay in both records agrees well with the calculated attenuation rate, there is a large discrepancy in the inductive channel between the observed and calculated values. However, a logical extrapolation of the record for ΔL would agree well with the predicted value at time zero (i.e. for a uniform plasma). While the theory fails to explain the behaviour for this channel, satisfactory agreement exists between the measured and observed time history for the resistance change. Also the corrected reading for this channel (at time zero) is very close to the expected reading of 2.4 Ω at a plasma conductivity of 1800 mho/m as calculated from the initial conditions.

One concludes that the theory dealing with the thermal effects on the probe response explains partly the actual phenomena and may need some modification to fully describe the cooling process. Also the assumption of ideal shock tube conditions behind the reflected shock may not be quite realistic and needs some further examination.

Discounting any corrections for cooling, the measured electrical conductivities of the plasma are in satisfactory agreement with the predicted values for most practical applications.

CONCLUSION

An immersed, inductive plasma conductivity probe has been constructed and used in the reflected shock zone of an argon filled shock tube with and without applied axial magnetic field.

The resistive and reactive response of the probe to the presence of a uniform, non-uniform, isotropic and anisotropic plasmas has been calculated by solving numerically the Maxwell equations exactly and by providing useful approximate design formulas for certain circumscribed regimes. Utilising a two-channel phase-discriminating circuit, it was possible to measure the in-phase and quadrature component of the output signal separately.

Conductivity and Hall coefficient of the argon plasma were calculated through an adaptation of Shkarosfsky's plasma kinetic theory and used as a basis for comparison with measurements. The latter confirmed the theoretical predictions for conductivity in a satisfactory manner through six orders of magnitude from electrolytes through plasmas right up to metallic conductivity values.

It is further shown that Hall coefficients can be satisfactorily measured with the same device and that the non-uniformity in the gaseous plasma caused by the growth of the thermal boundary layer near the probe can be adequately accounted for by an appropriate modification of the probe theory.

REFERENCES

(1) Z. Croitoru and A. de Montardy,
"Electrode phenomena, tensor conductivity and electrode heating in seeded Argon."
Proc. 4th Symposium on Engineering Aspects of MHD, Berkeley, 1963.

(2) J.C. Ralph,
"Electrical-conductivity measurements on Caesium vapour and caesium-plus-inert-gas mixtures."
Magnetoplasmadynamic Power Generation Symposium, I.E.E. Conf. Report Ser. No 4, 1962.

(3) K. Kato, S. Kiyama and H. Shimahara,
"Electrical conductivity of a turbulent plasma."
J. Phys. Soc. Japan, vol. 20, 1965.

(4) P. Valentin, J.C. Leboucher and M. Pinegre,
"Densites électroniques devant un choc intense dans l'argon."
6th International Shock Tube Symposium, 1967.

(5) M. A. Gorelova, V.A. Gorelov and L.A. Kil'dyushova,
"Measurement of air conductivity behind incident and reflected shock waves by an electrode method."
High Temperature Physics vol. 7, No 1, 1969.

(6) R. Hochschild,
"Non-destructive testing by impedance analysis."
US-AEC NYO-3579, June 1953.

(7) R.C. McMaster,
"Eddy current test principles."
Non destructive testing handbook, vol. II, section 36, Ronald Press Co., New York, 1959.

(8) I.G. Scott,
"Specimen size and shape effects in eddy current testing."
Australian Defence Scientific Service, Metallurgy Report 71, 1968.

(9) C.P. Bean, R.W. de Blois and L.B. Nesbitt,
"Eddy-current method for measuring the resistivity of metals."
Journal of Applied Physics, vol. 30, No 12, 1959.

(10) E.W. Johnson and H.H. Johnson,
"Technique for measuring position dependent electrical resistivity."
Review of Scientific Instruments, vol. 35, No 11, 1964.

(11) J.E. Zimmerman,
"Measurements of electrical resistivity of bulk metals."
Review of Scientific Instruments, vol. 32, No 4, 1961.

(12) R.G. Chambers and J.G. Park,
"Measurement of electrical resistivity by a mutual inductance method."
British Journal of Applied Physics, vol. 12, 1961.

(13) V.V. Klyuev,
"Design of an eddy-current transducer for testing moving objects."
Translated from Russian Journal: Measurement Techniques, No 4, 1969.

(14) J.E. Neighbor,
"Eddy-current method for measuring anisotropic resistivity."
Journal of Applied Physics, vol. 40, No 8, 1969.

(15) V.H. Blackman,
"Magnetohydrodynamic flow experiments of a steady state nature."
American Rocket Society, Report 1007-59, November 1959.

(16) K. Körper,
"Die Impedanz einer Spule mit einem Plasma als Dielectricum."
Zeitschrift für Naturforschung, vol. 15, 1960.

(17) D.H. Cheng,
"The reflected impedance of a circular coil in the proximity of a semi-infinite medium."
IEEE Transactions on Instrumentation and Measurement, vol. IM-14, No 3, 1965.

(18) C.V. Dodd and W.E. Deeds,
"Analytical solutions to eddy-current probe-coil problems."
Journal of Applied Physics, vol. 39, No 6, 1968.

(19) W.R. Grabowsky and H.E. Wohlwill,
"A measurement of the electrical conductivity of ionized gases."
Space Technology Lab. Inc., Report STL/TR-60-0000-19414, 1960.

(20) P. Savic and G.T. Boult,
"A frequency modulation circuit for the measurement of gas conductivity and boundary layer thickness in a shock tube."
Journal of Scientific Instruments, vol. 39, June 1962.

(21) J. Moulin and J. Massé,
"Sur la mesure par sonde haute fréquence de la conductivité d'un plasma faiblement ionisé."
Proceedings of International Symposium on MHD, Paris, vol. 11, 1964.

(22) L.P. Poberezhskii,
"Measurement of the electrical conductivity of gas jets."
Soviet Physics, Technical Physics, vol. 8, No 12, June 1964.

(23) G.F. Anderson,
"An experimental method for measuring the electrical conductivity of high temperature gases."
Brown University, Providence R.I., Technical Report WT-35, June 1962.

(24) R.A. Olson and E.C. Lary,
"Conductivity probe measurements in flames."
AIAA Journal, vol. 1, November 1963.

(25) S.A. Gol'denberg, V.N. Ievlev and Z.S. Leont'eva,
"Measurement of the electrical conductivity of high-temperature gas jet."
High Temperature, vol. 2, No 5, 1964.

(26) C.E. Wharton,
"Plasma diagnostics."
AIAA Paper 63-367, Evanston, Illinois, August 1963.

(27) J.A. Sprouse,
"Measurement of electrical conductivity in a low-density supersonic plasma."
Rocket Test Facility AEDC, Report No AEDC-TR-65-146, 1965.

(28) L.P. Poberezhskii,
"Method of measuring electrical conductivity of plasma with a high time resolution."
High Temperature, vol. 6, No 6, 1968.

(29) A.E. Fuhs,
"An instrument to measure the electrical conductivity of arc plasma jet."
American Rocket Society, Report No 2635-62, 1962.

(30) S. Mikoshiba and P. Smy,
"Two coil RF determination of plasma conductivity."
Review of Scientific Instruments, vol. 40, No 9, 1969.

(31) D.O. Hollister,
"A technique for the experimental determination of the electrical conductivity of plasmas."
AIAA Journal, vol. 2, No 9, 1964.

(32) S.R. Gupta and G.J. Hills,
"A precision electrodeless conductance cell for use at audio frequencies."
Journal of Scientific Instruments, vol. 33, August 1956.

(33) R.A. Williams, E.M. Gold and S. Naiditch,
"Two transformer method for electrodeless conductivity measurements."
Review of Scientific Instruments, vol. 36, No 8, August 1965.

(34) F.N. Holmquist,
"A conductivity probe for tenuous plasmas."
AIAA Paper, No 68-170, 1968.

(35) S. Lin, E.L. Resler and A. Kantrowitz,
"Electrical conductivity of highly ionized Argon produced by shock waves."
Journal of Applied Physics, vol. 26, No 1, 1955.

(36) J.H. Williamson,
"A high resolution probe for measuring the electrical conductivity of a shock heated plasma."
British Journal of Applied Physics, vol. 18, 1967.

(37) E.W. Vendell, R. Posch and G.R. Cook,
"A coaxial, three-coil probe for measuring local values of electrical conductivity and velocity in plasma streams."
AIAA Paper, 69-327, 1969.

(38) A.H. Luther,
"A non-uniform-plasma, electrical-conductivity probe."
Report NOLTR 63-165, U.S. Naval Ordnance Laboratory,
White Oak, Silver Spring, Maryland, 1963.

(39) H.E. Koritz and J.C. Keck,
"A technique for measuring the electrical conductivity of wakes of projectiles at hypersonic speeds."
Review of Scientific Instruments, vol. 35, No 2, 1964.

(40) S.M. Pavlov and S.A. Shevchenko,
"Radial distribution of electrical conductivity in an ionised gas jet."
Soviet Physics, Technical Physics, vol. 10, No 7, 1966.

(41) L.P. Poberezhskii,
"Determination of electrical conductivity profile from the changes in circuit parameters."
High Temperature, vol. 7, No 1, 1969.

(42) M. Ciampi and N. Talini,
"Determination of average plasma conductivity by R.F. probes."
Journal of Applied Physics, vol. 38, No 9, 1967.

(43) S. Selâmoǧlu and P.F. Maeder,
"A.C. Solenoid of finite length in a conducting medium with Hall conductivity."
Brown University, Providence, R.I., Technical Report WT-40, 1964.

(44) P. Savic, F.T. Stock and T.J. Goldman,
"Performance of an electrodeless conductivity probe in anisotropic plasma."
Canadian Journal of Physics, vol. 46, No 23, 1968.

(45) K. Cruse,
"Neue Methoden zur Bestimmung von Leitfähigkeiten."
Zeitschrift für Chemie, vol. 5, No 1, 1965.

(46) P. Savic and E.J. Stubbe,
"Inductivity plasma conductivity probes."
National Research Council, Report 9248, 1966.

(47) A.E. Fuhs,
"Instrumentation for high speed plasma flow."
Gordon and Breach, Science Publishers, New York, 1965.

(48) E.C. Lary and R.A. Olson,
"A plasma conductivity probe."
Third Symposium on the Engineering Aspects of MHD.
University of Rochester, New York, March 1963.

(49) H.L. Libby,
"Broadband electromagnetic testing methods."
Hanford Atomic Products Operation, HW-59614 (1959).

(50) W. Smythe,
"Static and dynamic electricity."
New York, McGraw-Hill, 1950.

(51) S.I. Pai,
"Magnetogasdynamics and plasma Dynamics."
Prentice-Hall, Inc., New Jersey, 1962.

(52) G.N. Watson,
"A treatise on the theory of Bessel functions."
Cambridge University Press; Cambridge, England, 1958.

(53) "National Bureau of Standards, Tables of Associated
Legendre Functions. Columbia Univ. Press, New York, N.Y. 1945.

(54) I. Gradshtein and I. Ryzhik,
"Tables of integrals series and products."
New York: Academic Press, 1965, p. 30.

(55) R.A. Robinson and R.H. Stokes,
"Electrolyte solutions."
London : Butterworths Scientific publications, 1959.

(56) I.I. Glass and J. Gordon Hall,
"Handbook of supersonic aerodynamics. Section 18 :
Shock Tubes."
Navord Report 1488, vol. 6, 1959.

(57) H.N. Olson,
"The measurement of Argon transition probabilities and
computation of thermodynamic properties of Argon plasma."
AIAA Paper, No 63-369, August 1963.

(58) K.S. Drellishak, C.F. Knopp and Ali Bulent Cambel,
"Partition functions and thermodynamic properties of Argon plasma."
Report No AEDC-TDR-63-146, Arnold Engineering Development Center, August 1963.

(59) S. Chapman and J. Cowling,
"The mathematical theory of non-uniform gases."
Cambridge University Press, 1952.

(60) W.P. Allis,
"Handbuch der Physik."
Springes Verlag, Berlin, 1956, vol. XXI, p. 413.

(61) L. Spitzer and R. Härm,
"Transport phenomena in a completely ionized gas."
Physical Review, vol. 89, No 5, 1953.

(62) R. Landshoff,
"Transport phenomena in a completely Ionized gas in the presence of a magnetic field."
Physical Review, vol. 76, No 7, 1949.

(63) I.P. Shkarofsky,
"Conductivity values for any degree of ionization based on a Maxwellian distribution."
American Journal of Physics, vol. 39, 1961.

(64) L.S. Frost,
"Conductivity of seeded atmospheric pressure plasmas."
Journal of Applied Physics, vol. 32, No 10, 1961.

(65) I.P. Shkarofsky,
"Values of the transport coefficients in a plasma for any degree of ionization based on a Maxwellian distribution."
Canadian Journal of Physics, vol. 39, 1961.

(66) L.S. Frost and A.V. Phelps,
"Momentum-transfer cross sections for slow electrons in He, Ar, Kr and Xe from transport coefficients."
Physical Review, vol. 136, No 6A, 1964.

(67) W.L. Nighan,
"Electrical conductivity of partially ionized noble gases."
Physics of Fluids, vol. 12, No 1, 1969.

(68) Ali Bulent Cambel,
"Plasma physics and magnetofluidmechanics."
McGraw-Hill Book Co., 1963.

(69) Z. Al-Attar, M.R. Barrault and M. McChesney,
"Electronic conductivity of shock heated partially ionized argon in the presence of a magnetic field."
British Journal of Applied Physics, vol. 15, 1964.

(70) E.H. Dudgeon and G. Michaud,
"Calculations of the electrical conductivity of Helium and Argon seeded with Potassium".
National Research Council Report No 7923, Ottawa 1963.

(71) J. Lau,
"Electrical conductivity of inert gases-seed combination in shock tubes."
Canadian Journal of Physics, vol. 42, 1964.

(72) R.J. Arave, O.A. Huseby, R.A. Mahugh, E.A. Brown and C.Y. Chen,
"Aerothermodynamic properties of high temperature Argon."
Document No: D2-11238 1962. Boeing Company, Seattle.

(73) B. Zauderer,
"Measurement of electrical transport properties in a shock tube."
Proceedings of 7th International Conference on Phenomena in ionized gases. August 1965, vol. II.

(74) M. Nagata,
"Plasma diagnostics by means of Hall currents."
Electrical Engineering in Japan, vol. 86, No 5, 1966.

(75) H.W. Emmons, R.I. Land,
"Poiseuille plasma experiment."
Physics of fluids, vol. 5, No 12, 1962.

(76) J. Lau and E. Mills,
"Electrical conductivity of inert gases-seed combination in shock tubes." Part II : Reflected shock measurements in Argon.
Canadian Journal of Physics, vol. 43, 1965.

(77) H.S. Carslaw and J.C. Jaeger,
"Conduction of heat in solids."
New York : Oxford University Press, 1959, pp. 336-338.

(78) T.A. Thomson,
"Heat transport to a solid wall from a suddenly heated gas."
Australian Defense Scientific Service, Aero Research Lab.
Aerodynamics note 186, 1960.

(79) J.O. Bunting, R.S. Devoto and D. Bershader,
"Shock tube study of the thermal conductivity of Argon."
Department of Aeronautics and Astronautics, Stanford University, Report SUDAAR 313, 1967.

(80) N.W. McLachlan,
"Theory and applications of Matthieu functions."
Oxford Clarendon Press, 1947.

(81) J.H. de Leeuw,
"The interaction of a plane strong shock wave with a steady magnetic field."
UTIAS Report No 49, 1958.

(82) W.N. Tuttle,
"Bridged-T and parallel-T Null circuits for measurements at radio frequencies."
Proceedings of the IRE, vol. 28, January 1940.

(83) V.G. Welsby,
"The theory and design of inductance coils."
London : MacDonald, 1960.

(84) A. Roshko,
"On flow duration in low-pressure shock tubes."
Physics of Fluids, vol. 3, No 6, 1960.

(85) C.V. Brown, L. Flax, E.C. Itean and J.C. Laurence,
"Axial and radial magnetic fields of thick finite-length solenoids."
NASA Tech. Report R-170, 1963.

(86) P. Silvester,
"Network analogue solution of skin and proximity effect problems."
IEEE International Convention Record, vol. 14, Pt 8, 1966.

(87) H.B. Dwight,
"Electrical coils and conductors."
McGraw-Hill Book Company, Inc., 1945.

(88) A. Erdelyi et al.,
"Tables of integral transforms."
New York; McGraw-Hill, 1954, vol. 1.

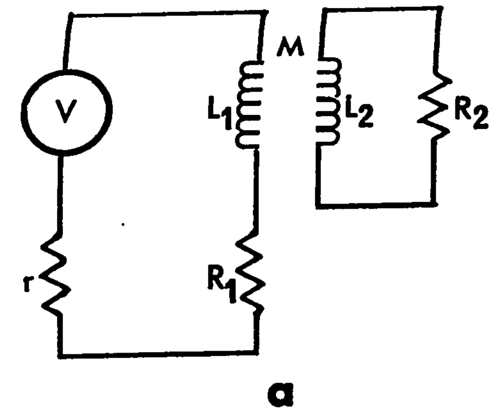

$$Z_1 = r + R_1 + j\omega L_1$$

$$Z_2 = R_2 + j\omega L_2$$

$$Z_c = j\omega M$$

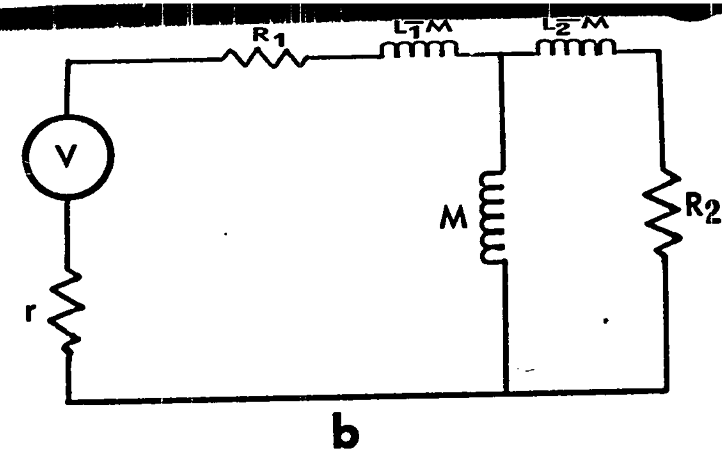

$$\Delta Z = -\frac{Z_c^2}{Z_2} = \frac{\omega^2 M^2}{R_2^2 + \omega^2 L_2^2} R_2 - j\,\frac{\omega^2 M^2}{R_2^2 + \omega^2 L_2^2}\,\omega L_2$$

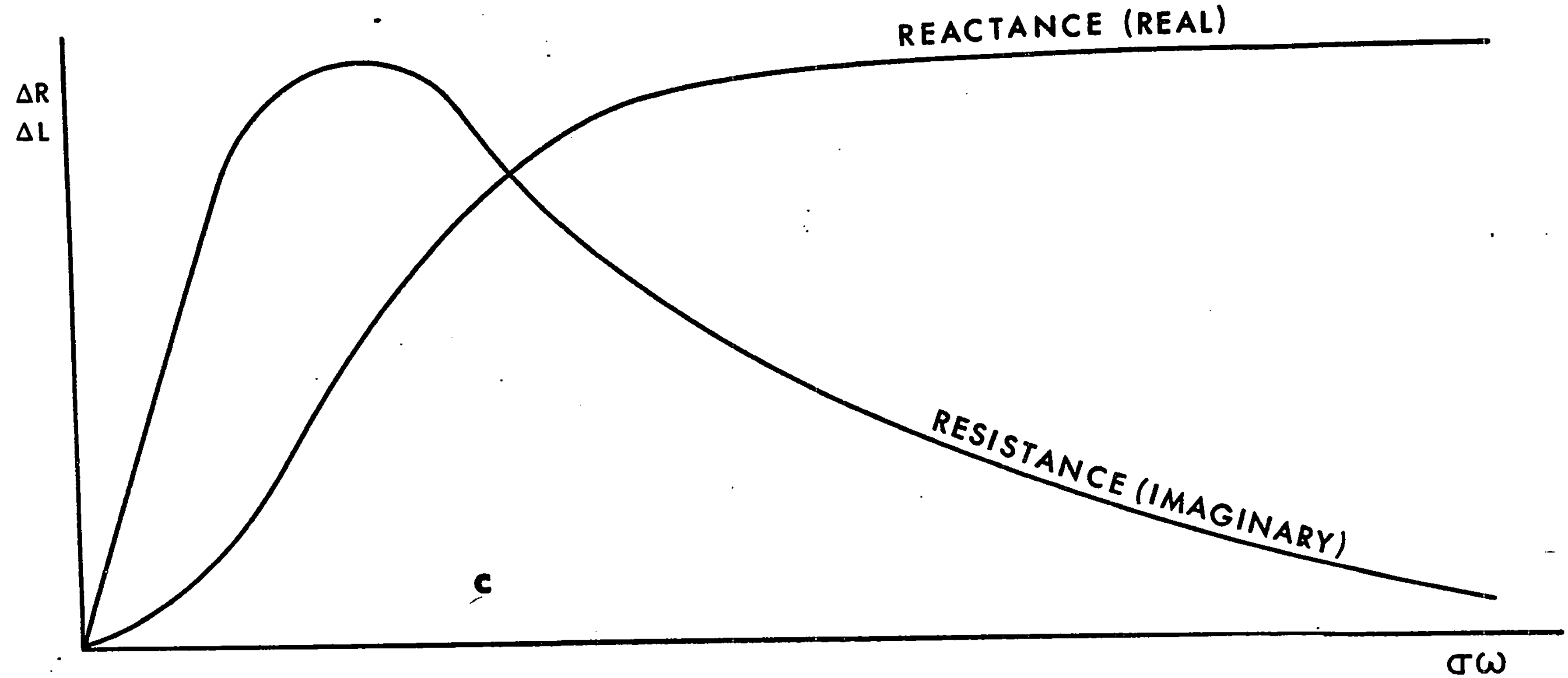

FIG.1 EQUIVALENT ELECTRICAL CIRCUIT FOR PLASMA COUPLING.

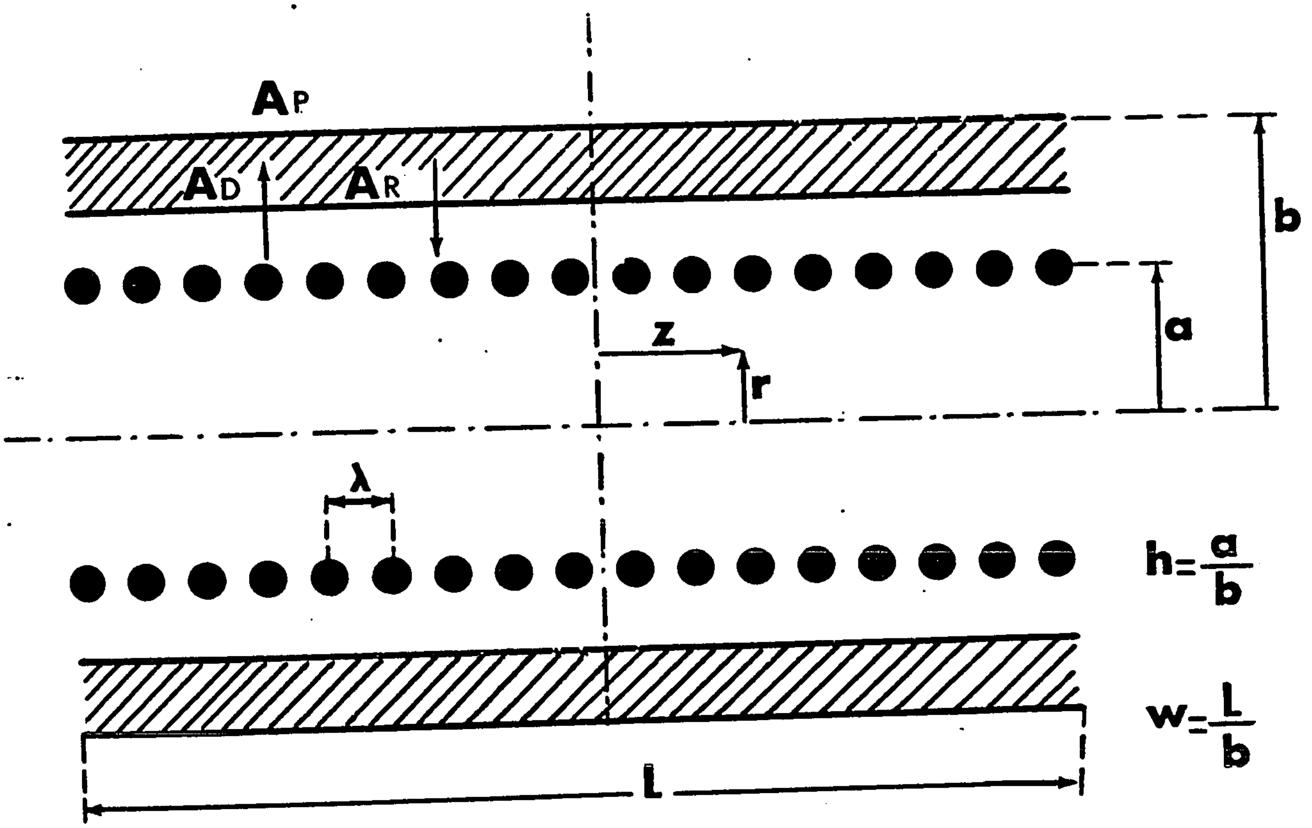

FIG.2 SKETCH OF PROBE COIL CONFIGURATION.

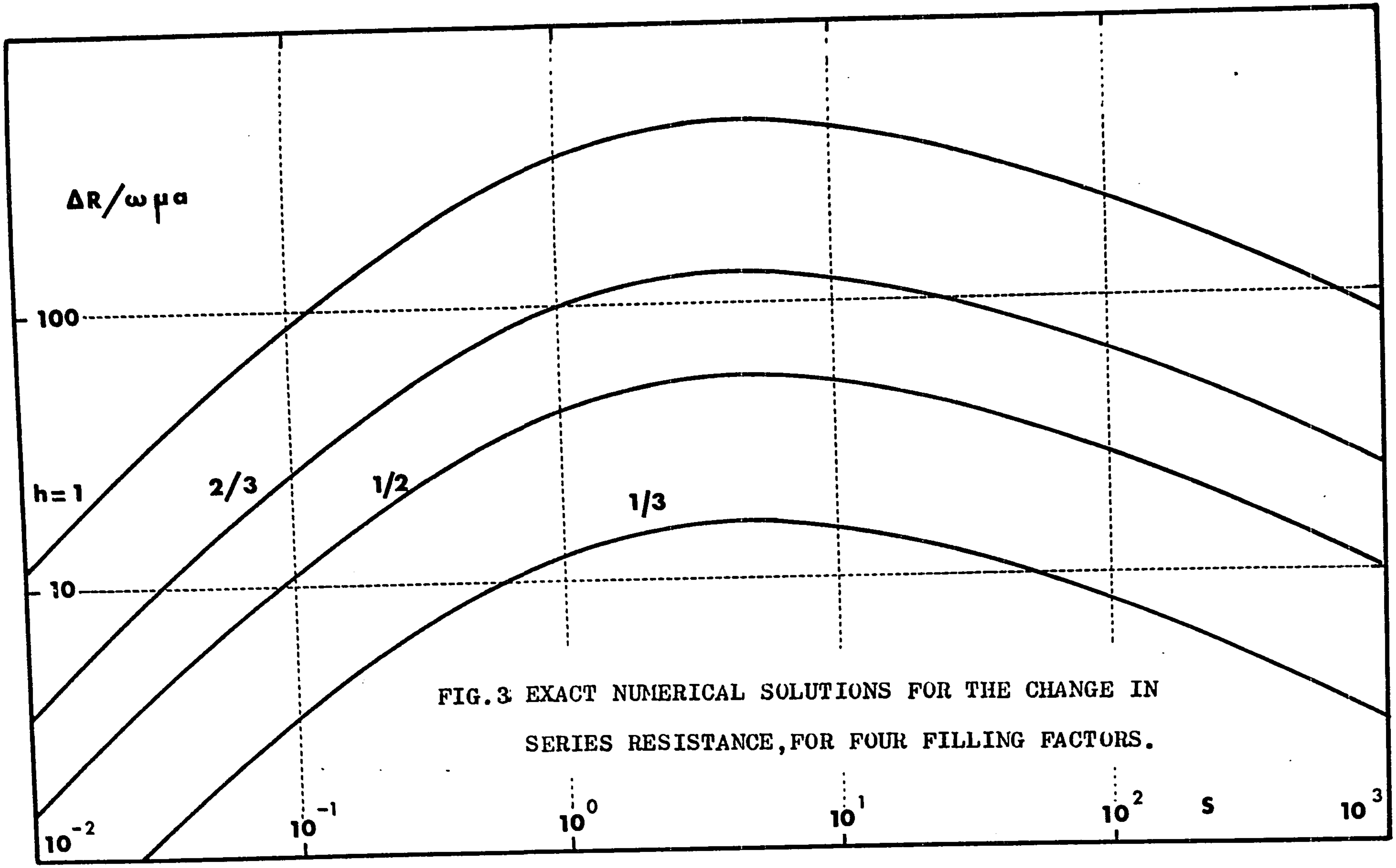

FIG.3 EXACT NUMERICAL SOLUTIONS FOR THE CHANGE IN SERIES RESISTANCE, FOR FOUR FILLING FACTORS.

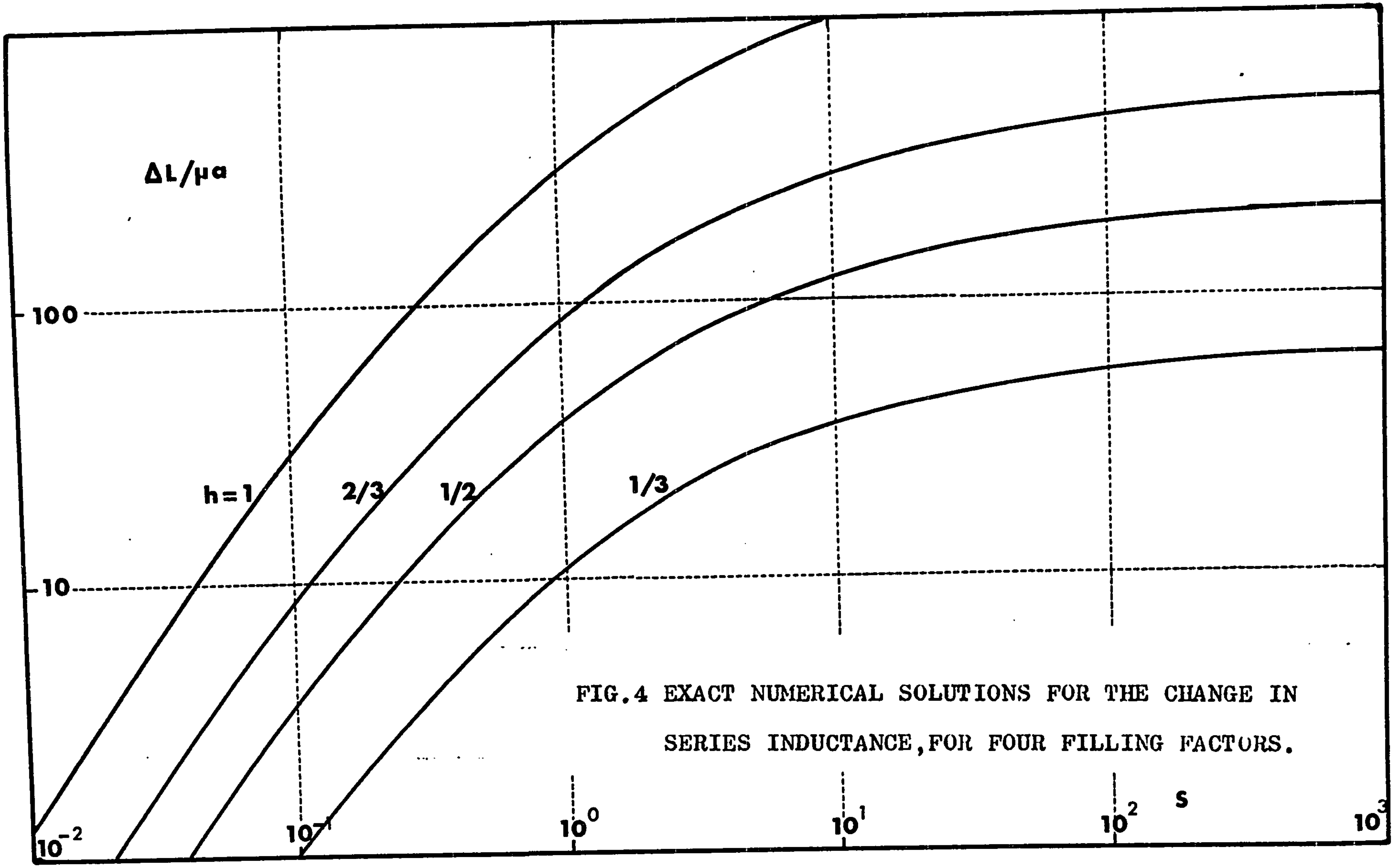

FIG.4 EXACT NUMERICAL SOLUTIONS FOR THE CHANGE IN SERIES INDUCTANCE, FOR FOUR FILLING FACTORS.

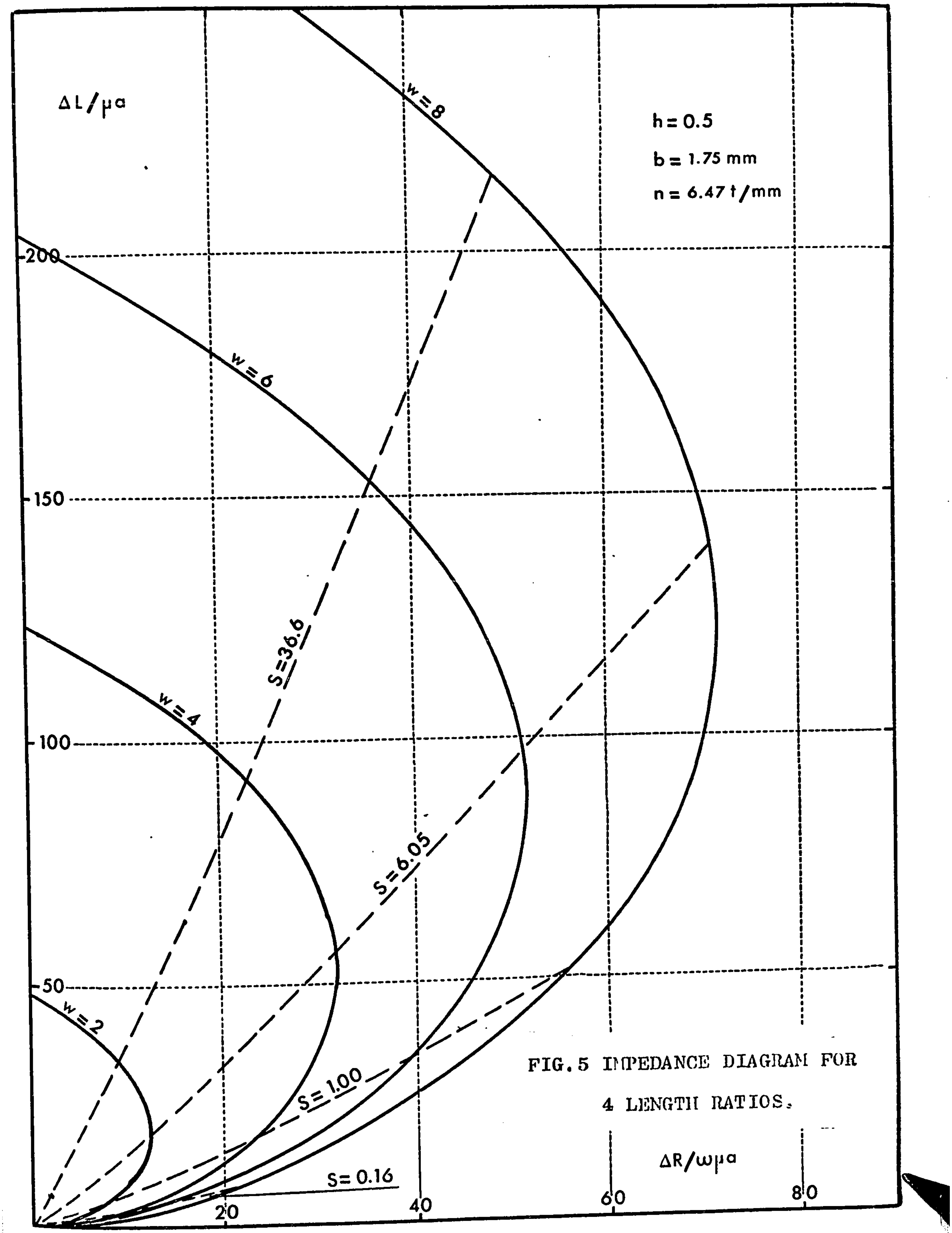

FIG. 5 IMPEDANCE DIAGRAM FOR
4 LENGTH RATIOS.

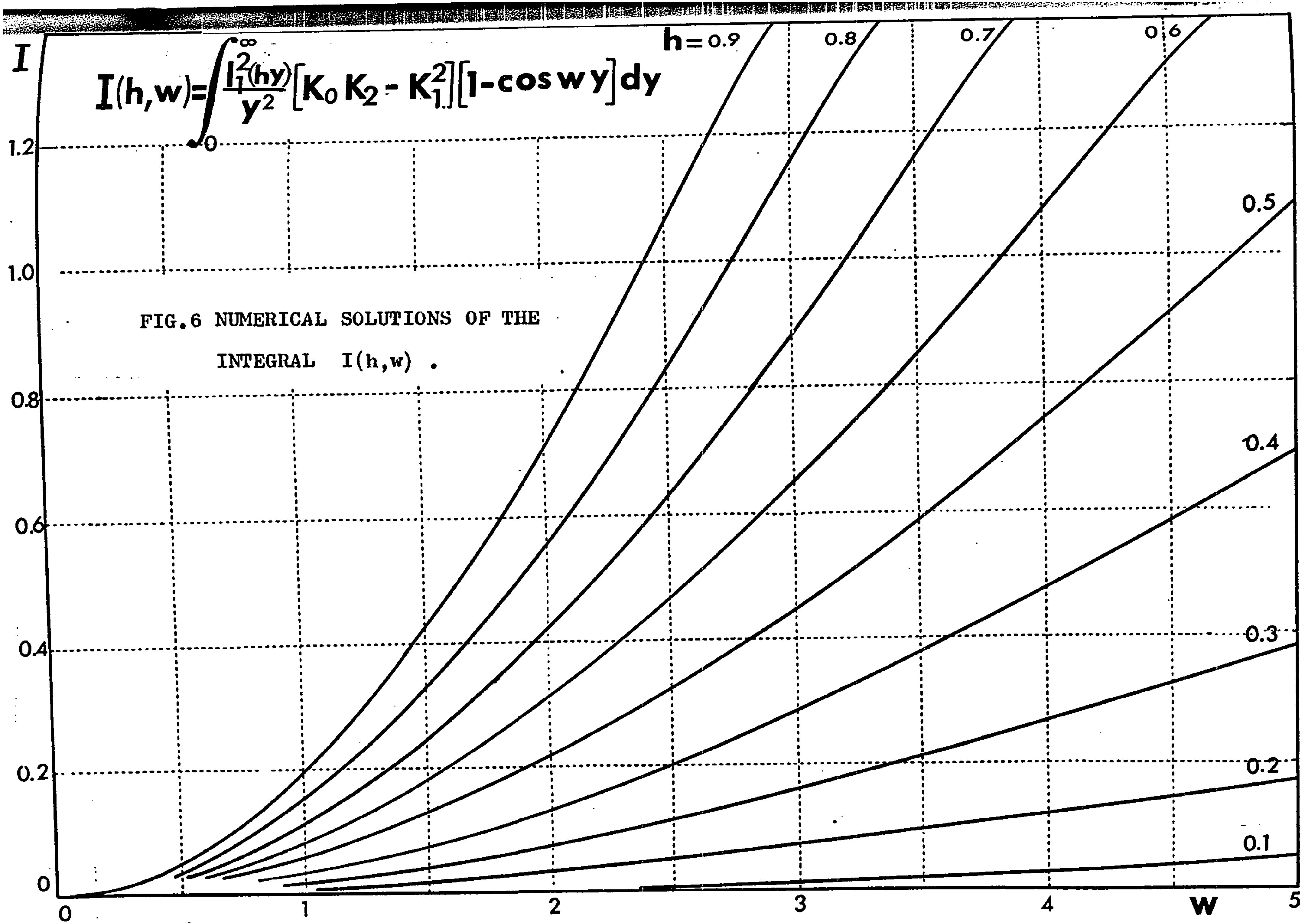

FIG.6 NUMERICAL SOLUTIONS OF THE INTEGRAL I(h,w) .

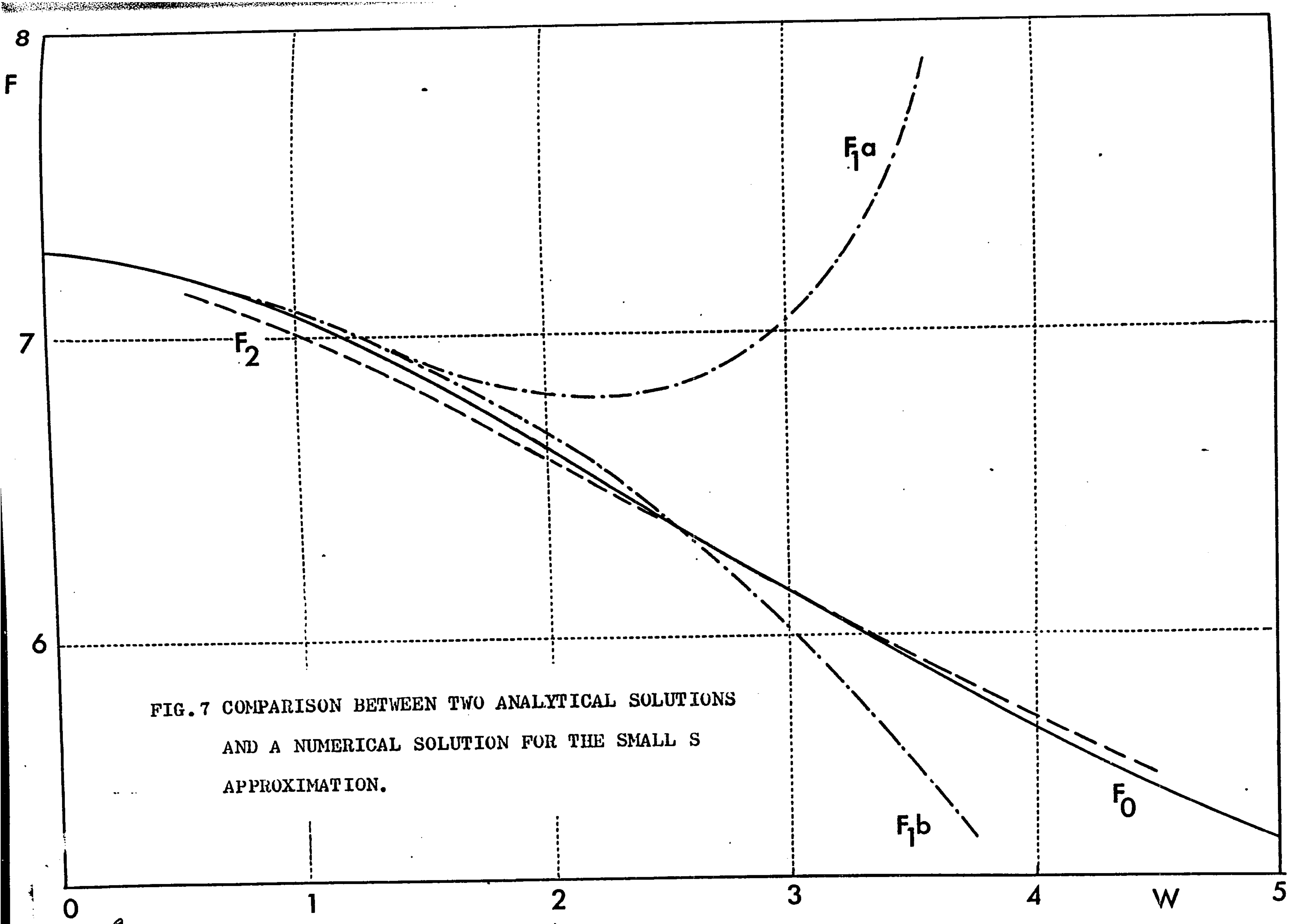

FIG. 7 COMPARISON BETWEEN TWO ANALYTICAL SOLUTIONS AND A NUMERICAL SOLUTION FOR THE SMALL S APPROXIMATION.

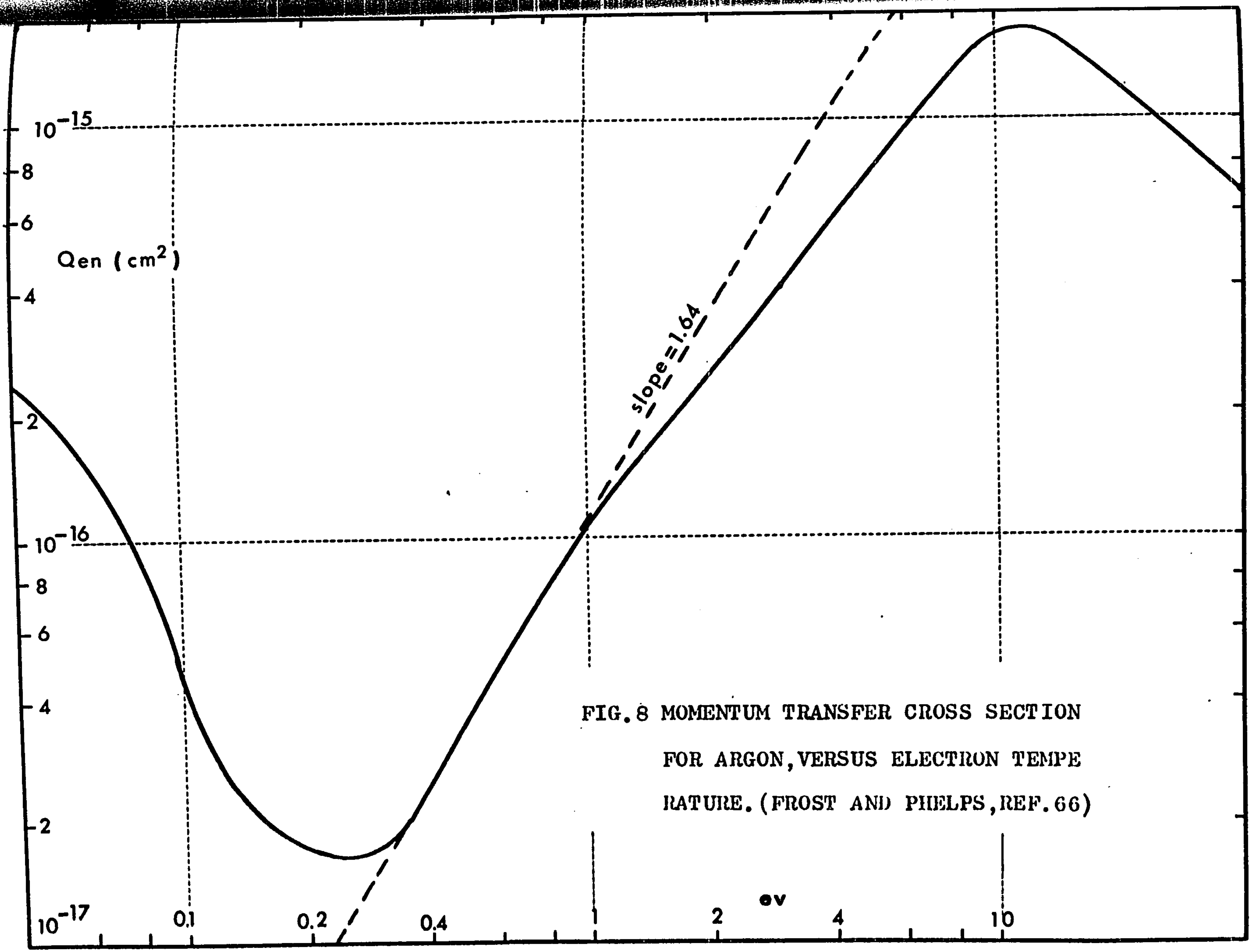

FIG. 8 MOMENTUM TRANSFER CROSS SECTION FOR ARGON, VERSUS ELECTRON TEMPERATURE. (FROST AND PHELPS, REF. 66)

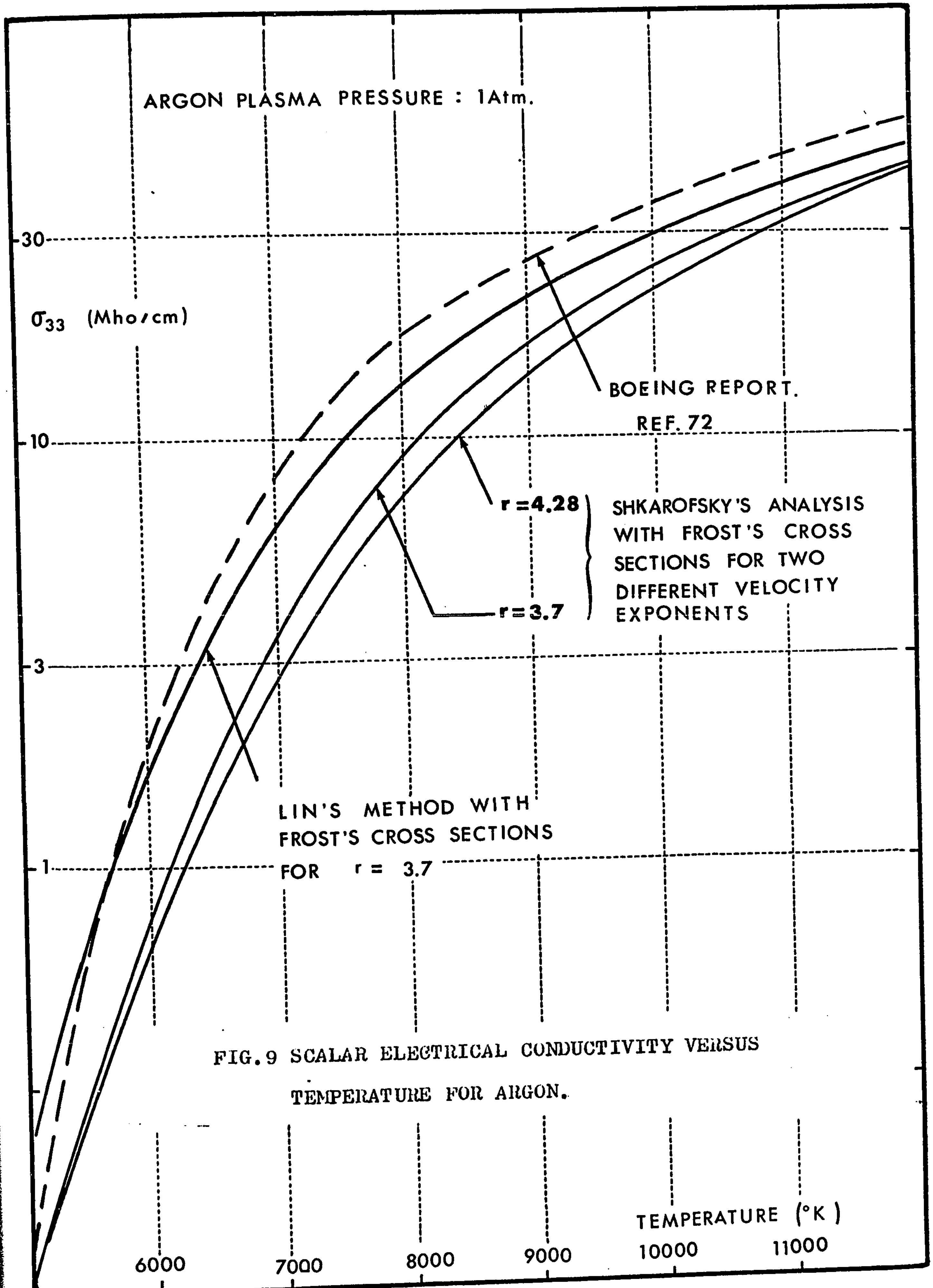

FIG. 9 SCALAR ELECTRICAL CONDUCTIVITY VERSUS TEMPERATURE FOR ARGON.

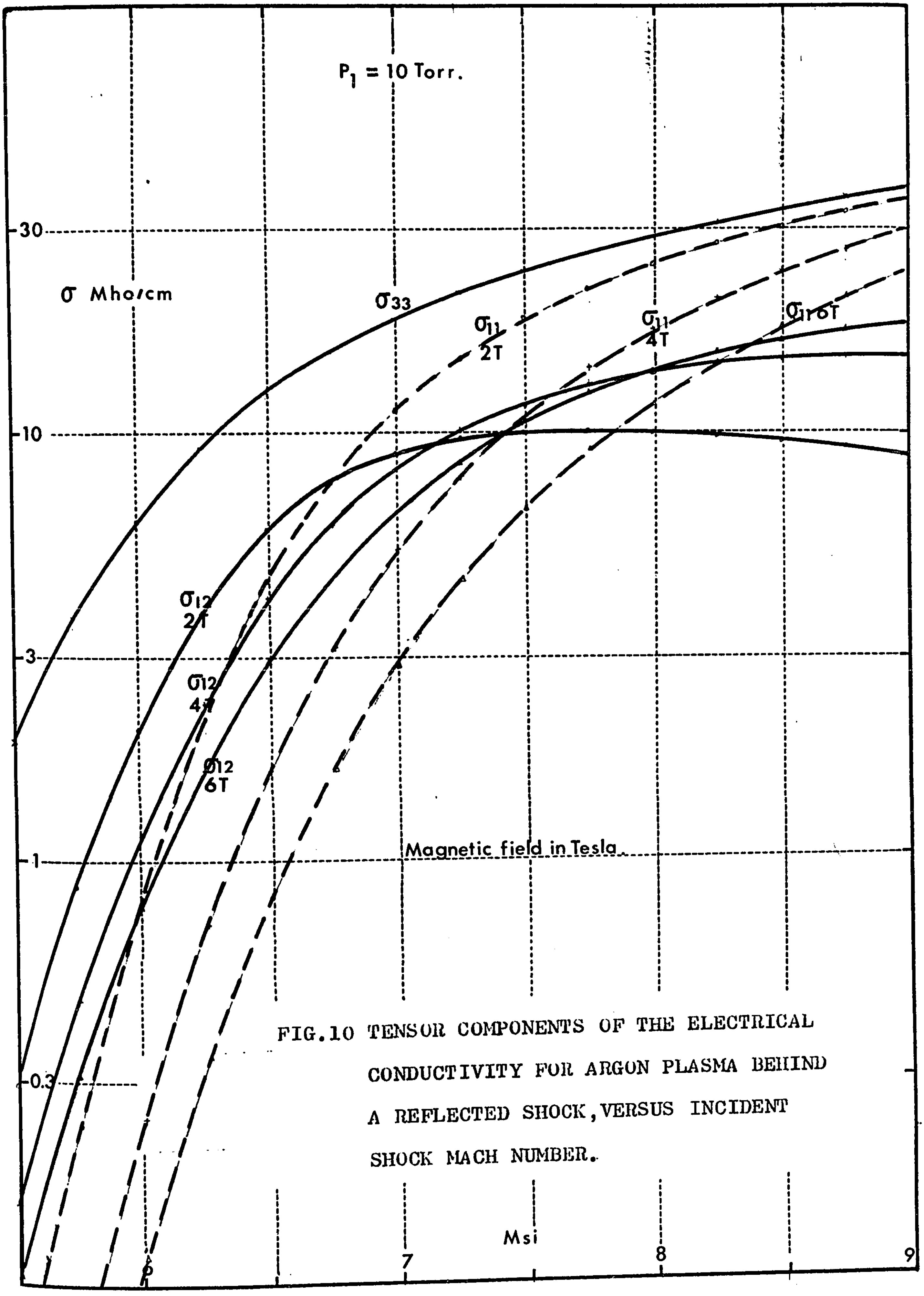

FIG.10 TENSOR COMPONENTS OF THE ELECTRICAL CONDUCTIVITY FOR ARGON PLASMA BEHIND A REFLECTED SHOCK, VERSUS INCIDENT SHOCK MACH NUMBER.

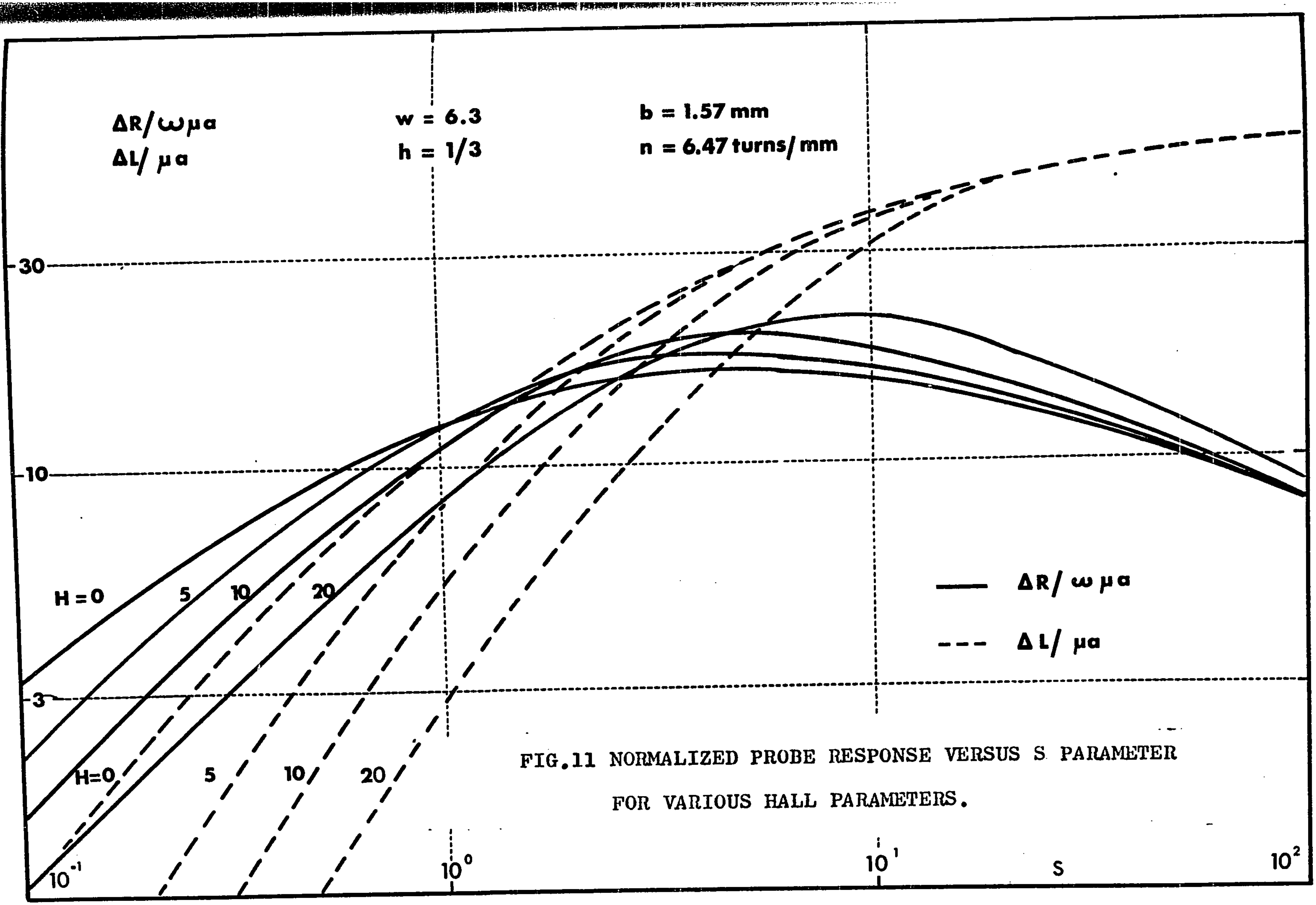

FIG.11 NORMALIZED PROBE RESPONSE VERSUS S PARAMETER FOR VARIOUS HALL PARAMETERS.

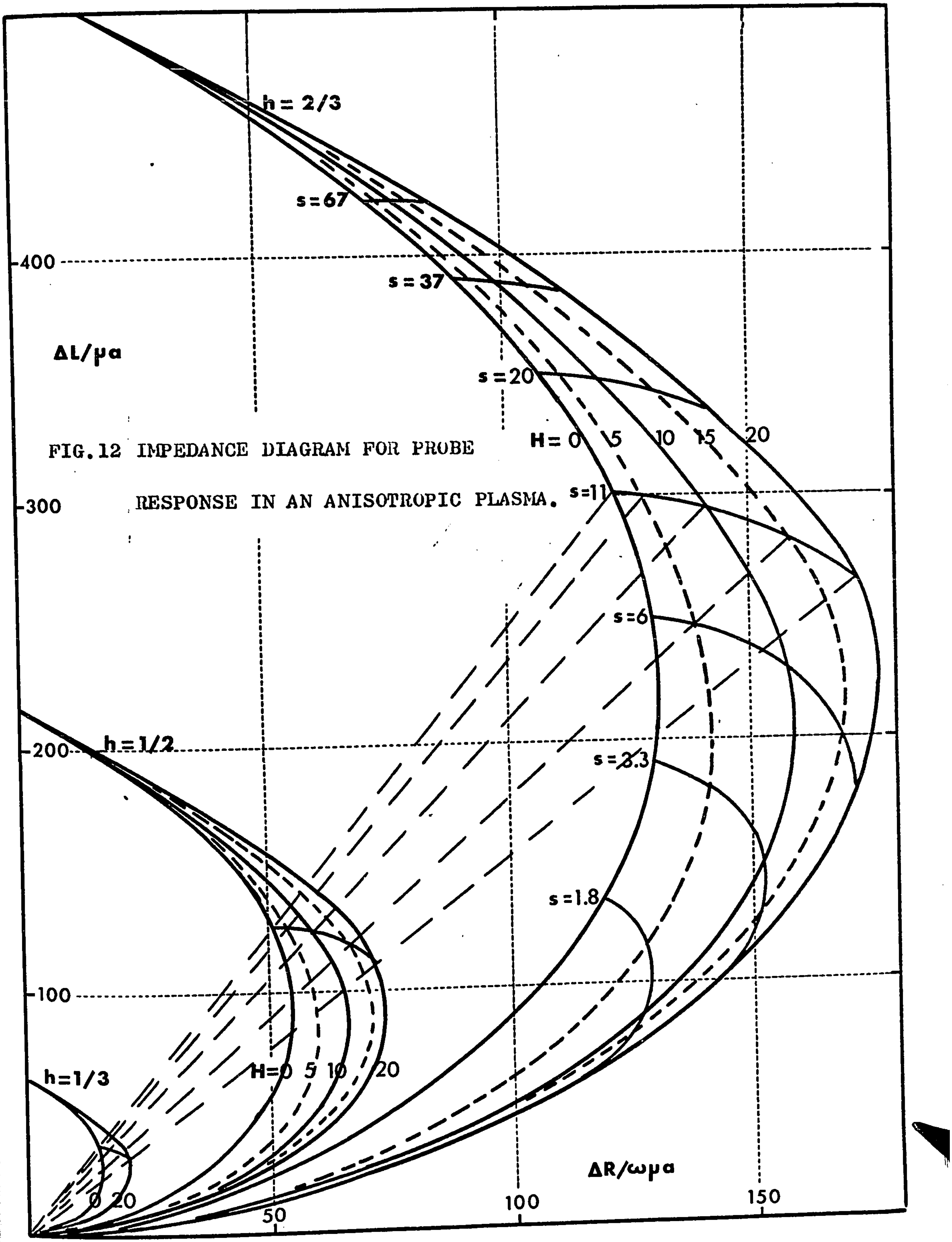

FIG. 12 IMPEDANCE DIAGRAM FOR PROBE RESPONSE IN AN ANISOTROPIC PLASMA.

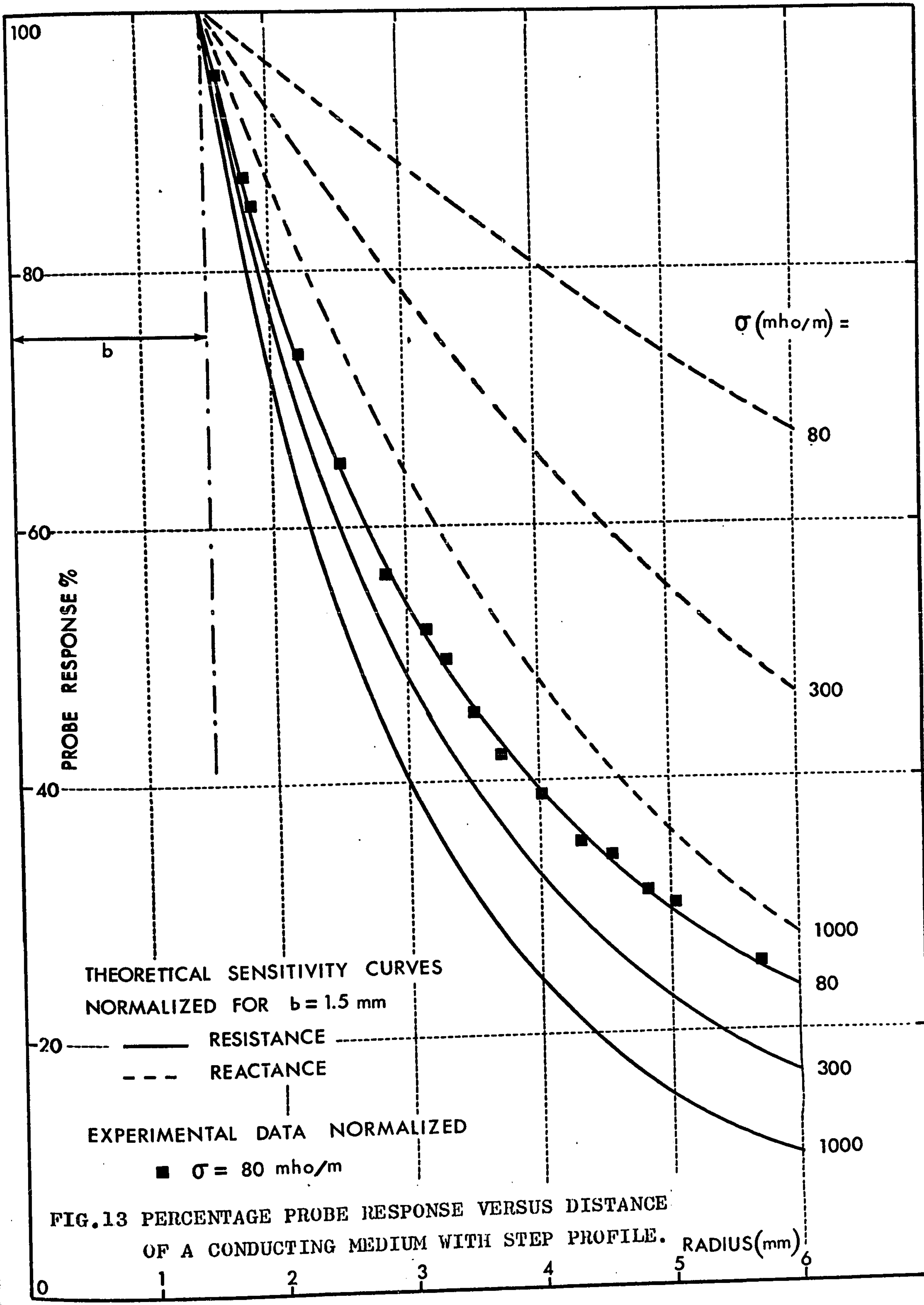

FIG.13 PERCENTAGE PROBE RESPONSE VERSUS DISTANCE OF A CONDUCTING MEDIUM WITH STEP PROFILE.

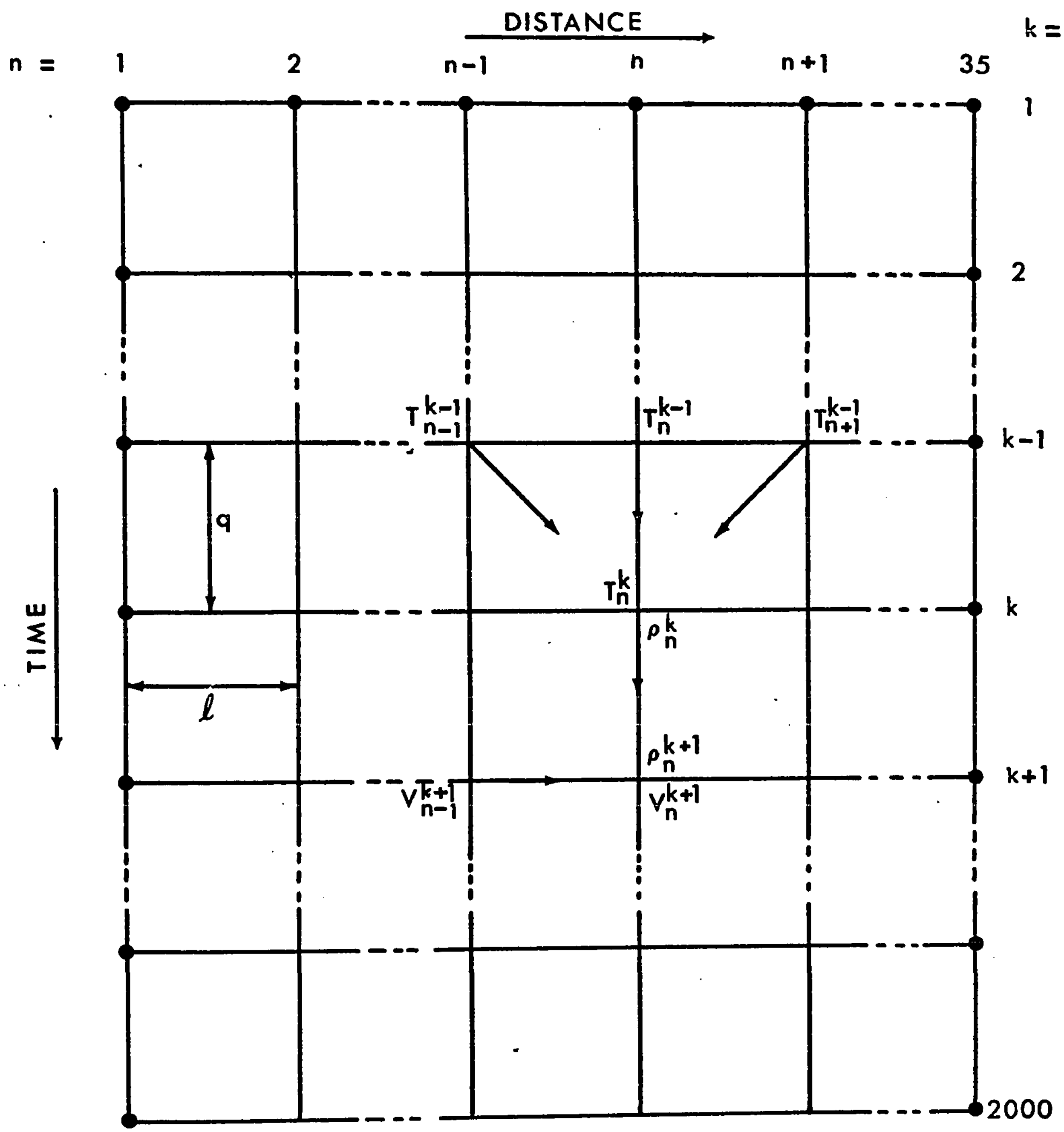

$r/b = \mathrm{EXP}(c)$ $\quad c = (n-1)\ell$ $\quad \ell = 0.05$ $\quad 1 \leq n \leq 35$

$t/t_o = \mathrm{LN}(1/P)$ $\quad p = 1-(k-1)q$ $\quad q = 0.0002$ $\quad 1 \leq k \leq 2000$

● Known boundary conditions for T, ρ, V

FIG.14 GRID STRUCTURE FOR NUMERICAL SOLUTION OF THE THERMAL BOUNDARY LAYER PROBLEM.

FIG.15 ELECTRICAL CONDUCTIVITY PROFILES AT VARIOUS TIME INTERVALS.

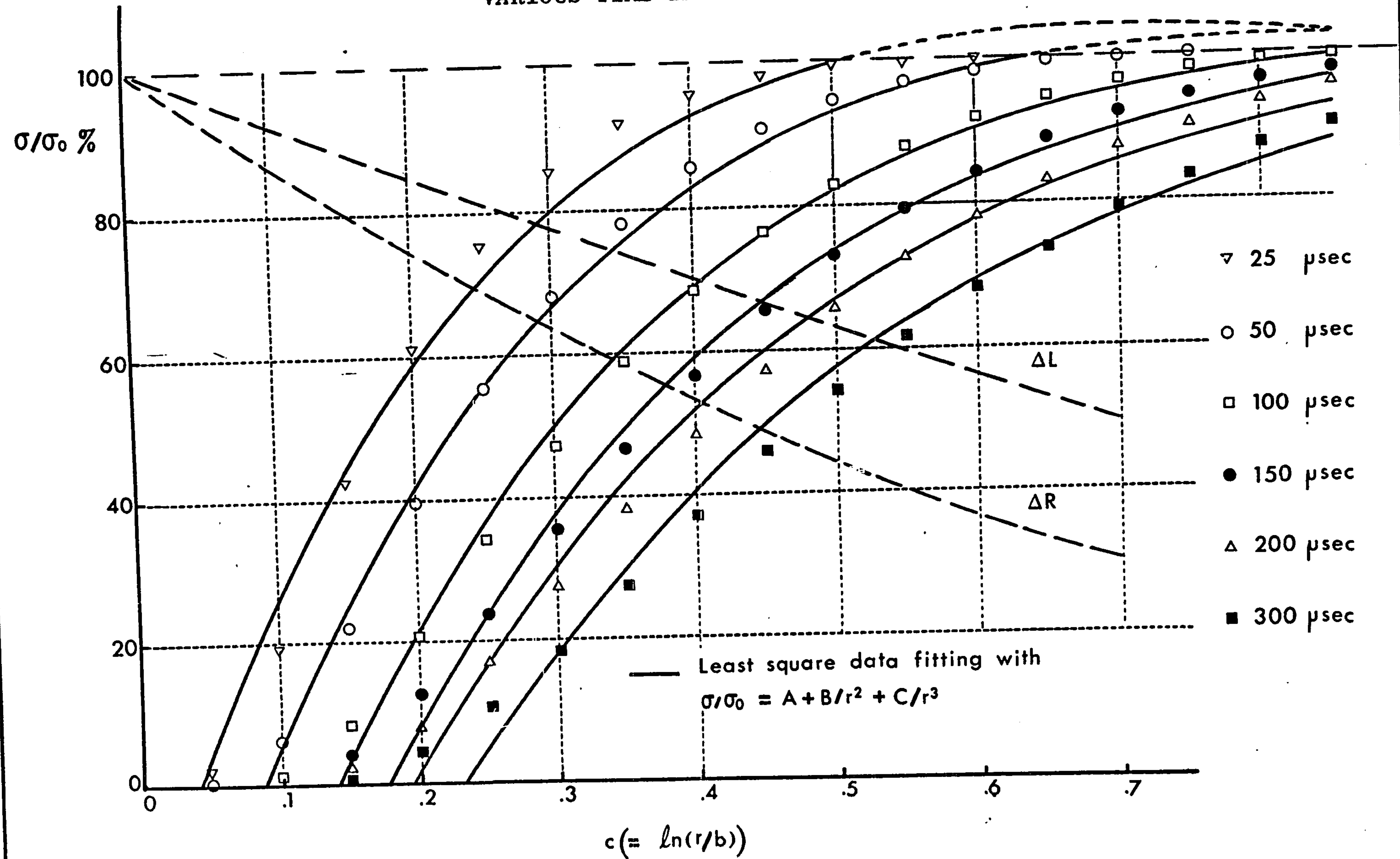

FIG.16 COMPARISON BETWEEN CALCULATED AND MEASURED PROBE RESPONSE IN A NON UNIFORM PLASMA.

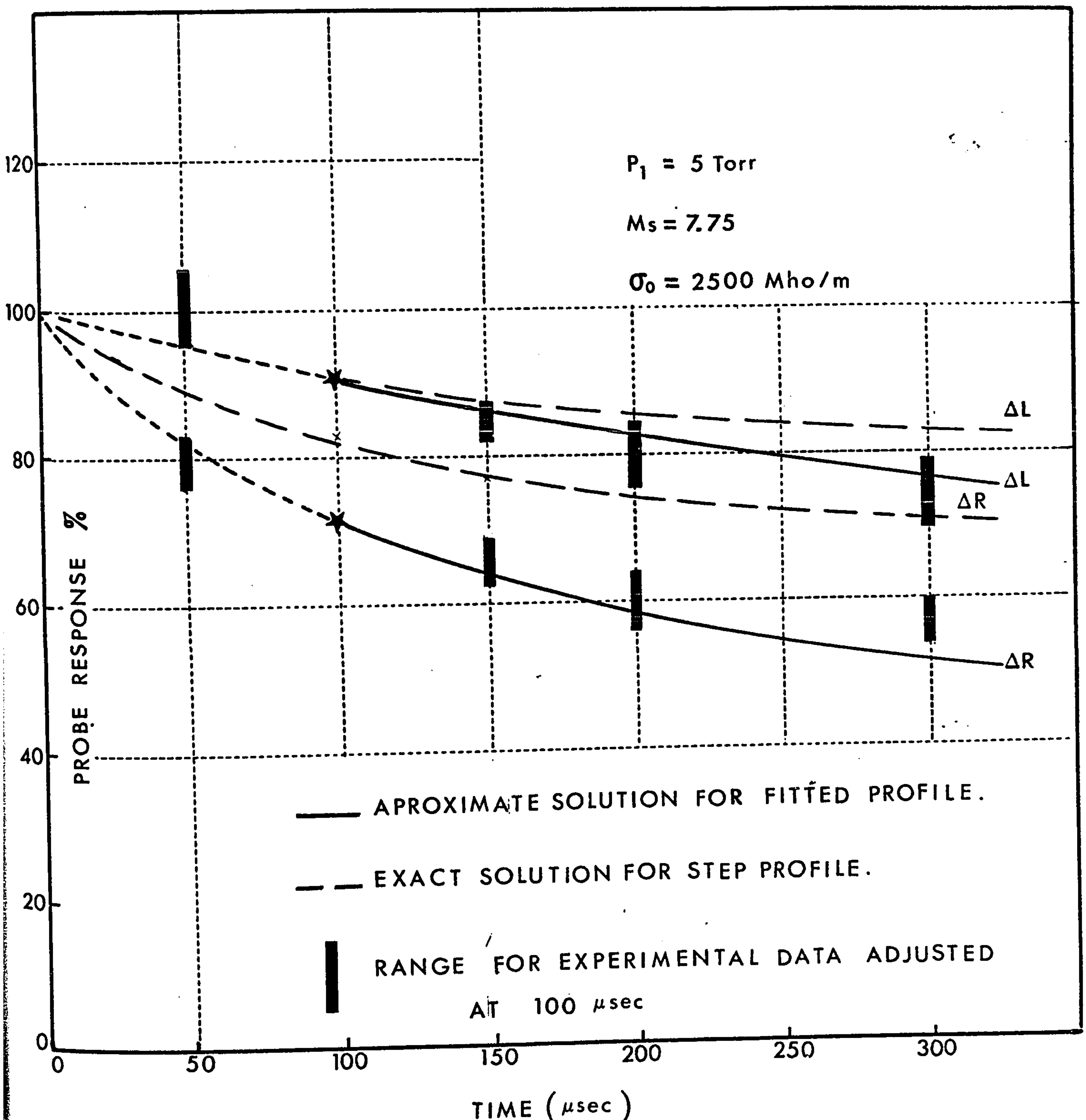

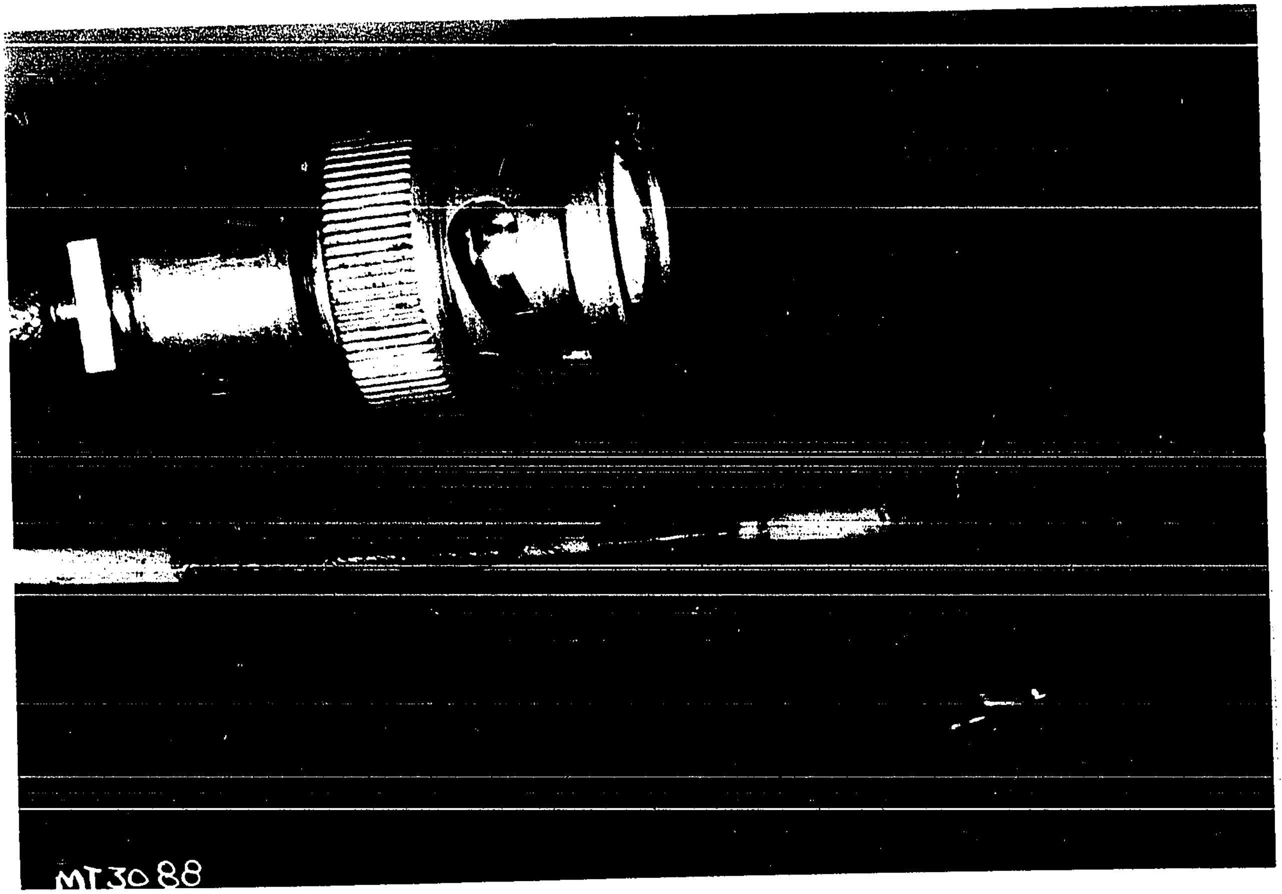

FIG.17 ENLARGED VIEW OF A TYPICAL PROBE

ASSEMBLY. QUARTZ TUBE,COIL,BNC CONNECTOR.

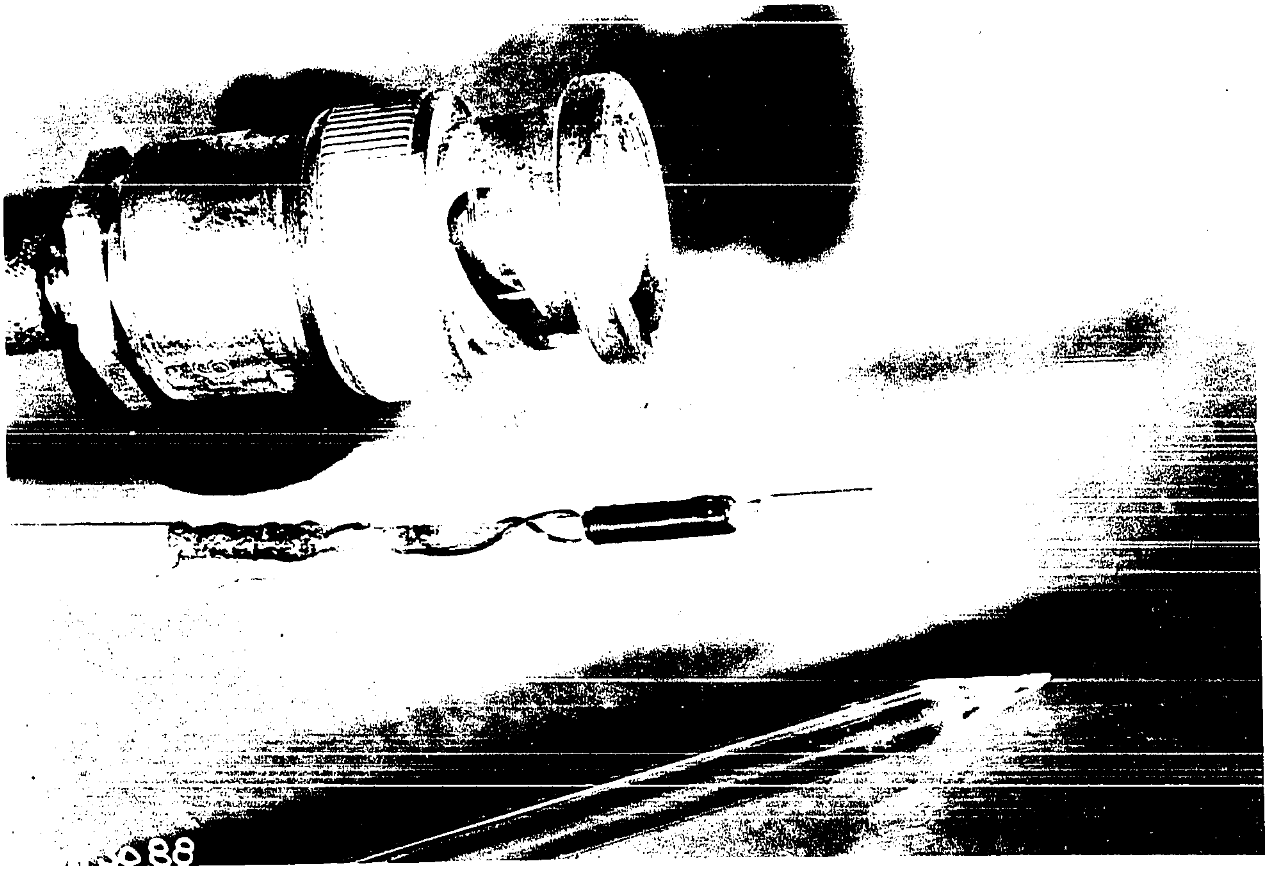

FIG.17 ENLARGED VIEW OF A TYPICAL PROBE

ASSEMBLY. QUARTZ TUBE,COIL,BNC CONNECTOR.

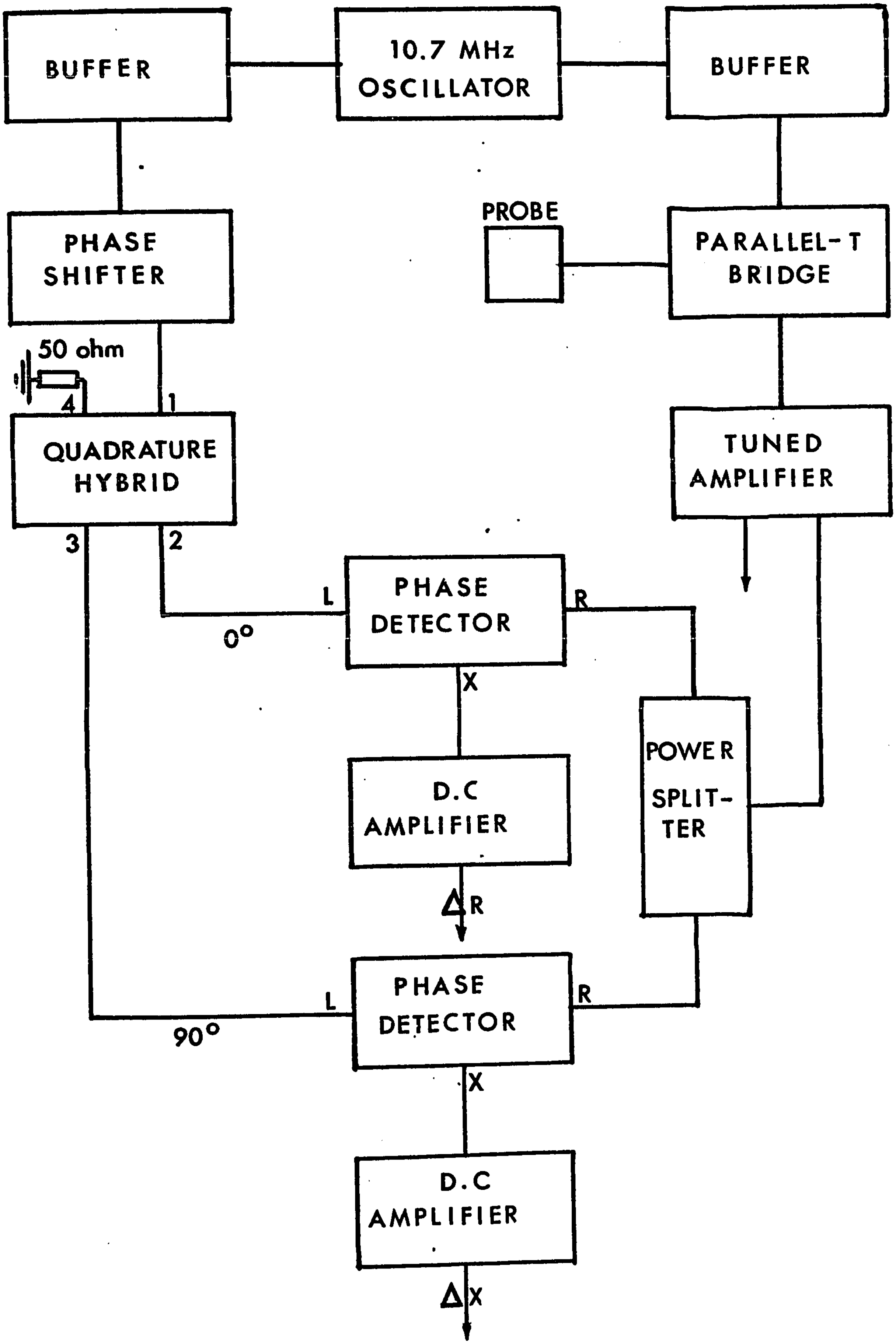

FIG. 18 BLOCK DIAGRAM OF THE TWO CHANNEL SYSTEM.

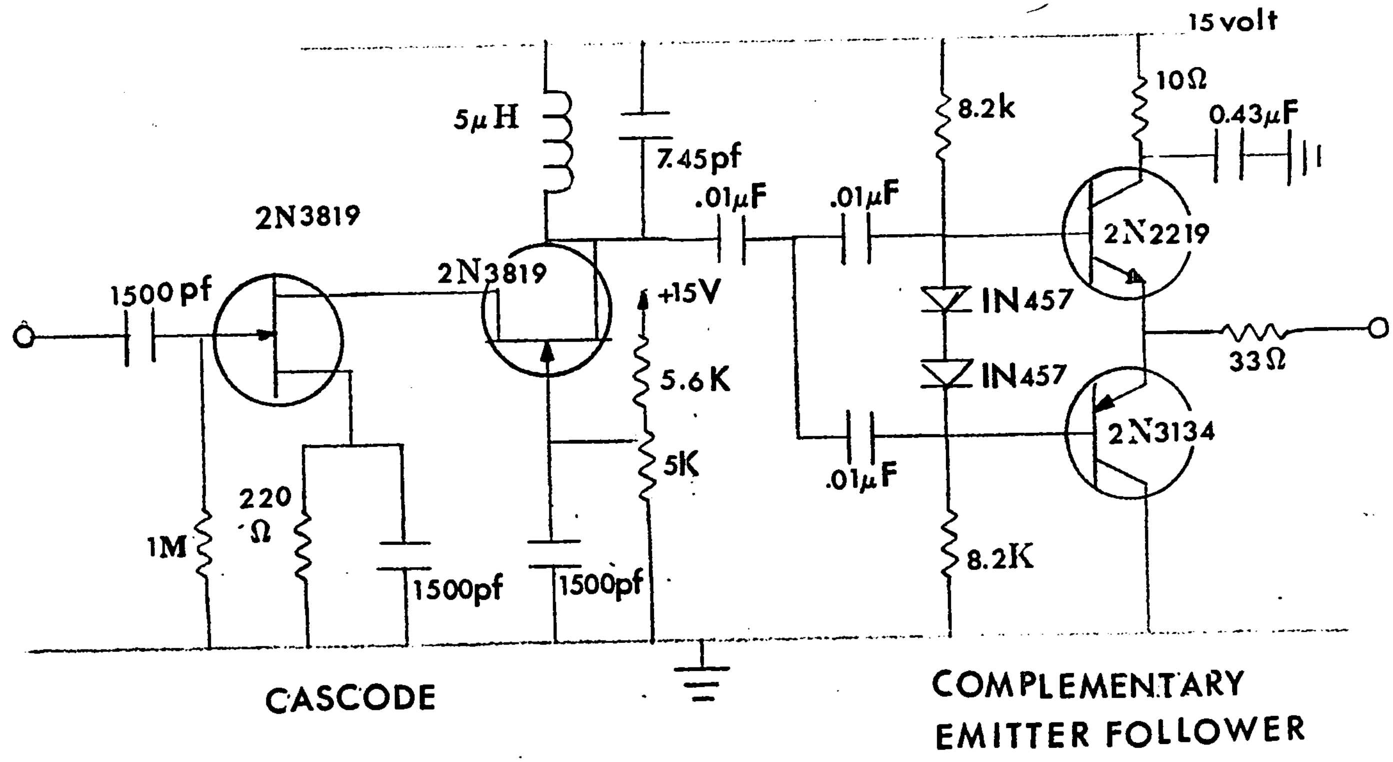

FIG.19 CIRCUIT DIAGRAM OF A BUFFER STAGE.

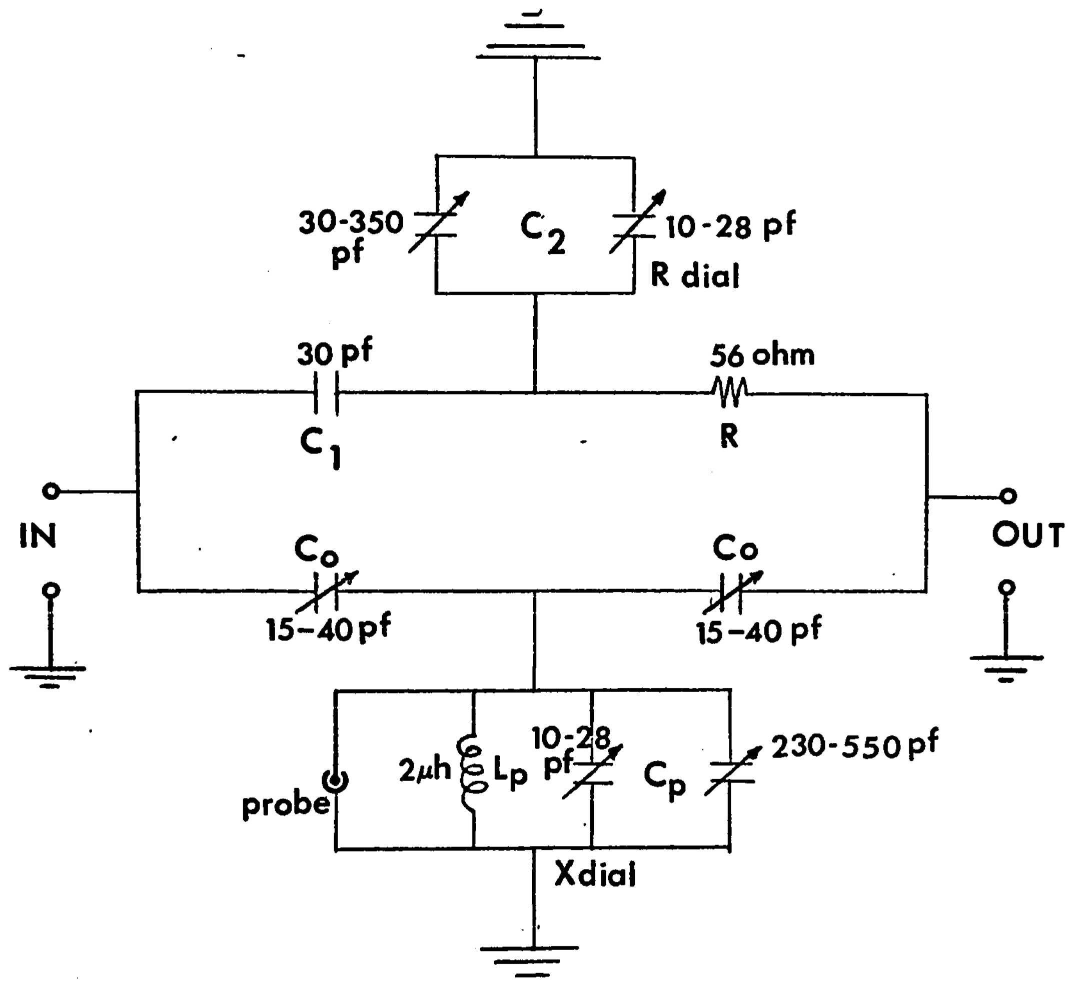

FIG.20 PARALLEL-T BRIDGE.

FIG.21 CIRCUIT DIAGRAM OF A DOUBLE TUNED AMPLIFIER.

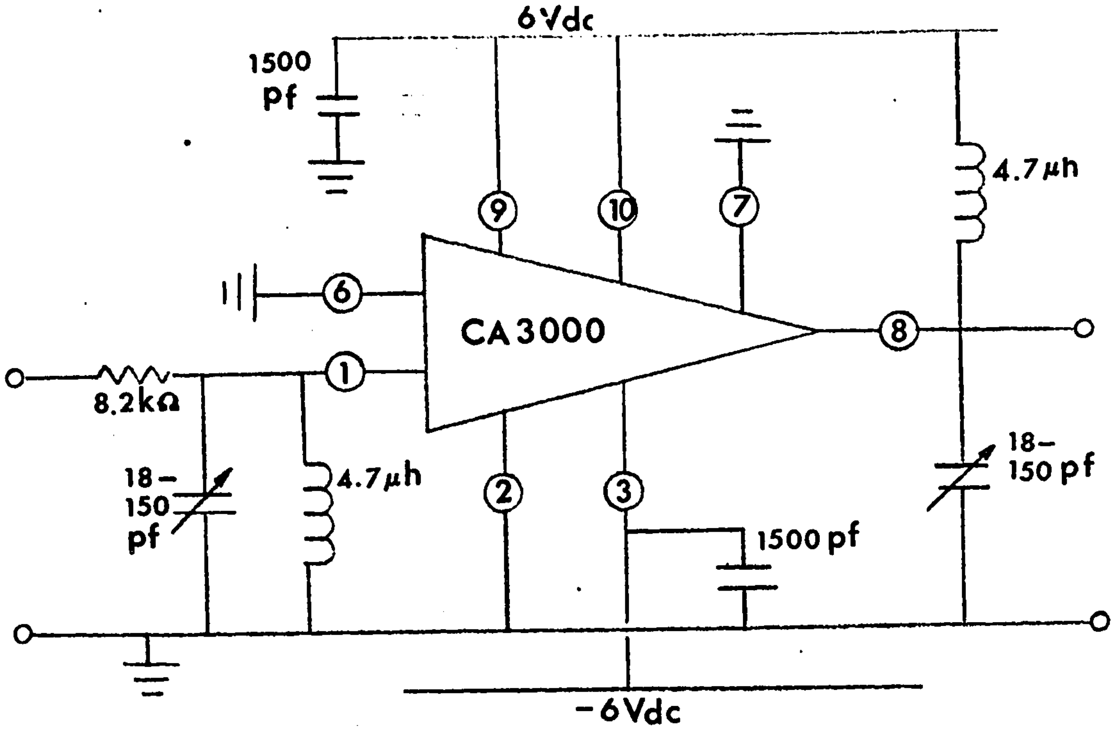

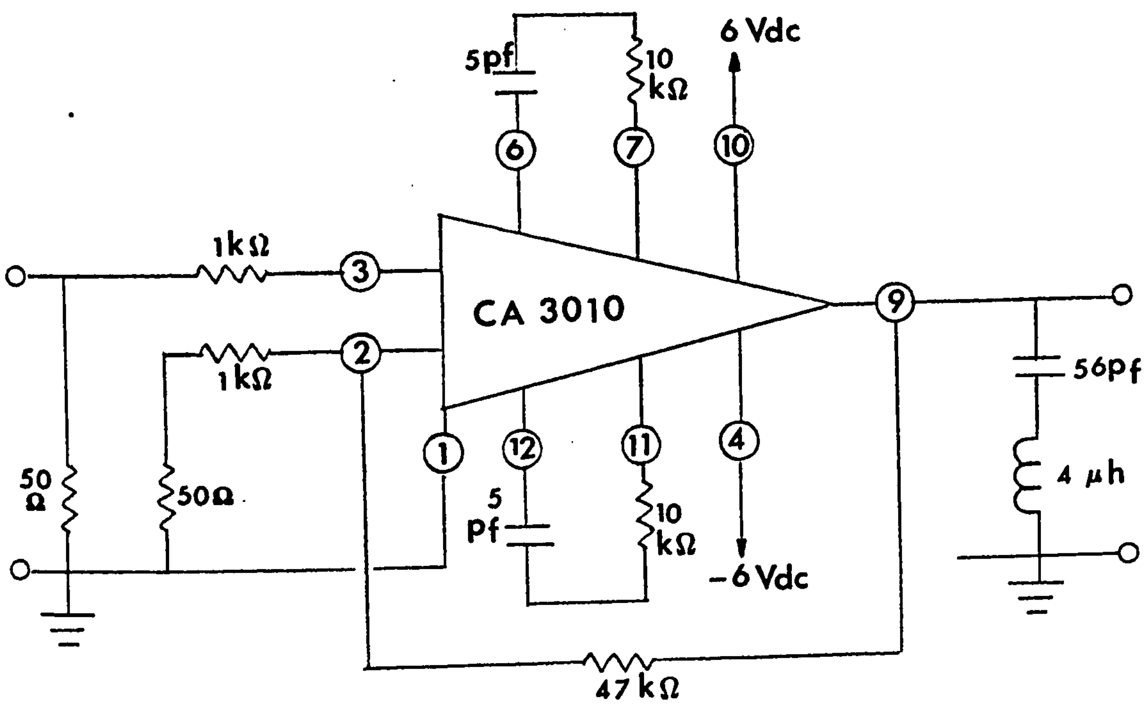

FIG.22 CIRCUIT DIAGRAM OF A D.C. AMPLIFIER.

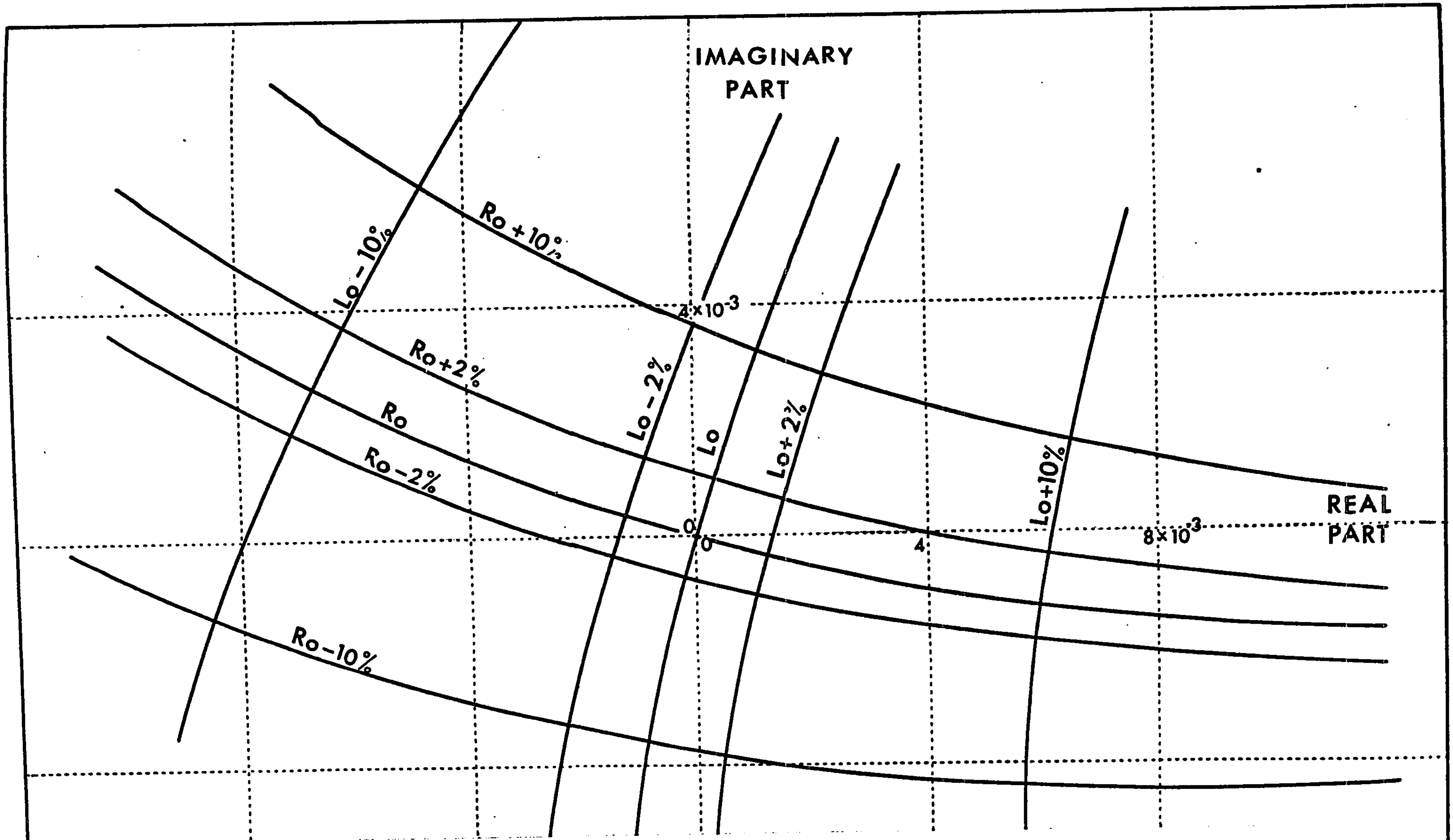

FIG.23 SOLUTIONS OF GENERAL TRANSFER FUNCTION OF A PARALLEL-T BRIDGE, FOR VARIATIONS OF Ls AND Rs.

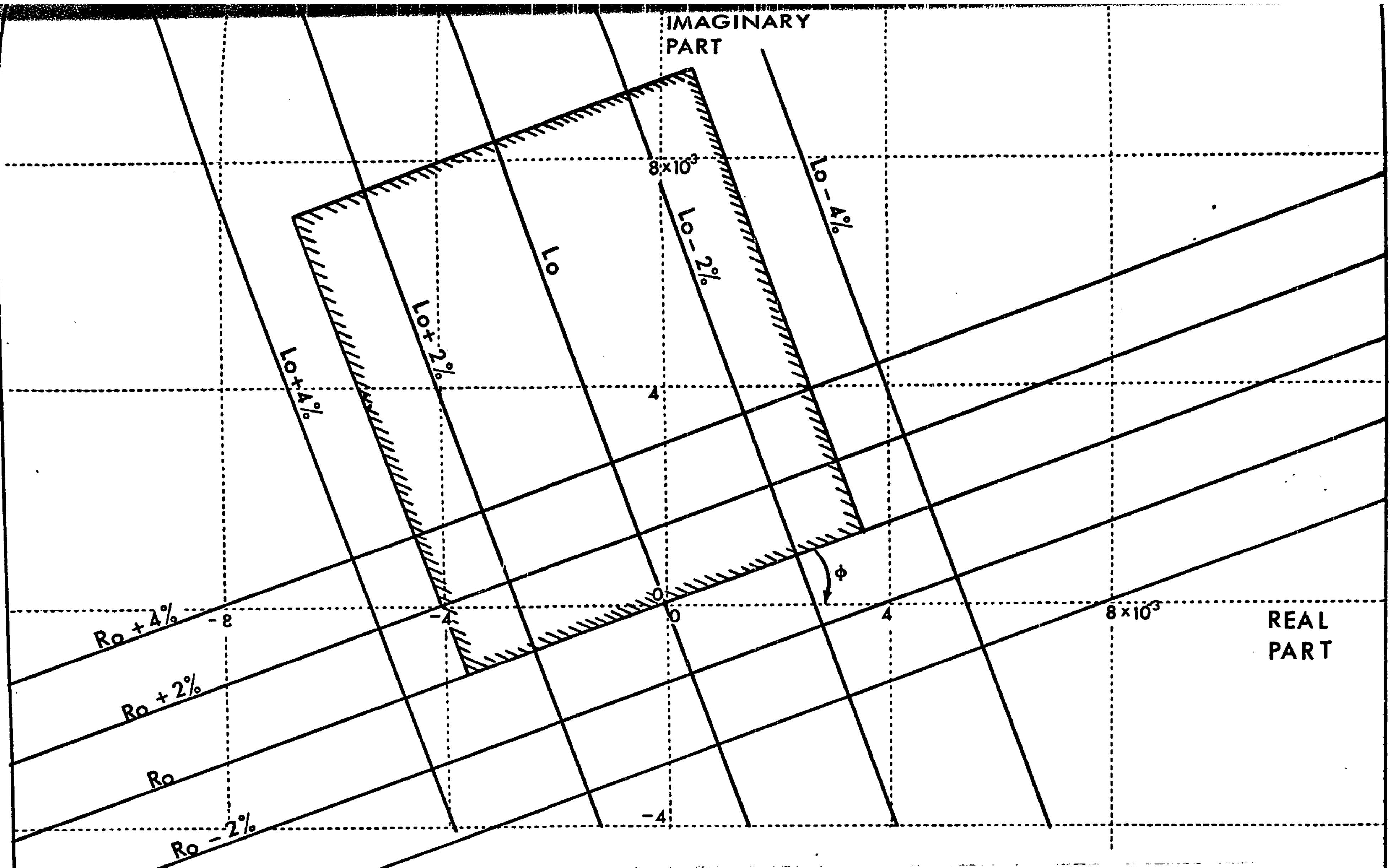

FIG. 24 SOLUTIONS OF OPTIMIZED TRANSFER FUNCTION FOR VARIATIONS OF Ls AND Rs.

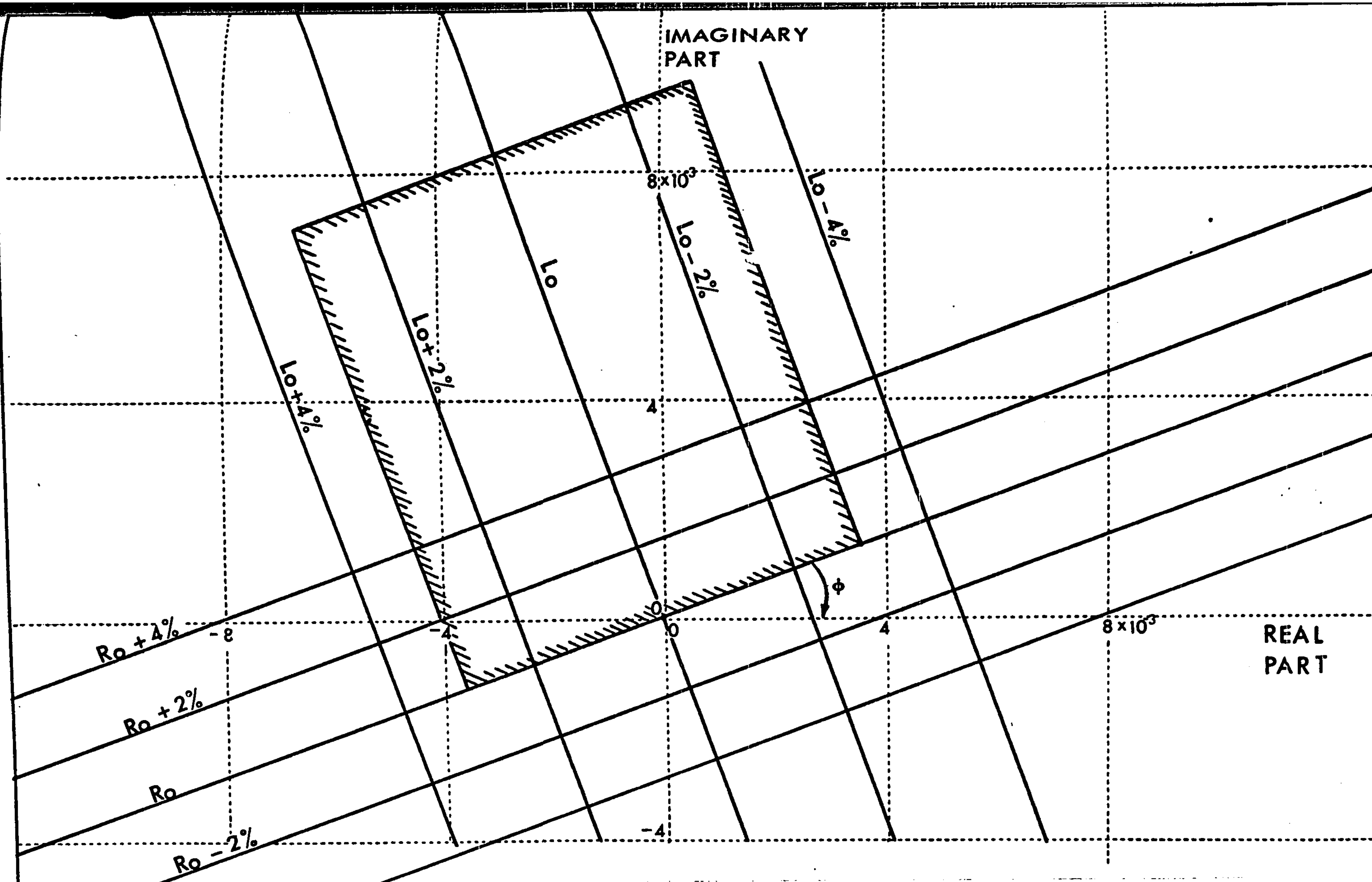

FIG. 24 SOLUTIONS OF OPTIMIZED TRANSFER FUNCTION FOR VARIATIONS OF Ls AND Rs.

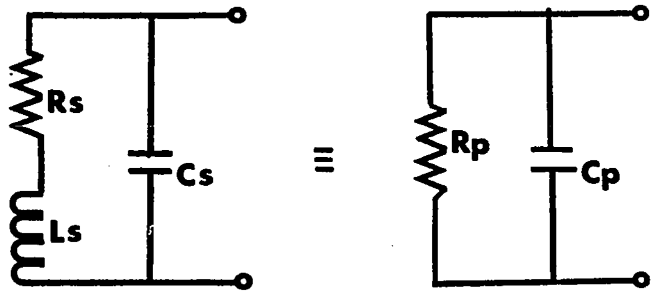

$$\frac{1}{Z} = \frac{1}{R_s + j\omega L_s} + \frac{1}{jC_s\omega} = \frac{1}{R_p} + \frac{1}{jC_p\omega}$$

FIG. 25 EQUIVALENT SERIES AND PARALLEL REPRESENTATION OF THE PROBE COIL.

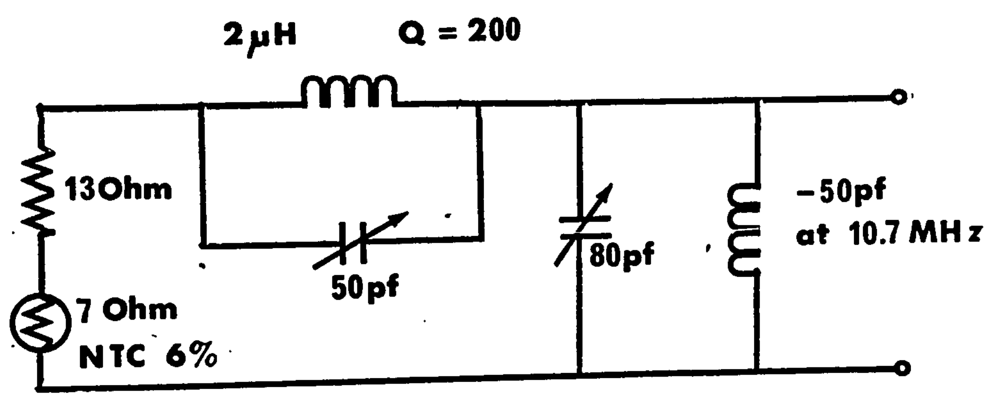

FIG.26 ANALOG LUMPED MODEL FOR THE PROBE COIL.

FIG. 27 CALIBRATION CURVE FOR THE RESISTIVE CHANNEL.

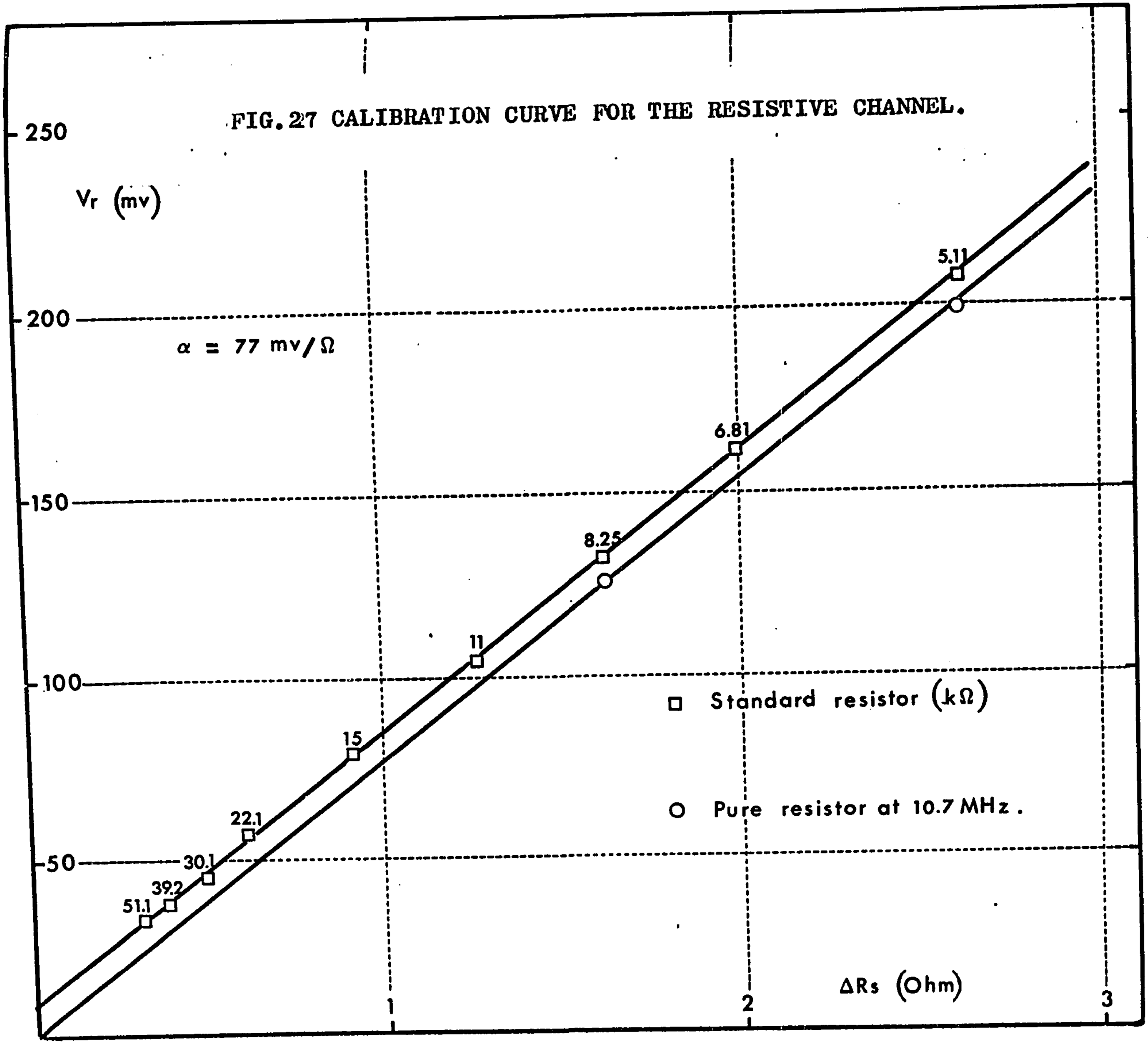

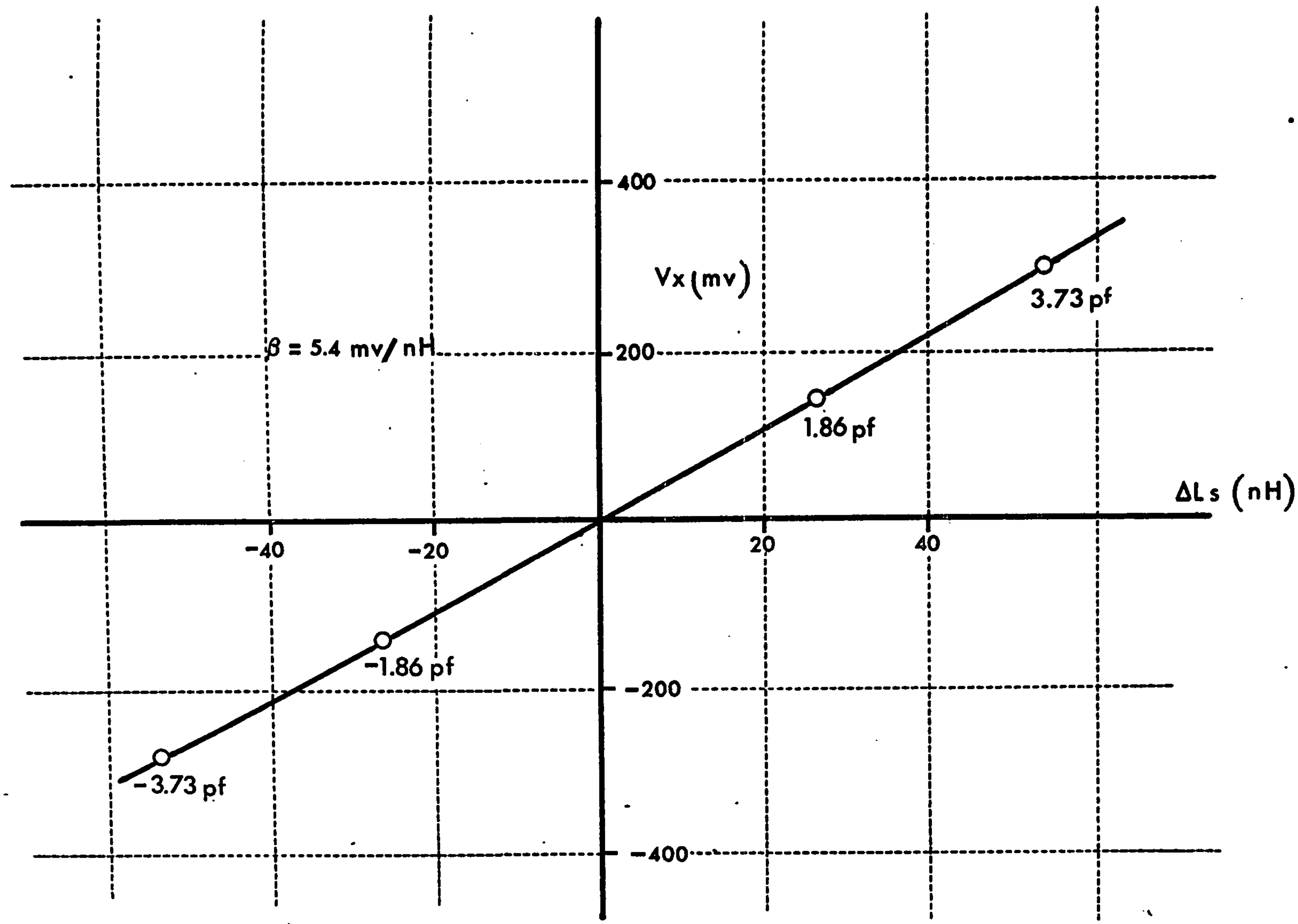

FIG. 28 CALIBRATION CURVE FOR THE REACTIVE CHANNEL.

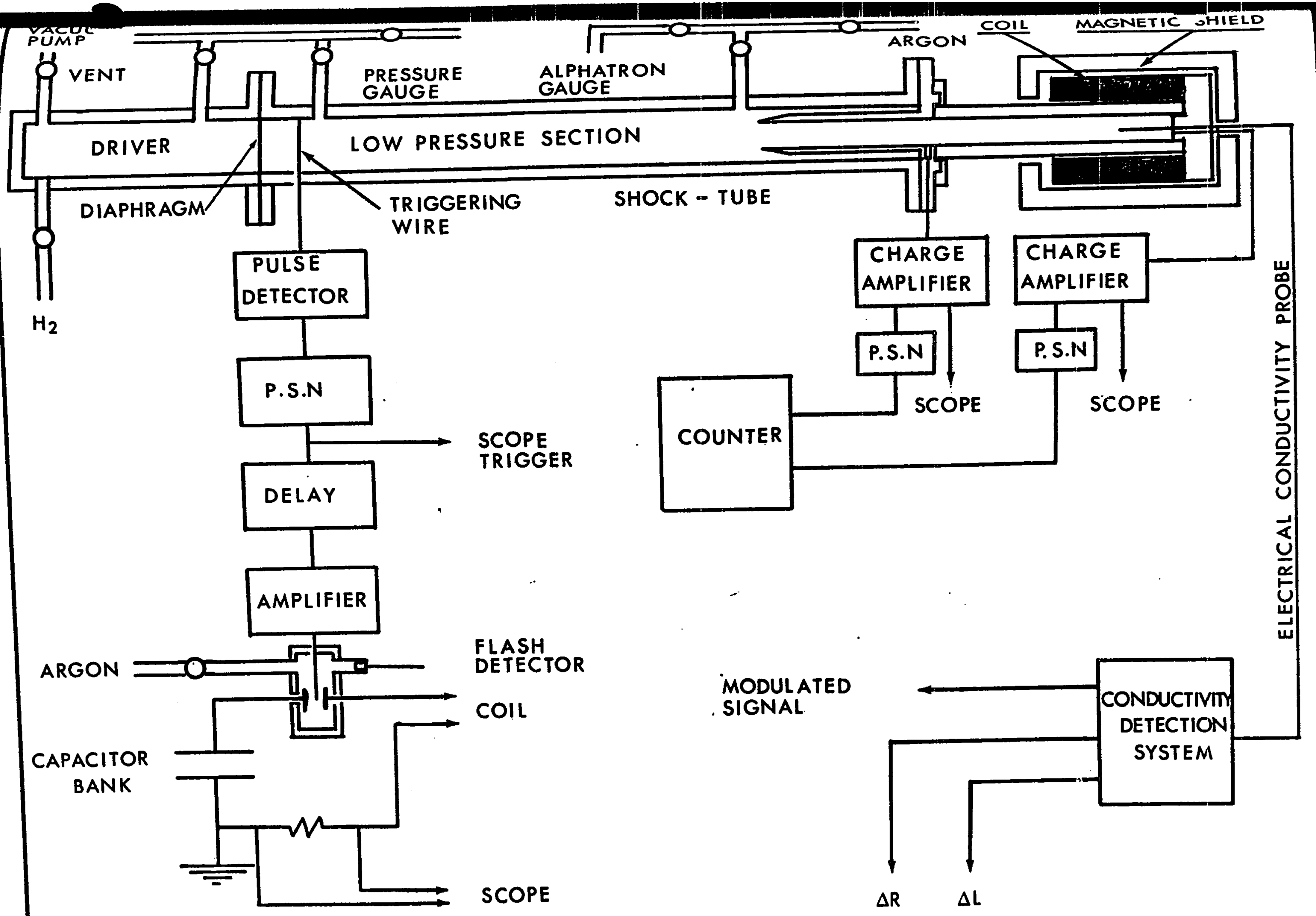

FIG.29 SCHEMATIC DIAGRAM OF THE EXPERIMENTAL APPARATUS.

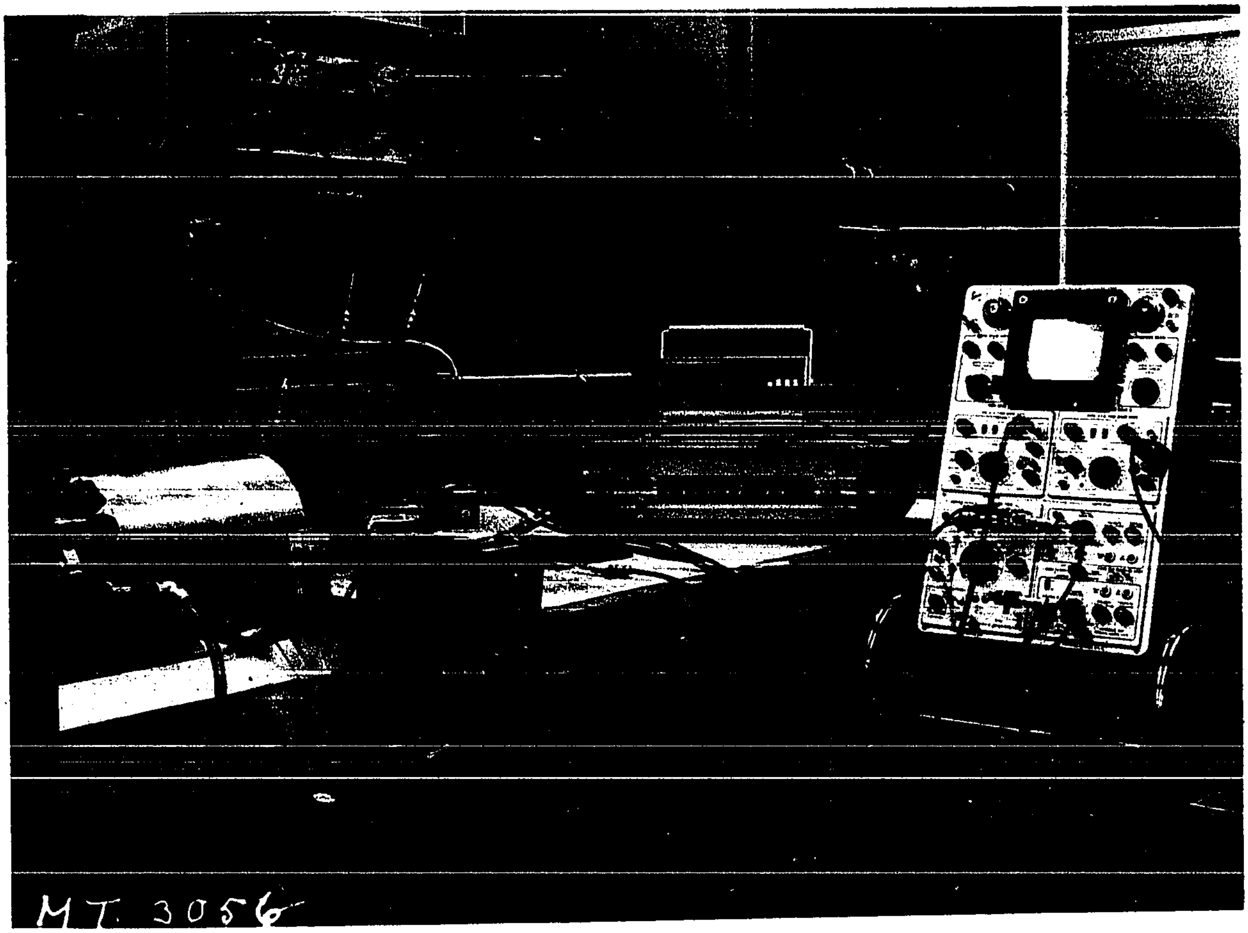

FIG.30 VIEW OF TEST SECTION AND EQUIPMENT.

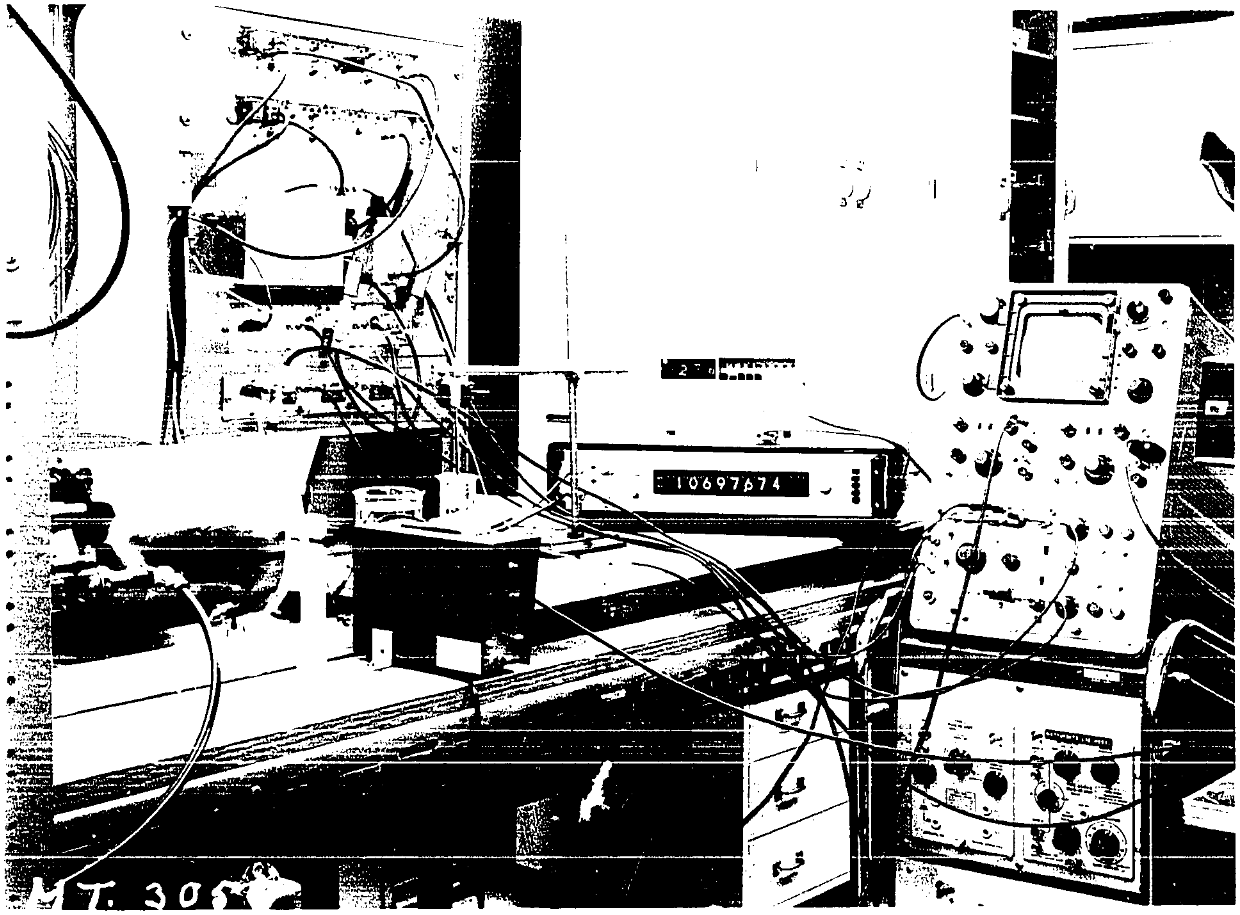

FIG.30 VIEW OF TEST SECTION AND EQUIPMENT.

FIG. 31 AXIAL AND RADIAL MAGNETIC FIELD DISTRIBUTION.

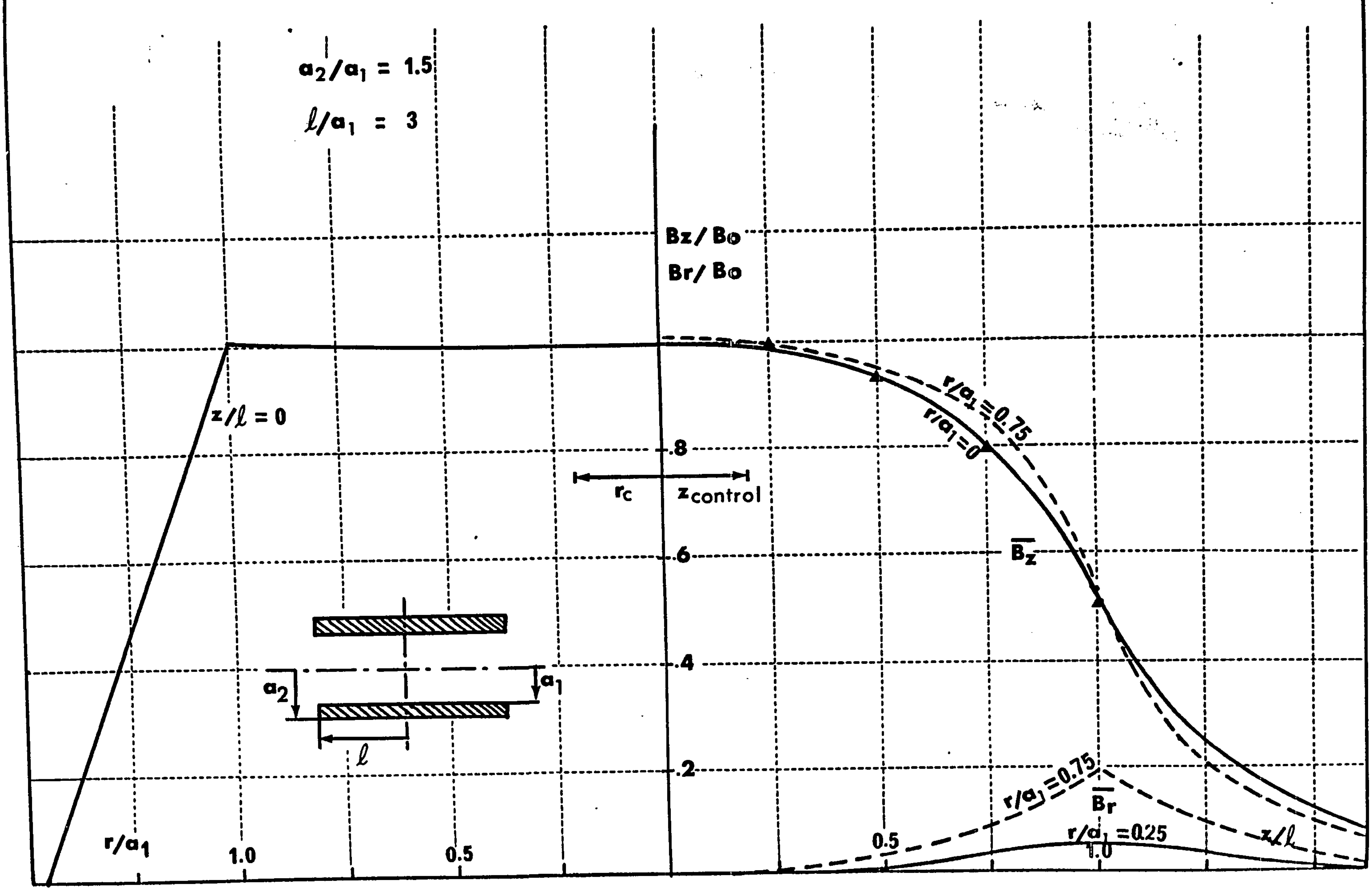

FIG. 32 CALIBRATION CURVES OF THE MAGNETIC FIELD AND CURRENT IN THE FIELD COIL.

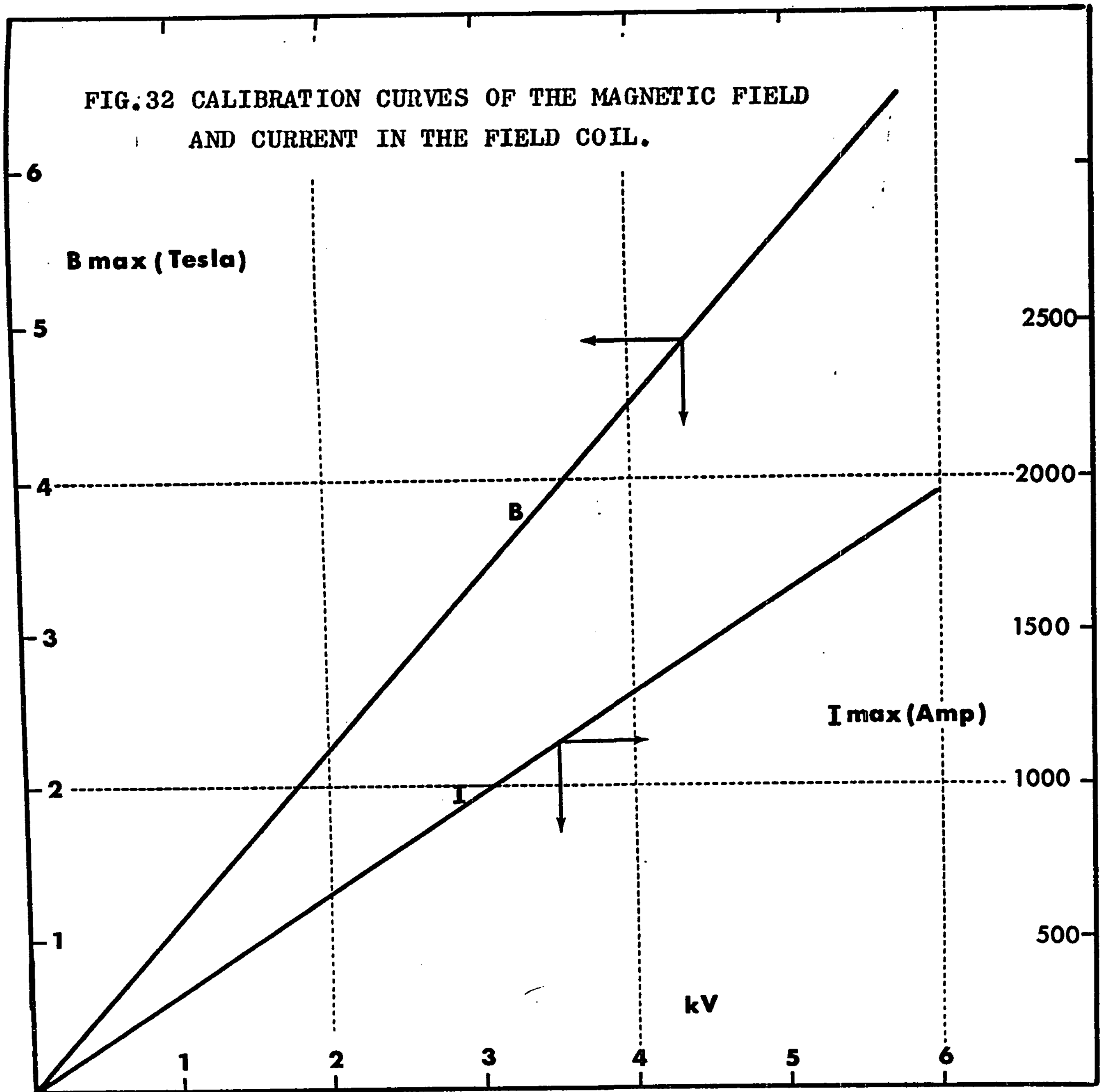

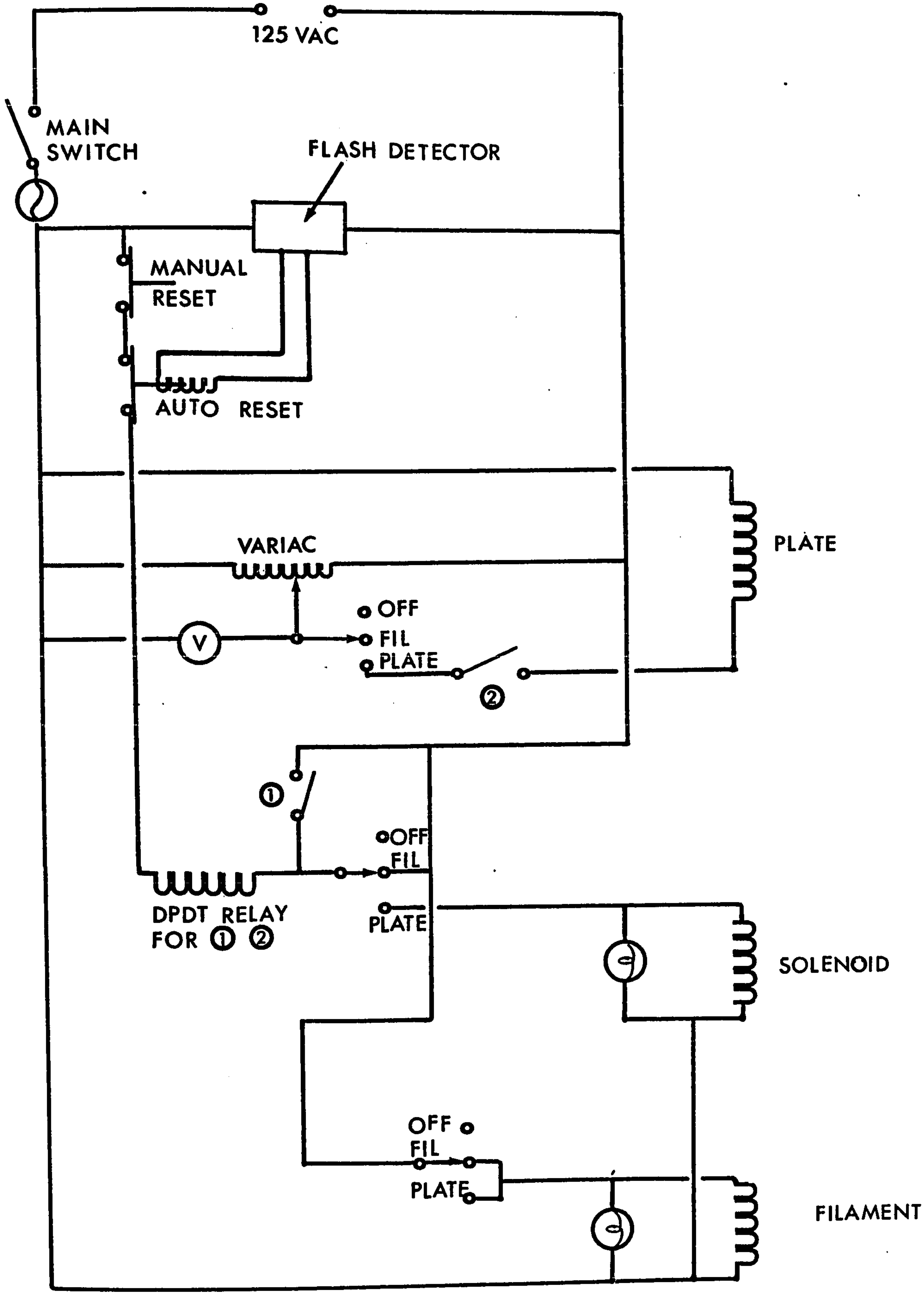

FIG.33 LAYOUT OF THE POWER SUPPLY.

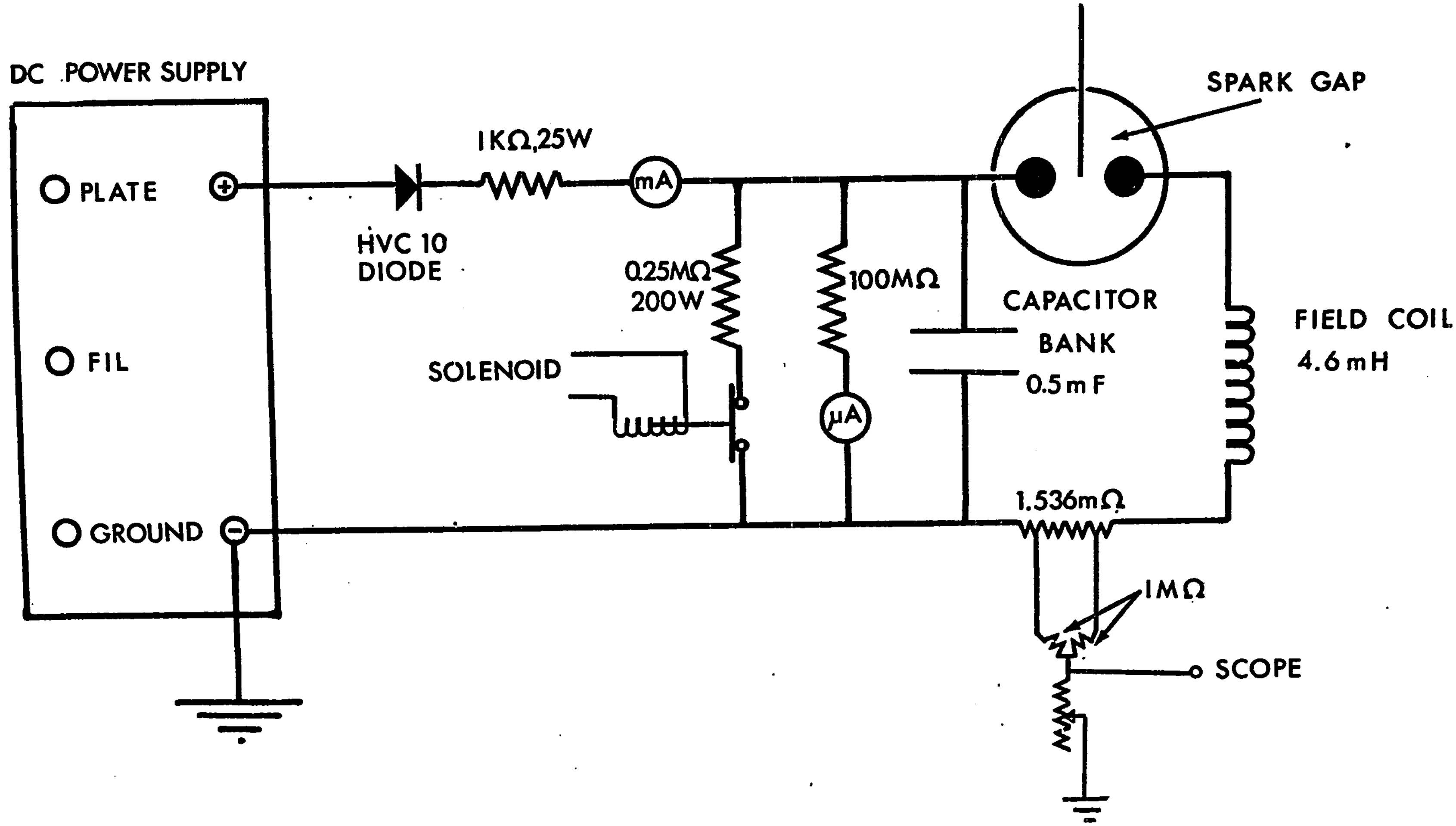

FIG.34 DIAGRAM OF THE DISCHARGE CIRCUIT AND CONTROLS.

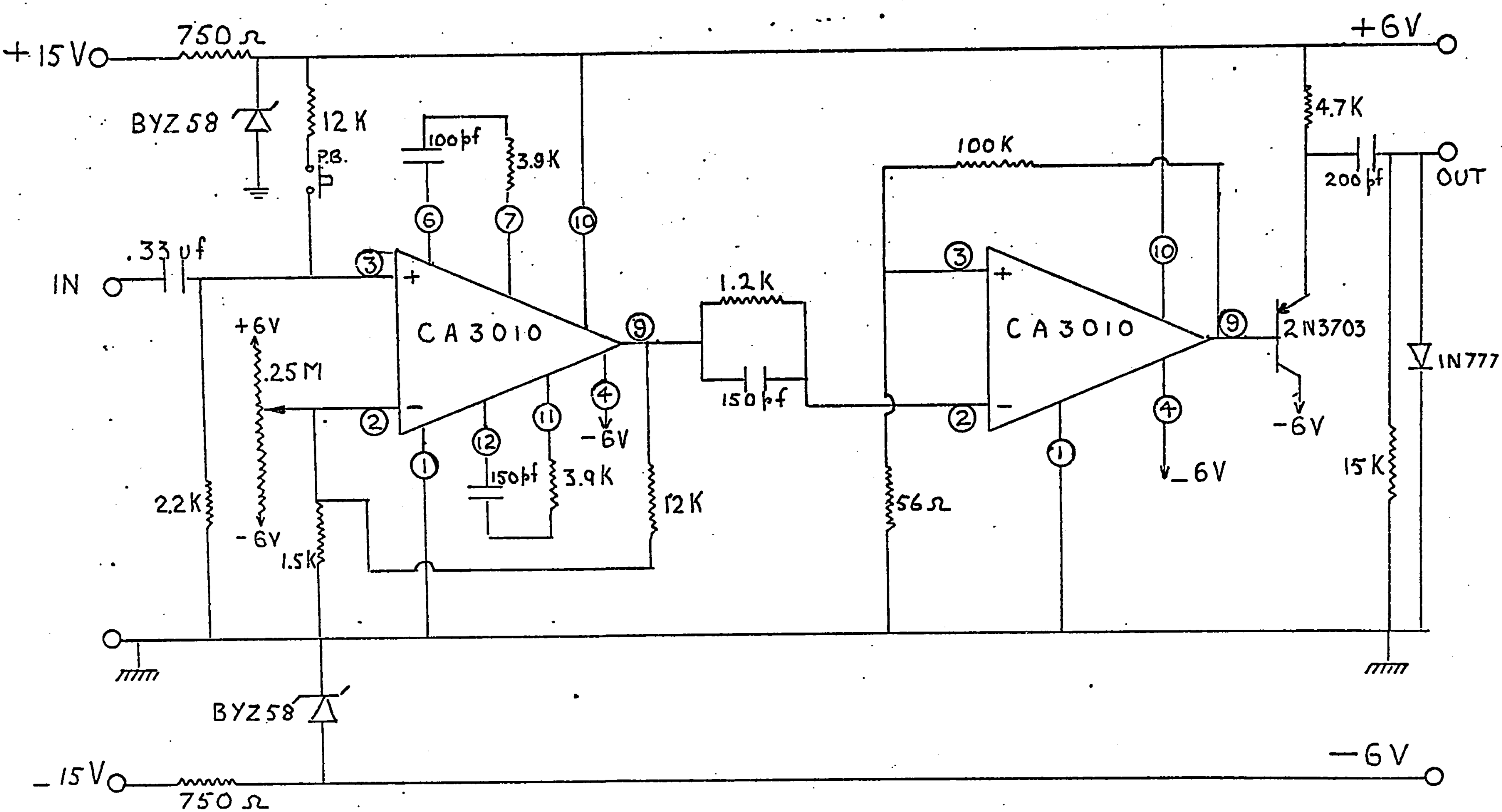

FIG.35 CIRCUIT DIAGRAM OF A PULSE SHAPING NETWORK.

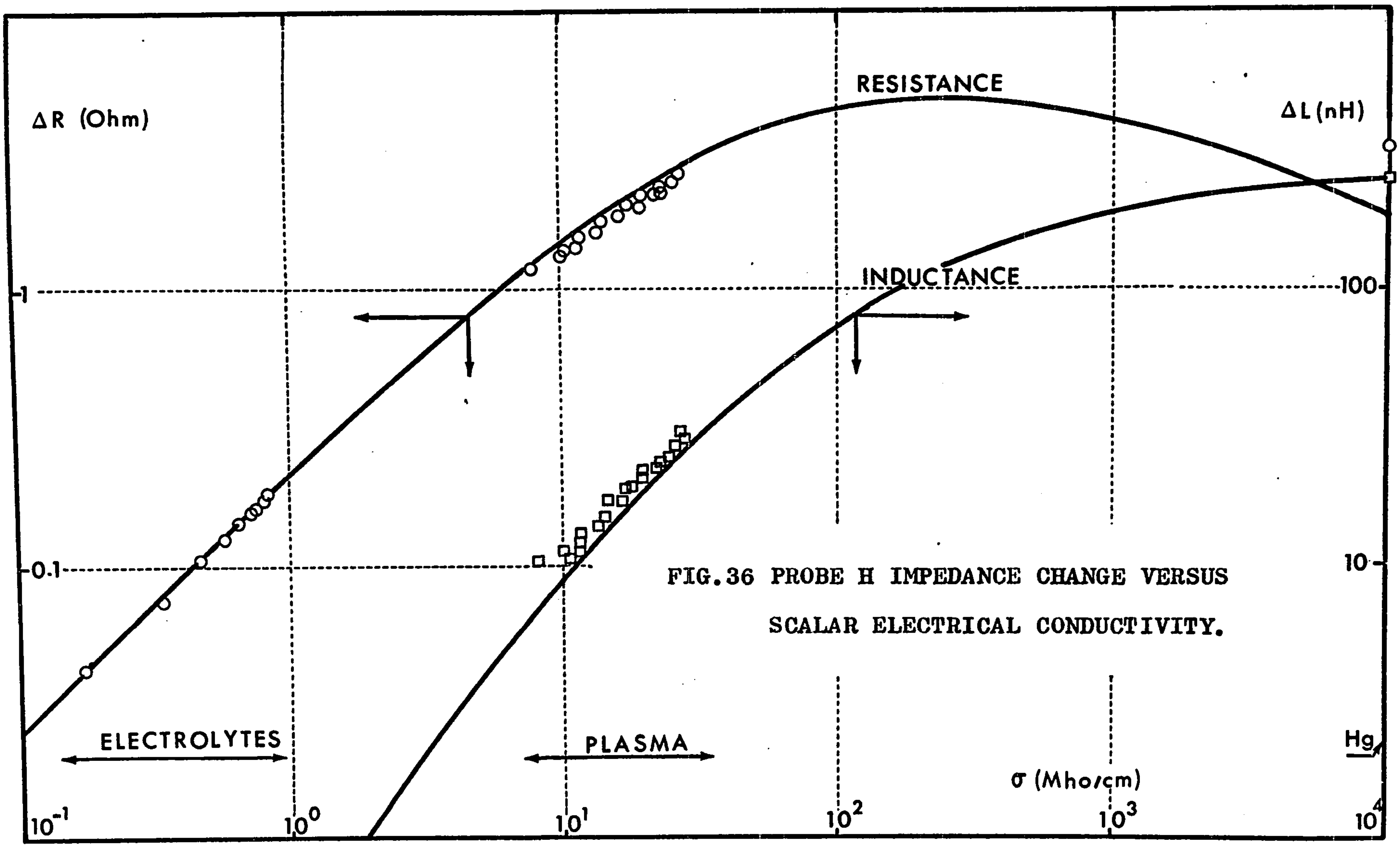

FIG. 36 PROBE H IMPEDANCE CHANGE VERSUS SCALAR ELECTRICAL CONDUCTIVITY.

FIG. 37 EXPERIMENTAL DATA FOR ELECTROLYTIC SOLUTIONS COMPARED WITH THEORY.

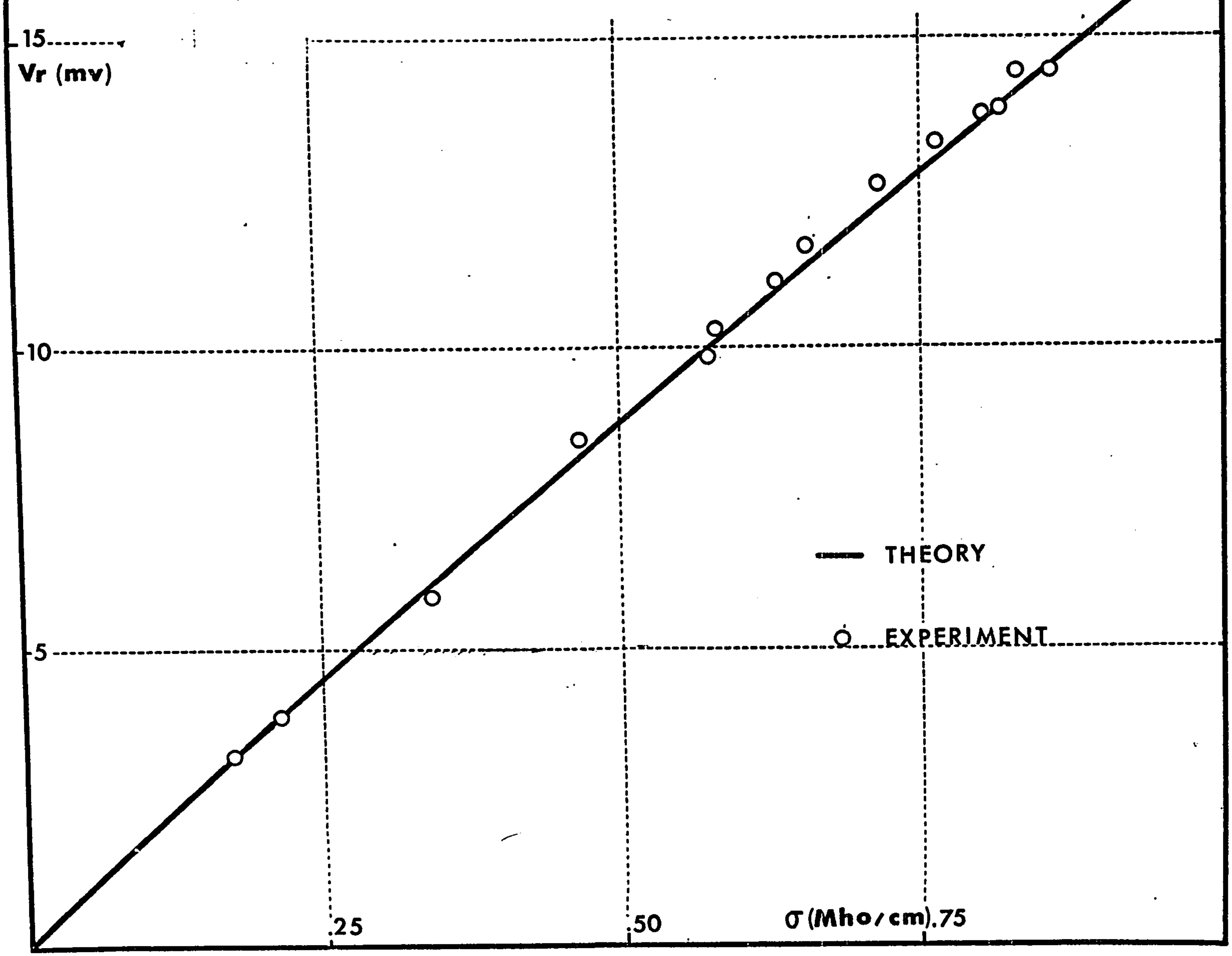

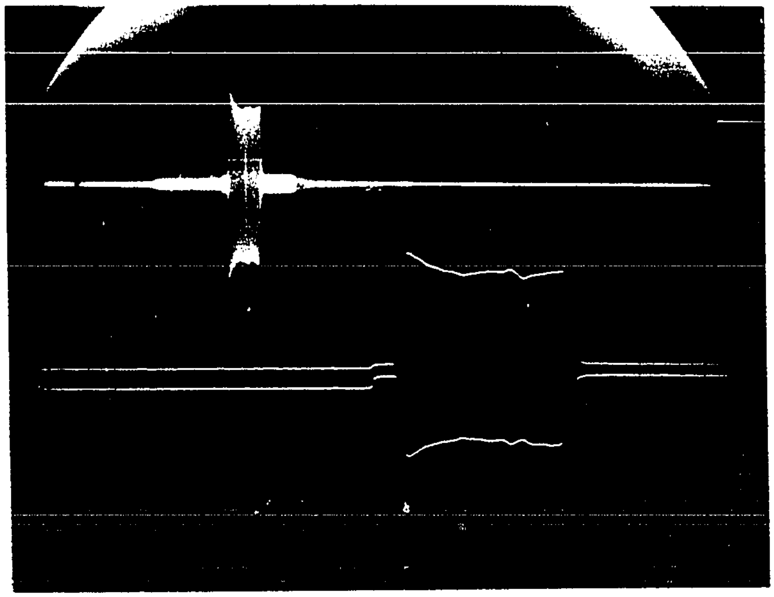

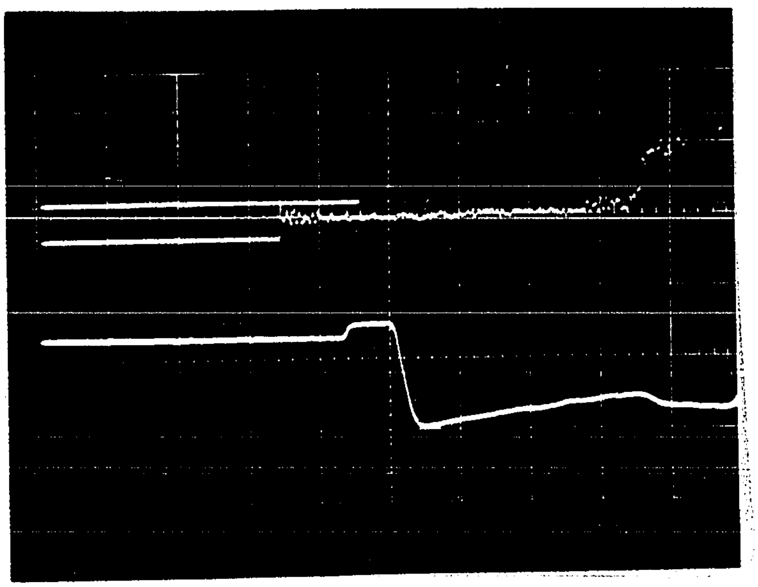

FIG.38 OSCILLOSCOPE RECORDS FOR AN ISOTROPIC PLASMA.

EXPERIMENT 155,RUN 6 : P_1=5 Torr,M_{si}= 7.7

Trace 1 : Conductivity modulated carrier.
10 mv/cm, 1 msec/cm.

Trace 2 : R : 100 mv/cm, 200 μsec/cm.

Trace 3 : L : 100 mv/cm, 200 μsec/cm.

Trace 4 : Pressure record at end plate of shock tube.

Trace 5 : Pressure record ahead of the test section.

Trace 6 : L : 100 mv/cm, 100 μsec/cm.

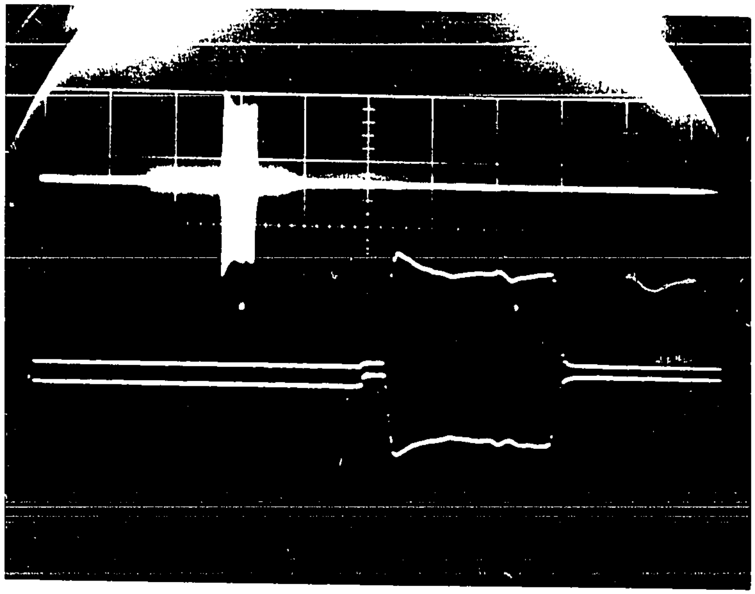

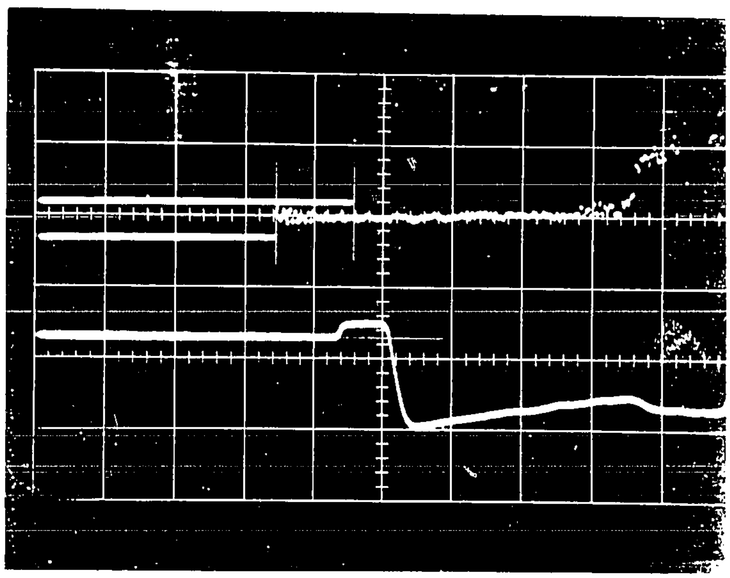

FIG.38 OSCILLOSCOPE RECORDS FOR AN ISOTROPIC PLASMA.

EXPERIMENT 155, RUN 6 : P_1=5 Torr, M_{si}= 7.7

Trace 1 : Conductivity modulated carrier.

10 mv/cm, 1 msec/cm.

Trace 2 : R : 100 mv/cm, 200 μsec/cm.

Trace 3 : L : 100 mv/cm, 200 μsec/cm.

Trace 4 : Pressure record at end plate of shock tube.

Trace 5 : Pressure record ahead of the test section.

Trace 6 : L : 100 mv/cm, 100 μsec/cm.

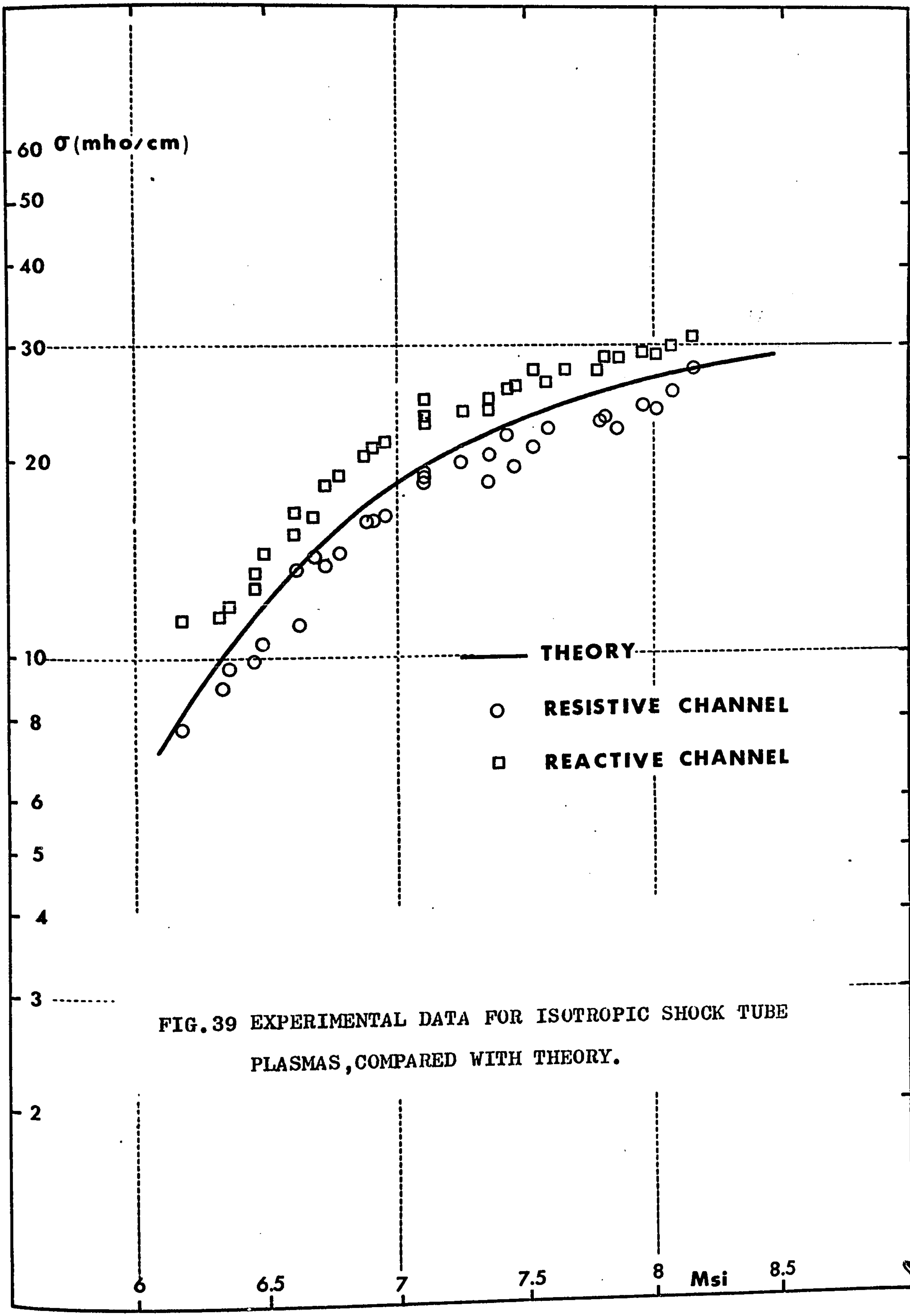

FIG. 39 EXPERIMENTAL DATA FOR ISOTROPIC SHOCK TUBE PLASMAS, COMPARED WITH THEORY.

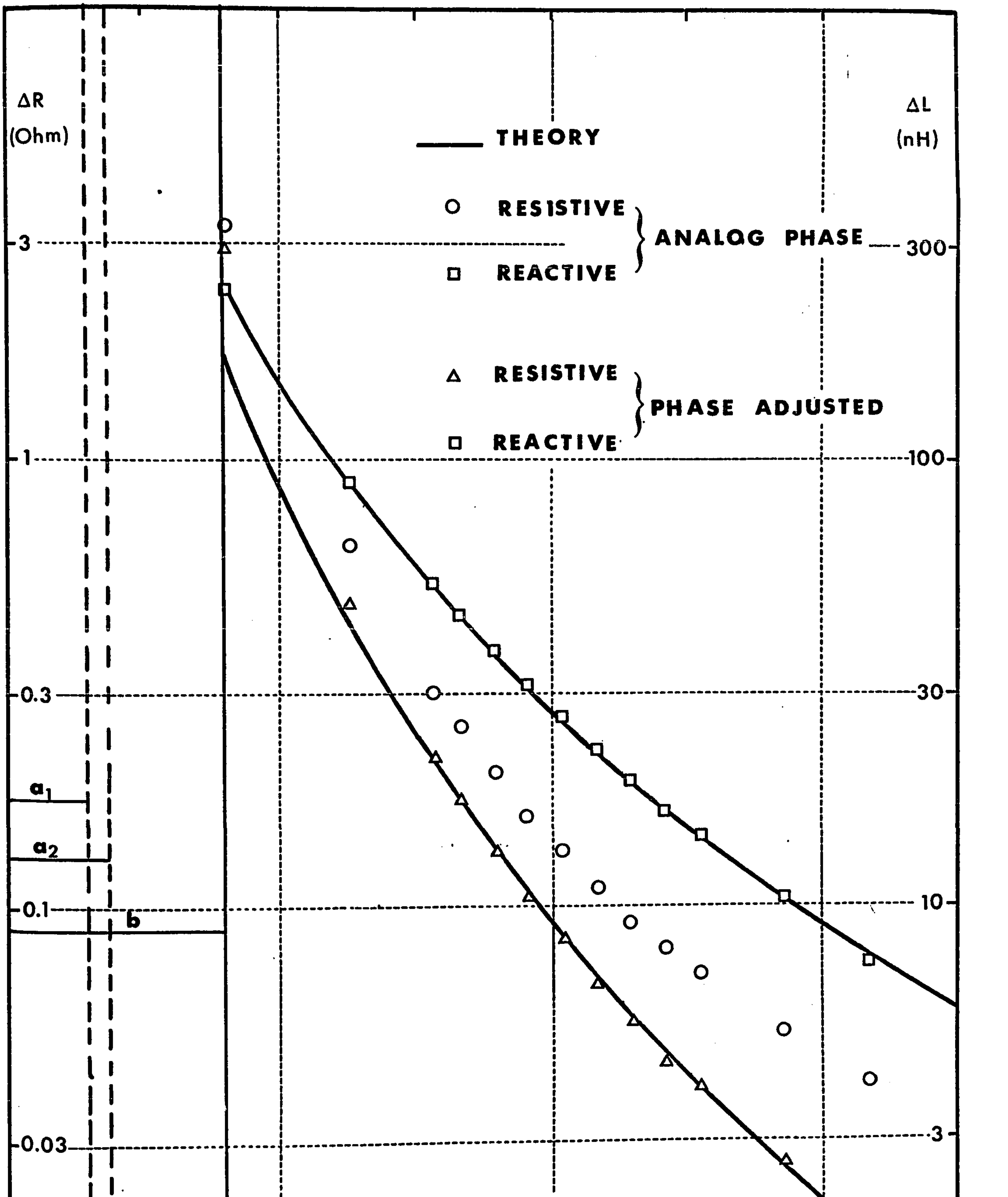

FIG. 40 EXPERIMENTAL DATA FOR MERCURY, COMPARED WITH THEORY.

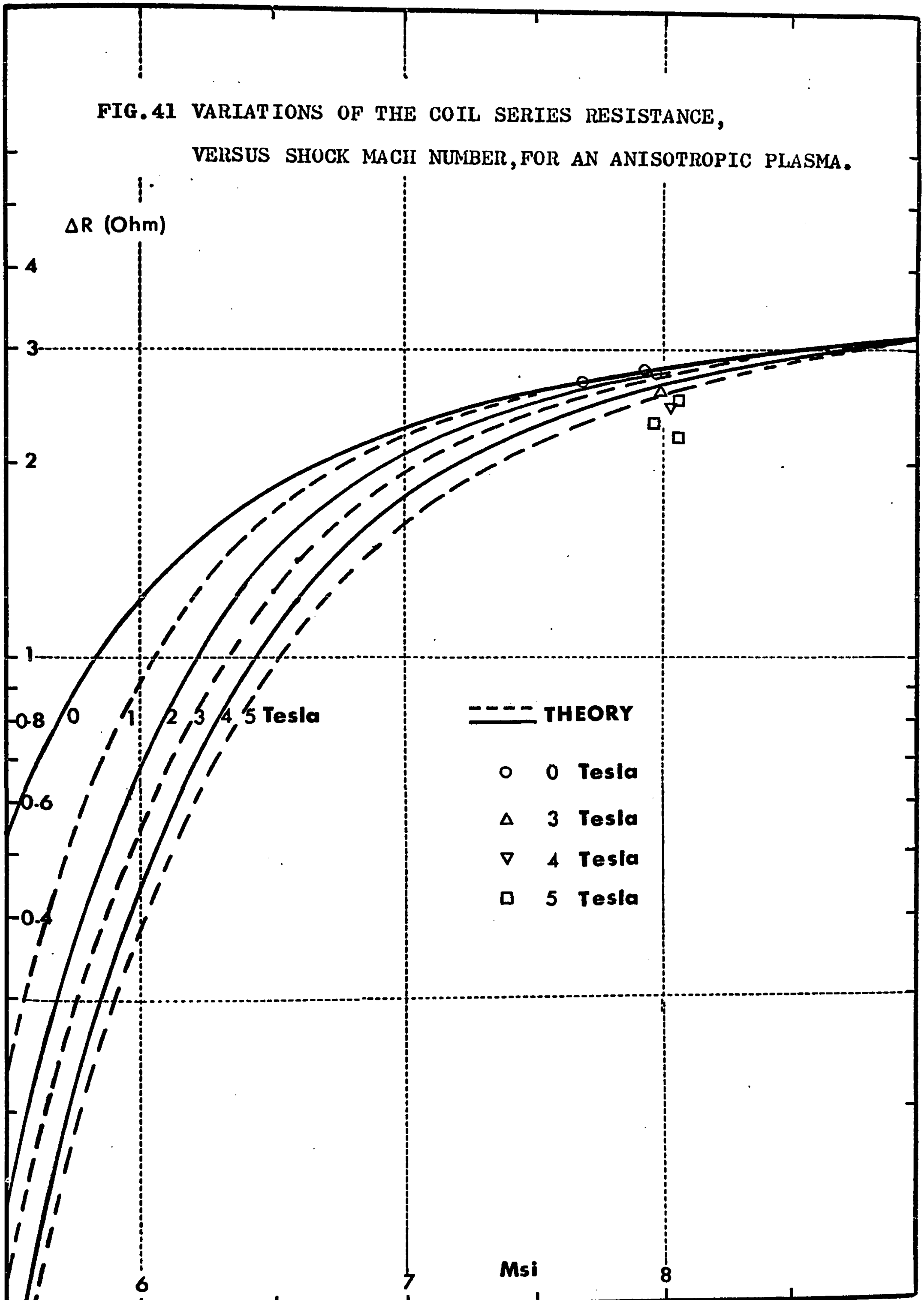

FIG. 41 VARIATIONS OF THE COIL SERIES RESISTANCE, VERSUS SHOCK MACH NUMBER, FOR AN ANISOTROPIC PLASMA.

FIG. 42 VARIATIONS OF THE COIL SERIES INDUCTANCE, VERSUS SHOCK MACH NUMBER, FOR AN ANISOTROPIC PLASMA.

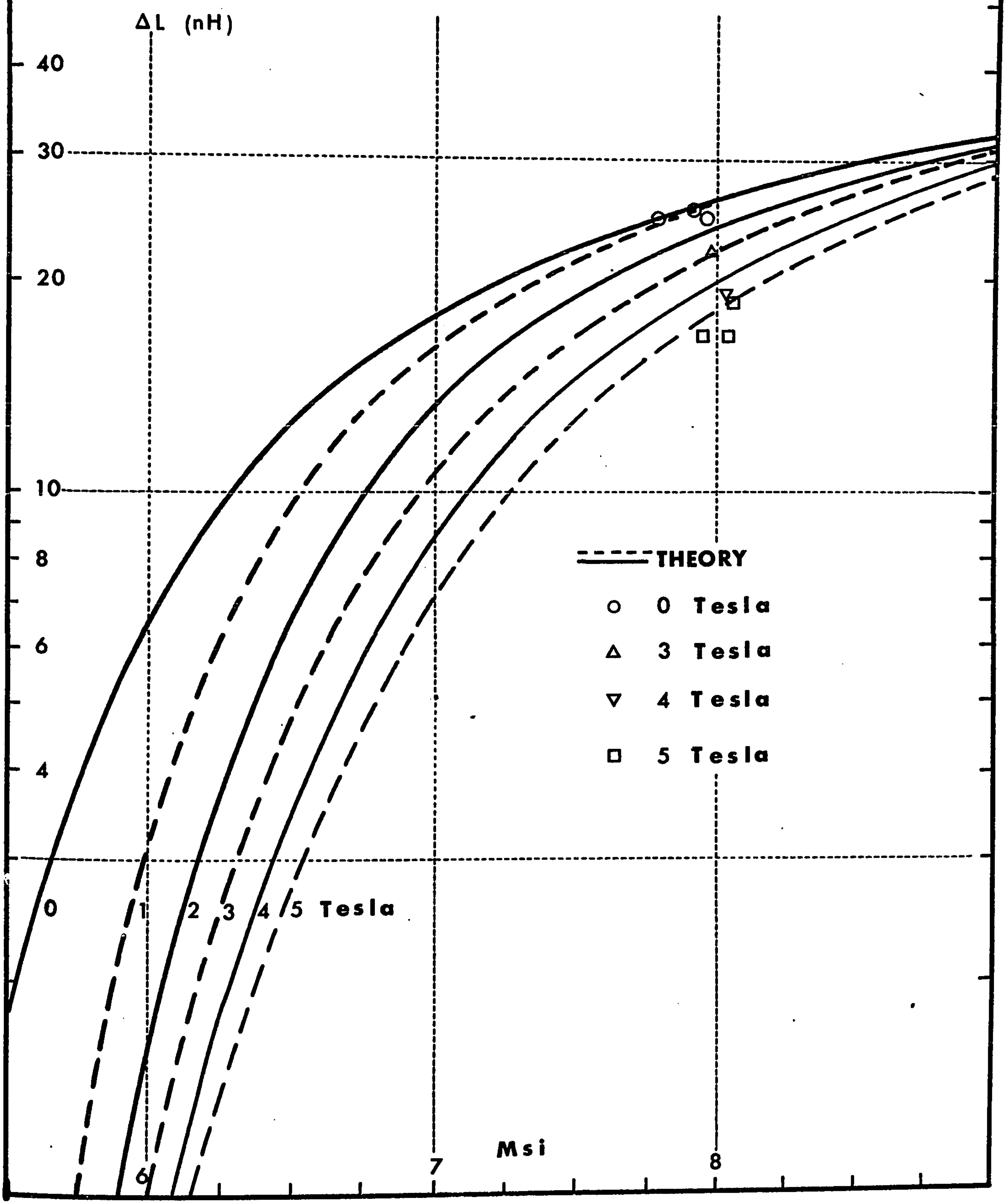

FIG.43 RELATIONSHIP BETWEEN HALL PARAMETER AND SHOCK MACH NUMBER,AT VARIOUS INITIAL PRESSURES.

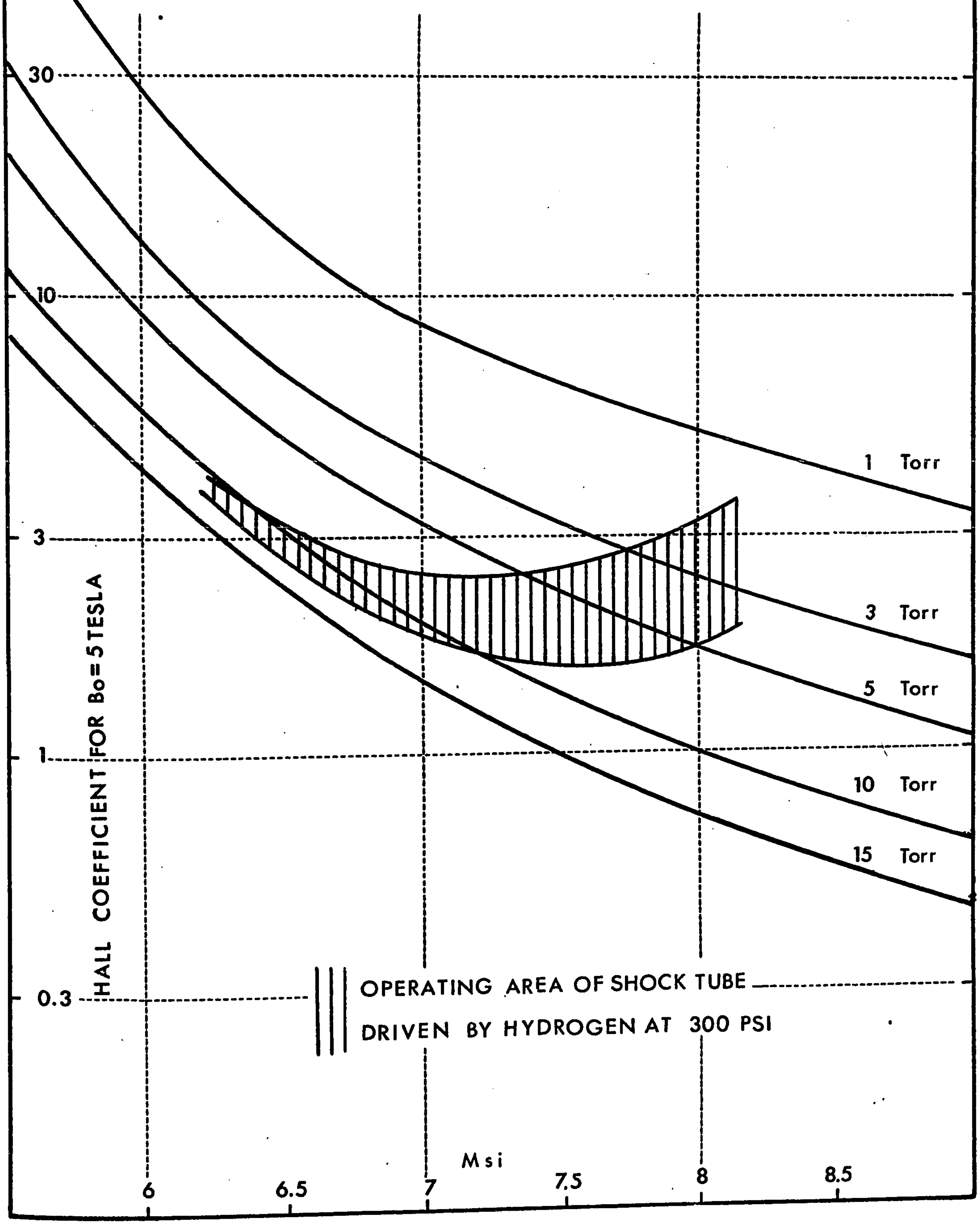

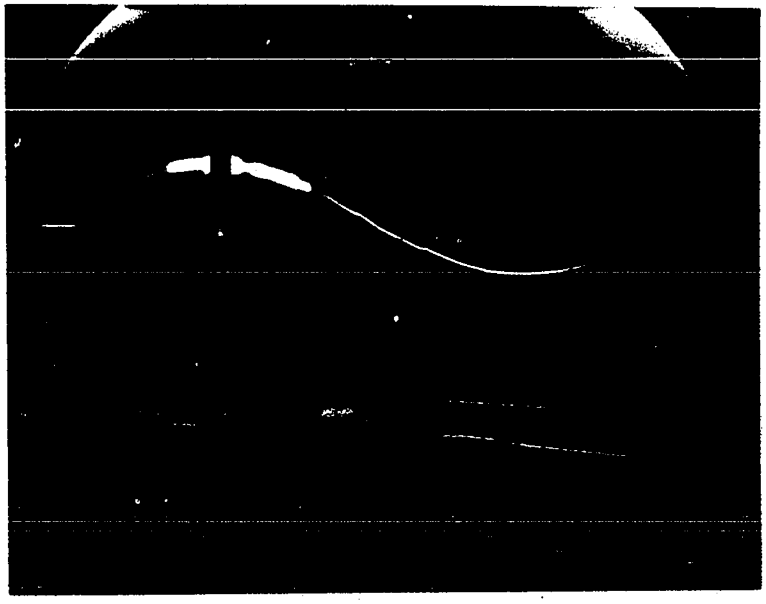

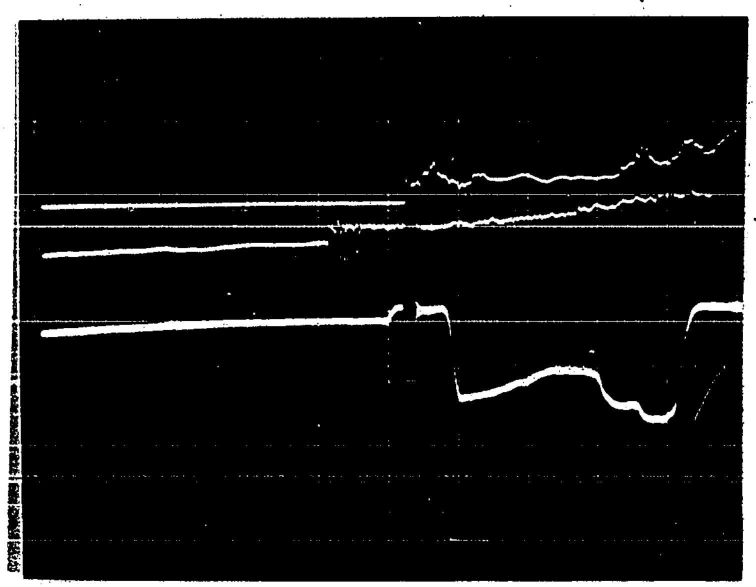

FIG.44 OSCILLOSCOPE RECORDS FOR AN ANISOTROPIC PLASMA.

EXPERIMENT 156, RUN 4 :P_1 = 3Torr,M_{si}=8.05,B_0=5 Tesla.

Trace 1 : Conductivity modulated carrier,added to the discharge current through the field coil. 10 mv/cm,1 msec/cm.

Trace 2 : R : 100 mv/cm, 200 μsec/cm.

Trace 3 : L : 100 mv/cm, 200 μsec/cm.

Trace 4 : Pressure record at end plate of shock tube.

Trace 5 : Pressure record ahead of the test section.

Trace 6 : L : 100 mv/cm, 100 μsec/cm.

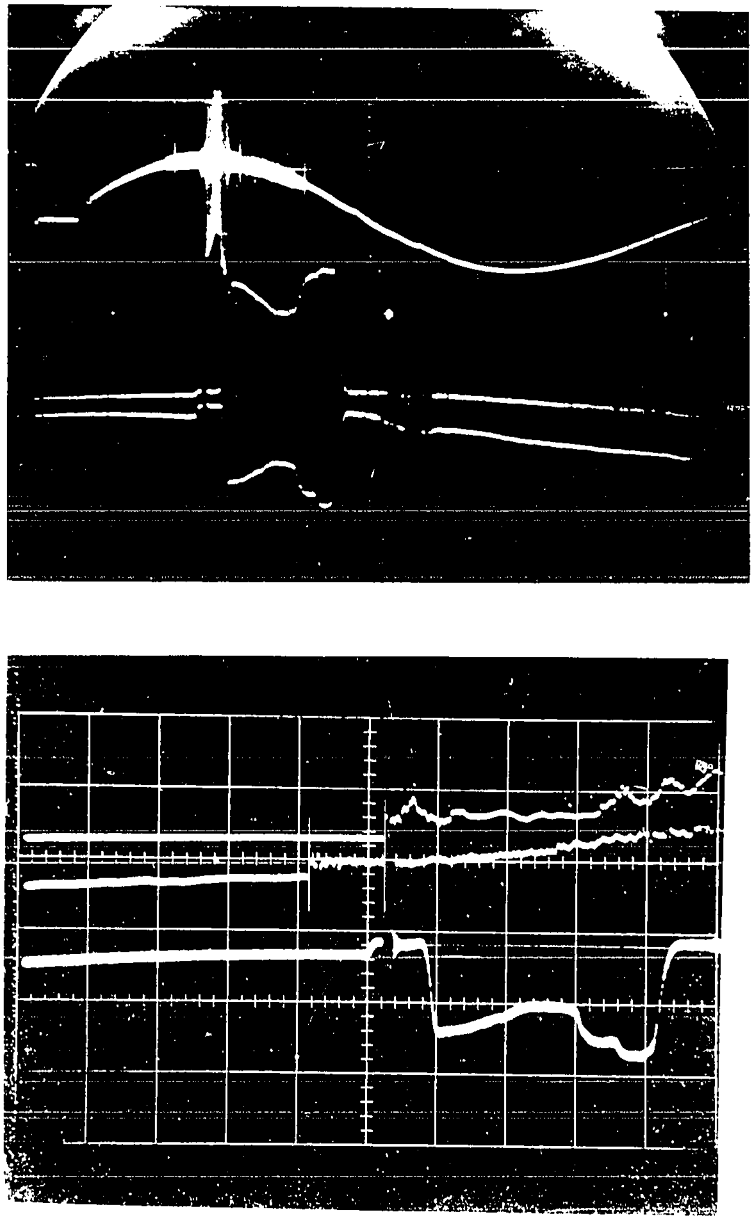

FIG. 44 OSCILLOSCOPE RECORDS FOR AN ANISOTROPIC PLASMA.

EXPERIMENT 156, RUN 4 : P_1 = 3Torr, M_{si}=8.05, B_0=5 Tesla.

Trace 1 : Conductivity modulated carrier, added to the discharge current through the field coil. 10 mv/cm, 1 msec/cm.

Trace 2 : E : 100 mv/cm, 200 μsec/cm.

Trace 3 : j : 100 mv/cm, 200 μsec/cm.

Trace 4 : Pressure record at end plate of shock tube.

Trace 5 : Pressure record ahead of the test section.

Trace 6 : [illegible] 100 mv/cm, 100 μsec/cm.

FIG.45 RECORDED CONDUCTIVITY HISTORY FOR A SHOCK TUBE PLASMA, COMPARED WITH ESTIMATED PROBE RESPONSE.

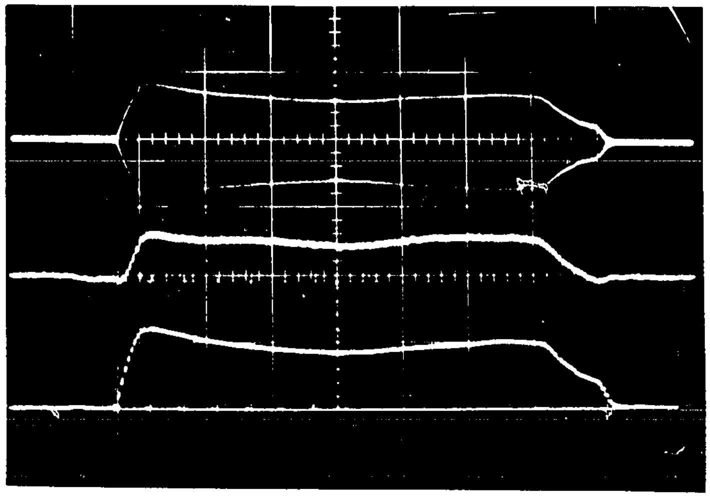

EXP. 122, RUN 15: P_1=15 Torr, M_s=7.03, σ_0=1800 mho/m. PROBE D.

Upper trace: Modulated carrier, 100 μsec/cm

Middle trace: ΔL : 200 mv/cm, 7.8 mv/nH, 100 μsec/cm.

Lower trace: ΔR : 200 mv/cm, 117 mv/Ohm, 100 μsec/cm.

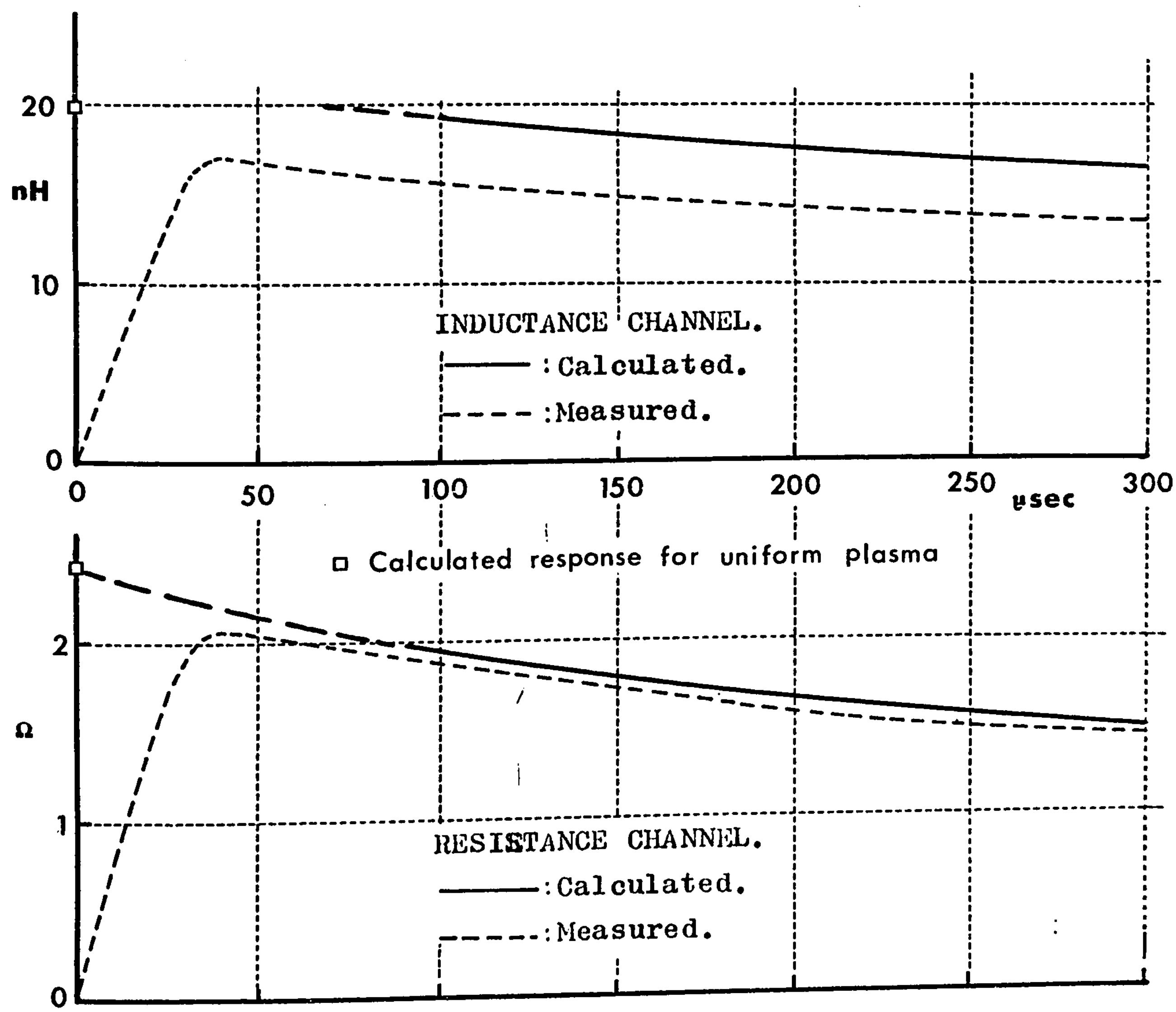

FIG.45 RECORDED CONDUCTIVITY HISTORY FOR A SHOCK TUBE PLASMA,COMPARED WITH ESTIMATED PROBE RESPONSE.

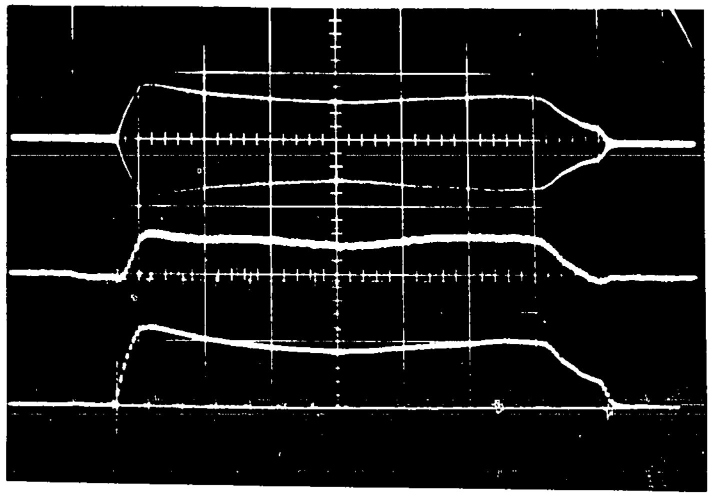

EXP. 122,RUN 15: P_1=15 Torr,M_s=7.03, σ_0=1800 mho/m. PROBE D.
Upper trace:Modulated carrier,100 μsec/cm
Middle trace: Δ L :200 mv/cm,7.8 mv/nH,100 μsec/cm.
Lower trace: Δ R :200 mv/cm,117 mv/Ohm,100 μsec/cm.

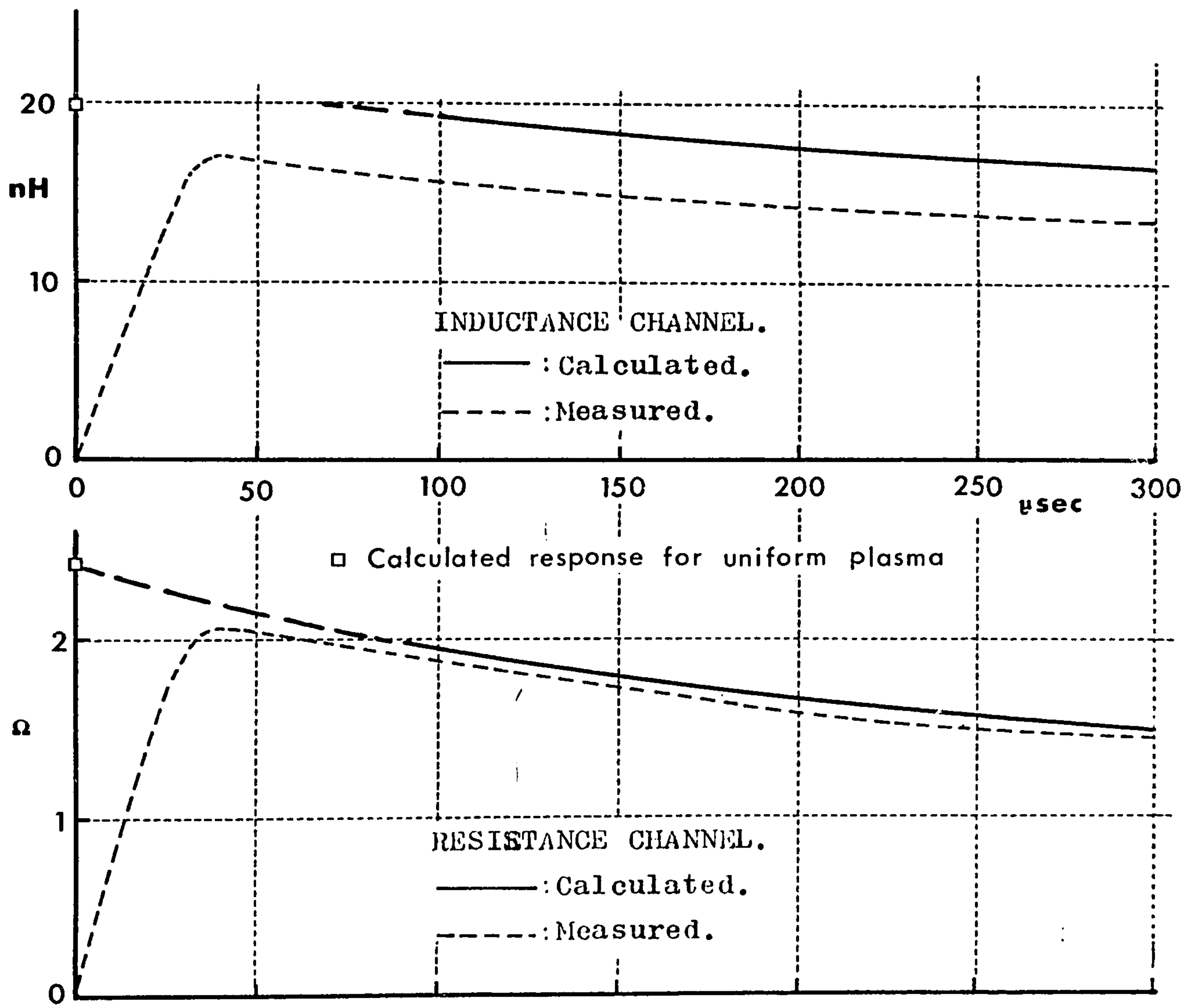

TABLE I: Aerothermodynamic properties for argon plasma

	P2/P1 P5/P1	RHO2/RHO1 RHO5/RHO1	T2/T1 T5/T1	ALPHA2 ALPHA5	P2(ATM) P5(ATM)	RHO2(GR/CC) RHO5(GR/CC)	T2(K) T5(K)
		NE(#/M**3)	NN(#/M**3)		<NUEI>	<NUEN>	<NUG>
		<NUEN>/<NUEI>	PLASMAFREQ		DEBYE LENGTH		

P1 =10.00 TORR T1 =300.0 K

MS = 9.00	101.40	3.90	25.96	0.969D-03	0.133D+01	0.833D-04	0.779D+04
	526.89	12.37	40.55	0.505D-01	0.693D+01	0.264D-03	0.122D+05
		0.201D+24	0.378D+25		0.197D+13	0.290D+12	0.226D+13
		0.147D+00	0.403D+13		0.170D-07		
MS = 8.50	90.16	3.85	23.39	0.248D-03	0.119D+01	0.823D-04	0.702D+04
	470.72	11.62	39.02	0.380D-01	0.619D+01	0.248D-03	0.117D+05
		0.142D+24	0.360D+25		0.152D+13	0.255D+12	0.178D+13
		0.167D+00	0.339D+13		0.198D-07		
MS = 8.00	79.77	3.82	20.86	0.470D-04	0.105D+01	0.816D-04	0.626D+04
	421.12	10.97	37.37	0.270D-01	0.554D+01	0.234D-03	0.112D+05
		0.953D+23	0.344D+25		0.113D+13	0.222D+12	0.135D+13
		0.197D+00	0.277D+13		0.237D-07		
MS = 7.50	70.07	3.80	18.45	0.636D-05	0.922D+00	0.811D-04	0.553D+04
	374.84	10.38	35.50	0.174D-01	0.493D+01	0.222D-03	0.107D+05
		0.583D+23	0.328D+25		0.778D+12	0.190D+12	0.967D+12
		0.244D+00	0.217D+13		0.295D-07		
MS = 7.00	61.00	3.77	16.18	0.573D-06	0.803D+00	0.805D-04	0.486D+04
	330.43	9.83	33.28	0.967D-02	0.435D+01	0.210D-03	0.998D+04
		0.306D+23	0.314D+25		0.475D+12	0.158D+12	0.633D+12
		0.332D+00	0.157D+13		0.394D-07		
MS = 6.50	52.56	3.73	14.07	0.308D-07	0.692D+00	0.797D-04	0.422D+04
	287.08	9.37	30.52	0.407D-02	0.378D+01	0.200D-03	0.916D+04
		0.123D+23	0.300D+25		0.234D+12	0.126D+12	0.359D+12
		0.538D+00	0.995D+12		0.596D-07		
MS = 6.00	44.75	3.69	12.12	0.843D-09	0.589D+00	0.788D-04	0.364D+04
	244.25	9.01	27.06	0.106D-02	0.321D+01	0.192D-03	0.812D+04
		0.308D+22	0.290D+25		0.779D+11	0.938D+11	0.172D+12
		0.120D+01	0.498D+12		0.112D-06		
MS = 5.50	37.56	3.64	10.32	0.942D-11	0.494D+00	0.777D-04	0.310D+04
	202.61	8.76	23.12	0.140D-03	0.267D+01	0.187D-03	0.694D+04
		0.395D+21	0.282D+25		0.146D+11	0.651D+11	0.798D+11
		0.445D+01	0.179D+12		0.289D-06		

TABLE II: Non-dimensional profile coefficients and fictitious probe radius versus time (fig. 15)

Time (μsec)	Radius b' (cm)	$A^*(t)$	$B^*(t)$	$C^*(t)$
0	0.157	1.00	0.00	0.00
25	0.164	0.80	2.95	-4.00
50	0.172	0.87	2.51	-3.88
100	0.181	0.94	1.78	-3.48
150	0.188	0.97	1.35	-3.28
200	0.191	1.01	0.66	-2.63
300	0.197	1.04	-0.01	-2.10

TABLE III: Experimental results for an anisotropic plasma

Exp	p_1 Torr	M_{si}	σ_{33} mho/m	B_o Tesla	Hall par.	ΔR_m Ohm	ΔR_i Ohm	ΔR_o Ohm	ΔL_m nH	ΔL_i nH	ΔL_o nH
156-1	3	7.97	2670	0	0	2.69	2.78	2.78	24.4	25.7	25.7
156-2	3	8.03	2720	4	2.0	2.46	2.67	2.81	19.4	20.4	26.2
156-3	3	8.05	2740	5	2.4	2.21	2.60	2.82	16.8	18.7	26.3
156-4	3	8.05	2740	5	2.4	2.54	2.60	2.82	18.9	18.7	26.3
156-5	3	7.95	2660	5	2.5	2.30	2.53	2.78	16.8	17.7	25.7
156-6	3	7.92	2650	0	0	2.80	2.75	2.75	25.3	25.2	25.2
156-7	3	7.98	2680	3	1.5	2.54	2.72	2.78	22.3	22.0	26.0
156-8	3	7.78	2530	0	0	2.69	2.70	2.70	24.4	24.3	24.3
155-1	5	7.53	2380	0	0	2.66	2.52	2.52	23.3	22.6	22.6
155-2	5	7.51	2350	4	1.9	2.48	2.45	2.52	20.4	19.0	22.5
155-3	5	7.51	2350	0	0	2.55	2.52	2.52	23.6	22.5	22.5
155-4	5	7.42	2250	5	2.3	2.40	2.22	2.47	17.3	15	21.6
155-6	5	7.70	2530	0	0	2.56	2.61	2.61	22.4	24.0	24.0
155-7	5	7.55	2400	4	1.8	2.36	2.35	2.55	18.5	18.3	22.7
155-8	5	7.43	2280	5	2.3	2.15	2.25	2.47	17.8	15.2	21.7
155-9	5	7.65	2500	5	2.0	2.44	2.43	2.60	19.6	18.0	23.5
155-10	5	7.45	2300	4	1.85	2.40	2.34	2.50	18.6	17	21.9

TABLE IV: Experimental results for an isotropic plasma including corrections for boundary layer cooling

No.	p_1 Torr	M_s	σ_o mho/cm	ΔR_{meas} Ohm	ΔR_{corr} Ohm	σ_R mho/cm	ΔL_{meas} nH	ΔL_{corr} nH	σ_L mho/cm
1	5	7.52	23.7	2.33	2.84	29.5	25.9	27.2	29.5
3	3	8.00	27.0	2.53	2.98	33.0	27.2	28.3	31.0
4	2	7.95	26.7	2.55	3.00	33.0	27.4	28.6	31.0
5	3.5	8.06	28	2.62	2.98	33.0	29.0	29.9	33.0
6	4.5	7.8	25.7	2.50	2.90	31.0	27.9	29.0	31.0
8	6.5	7.36	22.2	2.18	2.60	25.0	22.8	23.7	25.5
9	7.5	7.36	22.2	2.30	2.71	27.0	23.5	24.5	26.5
11	8.5	7.10	19.5	2.26	2.66	26.0	23.3	24.3	26.0
12	9	6.95	17.8	2.02	2.50	23.5	19.8	20.8	22.5
13	9.5	7.08	19.4	1.99	2.6	25.0	21.4	22.5	24.5
14	10	6.87	17.0	2.00	2.47	22.5	19.1	20.1	21.5
15	10.5	6.9	17.2	2.00	2.50	23.5	19.6	20.8	22.5
16	12	6.78	16.7	1.88	2.36	21.0	17.7	19.1	20.5
19	12	6.61	13.6	1.81	2.06	17.0	14.3	14.7	16.0
24	8	7.1	19.5	2.20	2.59	25.0	21.9	22.8	24.5
25	7	7.42	22.7	2.40	2.79	28.5	24.3	25.0	27.0
26	7.5	7.15	20.0	2.28	2.73	27.5	22.6	23.8	26.0
27	7.25	7.25	21.0	2.28	2.68	27.0	22.6	23.6	25.5
28	5.0	7.58	24.0	2.44	2.84	29.5	24.6	25.5	27.5
29	4.5	7.78	25.5	2.47	2.90	31.0	25.5	27.6	30.0
32	12.5	6.72	14.9	1.80	2.34	21.0	17.2	18.5	20.0
36	4.5	7.45	23.0	2.25	2.78	28.5	24.6	25.9	29.0

COMPUTER PROGRAM LISTING

```
C  PROGRAM TO EVALUATE THE RESPONSE OF A DOUBLE LAYER IMMERSED PLASMA
C  CONDUCTIVITY PROBE.
C  INPUT DATA:- PROBE DIMENSION
C             - RANGE PARAMETERS,FOR CONTROL OVER THE PROPER PARAMETERS
C  IN A PARAMETRIC STUDY AND TO SELECT THE PROPER OPERATIONS.
C   FOR NONUNIFORM PLASMAS,THE PROFILE COEFFICIENTS,FOR A PROFILE OF
C   THE FORM SIGO/SIG=APN+BPN/(R**2)+CPN/(R**3) ,MUST BE READ IN.
C  OUTPUT DATA:-PROBE PARAMETERS.(H1,H2,W,S)
C              -RESISTANCE CHANGE(DELR),REACTANCE CHANGE(DELL).
C  THIS PROGRAM CALLS THE SUBROUTINES DBESI,DBESK,ALLHA FOR EVALUATING
C  RESPECTIVELY THE I(K) BESSEL FUNCTION,K(K) BESSEL FUNCTION AND THE
C  HANKEL FUNCTIONS FROM WHICH THE K(X) BESSEL FUNCTIONS WITH COMPLEX
C  ARGUMENTS ARE DERIVED.
C
C  SYSTEM OF UNITS : M,KGR,SEC.
      IMPLICIT REAL*8(A-H,O-Z)
      DIMENSION Y(400),BK0(400),BK1(400),BI0(400),BI1(400),
     1B(1000),SIG33(100),SIG11(100),SIG12(100),TRM2(400),
     2ENTA11(400),ENTA12(400),ENTA22(400),ENTB11(400),ENTB12(400),
     3ENTB22(400),BB(20),BC(20),CBC(20),TIME(20),APN(20),BPN(20),
     4CPN(20)
      COMPLEX*16 UC,QS1,QS2,QS3,QS4,ZC0,ZC1,ZC2,X0,X1,X2,TRM3(400),
     1BK00,BK01,BK02,BK10,BK11,BK12,EE,EE0,EE1,EE2,RA0,RA1,RA2,
     2PR0,PR1,PR2,BK0S,BK1S,PMU,EPS,G0C,G1C,UU,UU1,UU2
C  PROBE PARAMETERS.
C    PROBE D  EXPERIMENT 122,RUN 15.
C THERMAL EFFECTS ON PROBE RESPONSE AT:MS = 7.03,P1 = 15 TORR
C COIL RADII(A1,A2),LENGTH(DL),TURN DENSITY(DN1,DN2),PROBE RADIUS(BBP)
      A1 = 0.585D-03
      A2 = 0.735D-03
      DL = 0.756D-02
      DN1 = 0.648D+04
      DN2 = 0.648D+04
      BBP = 0.161D-02
C    RANGE PARAMETERS.
C  N CONTROLS HALL PARAMETER.
C  L CONTROLS CONDUCTIVITY RANGE
C  I CONTROLS RANGE FOR FILLING FACTOR.
C  K CONTROLS THE EFFECTIVE PROBE RADIUS
C  J CONTROLS CONDUCTIVITY PROFILE.
      NMIN = 1
      NMAX = 1
      LMAX = 1
      IMAX = 1
      KMAX = 18
      JMAX = 13
      IF(JMAX.EQ.0)  GO TO 8
      READ(5)   JMAX,SIG3P,(J,TIME(J),CBC(J),APN(J),BPN(J),
     1CPN(J),J=1,JMAX)
  100 FORMAT(I4,D15.5/(I4,5D13.5))
      DO 7  J=1,JMAX
    7 BB(J) = CBC(J)
      KMAX = JMAX
```

```
 8    CONTINUE
C  STEPSIZE FOR INDEPENDANT VARIABLE X  : DD = 0.05
      DD = 0.500D-01
C NUMBER OF STEPS IN THE INTEGRATION: NOST = 350
      NOST = 350
      FO = 0.1069775D+08
      PERV = 8.854D-12
      D = 0.500D-15
      PI = 3.14159D+00
      PO2 = PI/2.0D00
      DMU = 4.0D+00*PI*1.0D-07
      OM = 2.0D00*PI*FO
      DISPL = DMU*OM*OM*BB(1)*BB(1)*PERV*0.60D+02
C  CALCULATION OF MODIFIED BESSEL FUNCTIONS WITH REAL ARGUMENTS.
      DO 1  M=1,NOST
      DM = M
      X = DD*(DM-3.0D+02)
      Y(M) = DEXP(X)
      CALL DBESK (Y(M),0,BK,B,IER)
      BKO(M) = BK
      CALL DBESK (Y(M),1,BK,B,IER)
      BK1(M) = BK
      CALL DBESI (Y(M),0,BJ,D,B,IER)
      BIO(M) = BJ
      CALL DBESI (Y(M),1,BJ,D,B,IER)
 1    BI1(M) = BJ
      DO 9  N=NMIN,NMAX
      HALL = (N-1)*5.0D00
      WRITE(3,109)  HALL
 109  FORMAT(50X,'HALL COEFFICIENT = ',F4.1,//)
C  CALCULATION OF EFFECTIVE PROBE RADIUS.
      DO 50 K=1,KMAX
      W = DL/BB(K)
      DO 51   M=1,NOST
      C = Y(M) *W
 51   TRM2(M) = 1.0D00-DCOS(C)
C  SETUP FOR RANGE OF THE S PARAMETER.
      DO 2 L=1,LMAX,2
      DPL = L
      SIG33(L) = 0.2525D+04
      IF(JMAX.NE.0)  SIG33(L) = SIG3P
      IF(HALL.EQ.0.0D00)    GO TO 10
C  NON ISOTROPIC PLASMAS.
C  CALCULATION OF THE COMPONENTS OF THE CONDUCTIVITY TENSOR.
      SO = SIG33(L)*DMU*OM*BB(K)*BB(K)
      SIG11(L) = SIG33(L)/(1.0D00+HALL*HALL)
      SIG12(L) = SIG33(L)*HALL/(1.0D00+HALL*HALL)
      IF (HALL.EQ.0.0D00)  GO TO 10
      ST = SIG11(L)/(SIG11(L)**2+SIG12(L)**2)
      SH = SIG12(L)/(SIG11(L)**2+SIG12(L)**2)
      HC = HALL
      GC = 1.0D00
      FC = SO
```

```
C  SOLUTION OF THE COMPATIBILITY EQUATION.
      DO 3 M=1,NOST
      UC     = DCMPLX(Y(M)*Y(M),FC)
      QS1 = ((1.0D0+GC)*UC    +HC*HC*Y(M)*Y(M))/(2.0D00*GC)
      QS2 = (UC    *UC    +HC*HC*(Y(M)**4))/GC
      QS3 = QS1*QS1-QS2
      QS4 = CDSQRT(QS3)
      ZC1 = QS1+QS4
      X1 = CDSQRT(ZC1)
      XC1A = DREAL(X1)
      XC1B = DIMAG(X1)
      ZC2 = QS1-QS4
      X2 = CDSQRT(ZC2)
      XC2A = DREAL(X2)
      XC2B = DIMAG(X2)
C  CALCULATION OF THE MODIFIED BESSEL FUNCTIONS WITH COMPLEX ARGUMENTS.
      R1 = CDABS(X1)
      FI1 = DATAN(XC1B/XC1A)
      IF(R1.GT.0.30D+02)  GO TO 20
      THETA1 = FI1+PO2
      CALL SLITE(1)
      CALL ALLHA(R1,THETA1,H01A,H01B,H02A,H02B,H11A,H11B,H12A,H12B,IT)
      IF(IT.NE.1)  WRITE(3,111) M,Y(M),R1,THETA1,H01A,H01B,H11A,H11B,IT
      BK01     = DCMPLX(-PO2*H01B,PO2*H01A)
      BK11     = DCMPLX(-PO2*H11A,-PO2*H11B)
      RA1 = BK01/BK11
      GO TO 21
  20  PR1 = 0.80D+01*X1
      BK0S=1.0D0-1.0D0/PR1+9.0D0/(2.0D0*PR1**2)-0.75D+02/(2.0D0*PR1**3)
      BK1S=1.0D0+3.0D0/PR1-0.15D+02/(2.0*PR1**2)+0.105D+03/(2.0*PR1**3)
      RA1 = BK0S/BK1S
  21  R2 = CDABS(X2)
      FI2 = DATAN(XC2B/XC2A)
      IF (R2.GT.0.30D +02)      GO TO 22
      THETA2 = FI2+PO2
      CALL SLITE(1)
      CALL ALLHA(R2,THETA2,H01A,H01B,H02A,H02B,H11A,H11B,H12A,H12B,IT)
      IF(IT.NE.1)  WRITE(3,111) M,Y(M),R2,THETA2,H01A,H01B,H11A,H11B,IT
      BK02     = DCMPLX(-PO2*H01B,PO2*H01A)
      BK12     = DCMPLX(-PO2*H11A,-PO2*H11B)
      RA2 =BK02/BK12
      GO TO 23
  22  PR2 = 0.80D+01*X2
      BK0S=1.0D0-1.0D0/PR2+9.0D0/(2.0D0*PR2**2)-0.75D+02/(2.0D0*PR2**3)
      BK1S=1.0D0+3.0D0/PR2-0.15D+02/(2.0*PR2**2)+0.105D+03/(2.0*PR2**3)
      RA2 = BK0S/BK1S
C  CALCULATION OF THE ENTEGRAND (HALL EFFECT)
  23  EE1 = (X1/(ZC1-ZC2))*(UC    -ZC2)*RA1
      EE2 = (X2/(ZC1-ZC2))*(UC    -ZC1)*RA2
      EE     = EE1-EE2
   3  TRM3(M) = (Y(M)*BK0(M)-EE    *BK1(M))/(Y(M)*BI0(M)+EE    *BI1(M))
      GO TO 11
C  ISOTROPIC PLASMAS.
```

```
10    SO = SIG33(L)*DMU*OM*BB(K)*BB(K)
      IF (JMAX.NE.0)   GO TO 16
      DO 4 M=1,NOST
      ZCO = DCMPLX(Y(M)*Y(M),SO)
      XO = CDSQRT(ZCO)
      XCOA = DREAL(XO)
      XCOB = DIMAG(XO)
      RO = DSQRT(XCOA*XCOA+XCOB*XCOB)
      FIO = DATAN(XCOB/XCOA)
      IF (RO.GT.0.30D+02)  GO TO 30
      THETAO = FIO+PO2
      CALL SLITE(1)
      CALL ALLHA(RO,THETAO,HO1A,HO1B,HO2A,HO2B,H11A,H11B,H12A,H12B,IT)
      IF(IT.NE.1)  WRITE(3,111) M,Y(M),RO,THETAO,HO1A,HO1B,H11A,H11B,IT
      BK00     = DCMPLX(-PO2*HO1B,PO2*HO1A)
      BK10     = DCMPLX(-PO2*H11A,-PO2*H11B)
      RAO = BK00/BK10
      GO TO 31
30    PRO = 0.80D+01*XO
      BKOS=1.0D0-1.0D0/PRO+9.0D0/(2.0D0*PRO**2)-0.75D+02/(2.0D0*PRO**3)
      BK1S=1.0D0+3.0D0/PRO-0.15D+02/(2.0*PRO**2)+0.105D+03/(2.0*PRO**3)
      RAO = BKOS/BK1S
31    EEO = XO*RAO
C  CALCULATION OF THE ENTEGRAND(NO HALL EFFECT)
4     TRM3(M)   = (Y(M)*BKO(M)-EEO   *BK1(M))/(Y(M)*BIO(M)+EEO   *BI1(M))
      GO TO 11
C  NON UNIFORM PLASMAS.
16    SP = SIG3P*DMU*OM*BB(K)*BB(K)
      SO = SIG33(L)*DMU*BBP*BBP*OM
      EPS = DCMPLX(0.0D00,BPN(K)*SO/2.0D00)
      PMU = DCMPLX(0.0D00,CPN(K)*SO*BBP/BB(K))
      DO 17   M=1,NOST
      ZCO = DCMPLX(Y(M)*Y(M),SP)
      XO = CDSQRT(ZCO)
      XCOA = DREAL(XO)
      XCOB = DIMAG(XO)
      RO = DSQRT(XCOA*XCOA+XCOB*XCOB)
      FIO = DATAN(XCOB/XCOA)
      IF (RO.GT.0.30D+02)  GO TO 19
      THETAO = FIO+PO2
      CALL SLITE(1)
      CALL ALLHA(RO,THETAO,HO1A,HO1B,HO2A,HO2B,H11A,H11B,H12A,H12B,IT)
      IF(IT.NE.1)  WRITE(3,111) M,Y(M),RO,THETAO,HO1A,HO1B,H11A,H11B,IT
111   FORMAT(1X,I4,7D15.5,I4)
      BK00     = DCMPLX(-PO2*HO1B,PO2*HO1A)
      BK10     = DCMPLX(-PO2*H11A,-PO2*H11B)
      GO TO 18
19    PRO = 0.80D+01*XO
      BKOS=1.0D0-1.0D0/PRO+9.0D0/(2.0D0*PRO**2)-0.75D+02/(2.0D0*PRO**3)
      BK1S=1.0D0+3.0D0/PRO-0.15D+02/(2.0*PRO**2)+0.105D+03/(2.0*PRO**3)
18    GOC = 4.0D0*BK00/3.0D0+2.0D0*BK10/(3.0D0*XO)
      G1C = (4.0D0*XO/3.0D0+2.0D0/(XO*3.0D0))*BK10-2.0D0*BK00/3.0D0
      UU1 = XO*BK00+EPS*BK10+PMU*XO*G1C/2.0D0
```

```
      UU2 = BK10+EPS*BK00/X0+PMU*X0*GOC/2.0D00
      UU = UU1/UU2
17    TRM3(M) = (Y(M)*BK0(M)-UU*BK1(M))/(Y(M)*BI0(M)+UU*BI1(M))
11    CONTINUE
      DO 12  I =1,IMAX
      H1 = A1/BB(K)
      H2 = A2/BB(K)
      DO 13  M=1,NOST
      A = Y(M) *H1
      CALL DBESI(A,1,BJ,D,B,IER)
      BIA1 = BJ
      A = Y(M)*H2
      CALL DBESI(A,1,BJ,D,B,IER)
      BIA2 = BJ
      TRM11 = BIA1*BIA1/Y(M)
      TRM12 = BIA1*BIA2/Y(M)
      TRM22 = BIA2*BIA2/Y(M)
      ENTA11(M) = TRM11*TRM2(M)*DREAL(TRM3(M))
      ENTA12(M) = TRM12*TRM2(M)*DREAL(TRM3(M))
      ENTA22(M) = TRM22*TRM2(M)*DREAL(TRM3(M))
      ENTB11(M) = TRM11*TRM2(M)*DIMAG(TRM3(M))
      ENTB12(M) = TRM12*TRM2(M)*DIMAG(TRM3(M))
13    ENTB22(M) = TRM22*TRM2(M)*DIMAG(TRM3(M))
C  INTEGRATION USING SIMSON RULE.
      ARA11 = 0.0D00
      ARA12 = 0.0D00
      ARA22 = 0.0D00
      ARB11 = 0.0D00
      ARB12 = 0.0D00
      ARB22 = 0.0D00
      J = 0.0D00
      DO 5 M=1,NOST
      J = J+1
      IF (J-2) 14,15,14
14    J=1
      GO TO 6
15    J=2
6     ARA11 = ARA11+(DD/3.0D00)*(2.0D00*J)*ENTA11(M)
      ARA12 = ARA12+(DD/3.0D00)*(2.0D00*J)*ENTA12(M)
      ARA22 = ARA22+(DD/3.0D00)*(2.0D00*J)*ENTA22(M)
      ARB11 = ARB11+(DD/3.0D00)*(2.0D00*J)*ENTB11(M)
      ARB12 = ARB12+(DD/3.0D00)*(2.0D00*J)*ENTB12(M)
5     ARB22 = ARB22+(DD/3.0D00)*(2.0D00*J)*ENTB22(M)
      ALFA11 = DMU*A1*4.0D00*H1*BB(K)*BB(K)*DN1*DN1
      ALFA12 = DMU*A2*8.0D00*H1*BB(K)*BB(K)*DN1*DN2
      ALFA22 = DMU*A2*4.0D00*H2*BB(K)*BB(K)*DN2*DN2
      BETA11 = -OM*ALFA11
      BETA12 = -OM*ALFA12
      BETA22 = -OM*ALFA22
      DELL11 = ALFA11*ARA11
      DELL12 = ALFA12*ARA12
      DELL22 = ALFA22*ARA22
      DELR11 = BETA11*ARB11
```

```
      DELR12 = BETA12*ARB12
      DELR22 = BETA22*ARB22
      DELL = DELL11+DELL12+DELL22
      DELR = DELR11+DELR12+DELR22
      RAND = DELL/(DMU*BB(K))
      REND = DELR/(OM*DMU*BB(K))
 12   WRITE(3,107)L,SO,SIG33(L),SIG12(L),DELL11,DELL12,DELL22,DELL,RAND,
     1DELR11,DELR12,DELR22,DELR,REND
107   FORMAT(' ',I4,3D15.5/4X,5D15.5/4X,5D15.5)
  2   CONTINUE
      WRITE(3,108) A1,A2,BB(K),DL,DN1,DN2,H1,H2,SP,EPS,PMU
108   FORMAT('0',8D15.5/5D15.5///)
 50   CONTINUE
  9   CONTINUE
      CALL EXIT
      END
```

APPENDIX A

Solution of the vector Laplacian $\bar{\nabla}^2\bar{A}=0$ in cylindrical coordinates

Due to circular cylindrical symmetry we have only an azimuthal component $\bar{A}_m$ of the magnetic vector potential and using the symmetry condition $\frac{\partial}{\partial\varphi} = 0$, we can express the vector Laplacian in circular cylindrical coordinates as follows:

$$\frac{\partial^2 A_\varphi}{\partial r^2} + \frac{1}{r}\frac{\partial A_\varphi}{\partial r} - \frac{A_\varphi}{r} + \frac{\partial^2 A_\varphi}{\partial z^2} = 0 \qquad \text{(A-1)}$$

Separation of variables demands: $A_m = R(r)Z(z)$ wherein $R(r)$ and $Z(z)$ are respectively functions or r and z only. Substituting this solution into (A-1) we get:

$$\frac{1}{R(r)}\frac{\partial^2 R(r)}{\partial r^2} + \frac{1}{R(r)r}\frac{\partial R(r)}{\partial r} - \frac{1}{r^2} + \frac{1}{Z(z)}\frac{\partial^2 Z(z)}{\partial z^2} = 0 \qquad \text{(A-2)}$$

This indicates that the variables R and Z can be separated and the derivatives must be equal to constants or:

$$\frac{1}{Z(z)}\frac{\partial^2 Z(z)}{\partial z^2} = -k^2 \qquad \text{(A-3)}$$

with the solution:

$$Z(z) = C_1\cos(kz) + D\sin(kz) \qquad \text{(A-4)}$$

and

$$r^2\frac{\partial^2 R(r)}{\partial r^2} + r\frac{\partial R(r)}{\partial r} - R(r)\left[1 + (kr)^2\right] = 0 \qquad \text{(A-5)}$$

This is a first order modified Bessel equation and has the solution

$$R(r) = A\,K_1(kr) + B\,I_1(kr) \qquad \text{(A-6)}$$

Combining the solutions we have

$$A_\varphi(r,z) = \left[A K_1(kr) + B I_1(kr)\right] \cdot \left[C \cos(kz) + D \sin(kz)\right] \qquad \text{(A-7)}$$

The four constants A, B, C, D are functions of the so-called separation constant "k" and are usually different for each value of k. The complete solution would be a sum of all individual solution, but since the region is unlimited in the z direction, the complete solution is an integral over the entire range of k. Thus the general solution is:

$$A_\varphi(r,z) = \int_0^\infty \left[A K_1(kr) + B I_1(kr)\right] \cdot \left[C \cos(kz) + D \sin(kz)\right] dk \qquad \text{(A-8)}$$

(1) Calculation of the magnetic vector potential inside a loop of wire of radius a located at z=o and carrying a current I.

The unknown constants of expression (A-8) can be determined by introducing symmetry consideration and boundary conditions.

- From planar symmetry about z=o follows D=o
- Inside the coil, the magnetic vector potential must be finite or A=o.

Expression (A-8) becomes:

$$A_\varphi(r,z) = \int_0^\infty f_1(k)\, I_1(kr) \cos(kz)\, dk \qquad \text{(A-9)}$$

- The remaining unknown can be calculated from the known magnetic field strength at the axis of the loop:

Since $\bar{B} = \bar{\nabla} X \bar{A}$ we can write at the axis

$$B_z\big|_{r=0} = \frac{1}{r}\frac{\partial}{\partial r}(r A_\varphi)\Big|_{r=0}$$

$$= \left[\int_0^\infty f_1(k)\, k\, I_0(kr) \cos(kz)\, dk\right]_{r=0}$$

The magnetic field strength at the axis can also be expressed as:

$$B_z\big|_{r=0} = \frac{\mu I}{2}\frac{a^2}{(a^2+z^2)^{3/2}} = \int_0^\infty f_1(k)\, k \cos(kz)\, dk \qquad \text{(A-10)}$$

This can be solved, using a cosine integral transform (Ref. 88) with the following relationship:

$$\int_0^\infty \frac{k}{a} K_1(ak) \cos(kz) \equiv \frac{\pi}{2}\frac{1}{(a^2+z^2)^{3/2}} \qquad \text{(A-11)}$$

which, by multiplying by $\frac{\mu I a^2}{\pi}$ becomes:

$$B_z\big|_{r=0} = \int_0^\infty \frac{\mu a I}{\pi} K_1(ak).k.\cos(kz)\, dk = \int_0^\infty f_1(k).k.\cos(kz)\, dk$$

Hence $f_1(k) \equiv \frac{\mu a I}{\pi} K_1(ak)$ and the solution becomes:

$$A_\varphi(r,z) = \frac{\mu a I}{\pi} \int_0^\infty K_1(ak)\, I_1(kr) \cos(kz)\, dk \qquad \text{(A-12)}$$

at r=a this reduces to

$$A_\varphi(a,z) = \frac{\mu a I}{\pi} \int_0^\infty K_1(ak)\, I_1(ak) \cos(kz)\, dk \qquad \text{(A-13)}$$

(2) Calculation of the magnetic vector potential outside a loop of wire of radius a, carrying a current I and located at z=o.

Again starting from expression A-7 we can eliminate one unknown from symmetry consideration: D=o.

At infinite radius, the vector potential must be zero, and only the $K_1(kr)$ Bessel function satisfies this condition or B=o.

At the radius r=a, the value of the vector potential must be identical to the value for expression (A-13). The solution becomes:

$$A_\varphi(r,z) = \frac{\mu a I}{\pi} \int_0^\infty I_1(ak)\, K_1(kr) \cos(kz)\, dk \qquad \text{(A-14)}$$

The solutions A-12 and A-14 are given by W. Smythe (Ref. 50, p. 302) and are used repeatedly in Chapter I and Chapter III.

APPENDIX B

Design procedure for pulsed magnetic field coil

The design is carried out in three steps. The coil geometry is fixed first, based on the requirements of a homogeneous magnetic field over a specified control volume. The wire size and number of turns is calculated next on the basis of the required magnetic field strength and the permissible fluctuation of the magnetic field during the testing time. This is concluded by a calculation of the material stresses under the influence of static and dynamic loading of the coil.

1. Coil geometry

The coil length and inner radius are fixed as described in Chapter V.

Coil length : $2\ell = 15$ cm

Coil inner radius: $a_1 = 2.5$ cm

Extensive use was made of Ref. 85. This report shows that for $\beta = \ell/a_1 = 3$, and a ratio of the outer coil radius over inner coil radius: $\alpha = a_2/a_1 = 1.5$, the axial magnetic field satisfies the conditions for a spatial homogeneous field over the control volume. In fact, the axial field varies less than 1 percent over the total length of the control volume. (Fig. 31)

2. <u>Calculations of detailed coil design</u>

Since a high space factor is needed to meet the requirements, a square wire was chosen. We decided on FORMSET square magnet wire since it combines a high space factor with thermosetting self-bonding properties of the insulation. The dielectric strength for single insulated FORMSET is quoted to be 2000 volt/mil. Since the total voltage impressed on the coil does not exceed 6 KV over several layers, a single insulation would be more than adequate to prevent breakdown.

To determine the total number of turns and the distribution among several layers, we start with the following known requirements:

An axial magnetic flux density of 6 Tesla is required at the center. Reference 85 lists the constant $\frac{B_o}{\mu J a_1}$ for different coil geometries.

For $\alpha = 1.5$ and $\beta = 3$ $\quad \frac{B_o}{\mu J a_1} = 0.461285$

from which follow the total current density and the total current.

It is possible to set up a small computer programme to calculate the various coil parameters with the total number of turns N as independent parameters. This programme steps through a range of N, from which we selected that coil configuration satisfying all our conditions.

Given the total number of turns, the following data can now be calculated:

(1) Assuming a space factor of 90 percent for square wire, the wire gauge, total wire length and total resistance can be calculated. Indeed, the catalogue specifies the resistance of the magnet wire in Ohm/km for the various wire gauges. For single insulation magnet wire, the resistance follows very closely the relationship:

$$R = 19.5/X^{2.04} \text{ Ohm/km}$$

where X is the square wire side dimension in mm.

(2) The inductance of the coil can now be calculated from:

$$\mathcal{L} = \frac{\mu N^2 A}{\ell} K_n$$

wherein A is the coil cross-sectional area.

K_n is the Nagaoka constant (Ref. 83):

$$K_n = \frac{1}{1.0 + 0.9\, r_m/\ell + 0.32\, t/r_m + 0.84\, t/\ell}$$

wherein r_m is the mean radius: $\frac{a_1+a_2}{2}$

t coil thickness: a_2-a_1

ℓ coil length

(3) To meet the requirement that the axial field should vary less than 2 percent, during a time of 400 μsec, the total period of the discharge should not be less than 8 μsec. The period for an under-damped oscillatory discharge can be expressed as:

$$T = \frac{4\pi \mathcal{L}}{Q} \quad \text{wherein} \quad Q^2 = \frac{4\mathcal{L}}{C} - R^2$$

Knowing T, Q can be calculated. From a knowledge of the resistance, the capacitance is determined.

(4) Knowing the parameters of the coil-capacitor system, the voltage can be calculated.

The current-voltage relationship for an under-damped discharge is:

$$I(t) = \frac{2V}{Q} \exp\left(-\frac{Rt}{2L}\right) \sin\left(\frac{Qt}{2L}\right)$$

from which we derive the time for peak current:

$$T_{Imax} = \frac{2L}{Q} \operatorname{arctg} \frac{Q}{R}$$

and the peak current itself:

$$I_{max} = \frac{2V}{Q} \exp\left(-\frac{RT_{Imax}}{2L}\right) \sin\left(\frac{QT_{Imax}}{2L}\right)$$

The only unknown is the voltage V needed to obtain the required peak current.

A suitable combination of parameters was found for N = 453 and are:

wire dimension	:	1.93 mm (gauge 13)
coil resistance	:	0.47 Ohm
coil inductance	:	3.81 mH
capacitance	:	0.423 mF
peak current	:	1.713 K Amp
time of peak current	:	1.9 msec

bank voltage	:	5785 volt
total energy	:	7.077 kJ

At the moment of peak current, 79 percent of the energy is stored in the coil while 21 percent is dissipated in the resistance. The coil consists of 13 gauge single insulation formset, arranged in 6layers of 75 turns each.

3. Stress calculations

The magnetic pressure ($P_m = \frac{B^2}{2\mu}$) at a field of 6 Tesla amounts to 1.46 10^6 kg/m^2 (2080 psi).

The safe limit for the material stress for copper is quoted as: $\eta \approx 6000$ psi. Assuming a cross-sectional area of 6 square inches, the safe permissible force is 36000 lbs.

The magnetic force perpendicular to this cross section can be calculated from: $F_m = \frac{B^2 a_1 2\ell}{\mu}$ is of the order of 11000 kg (24000 lbs) and is considered to be safe for static loading.

To investigate the effect of dynamic loading at the characteristic discharge frequency of 100 Hz, one calculates the strain ε from Hooke's law $\eta = \varepsilon E$ wherein E is the Young's modulus for copper (16×10^6 psi). Since $\varepsilon = \frac{\Delta\ell}{\ell}$, one calculates the variation in the coil radius from which we determine the spring constant for the coil being $\chi = \frac{F}{\Delta\ell}$, F being the total magnetic force experienced by the inner coil layer.

Knowing the total mass of the coil (M = 0.254 kgm), the natural mechanical frequency is:

$$f_m = \frac{1}{2\pi}\sqrt{\frac{\varkappa}{M}} \approx 20\ \mathrm{kHz}$$

Since the driving frequency (100 Hz) is considerably smaller than the resonance frequency of the coil, dynamic loading will not effect the coil appreciably.

CURRICULUM VITAE

NAME	Elie Jozef Stubbe
BORN	Belgium, September 1937

STUDIES

SECONDARY	St-Lodewijks College, Brugge, Belgium
GRADUATE STUDIES	Faculty of Applied Sciences, University of Louvain, Belgium
POST GRADUATE STUDIES	Institute for Aerospace Studies, University of Toronto

DEGREES

Diploma of Electrical Engineering, 1962, Louvain

Diploma of Mechanical Engineering, 1962, Louvain

Master of Applied Sciences: Aeronautical Engineering, 1964, Toronto

An Absolute Immersion-Type Electrical Plasma Conductivity Probe

ELIE J. STUBBE

Abstract—The feasibility of measuring the spatial distribution of the electrical conductivity in plasmas by means of an immersed plasma probe has been examined. By solving the Maxwell-Helmholtz equations for the case of a coil inside a cylinder immersed in an electrically conducting medium, the change in coil impedance due to the presence of the medium is predicted. The exact solution is numerical, but for certain limiting cases analytical and empirical design formulas are obtained. A bridge and phase-sensitive demodulator allows separation of the resistive and reactive signal components; experiments with electrolytes and with shock-tube plasmas show that the theoretical predictions are borne out in practice to a good degree of accuracy, thereby providing an absolute method for which no known electrical conductivity standards are required. The plasma cooling effect of the probe is considered and an estimate for corrections is suggested.

NOMENCLATURE

A	magnetic vector potential
A_{01}	magnetic vector potential created by coil currents
A_{02}	magnetic vector potential at coil created by eddy currents
A_i	induced magnetic vector potential in plasma
a	radius of coil
B	magnetic flux density
b	radius of probe
C	capacitance
d	$=[k^2+j\sigma\mu\omega]^{1/2}$
E	electric field
$f(k)$	function of k
h	$=a/b$
I	current
I_0	modified Bessel function of first kind (zero order)
I_1	modified Bessel function of first kind (first order)
j	imaginary unit
j	current density
K_0	modified Bessel function of second kind (zero order)
K_1	modified Bessel function of second kind (first order)
K_2	modified Bessel function of second kind (second order)
k	integration variable
L	inductance
l	coil length
N	total number of turns
n	number of turns per unit length
P_i^j	associated Legendre functions
p	$=nb$
Q	quality factor
R	resistance
r	radial component in cylindrical coordinates
s	probe parameter ($=\sigma\mu\omega b^2$)
V	voltage
w	$=l/b$
x	$=db$
y	$=kb$
Z	impedance
z	axial component in cylindrical coordinates
α	$=\kappa\tau/b^2$
Δ	increment
ϕ	phase angle
κ	thermal diffusivity
μ	magnetic permeability for free space
σ	electrical conductivity
τ	time elapsed since passage of the reflected shock
ω	circular frequency

Subscripts

c	coupling
i	induced
l	leakage
0	without conducting medium present
p	primary; parallel
r	radial
s	series
z	axial
ϕ	azimuthal

Manuscript received April 1, 1968. This contributed paper appears only in the PROCEEDINGS.—*The Editor*. This work was submitted to the Electrical Engineering Department, University of Ottawa, Ottawa, Canada, in partial fulfillment of the requirements for the Ph.D. degree.

The author is with the Gas Dynamics Section, National Research Council, Ottawa, Canada.

I. INTRODUCTION

THE MEASUREMENT of transport properties of a plasma is an important task of the diagnostic study of plasma physics in engineering. The large number of articles published on the subject of plasma conductivity measurements reflects a special interest in this branch of plasma diagnostics. Reference [1] presents a survey of the subject for different probe configurations based on the electromagnetic coupling between a radio-frequency magnetic field and an electrically conducting medium, together with an extensive review of the literature.

Two references are worth mentioning in connection with the immersed type of conductivity probe. Olson and Lary [2] conceived the idea of the immersed probe to measure the electrical conductivity of flames. Sprouse [3] also uses an immersed probe coil to measure the electrical conductivity in an arc heated, low-density supersonic plasma. The results are presented in terms of a nondimensional parameter Q_s, which, for a particular coil, is a function only of the electrical conductivity of the surrounding medium. Since the range of electrical conductivities most often encountered in laboratory plasmas (between 1 mho/cm and 100 mho/cm) falls outside the readily available range of calibration standards, particular emphasis is placed on the development of an absolute device. It should be mentioned that some materials exist with suitable conductivities, but most present some difficulties. Examples include the following.

1) Fused salts fall in the proper range only at elevated temperatures.

2) Semiconductors are anisotropic or contain grain boundaries.

3) Metal-ammonia solutions at subzero temperatures have an electrical conductivity continuously variable from 10^{-3} mho/cm to 10^3 mho/cm. However, special techniques must be used to produce these solutions and they are difficult to conserve for useful periods.

In [4], the basic principles of the behavior of this type of probe were explained on the basis of the transformer equivalent circuit which provides a crude explanation of the obtained results.

The present analysis will present a more rigorous approach to the problem of correlating a detectable change in the impedance of the probe coil to the electrical conductivity of the medium which surrounds the probe. Absolute calibration can then be performed by artificially changing the impedance of the probe by external circuit adjustment and recording the response of the electronic circuit.

It is the purpose of this paper to present experimental results in agreement with the theoretical solutions, establishing the basic feasibility of bypassing any tedious direct calibration procedures. Plasma disturbance and conduction cooling are two main drawbacks of an immersed probe. It is shown that this can be overcome or accounted for by proper probe and circuit design.

II. Theoretical Treatment

A. Analysis of the Internal Coil Impedance in the Presence of an Electrically Conducting Medium

The conductivity probe is basically a single-layer, tightly wound, helical coil excited by a radio-frequency current produced by an external generator. The coil behaves as the primary of an RF transformer whereby the plasma can be considered as a single-turn, short-circuited secondary wherein eddy currents are induced.

This loading effect of the plasma on the driver coil can be expressed by evaluating the ratio of the induced voltage over the driving current. The primary RF current in the coil I_p produces a dipolar magnetic field, the time variation of which gives rise to an electric field $\boldsymbol{E}$ in the azimuth direction. Using Maxwell's equation together with the definition of a vector potential $\boldsymbol{A}$ according to: $\boldsymbol{B}=\nabla\times\boldsymbol{A}$, the voltage induced in the plasma can be expressed as

$$V_i = -j\omega\oint \boldsymbol{A}\cdot d\boldsymbol{l}. \tag{1}$$

Due to the azimuthal symmetry of the magnetic vector potential, the induced voltage at the location of the primary with radius a is

$$V_{ip} = -j\omega a\int_0^{2\pi} A_\phi d\phi = -2\pi a j\omega A_\phi. \tag{2}$$

Since the vector potential $\boldsymbol{A}$ is related to the current density $\boldsymbol{j}$ by the Laplacian $\nabla^2 A=\mu j$, a relationship between voltage and current can be obtained, from which the impedance can be calculated. If no plasma is present, i.e., with an open secondary, the coil impedance Z_0 is according to Ohm's law equal to the ratio of the primary voltage V_{p0} over the primary current I_0, or $Z_0=V_{p0}/I_p$.

If the medium around the probe becomes electrically conducting, induced eddy currents in the plasma will induce a voltage in the primary V_{pi}. Also the vector potential A_ϕ at the coil radius $r=a$ will be changed due to the eddy currents in the plasma. Calling A_{02} the additional vector potential at the coil, set up by the eddy currents, the same relationship as (2) can be written

$$V_{ip} = -2\pi a j\omega A_{02\phi}. \tag{3}$$

Since $A_{02\phi}$ is the only cylindrical component of the vector A_{02}, the subscript ϕ will be dropped in the following. The total current in the primary will be

$$I = \frac{V_{p0}+V_{pi}}{Z_0} = \frac{V_{p0}-2\pi a j\omega A_{02}}{Z_0}. \tag{4}$$

The input impedance seen at the coil terminals is

$$Z = \frac{V_{p0}}{I} = \frac{Z_0}{1-2\pi a j\omega A_{02}/V_{p0}}. \tag{5}$$

The change of the coil impedance due to the presence of a plasma is

$$\begin{aligned}\Delta Z = Z - Z_0 &= Z_0\left[\frac{1}{1-2\pi a j\omega A_{02}/V_{p0}} - 1\right]\\ &= Z_0\left[\frac{2\pi a j\omega A_{02}/V_{p0}}{1-2\pi a j\omega A_{02}/V_{p0}}\right].\end{aligned} \tag{6}$$

For most of the cases for which this study is intended, the term $2\pi a j\omega A_{02}/V_{p0}$ is very much smaller than unity so that the impedance change seen at the primary becomes

$$\Delta Z = 2\pi a j\omega A_{02}Z_0/V_{p0} = 2\pi a j\omega A_{02}/I_p. \tag{7}$$

Hereby, the problem is reduced to establishing a relationship between the vector potential A_{02} and the electrical conductivity of the plasma. Calling A_{01} the vector potential in unlimited space (see Fig. 1) produced by a current I_p in a single loop of wire with radius a, Smythe [5] gives the solution of the vector Laplacian $\nabla^2 A_{01}=0$ in cylindrical coordinates as

$$(A_{01})_\phi = \frac{\mu a I}{\pi}\int_0^\infty I_1(ak)K_1(kr)\cos(kz)dk. \tag{8}$$

In order to calculate the vector potential A_i in the conducting region (for $r>b$) one has to include the induced

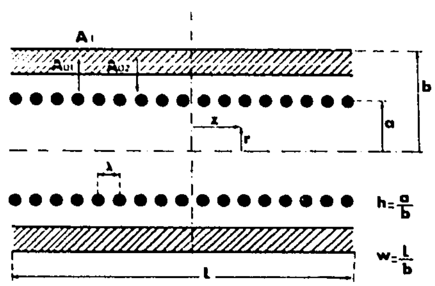

Fig. 1. Sketch of probe coil configuration.

currents and Maxwell's equation becomes

$$\nabla^2 A_i = j\sigma\mu\omega A_i.$$

The solution can be written in the following form by including the boundary condition at infinity

$$(A_i)_\phi = \int_0^\infty f_i(k) K_1(dr) \cos(kz) dk \tag{9}$$

where

$$d = \left[k^2 + j\sigma\mu\omega\right]^{1/2}$$
$$f_i(k) = \text{function of } k. \tag{10}$$

The induced eddy currents, flowing in the conducting medium, in turn produce a magnetic vector potential A_{02} in the region for $r<b$, which is superimposed on the existing magnetic vector potential A_{01} produced by the RF currents in the coil. This magnetic vector potential A_{02} contains the required information about the electrical conductivity of the plasma.

Tne calculation of the reflected potential A_{02} in the region $a<r<b$ can again be calculated by solving the Laplacian $\nabla^2 A=0$:

$$(A_{02})_\phi = \int_0^\infty f_{02}(k) I_1(kr) \cos(kz) dk$$
$$f_{02}(k) = \text{function of } k. \tag{11}$$

Boundary conditions at $r=b$ are as follows.

1) The tangential components of A are continuous:

$$\left[A_{01} + A_{02}\right]_{r=b} = \left[A_i\right]_{r=b}. \tag{12}$$

2) Since μ is constant throughout, the tangential components of $\boldsymbol{B}$ are continuous or:

$$\left[\frac{\partial}{\partial r}(rA_{01} + rA_{02})\right]_{r=b} = \left[\frac{\partial}{\partial r}(rA_i)\right]_{r=b}. \tag{13}$$

Since any surface current causes a jump in the magnetic field or an increase in the magnetic potential $\Delta A = \mu j$, it should be noted that this second boundary condition applies only in the absence of a current sheet. Therefore, any highly conducting coating of the probe, which is used to prevent capacitive coupling with the plasma, should be designed to inhibit closed circuit eddy currents in the coating. A longitudinal slit will usually serve this purpose. Combining boundary conditions (12) and (13) together with (8), (9), and (11), we can solve for $(A_{02})_\phi$:

$$(A_{02})_\phi = \frac{\mu a I}{\pi} \int_0^\infty I_1(ka) I_1(kr) \cdot \frac{kK_0(kb)K_1(db) - dK_1(kb)K_0(db)}{dI_1(kb)K_0(db) + kI_0(kb)K_1(db)} \cos(kz) dk. \tag{14}$$

Substituting this expression for A_{02} into (7) gives the required change of impedance ΔZ experienced by a single loop of wire with radius a, located at $z=0$ under the influence of a conducting medium bounded internally by the cylinder with radius b.

The change of impedance experienced by a single-layer multiturn coil located between $z=-l/2$ and $z=l/2$ can be obtained by integrating (7) twice, as follows:

$$\Delta Z = \frac{2\pi j\omega a}{I} n^2 \int_{-l/2}^{+l/2} \int_{-l/2}^{+l/2} A_{02}\Big|_{z-z_0} dz\, dz_0 \tag{15}$$

where n = number of turns per unit length.

We introduce the following nondimensional factors:

$$y = kb \quad x = db \quad h = \frac{a}{b} \quad w = \frac{l}{b} \quad s = \sigma\mu\omega b^2.$$

Substituting (14) in (15), working out the double integral, and using the nondimensional parameters above, the general solution for the impedance change experienced by a coil immersed in an electrically conducting medium is as follows:

$$\frac{\Delta Z}{\omega\mu a} = +\,4jhb^2n^2 \int_0^\infty \frac{I_1^2(hy)}{y^2} \cdot \frac{yK_0(y)K_1(x) - xK_1(y)K_0(x)}{xI_1(y)K_0(x) + yI_0(y)K_1(x)} \left[1 - \cos(wy)\right] dy. \tag{16}$$

Since the integral involves complex quantities, the change in impedance will contain both a resistive and a reactive component.

B. Numerical Solution

Equation (16) can be solved numerically by using the subroutines for the modified Bessel functions $K_0(x)$ and $K_1(x)$ with complex arguments. A coordinate transformation in the integration variable of the form $Y = \ln y$ proved useful to cover the entire range for y wherein the integrand is finite.

The results of the numerical solution are plotted in Figs. 2 and 3, respectively, for the resistive and reactive changes of the coil impedance as a function of the nondimensional parameter $s(=\sigma\mu\omega b^2)$. The curves represent solutions for four different values of the coil parameter h.

These curves show the same behavior as indicated in [1]. The change of the series resistance reaches a maximum for s between 1 and 10, and decays to zero at very large conductivities due to decreasing skin depth which completely shields the coil from the plasma. The monotonically increasing value of the series inductance of the coil, as the conductivity increases, indicates an increasing phase shift between primary current and induced eddy currents, reaching 90° at infinite conductivity.

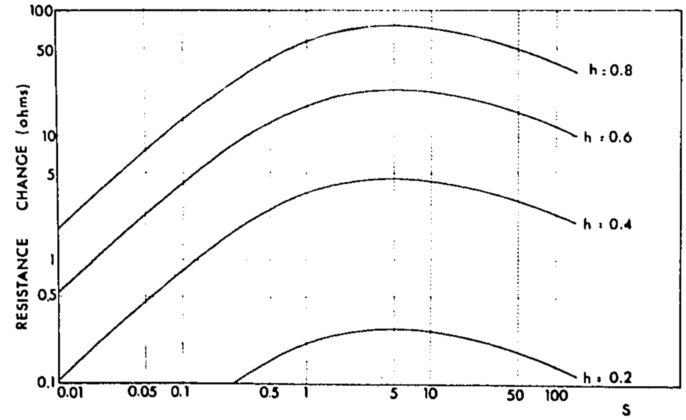

Fig. 2. Exact numerical relationship between the change in series resistance of the probe coil versus parameter s for four probe geometries.

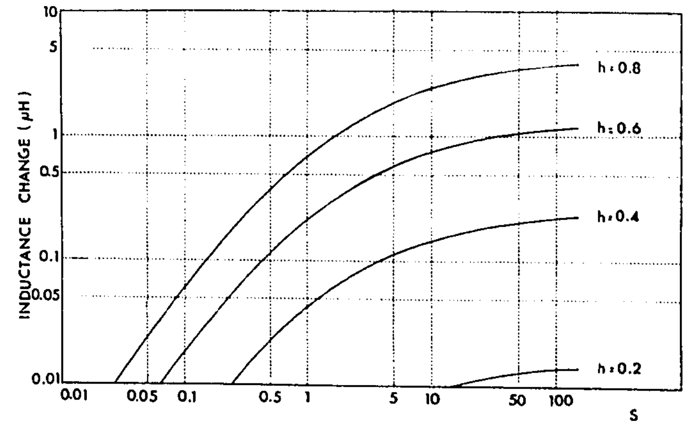

Fig. 3. Exact numerical relationship between the change in series inductance of the probe coil versus parameter s for four probe geometries.

Close to the origin, say for values of s smaller than 0.1, the series resistance varies linearly with s, while the inductance change following a parabolic behavior can be entirely neglected. Therefore, an approximate solution must exist for (16), which does not involve complex quantities and hence is much easier to apply.

C. Approximate Numerical, Analytical, and Empirical Solutions for $s<0.1$

The definition for d expressed in (10) can be nondimensionalized by using the nondimensional factors introduced in Section II-B

$$db = \left[(kb)^2 + j\sigma\mu\omega b^2\right]^{1/2} \quad \text{or} \quad x = \left[y^2 + js\right]^{1/2}. \tag{17}$$

We introduce the small s approximation:

$$x \simeq y + \frac{js}{2y}. \tag{18}$$

Using a Taylor expansion to evaluate $K_0(x)$ and $K_1(x)$ of (16) in terms of y according to (18), the general expression (16) can be reduced to:

$$\frac{\Delta Z}{\omega\mu a} = 2shn^2b^2 \int_0^\infty \frac{I_1^2(hy)}{y^2}\left[K_0(y)K_2(y) - K_1^2(y)\right] \cdot \left[1 - \cos wy\right] dy. \tag{19}$$

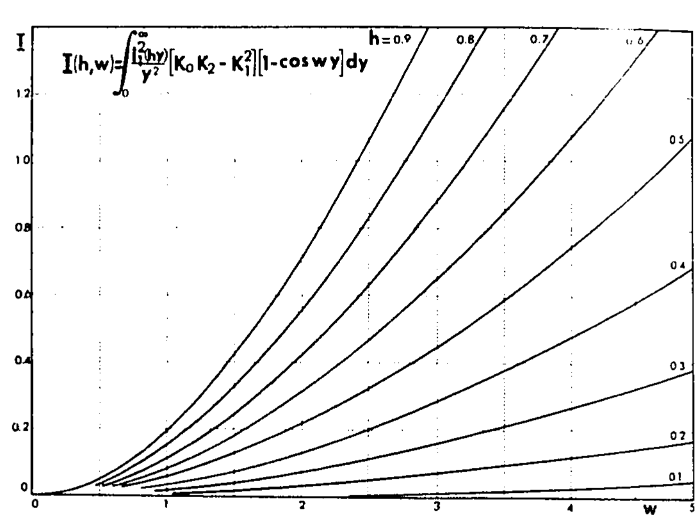

Fig. 4. Approximate numerical solutions of $I(h, w)$ for various probe coil geometries.

Since all factors are real, the impedance change will be purely resistive indicating no phase shift between primary current and induced eddy currents.

The numerical solutions for the integral

$$I(h, w) = \int_0^\infty \frac{I_1^2(hy)}{y^2}\left[K_0(y)K_2(y) - K_1^2(y)\right] \cdot \left[1 - \cos wy\right] dy \tag{20}$$

are plotted in Fig. 4 for various values of the parameters h and w.

An analytic solution for this small s approximation can be obtained by using a series expansion for the modified Bessel function $I_1(hy)$ and the cos (wy). Using two integral transforms, (19) can be expressed as an infinite series which can be written as follows by including only the first three terms in the series expansion:

$$\frac{\Delta R}{\omega\mu a} = sh^3w^2n^2b^2\,\frac{\pi^2}{4}\left[\frac{3}{16} + \frac{15}{356}\left(\frac{h^2}{4} - \frac{w^2}{12}\right) + \frac{315}{2048}\left(\frac{w^4}{360} + \frac{5h^4}{192} - \frac{h^2w^2}{48}\right) + \cdots\right]. \tag{21}$$

For better comparison between the approximate numerical solution and approximate analytical solution (21), the following expressions are plotted in Fig. 5 for the value of $h=0.554$:

$$F_0 = \frac{I(h, w)}{w^2} \quad \text{for the numerical solution} \tag{22}$$

$$F_{1a} = \frac{\pi^2h^2}{8}\left[\frac{3}{16} + \frac{15}{356}\left(\frac{h^2}{4} - \frac{w^2}{12}\right) + \frac{315}{2048}\left(\frac{w^4}{360} + \frac{5h^4}{192} - \frac{h^2w^2}{48}\right)\right] \tag{23}$$

$$F_{1b} = \frac{\pi^2h^2}{8}\left[\frac{3}{16} + \frac{15}{356}\left(\frac{h^2}{4} - \frac{w^2}{12}\right)\right]. \tag{24}$$

Judging from the discrepancy between F_1 and F_0, this series expansion solution can only be used for very short coils

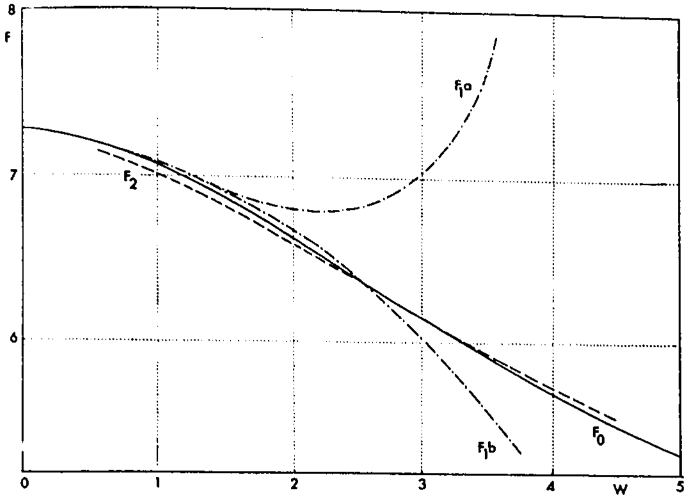

Fig. 5. Comparison between two analytical solutions and a numerical solution for small s approximation.

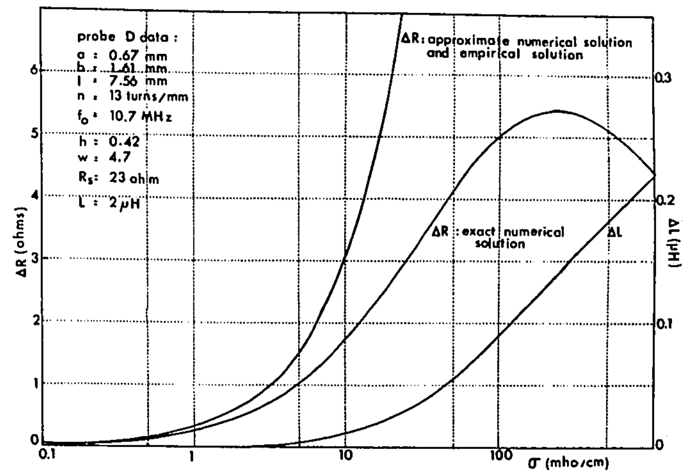

Fig. 6. Relation between the impedance change (exact, approximate, and empirical) and the electrical conductivity for the probe D used in the experiments.

($w < 1$). For longer coils further terms of the expansion have to be included, making it rather cumbersome. A more accurate analytical solution for longer coils can be obtained by using hypergeometric functions.

Expression (19) can also be written

$$\frac{\Delta Z}{\omega\mu a} = 2shn^2b^2 \int_0^\infty \frac{I_1^2(hy)}{y^2} \cdot \left[K_0^2(y) + \frac{2K_0(y)K_1(y)}{y} - K_1^2(y)\right][1 - \cos wy]dy. \tag{25}$$

Applying a series expansion for $I_1(hy)$ together with a cosine integral transformation, (25) can be transformed into

$$\frac{\Delta Z}{\omega\mu a} = \frac{sh^3n^2b^2}{2}[Y_{30} + 2Y_{10} - Y_{20}] \tag{26}$$

where

$$Y_{10} \equiv \int_0^\infty \frac{K_0(y)K_1(y)}{y}(1 - \cos wy)dy = -\frac{\pi^2w^2}{2}\left[1 + \frac{w^2}{4}\right]^{\frac{1}{2}}\left[P_{-\frac{1}{2}}^{+1}\left(1 + \frac{w^2}{2}\right)\right]$$

$$Y_{20} \equiv \int_0^\infty K_1^2(y)(1 - \cos wy)dy = \frac{\pi^2}{4}\left[P_{1/2}^0\left(1 + \frac{w^2}{2}\right) - 1\right]$$

$$Y_{30} \equiv \int_0^\infty K_0^2(y)(1 - \cos wy)dy = \frac{\pi^2}{4}\left[1 - P_{1/2}^0\left(1 + \frac{w^2}{2}\right)\right]$$

where P_i^j are associated Legendre functions and are tabulated in [6].

Again, for comparison with the approximate numerical solution the following expression is plotted in Fig. 5:

$$F_2 \equiv \frac{h^2}{4w^2}[Y_{30} + 2Y_{10} - Y_{20}] \quad \text{for } h = 0.554. \tag{27}$$

The agreement between (27) and the numerical solution for $I(h, w)/w^2$ is very good for coil parameter w up to 5.

Finally, if the data, resulting from the approximate numerical solution of (19), are plotted on a log-log scale, it turns out that the following empirical expression can be used for correlating the coil resistance change and the electrical conductivity of the plasma:

$$\frac{\Delta R}{\omega\mu a} = 0.47\, sh^3w^{1.82}n^2b^2 = 0.47\, sh^3N^2\, w^{-0.18} \tag{28}$$

which gives reasonable accuracy (error smaller than 5 percent) if applied for the range of the coil parameters:

$$0.2 < h < 0.9$$
$$1 < w < 5.$$

Expression (28) can be used to make an approximate design of an immersed conductivity probe and to obtain readily the sensitivity of the probe. It also indicates what parameters influence most the sensitivity of the device.

Fig. 6 presents a plot on a semi-log scale for the change of the coil impedance (ΔR and ΔL) for the probe used throughout the experiments. A comparison is made between the exact numerical solution (16) and the approximate numerical (19) and empirical (28) solutions. From this graph, an idea can be obtained of the validity of the approximation at small electrical conductivities.

D. Effect of Small Number of Turns on the Exact Solution

For coils with a small number of turns, integration over the total number of turns (15) may overestimate the value of the impedance change. Instead, a summation of the value for the magnetic vector potential A_{02} over the total number of turns should replace the integral. The summation for a cosine can be expressed as [7]

$$\sum_{t=0}^{m} \cos(kt) = \frac{\cos\left(\frac{km}{2}\right)\sin\left(k\frac{m+1}{2}\right)}{\sin\left(\frac{k}{2}\right)}. \tag{29}$$

Substituting (29) for the double integral over the factor $\cos kz$ contained in A_{02} of (14), the following expression can be used for coils with a discrete number of turns:

$$\frac{\Delta Z}{\omega\mu a} = +\,2jh\int_0^\infty I_1^2(hy)\left[\frac{yK_0(y)K_1(x) - xK_1(y)K_0(x)}{xI_1(y)K_0(x) + yI_0(y)K_1(x)}\right] \times \left[2\,\frac{\cos\left(\frac{pw-1}{4p}\right)\sin\left(\frac{pw+1}{4p}\,y\right)}{\sin\left(\frac{y}{2p}\right)} - 1\right]^2 dy \tag{30}$$

where

$p = nb = N/w$
n = number of turns per unit length
N = total number of turns.

Numerical solutions of (30) were compared with the numerical solutions for (16) for a particular coil geometry (h, w) by varying the number of turns. The results show an error smaller than 1 percent for coils with two turns.

III. Experimental Apparatus

A. Construction and Operation of the Probe

The coil geometry is mainly determined by the proposed application. The main purpose of the probe is to monitor the electrical conductivity in a shock tube and a plasma jet. In order to obtain a good spatial resolution in a plasma jet with 1-inch nozzle diameter, a probe diameter not exceeding $\frac{1}{8}$ inch was chosen, thereby setting an upper limit for the probe radius b. Since the sensitivity of the device increases sharply with increasing values of $h(=a/b)$ (Fig. 2), a maximum value for the coil radius a is chosen within the available space. The conditions for good sensitivity and high quality factor give practical values for w between 2 and 5, depending on the type of coil wire and the turn density. Manganin coils proved to be successful. At 10.7 MHz, the ratio R_{AC}/R_{DC} is approximately 1.01 for AWG 38. Furthermore, the small temperature coefficient of manganin up to 25°C will reduce any thermal effect in the probe in experiments with electrolytic solutions. Since thermal effects also increase the series resistance of the coil, it is important to minimize this effect. In the shock tube and plasma jet, thermal effects can be filtered out since the thermal time constant is orders of magnitudes larger than the probing time.

The frequency is chosen to be considerably lower than the average collision frequency so that a dc conductivity can be measured. It is equally important that the measuring frequency avoids the plasma resonance frequency, electron cyclotron frequency, and any frequency characteristic of the flow of the plasma around the probe. This provides an upper limit for the carrier frequency. Since the sensitivity increases as the square of the frequency (19), a compromise has to be made; a frequency of 10.7 MHz was chosen, for which crystals are commercially available.

The data for the coils used in the experiment are:

$a = 0.67$ mm $\qquad l = 7.56$ mm
$b = 1.61$ mm $\qquad n = 13$ turns/mm

resulting in the following parameters:

$h = 0.42 \qquad w = 4.7.$

At 10.7 MHz the electrical data are:

$R_p = 740$ ohm $\qquad L = 2\mu$H
$R_s = 23$ ohm $\qquad Q = 5.61.$

The coil is wound on a ceramic tube (0.039 inch OD) which fits over the center conductor of a miniature coaxial cable (Microdot 250-3919). The coil ends are soldered to the center wire and the shield of the cable. This assembly is inserted into a quartz tube (2 mm ID, 3 mm OD). Such an arrangement minimizes coupling capacitance between the coil and the outside medium while the characteristic impedance is the same throughout. A Microdot cable, 2 feet long, connects the coil to the parallel-T bridge. This assembly is called the probe in the following.

B. Design and Operation of the Impedance Measuring Circuit

The results of the theoretical analysis indicate both a resistive and a reactive change for the probe coil impedance when immersed in an electrical conducting medium. Therefore, a phase-sensitive detection system is required which will discriminate between resistance and reactance components of the signal. The block diagram of the circuit is shown in Fig. 7.

Parallel-T Network: A parallel-T-null circuit for plasma conductivity measurements is described in [8], and is shown in Fig. 8. When balanced, the circuit is capable of detecting very small changes in resistance and reactance. The main advantages for such a bridge are as follows.

1) Independent balancing exists for active and reactive components of the impedance by using variable air capacitors only.

2) Shielding and grounding problems are eliminated due to a common ground connection for the input, output, probe, and the two balancing capacitors.

3) There is very fast response.

A study of the transfer function of this parallel-T bridge indicates that the amplitude of a small, purely resistive unbalance signal is linearly proportional to the resistive unbalance and the phase of the signal remains unchanged. Similarly, if the small unbalance is produced by a purely reactive component, the amplitude of the output signal again will be proportional to the value of the reactive component, and the phase, while remaining unchanged, is now 90 degrees out of phase compared to a purely resistive unbalance signal. Based on this property, single phase sensitive detection was possible.

Description of the Block Circuit: The 10.7-MHz, crystal-controlled oscillator is separated from the load by two high-input-impedance, low-output-impedance buffer stages which provide gain control (Fig. 7).

One buffer provides the input signal for the parallel-T

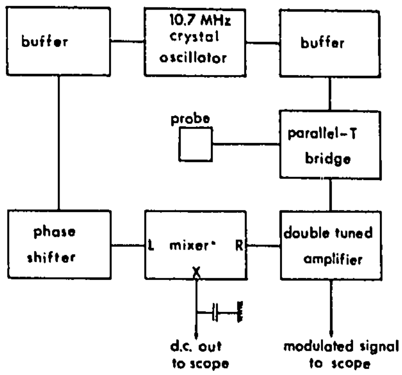

Fig. 7. Block diagram of circuitry.

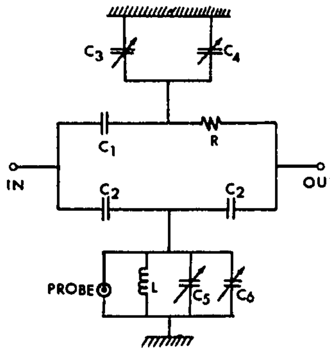

C1 : 30 pf
C2 : 15 pf
C3 : 30 - 350 pf COARSE RESISTANCE DIAL
C4 : 10 - 28 pf FINE RESISTANCE DIAL
C5 : 230 - 550 pf COARSE REACTANCE DIAL
C6 : 10 - 28 pf FINE REACTANCE DIAL
L : 2 μH Q : 154 at 10.7 MHz
R : 56 Ohms

Fig. 8. Detailed circuit for the parallel-T bridge.

bridge. The output signal is due to any variation of the probe impedance around a preset balance condition. This signal is amplified 20 dB in a double-tuned amplifier, the output of which is applied to port R, or the signal port of a balanced mixer.

A phase reference signal is obtained from the second buffer stage by passing it through a variable phase shifter. This is needed to compensate for any phase shift occurring in the circuit elements and to provide a phase adjustment of the reference signal such that it can be phase aligned with either a resistive or a reactive unbalance signal. This reference signal is applied to port L of the balanced mixer. Output from the mixer is taken at port X which is terminated in a 50-ohm ac load (or 300 pF at 10.7 MHz).

In this configuration, the mixer acts as a phase discriminator giving an output signal containing the sum and difference frequencies of the input signals. In this case, the output signal obtained at port X has a dc component which is proportional to $V(R)\cos\phi$, where $V(R)$ is the voltage of the signal fed in port R and ϕ is the phase angle between the signals applied to ports R and L. The double frequency is filtered out.

The dc voltage output is of the order of 40 mV for an electrical conductivity of 20 mho/cm, and the rise time is approximately 2 μs, which is important for shock-tube work as will be explained later.

C. Calibration of the Probe and Circuitry

For the range of electrical conductivities of interest ($0.1<\sigma<40$ mho/cm), it is evident from Fig. 6 that the change in series resistance of the probe coil is greater than the change of the reactance. Hence, the value of the electrical conductivity will be determined from the series resistance change in this experiment.

The calibration can be performed by artificially changing the series resistance of the coil by inserting a small resistor in series with the probe coil. However, due to the cable capacitance, this series resistance should be inserted at the coil itself which is rather difficult to achieve. It proved impractical to insert values of pure resistances of the order of 0.5 ohm at the probe coil itself. It is equally feasible to insert a parallel resistor across the probe coil, whereby the problem of parallel capacitance can be bypassed, and to determine equivalent series resistance at the coil using an R-X impedance bridge. Hence, the calibration is done in two steps as follows.

Step 1) The probe is connected to an R-X impedance bridge to measure the self-capacitance of the coil, stray capacitance, and cable capacitance. This capacitance C_0 can be determined by making a set of measurements of the capacitance required to resonate with the probe coil at various frequencies. The extrapolated value of the capacitance obtained at infinite frequency gives C_0 while the slope of the line gives the value of the coil inductance.

Next, several high-quality resistors are connected in parallel with the probe. This changes the total parallel resistance of the probe from which the equivalent series resistance change can be calculated as follows:

$$\Delta R_s = R_s - R_{s0} = \frac{R_p}{1+Q^2} - \frac{R_{p0}}{1+Q_0^2} \tag{31}$$

where

R_{p0} = parallel resistance of probe without additional parallel resistance
R_p = parallel resistance of probe with additional parallel resistance
R_{s0} = series resistance of coil itself
R_s = total series resistance of coil with additional parallel resistance
$Q_0 = R_{p0}C_{p0}\omega$, where C_{p0} is the negative capacitance reading on the C_p dial, corrected for the total capacitance C_0 described above
$Q = R_pC_p\omega$, where C_p is again corrected.

In effect this correction means that instead of measuring the coil properties (inductance and series resistance) through a cable we measure the coil properties at the terminals of the coil itself, having no stray capacitance. This correction is justified because most stray capacitance and parallel capacitance appears in parallel with the coil, and the losses in the short cable are negligible. Using (31), it is possible to

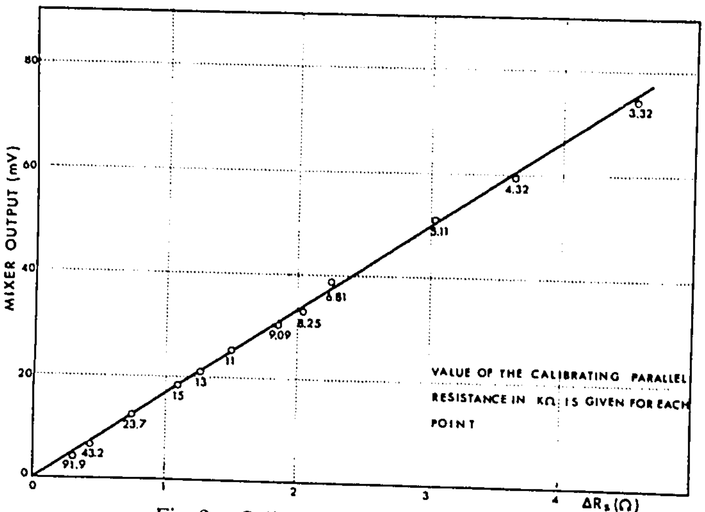

Fig. 9. Calibration curve for probe D.

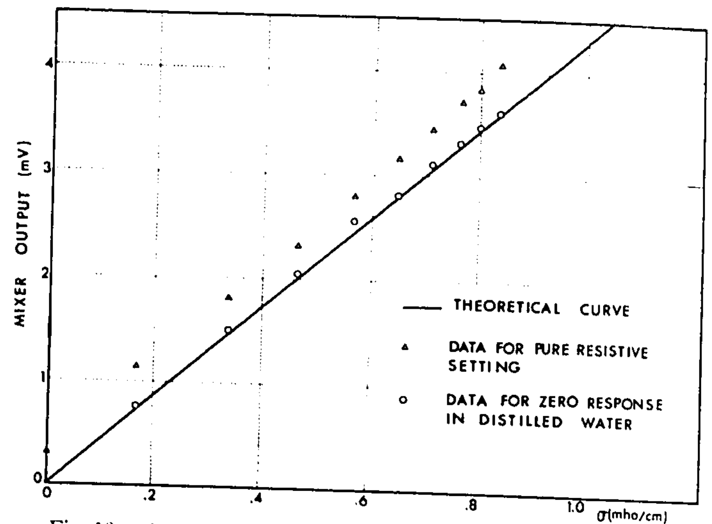

Fig. 10. Comparison between exact numerical and experimental results for electrolytic solutions.

simulate a wide range of series resistances by using several parallel resistances.

Step 2) The probe is connected to the parallel-T bridge and the same procedure is repeated for different values of parallel resistances and the mixer output signal recorded gives the missing relationship between circuit response in volts versus values of equivalent series resistances in ohms.

This then constitutes the calibration curve shown in Fig. 9 for a particular probe which is independent of a standard of electrical conductivity.

IV. Experimental Results

A. Experimental Data for Electrolytic Solutions

Electrolytic solutions of HNO_3 provide a range of electrical conductivities by varying the concentration, up to 0.85 mho/cm for a concentration of 5.5 mole/l at 22°C.

Before the probe is dipped in the solution, the bridge is balanced and the phase setting is adjusted for pure resistive changes of the coil impedance. The data recorded are shown in Fig. 10 together with the theoretical response curve for the probe at the low conductivity range.

If the same measurement is repeated for a phase setting whereby no response is obtained in distilled water, the data now agree very well with the theoretical values.

The constant offset voltage (approximately 0.3 mV) arises from a dissipation occurring in distilled water. This is due to the displacement currents present in dipolar liquids when subjected to a high-frequency electric field.

The close agreement with measured and numerically predicted values indicates that the theory presented in Section II explains the actual phenomena and may be used to bridge the gap in the existing electrical conductivity standards.

Most experimental data are obtained without an electrostatic shield between the probe coil and the electrical conducting medium. The reason why no coating is required can be explained by analyzing the equivalent circuit for coupling capacitances between plasma and coil proposed by Moulin and Massé [9]. A bypass for the RF current in the coil exists through the cylindrical coupling capacitance between coil and plasma in series with a leakage resistance in the conducting medium. The values for these capacitances and the leakage resistance in HNO_3 were calculated from expressions given in [9] and were verified with an R-X impedance bridge. The phase of this bypass current referred to the coil circuit can be calculated from

$$\tan \phi = \frac{2}{R_l C_c \omega}.$$

where

R_l = leakage resistance through the plasma between the coil ends

C_c = cylindrical coupling capacitance.

For a plasma with electrical conductivity of 25 mho/cm, the values of R_l and C_c are approximately:

$$R_l = 7.5 \times 10^{-2} \text{ ohm}$$

$$C_c = 1 \text{ pF}.$$

Substituting these values in the expression above gives a phase angle close to 90 degrees and the effect will therefore be completely rejected by the phase-sensitive detector and will not influence the results.

B. Sensitivity Curve of the Conductivity Probe

When the probe is immersed into a hot plasma, a thermal and viscous boundary layer will form around the sensing coil. This region close to the coil is also the most sensitive area since the power dissipation falls off as r^{-4}.

Using the exact numerical program, a set of sensitivity curves can be computed for various values of the electrical conductivity as shown in Fig. 11. These data have been normalized with respect to the outer radius $b = 1.61$ cm, this being the material boundary of the probe, and assigned 100 percent.

These sensitivity curves have been experimentally verified in an electrolytic solution of HNO_3 for 0.8 mho/cm. These data are also plotted in Fig. 11 and again indicate excellent agreement between theory and experiment.

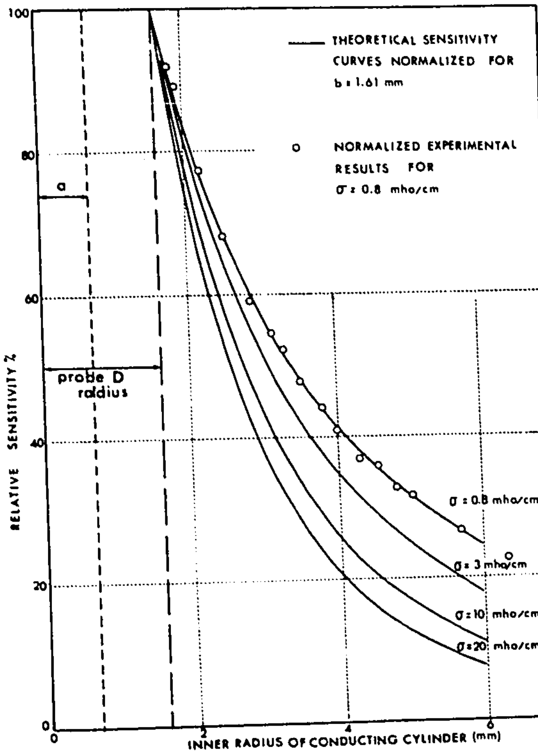

Fig. 11. Sensitivity curves for probe D at various electrical conductivities, compared with experimental results.

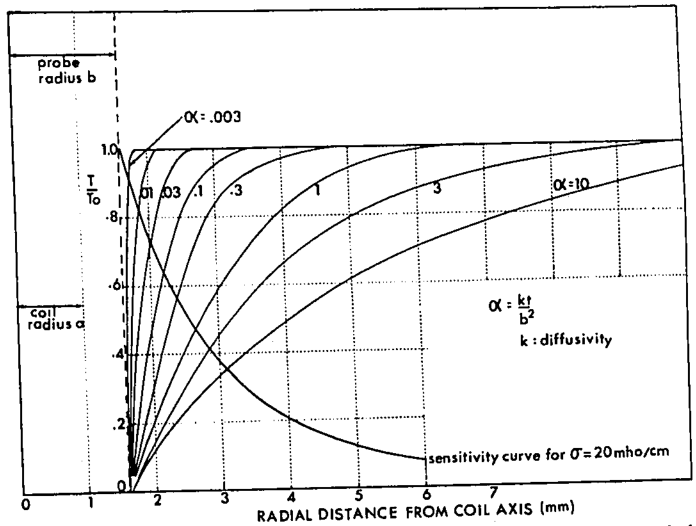

Fig. 12. Variation with time of temperature in the plasma bounded internally by the probe due to conduction cooling.

C. Experimental Results with Shock-Tube Plasmas

The plasma is produced in a $1\frac{1}{2}$-inch shock tube designed by Lau and Mills [10], who used it to experimentally verify the theory of Shkarofsky [11] relating to transport coefficients in an ionized gas.

Cold hydrogen is used as the driver gas, argon as the test gas.

The plasma conductivity probe was inserted through the end plate in the shock tube such that the sensing coil was fully immersed in the plasma about 2 inches from the end plate.

Neglecting boundary layer effects, the velocity of the plasma behind the reflected shock is zero. No flow disturbance could be detected from Kerr cell pictures, which indicates the absence of a viscous boundary layer. However, the probe will act as a heat sink for the plasma, and thermal boundary correction may be needed.

Both the estimate of the interphase temperature between hot plasma and the initially cold probe and thermocouple measurements of the probe temperature indicate that the temperature rise of the probe and coil during the testing time is negligible compared to the plasma temperature. Assuming conduction heat transfer only, the temperature in the region bounded internally by the cylinder with probe radius b can then be calculated for various times τ after the passage of the reflected shock over the coil. These calculations are given by Carslaw and Jaeger [12] and are shown in Fig. 12 for various values of the parameter $\alpha = \kappa\tau/b^2$.

On the same graph is plotted a sensitivity curve for the probe for an electrical conductivity of 20 mho/cm (Fig. 11) which is the average electrical conductivity of the plasma. From this, it appears that correction for cooling may not be needed if the conductivity reading can be obtained within a very short time after the passage of the reflected shock. Working out the above expression for α at 20 mho/cm ($\kappa = 24$ cm^2/s, $b = 1.6$ mm) gives a time of 30 μs for $\alpha = 0.03$ for which the drop in temperature is smaller than 10 percent. Since the circuit has a very small rise time, the reading of the conductivity can be done within 30 μs if no ionization relaxation is present.

Fig. 13 is a typical oscilloscope record at low pressures. This experiment was done with an uncoated probe so that the capacitive coupling between coil and plasma behind the incident shock shows up in the carrier as a reactive unbalance, but not in the output signal of the mixer which is set in the resistive mode. The rise of the conductivity is slow due to ionization relaxation. Before full conductivity is reached, cooling starts to show up as an exponential drop in conductivity, which roughly follows the curves shown in Fig. 12. Irregularities in the conductivity trace occur simultaneously with an increase in pressure (bottom trace) due to multiple shock reflection off the contact surface and shock-tube end plate whereby the gas temperature slightly increases. The electrical conductivity increases slightly until the contact surface passes over the probe when the conductivity drops to zero. The remaining unbalance in the carrier again is due to capacitive coupling.

Fig. 14 is a typical record at medium pressures for a platinum-coated probe. Since there is no coupling capacitance, the carrier signal shows no unbalance before and after testing time. Due to the higher pressures, ionization relaxation is reduced, resulting in a very short rise time of the plasma conductivity followed again by plasma cooling until multiple reflections take place.

Fig. 15 is a record obtained at medium pressures whereby the reference signal is phase aligned for reactive unbalance. If the probe is not coated, capacitive coupling between coil and plasma produces a reactive unbalance from the time the incident shock reaches the coil and shows up as a positive signal. When the reflected shock reaches the coil, the con-

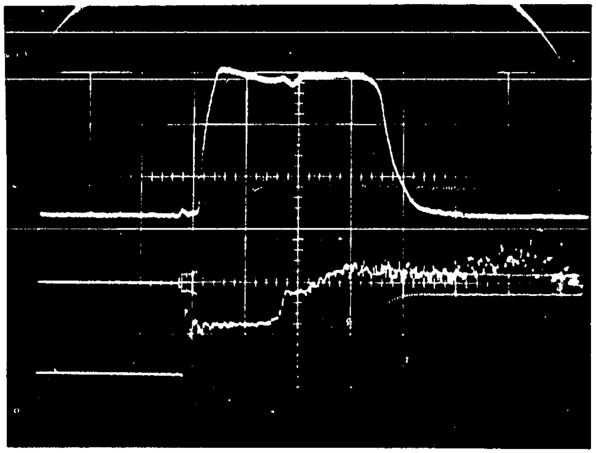

Fig. 13. Oscilloscope record for low-pressure, shock-tube plasma. *Upper trace:* Mixer output for resistive setting 10 mV/cm. *Middle trace:* Modulated signal from bridge 100 mV/cm. *Lower trace:* Pressure at probe 100 mV/cm. Sweep of all traces 200 μs/cm.

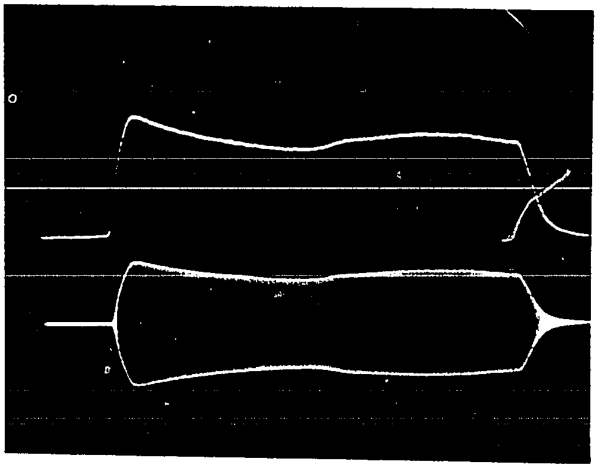

Fig. 14. Oscilloscope record for medium-pressure, shock-tube plasma. *Upper trace:* Mixer output for resistive setting 10 mV/cm. *Lower trace:* Modulated signal from bridge 50 mV/cm. Sweep 100 μs/cm. $P_1=10$ mm. $P_4=300$ psi. $M_s=7$. $\sigma_{id}=21$ mho/cm.

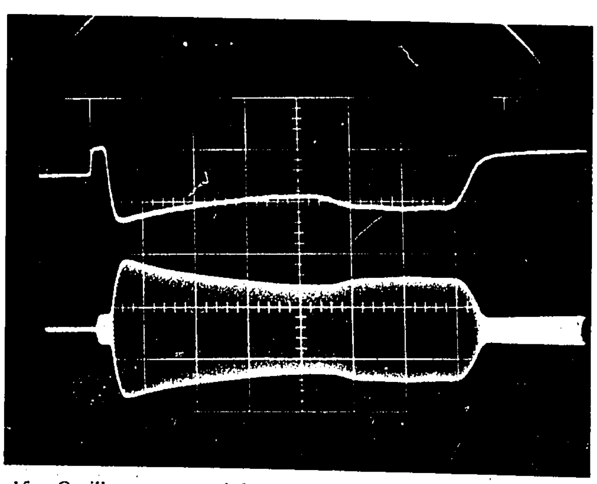

Fig. 15. Oscilloscope record for medium-pressure, shock-tube plasma. *Upper trace:* Mixer output for reactive setting 10 mV/cm. *Lower trace:* Modulated signal from bridge 10 mV/cm.

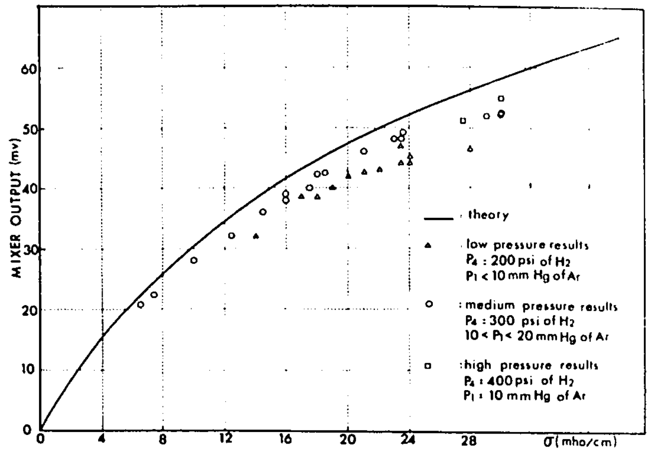

Fig. 16. Comparison between theoretical and experimental results for shock-tube plasma.

ductivity behind it increases sharply and the reactive unbalance created by the inductance change at these conductivity levels (Fig. 6) results in a negative signal, which is again a measure of the electrical conductivity if the system is calibrated for reactive settings. This feature can be used to double check the electrical conductivity in plasmas or to investigate other plasma properties such as boundary layer thickness or Hall effects.

The experimental data are plotted in Fig. 16 and compared with the theoretical results obtained by cross plotting Figs. 6 and 9 with the electrical conductivity as abscissa and the mixer output signal as ordinate. The electrical conductivity for the experiments was based on the incident shock Mach number and the relationship between the ideal electrical conductivity in the reflected shock and the incident shock Mach number from [10].

Since no correction was made for cooling, a discrepancy of 10 percent was expected for the experiments at medium pressure where the conductivity reading was made within 30 μs. At low pressures, the error is larger and can be corrected on the basis of the conduction cooling law (Fig. 12) by extrapolating the conductivity reading down to $\tau=0$. The close relationship between experiment and theory again confirms the feasibility of measuring electrical conductivities with an immersed probe, thereby allowing measurement of the spatial distribution of conductivities which is an important parameter, e.g., in MHD channels.

V. Conclusion

An immersion-type RF plasma conductivity probe has been designed, the performance of which can be predicted accurately by solving the Maxwell equations for the relevant probe geometry. It is shown how the exact solution is simplified in the case of low conductivity, from which assumptions a simple design formula is derived. A parallel-T bridge and phase-sensitive demodulator has been devised which discriminates against unwanted side effects, such as electrostatic coupling and phase misalignment, making possible the independent measurement of in-phase and quadrature components of the signal. Use of the probe with electrolytes and in a shock tube indicates that the theoretical predictions are obeyed with good accuracy over a wide range of conductivities, making the device an absolute measuring instrument, usable without calibration media of known conductivity. A method of allowing for the loss of signal strength due to plasma cooling by the probe is suggested and it is indicated how corrections can be bypassed to obtain experimental results for electrical conductivities within 10 percent of the ideal values, which in most cases is satisfactory.

ACKNOWLEDGMENT

The author thanks P. Savic for providing the theoretical basis and for his very helpful comments concerning this study. He also thanks B. A. Wightman of the NRC Computation Center for developing the Bessel function subroutine for complex arguments.

REFERENCES

[1] P. Savic and E. Stubbe, "Inductive plasma conductivity probes," Dept. of Mech. Engrg., Nat'l Research Council of Canada, Ottawa, Rept. NRC 9248, May 1966.
[2] R. Olson and E. Lary, "Conductivity probe measurements in flames," Research Lab., United Aircraft Corp., East Hartford, Conn., Rept. 2592-62, October 1962.
[3] J. Sprouse, "Measurement of electrical conductivity in a low-density supersonic plasma," Rocket Test Facility, Arnold Engrg. Develop. Ctr., Tenn., Rept. AEDC-TR-65-146, November 1965.
[4] E. Stubbe, "A measurement of the electrical conductivity of plasmas," AIAA Paper No. 66-181, March 1966.
[5] W. Smythe, *Static and Dynamic Electricity*. New York: McGraw-Hill, 1950, p. 302.
[6] A. Erdelyi *et al.*, *Tables of Integral Transforms*, vol. 1. New York: McGraw-Hill, 1954, p. 334, nos. 45 and 48.
[7] I. Gradshtein and I. Ryzhik, *Tables of Integrals Series and Products*. New York: Academic Press, 1965, p. 30, AD(361.2).
[8] W. N. Tuttle, "Bridged-*T* and parallel-*T* null circuits for measurements at radio frequencies," *Proc. IRE*, vol. 28, pp. 23–29, January 1940.
[9] T. Moulin and J. Massé, "Sur la mesure par sonde haute fréquence de la conductivité d'un plasma faiblement ionisé," O.N.E.R.A., France, Tech. Paper No. 111, July 1964.
[10] J. Lau and E. Mills, "Electrical conductivity of inert gases-seed combination in shock tubes," *Canadian J. Phys.*, vol. 43, pp. 1334–1341, July 1965.
[11] I. Shkarofsky, "Values of the transport coefficients in a plasma for any degree of ionization based on a Maxwellian distribution," *Canadian J. Phys.*, vol. 39, pp. 1619–1703, October 1961.
[12] H. S. Carslaw and J. C. Jaeger, *Conduction of Heat in Solids*, 2nd ed. New York: Oxford University Press, 1959, pp. 336–338.

Reprinted from the PROCEEDINGS OF THE IEEE
VOL. 56, NO. 9, SEPTEMBER, 1968
pp. 1483-1493